The early stages of planet formation

Ormel, Christiaan Wessel

rijksuniversiteit
groningen

The early stages of planet formation: how to grow from small to large

Proefschrift

ter verkrijging van het doctoraat in de
Wiskunde en Natuurwetenschappen
aan de Rijksuniversiteit Groningen
op gezag van de
Rector Magnificus, dr. F. Zwarts,
in het openbaar te verdedigen op
vrijdag 10 oktober 2008
om 14.45 uur

door

Christiaan Wessel Ormel

geboren op 6 juni 1981
te Tunis, Tunesië

Promotores	:	Prof. dr. A. G. G. M. Tielens Prof. dr. M. C. Spaans
Beoordelingscommissie	:	Prof. dr. J. Blum Prof. dr. L. B. F. M. Waters Prof. dr. S. Zaroubi

ISBN 978-90-367-3558-2

Cover design by Niels Bos

Printed by: PrintPartners Ipskamp B.V., Enschede, the Netherlands

Contents

1

Introduction

How do planets form? It is a simple question but the answer involves an array of diverse physical processes — complex as well as fascinating. It requires, first of all, to realize what planets really are. For centuries, humans were mystified by the 'wandering stars,' moving relative to a sky composed of thousands of fixed stars that could be seen in full glory on dark nights — as nights undoubtedly were in pre-industrial ages. The movement of the six known planets was explained in the most compelling way by the Ptolemaic (geocentric) model, in which Earth occupied the center of the universe, and where the planets and the sun revolved around it on perfect circular orbits within the celestial sphere composing the stars. To explain peculiarities as retrograde motion secondary circular orbits (epicycles) were superimposed on top of the primary orbit. By the Middle Ages the $\sim$80 epicycles made the Ptolemaic model very elaborate, but also very precise and successful: being fashionable for more than a thousand years, it clearly stood the test of time.

It is only for reasons of simplicity that Nicolaus Copernicus brought up his heliocentric model: putting the sun in the center and letting the planets, including Earth, revolve around it in circular orbits. However, the Copernican model was far short of an accurate explanation of reality — because of its simplicity we would say nowadays — and was only reluctantly put forward by its founder. The tide, however, could not be turned, especially not after the invention of the telescope in the Netherlands in 1608. Exported to Italy, Galileo Galilei used the instrument in perhaps the first series of dedicated pointing observations of the solar system, observing the sunspots, the craters of the Moon, the phases of Venus, and — most importantly — the satellites of Jupiter. His results clearly vindicated the validity of the Copernican model, reducing the status of Earth to that of a mere satellite.

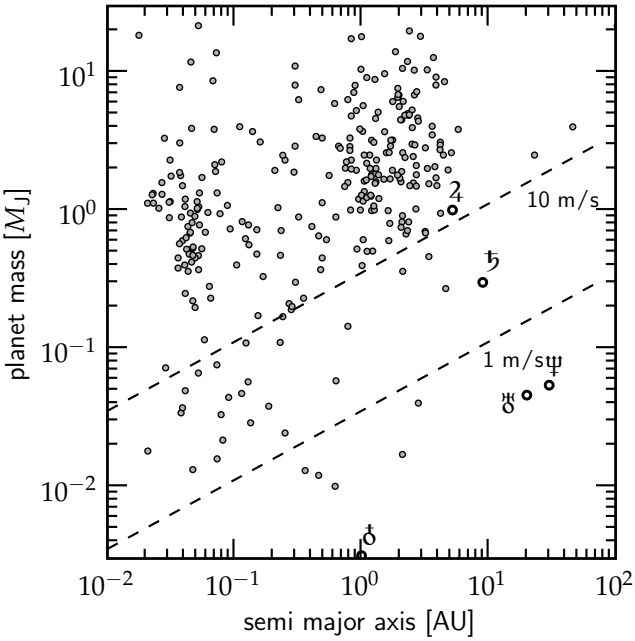

Fg. 1.1: A scatter plot of exoplanet properties as of July 18, 2008 taken from the 'The Extrasolar Planets Encyclopaedia' (see footnote 1). *Circles* show the semimajor axis *vs.* the mass of the planets. Most planets are of Jupiter mass or larger and orbit their star at relatively close heliocentric radii. The observed distribution, however, is affected by selection effects. *Dashed lines* show the mass-radius relation a planet should have in order to induce a motion of, respectively, 1 and 10 m s^{-1} to a star of solar mass. The positions of the Earth and the Jovian planets are indicated with *open circles*.

In the last ∼15 years the discoveries of planets *outside* the solar system marks another milestone in planetary science exploration.[1] In Fg. 1.1 the masses and the semimajor axes of the exoplanets are plotted. Most of the planets are found indirectly, by measuring the motion of the star induced by the presence of a planet. Both the planet as well as the star rotate around their common center of gravity; and although the stellar velocity is much less than the orbital motion of the planet, the resulting Doppler shift in the stellar spectral lines is tiny but detectable. Since recently, extra-solar planets are also found by transit methods, where a tiny dip in luminosity is measured as the planet moves in front of the star. Both methods have a bias towards large, massive objects that orbit the star at short distance, *i.e.,* towards the upper-left side of Fg. 1.1: the 'hot Jupiters.' Notwithstanding these selection effects, Fg. 1.1 shows that at least some planetary systems are quite unlike our solar system, in which the inner rocky planets are separated from the outer gas giants and all move on almost circular orbits. Questions like whether or not the solar system is typical certainly provide a strong motivation to understand the origin of the solar system, and that of planets in particular.

The nebula theory for the origin of the solar system is one of the oldest scientific theories still fashionable today. First proposed in the 18th century by the philosophers Emanuel Swedenborg and Immanuel Kant, and refined later that century by Pierre-Simon Laplace, the nebula theory states that the sun and the planets both condensed out of the same material: a gaseous nebula. The collapse of the nebula caused most of the material to end up in the sun, but conservation of angular momentum

[1] The tally is kept up-to-date at http://exoplanet.eu/ and http://exoplanets.org/.

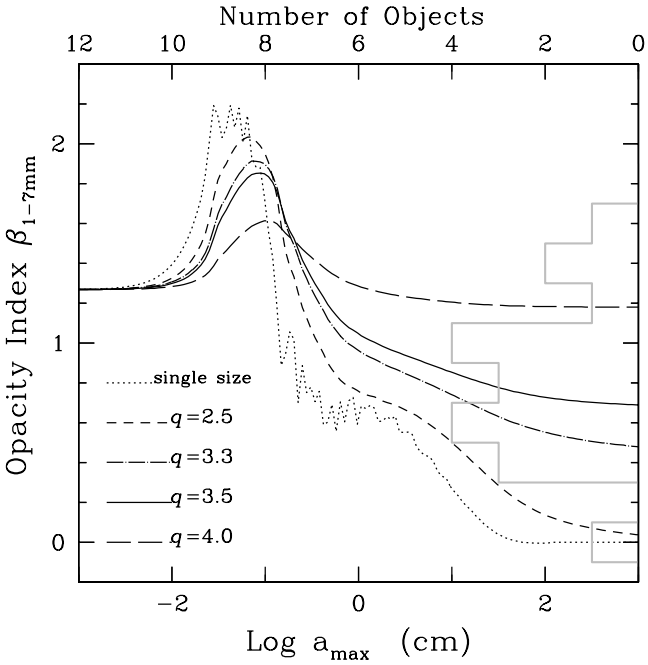

Fig. 1.2: *(curves)* The opacity index β as in $\kappa \propto \lambda^{-\beta}$ as function of the upper cut-off of the power-law size distribution of dust grains, $a_{\max}$. Different curves correspond to different exponents q of the power-law distribution; in all cases $a_{\min} \ll 1$ mm. *(histogram)* Measured opacity index from millimeter observations. Exponents $\beta \lesssim 1$ can only be explained by a high upper cut-off of the grain size distribution, indicating the presence of large particles (Natta & Testi 2004).

also resulted in the formation of a disk. Over the centuries the low specific rotation of the sun compared to that of the planets was an argument against a nebula origin of the planets.[2] In the previous century, however, the nebular theory has seen a re-emergence, with the Soviet scientist Viktor Safronov particularly influential in outlining many features of the current paradigm (Safronov 1969).

The pre-planetary nebula (also: protoplanetary disk) is therefore the place to look for the planet formation process and these disks have indeed been found since the early 80s of the preceding century by the Infra-Red Astronomy Satellite. However, detecting evidence for planet formation is quite a different matter. Because of their reduced surface area-to-mass ratio, larger objects are not favored radiatively and are often only indirectly detected (as with the exoplanets). Moreover, in the disk the macroscopic objects are eclipsed by the many small dust particles, obscuring a direct view of what is going on. Also, planet formation takes place at similar locations as in our solar system; *i.e.*, on AU-scales, small compared to the interstellar scale (parsecs) and even to the initial size of the disk ($\sim$100 AU). Adding, finally, that the process must proceed fast on astronomical timescales (at most millions of years rather than the Gyr lifetime of the average star), it is clear that *in situ* observations of planet formation are quite challenging indeed.

However, as of today there is solid observational evidence that the dust component in the protoplanetary disk is being transformed into bigger bodies. For example, mid-IR studies of the 10 μm silicate absorption line have shown that this

[2]The slowdown of the sun's rotation is now attributed to angular momentum transfer due to stellar winds or jets.

feature in disks differs from the interstellar medium, clearly indicating processing—growth, crystallization, or both—has taken place (van Boekel et al. 2005; Kessler-Silacci et al. 2006; Bouwman et al. 2008). Also, high-resolution imaging with the Hubble Space Telescope have likewise shown that the dust component is changing (Watson et al. 2007; Duchêne 2008). To probe larger particles, observations at longer wavelengths (millimeters) have to be performed. These wavelengths, furthermore, penetrate through the outer layers of the disk; it are observations at mm-wavelength that reveal dust particles have grown in size to millimeter, perhaps centimeter sizes (Natta et al. 2007; Lommen et al. 2007; see Fg. 1.2).

Most scientist agree that the growth of dust grains driven by intermolecular forces is the first step of the planet formation process. Through this process dust grains cluster together in aggregates that grow larger and larger. Numerical and laboratory studies, furthermore, have shown collisions between dust grains to result in growth, provided that the impact energy is sufficiently low (Blum & Wurm 2008). But how benign is the protoplanetary disk really for dust coagulation? The high densities in the disk ensure that initially direct sticking of dust particles by van der Waals forces is effective for small particles; however its effectiveness decreases for macroscopic ($\gtrsim$cm size) particles. Moreover, velocities induced by turbulence and other sources also increase with particle size. Is the growth assumption still probable for these larger particles?

To combine these different physical processes—*i.e.*, the efficiency of particle sticking and the particle relative motions between the particles—into a coherent picture is challenging, especially when this picture should be translated into a model that computes the particle coagulation with time: a collisional evolution model. These questions form a central theme of this thesis, in which we will investigate the feasibility of the dust accumulation processes. This thesis therefore focuses on the early stages of planet formation—the primary accretion process—before the stage where big, km-size bodies (planetesimals) will perturb each other through gravitational forces. In § 1.3 we outline the several topics of this theses (Chapters 2–6). This chapter continues to sketch a general overview of planet formation (§ 1.1) and also provides an introduction into a few concepts that serve as a background to the specialized topics of this thesis (§ 1.2).

1.1 Chronology of the planet formation process

The journey towards a planet starts with a dense cloud of gas and dust in the interstellar medium (ISM). There are many dense clouds in the galaxy, usually held together in huge complexes, giant molecular clouds, in which individual clouds (or cores) are embedded. Thermal pressure equilibrium between the cold, dense cloud and the diffuse, warm surroundings suffices to hold this cloud together (see Tielens 2005 for a review on the phases of the ISM). A special case forms the so called Bonnor-Ebert sphere: these are isothermal spheres in which external pressure balances the thermal pressure of the core. A limited amount of self-gravity can be included, with the sphere shrinking with increasing density. However, when the cloud becomes massive enough such that its mass exceeds a critical mass, referred to as the critical

Bonner Ebert mass or, more generally, the Jeans mass $M_{\rm J}$, gravity starts to dominate the force balance and the cloud collapses. The Jeans mass can be found by equating the gravitational and thermal energy of the cloud (which follows from the virial theorem), *i.e.*, $M_{\rm J} \sim (k_{\rm B}T/G)^{3/2}\rho_{\rm g}^{-1/2}$, where T is the kinetic temperature of the cloud, $\rho_{\rm g}$ the density, $k_{\rm B}$ Boltzmann's constant and G Newton's gravitational constant.[3] In astronomers units

$$M_{\rm J} \approx 2.9\ M_\odot \left(\frac{T}{10\ {\rm K}}\right)^{3/2} \left(\frac{n}{10^4\ {\rm cm}^{-3}}\right)^{-1/2}, \tag{1.1}$$

where $n = \rho/\mu m_{\rm H}$ is the particle density with $\mu \approx 2.34$ the mean molecular mass and $m_{\rm H}$ the hydrogen mass. The Jeans mass is the fundamental mass scale: it explains why stars are of the order of a solar mass. If the core becomes unstable, the collapse occurs on a free-fall (or dynamical) timescale $t_{\rm ff}$, *i.e.*,

$$t_{\rm ff} \sim \frac{1}{\sqrt{G\rho}} \sim 10^5\ {\rm yr} \left(\frac{n}{10^4\ {\rm cm}^{-3}}\right)^{-1/2}, \tag{1.2}$$

which is, from an astronomical perspective, a relatively short timescale. During the collapse, gravitational energy is converted into thermal energy and, when cooling agents are insufficient, the temperature increases, halting further fragmentation because $M_{\rm J}$ increases. Assuming spherical symmetry, the collapse of the cloud can be modeled as inside-out: *i.e.*, the shells near the center of the cloud collapse first (Shu 1977). However, the spherical geometry is quickly broken by the excess rotation of the cloud — rotation that is mainly present in the outer layers and is amplified due to conservation of angular momentum. Due to this angular momentum these shells do not collapse to the central point but end up in the disk.

From an observational point of view the collapse phase is usually identified as 'class 0'[4] (see Fg. 1.3), in which temperatures are still relatively low ($T \lesssim 30$ K). This stage evolves to class I when the central object contracts — forming a protostar — and heats the surrounding envelope and disk to temperatures $T \sim 100$ K. The disk accretion creates an outflow, opening a gap through which stellar photons can escape unhindered. The classical disk+outflow situation so common in astronomical settings is now in place. Initially, the disk is very massive and outflows can be very energetic, especially during so called 'FU-Orionis' outbursts where the accretion rate is much enhanced. After $t \sim 10^5$ yr, when most of the envelope has been blown away and the disk has been reduced to a few percent of the stellar mass, a more steady situation is achieved: the T-Tauri stage for stars of mass less than 2 $M_\odot$ and the Herbig Ae/Be stage for stellar masses of $2 - 8\ M_\odot$. This is the environment in which planet formation takes place.

Accretion[5] is caused by the viscosity of the gas — either molecular or turbulent —

[3] A list of symbols is provided on page 239.

[4] There is some ambiguity in this classification as the 'class' designation is mainly based on observational tracers. Therefore, a new classification scheme, stage 0, 1, 2, *etc.*, based on physical characteristics is occasionally used. For simplicity I will stick here to the more frequently-used 'class' terminology.

[5] Somewhat confusingly the process of dust coagulation — from micron size grains to planets — is also

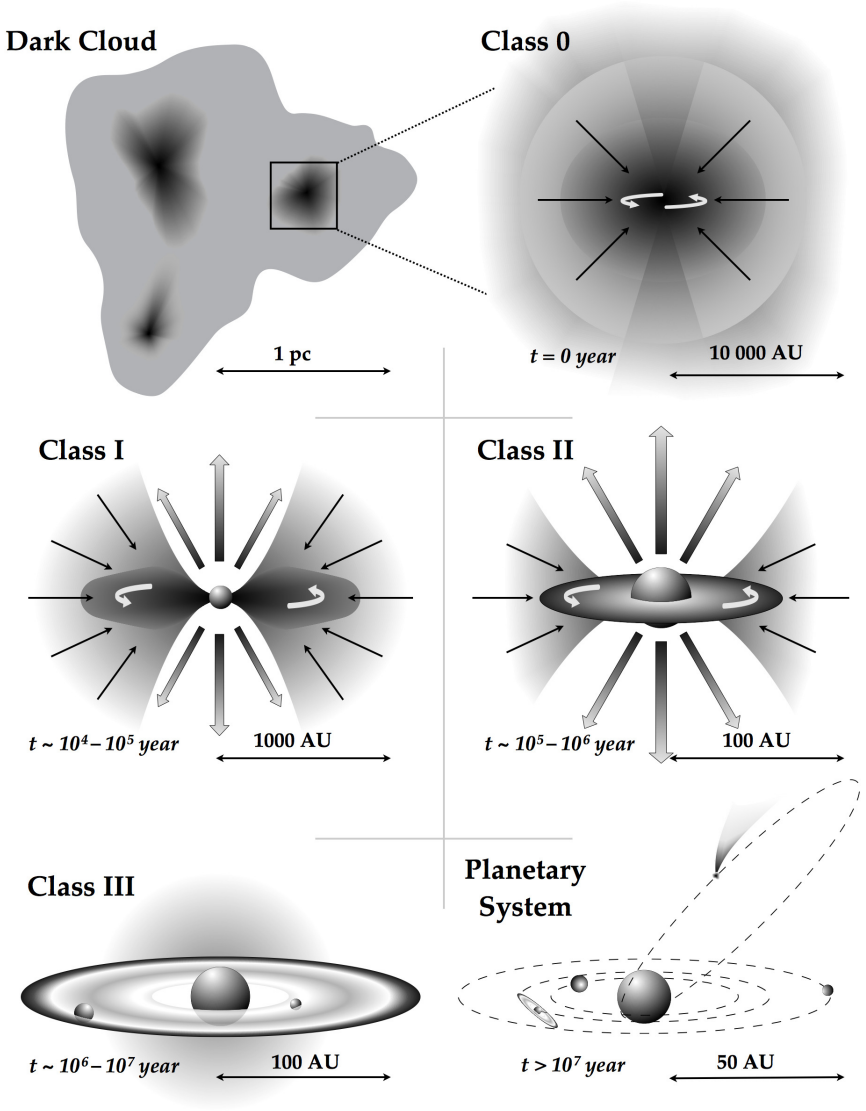

Fig. 1.3: Illustration of the evolving state of the star+disk system for low-mass stars. (*upper left*) Cores form inside a dark cloud and collapse under their gravity. (*upper right*) A central condensation forms; excess angular momentum causes core mass to accrete on a disk. (*middle left*) Heavy disk accretion and removal of angular momentum by an outflow, clearing up the envelope. (*middle right*) Onset of planet formation as disk accretion slows down: the T-Tauri stage; envelope disappears. (*lower left*) Gas disk dissipates away; giant planet formation completed and a debris disk remains. (*lower right*) Possible re-arrangement of the planetary bodies and clean-up. Figure courtesy: Wilfred Frieswijk.

and taps the potential energy in the disk: by moving gas inwards, enormous quantities of gravitational energy are released. Because the gradient in the (Keplerian) gravitational potential Φ is steepest near the inner cut-off, the energies released are determined by the inner radius of the disk, with the stellar radius R_0 being the extreme limit. Thus, the accretion luminosity is

$$L_{\rm A} \sim -\frac{1}{2}\Phi(R_0)\dot{M} \simeq 1.6 \times 10^2\, L_\odot \left(\frac{\dot{M}}{10^{-5} M_\odot\ {\rm yr}^{-1}}\right)\left(\frac{M_\star}{M_\odot}\right)\left(\frac{R_0}{R_\odot}\right)^{-1}, \quad (1.3)$$

where the value of $\dot{M} = 10^{-5}\ M_\odot\ {\rm yr}^{-1}$ for the accretion rate is motivated by the timescale in Eq. (1.2). However, for T-Tauri stars the accretion rate will have subsided significantly and usually values on the order of $10^{-8}\ M_\odot\ {\rm yr}^{-1}$ are observed (Calvet et al. 2004). Since angular momentum is a conserved quantity the disk will also spread to possibly hundreds of AU in radii. Near the protostar ($\sim$0.1 AU) the accretion couples to the stellar magnetic field, which is a complex and probably time-variable state (Hartmann 2005). In short, diverse physical processes operate — gravity, viscosity, magnetic fields — that shape the developing features (disk composition and structure, outflow, stellar properties) of the stellar-disk system.

Once the infall and heavy accretion subside the star becomes a class II object — a classical T-Tauri star for low mass stars. During this stage the star obtains most of its luminosity from gravitational contraction and evolution therefore proceeds on a Kelvin-Helmholtz timescale

$$t_{\rm KH} \sim \frac{GM^2}{R_\star L_\star} = 3 \times 10^7\ {\rm yr} \left(\frac{M_\star}{M_\odot}\right)^2 \left(\frac{L_\star}{L_\odot}\right)^{-1} \left(\frac{R_\star}{R_\odot}\right)^{-1} \quad (1.4)$$

During the T-Tauri phase the star moves from the stellar birthline to the zero-age mean sequence (Palla & Stahler 1999). For stars of low mass this evolution proceeds down along the Hayashi track in the HR-diagram ($\sim$4 000 K), while stars of mass larger than solar develop a radiative core and also move to the left (higher temperatures). Meanwhile, the disk will loose its gas. Several gas dispersal mechanisms may operate (Hollenbach et al. 2000): viscous evolution, stellar encounters, stellar winds or photo-evaporation. Especially photo-evaporation is of importance, where the required number of UV-photons is delivered by accretion. Observations with Spitzer in a sample of T-Tauri stars of age $\gtrsim$5 Myr did not detect any gas (Pascucci et al. 2006), consistent with the result of photo-evaporation models which suggest that the gas dissipates on timescales of $\sim$Myr (Alexander et al. 2006). This timescale is a key constraint on the planet-formation process: *i.e.*, to form the gas giants of our solar system and extra-planetary systems, objects capable of *binding* hydrogen must be present.

The T-Tauri phase is also the stage where the grains in the disk coagulate and a planetary system is formed. From an observational perspective, grain growth is equivalent to the removal of the dust component. Grain growth therefore manifest itself in a decreasing (and disappearing) IR-excess of the spectral energy distribution

referred to as accretion.

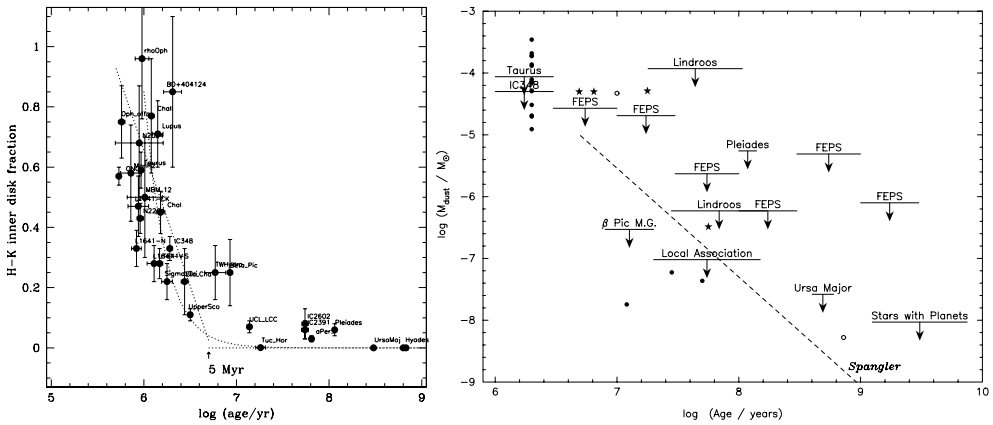

Fig. 1.4: (*left*) Fraction of disks that show near-IR excess with time, binned by cluster or association (Hillenbrand 2005). Near-IR wavelengths only probe the inner disks ($\lesssim$ 0.1 AU). The decay of the Near-IR excess occurs on timescales of $\sim 10^6$ yr, similar to the accretion and gas-dissipation timescale. (*right*) Total disk mass as inferred from sub-mm measurements (Carpenter et al. 2005). Points denoted FEPS results from Spitzer's formation and evolution of planetary systems program. Sub-mm data probe the outer cold dust, and the evolution timescales therefore extend into the debris disks stage.

(SED). The timescales of the decay of the IR-excess depend on wavelength, *i.e.*, on location in the disk. In the inner disk the decay seems to be tied to that of the gas, $\sim$Myr, while the removal of all the (cold) dust takes much longer than that of the gas (see Fg. 1.4).

The high densities in the protoplanetary disks are a prerequisite for coagulation. A key quantity to consider is the collision (or coagulation) timescale

$$t_{\rm coag} = \frac{1}{n_{\rm d}\sigma\Delta v} \sim \frac{a}{\Delta v}\frac{\rho_{\rm s}}{\rho_{\rm d}}, \tag{1.5}$$

where a monodisperse — *i.e.*, all particles have the same size — dust population is assumed with $n_{\rm d}$ the dust number density, $\sigma = 4\pi a^2$ the collisional cross section, Δv the relative velocity, a the size of a dust particle, $\rho_{\rm s}$ the internal density and $\rho_{\rm d}$ the dust spatial density. Inserting canonical values of $a = 1\,\mu$m, $\rho_{\rm s} \approx 3$ g cm^{-3}, and $\Delta v = 10$ cm s^{-1} the timescale for coagulation becomes $t_{\rm coag} \sim 10^{-12}/\rho_{\rm d}$ yr with $\rho_{\rm d}$ in units of g cm^{-3}. The prime difference between a molecular cloud and a protoplanetary disk is the density. Whereas for a $n = 10^4$ cm^{-3} molecular cloud ($\rho_{\rm g} \sim 10^{-20}$ g cm^{-3}) coagulation timescales are millions of years, this is merely on the order of years in disks where gas densities can easily approach 10^{-10} g cm^{-3} (note that the dust mass density $\rho_{\rm d}$ is lower by a factor $\sim 10^2$). While coagulation is already of importance in the molecular cloud phase or the collapse phase (Ossenkopf 1993; Weidenschilling & Ruzmaikina 1994; Suttner & Yorke 2001), significant acceleration takes place in the dense environment of the protoplanetary disk. From Eq. (1.5) it is clear that in protoplanetary disks dust can easily grow very fast to sizes $\gg$meters — but whether

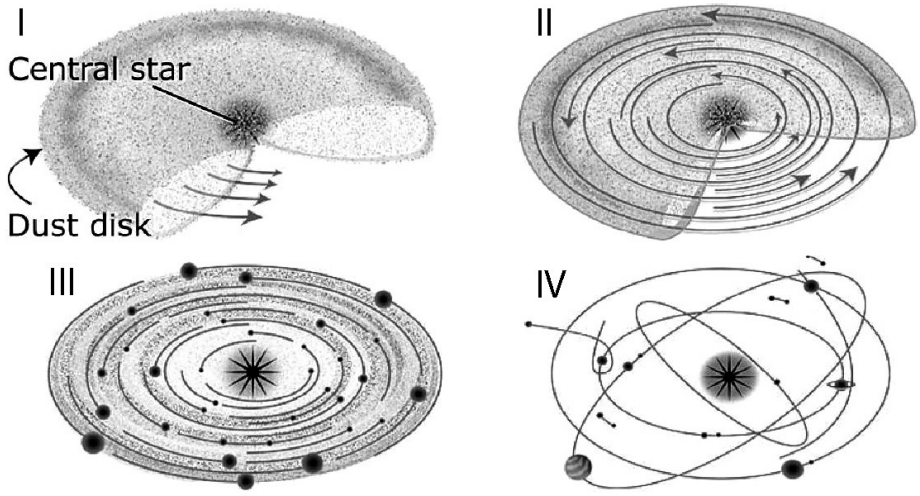

Fig. 1.5: Core-accretion paradigm of planet formation: (i) micron-size dust particles coagulate together into km-size planetesimals: the primary accretion process. (ii) Assisted by mutual gravitational attraction, planetesimals grow into protoplanets during the runaway and the oligarchic stages. Dynamical friction ensures protoplanets remain in circular orbits. (iii) Planets acquire a gaseous envelope from the disk and may migrate through disk-planet interactions. (iv) Long-term chaos due to gravitational interaction between planets push planets onto eccentric orbits or possible ejection out of the solar system.

it does depends on the sticking properties of aggregates.

The transition of the dust component from ISM-grains to planets can be divided in four stages (see Fg. 1.5). In the first phase (which is the topic of this thesis) dust grains coagulate into km-size bodies, the planetesimals. In stage II, gravitational forces between the planetesimals dominate their accretion and also act as a natural sticking mechanism: growth proceeds to from protoplanets of size $\sim 10^3$ km, capable of binding gas. In stage III the massive protoplanets bind gas. Moreover, the protoplanets may interact gravitationally with the gas disk, resulting in their migration. On long timescales (stage IV) the protoplanets will dynamically perturb themselves — resulting in a chaotic accretion phase and ejection. These stages constitute the *core-accretion* scenario of planet formation, in which a solid core is built first before gas is bound. The alternative paradigm for giant planet formation is the *disk instability* scenario, in which the gaseous disk becomes gravitationally unstable (see § 1.2.1).

Dust particles stick together through intermolecular forces, a process which is relatively easy for small particles in dense environments like the protoplanetary disk. However, with growth several processes make this scenario more difficult. First, sticking is a surface area against mass effect, and favors small particles. Second, impact velocities will increase as the particles start to decouple. Turbulence is probably most important in providing particles with a relative motion (see chapter 3) but even

in its absence will dust particles develop a large relative motion at the point where the particles start to decouple from the gas. This decoupling results in a headwind through which meter-size particles at 1 AU obtain a relative velocity of $\sim$10 m s^{-1} (see § 1.2.1)—hence, the meter size barrier. Additionally, the headwind removes angular momentum from the particles, causing it to spiral into the star in a matter of a few hundred years.

Therefore, for an incremental sticking scenario to be viable, the m-size barrier[6] has to be overcome quickly, requiring efficient sticking mechanisms. It is not clear whether this scenario can materialize, *i.e.*, whether the effectiveness of 'ordinary' sticking forces also holds for macroscopic particles, until at a size of $\sim$km gravity can take over. Alternatively, the m-size barrier can be overcome through a gravitational instability of the dust component. This requires one to concentrate particles, perhaps in combination with growth to an intermediate size (see § 1.2.1). Presently, these are all open questions. This lack of understanding is of course a consequence of the aforementioned mentioned observational constraints, although important clues can be obtained from the fossil record of our solar system in the form of chondritic meteorites (see § 1.2.3).

Leaving aside the questions how the dust coagulates and which timescales are involved, a new stage in the accretion process is reached when the particles have grown to sizes of kilometers (planetesimals). This is the size at which gravity drives the accretion and gas-friction may, to first order, be ignored. Due to their mutual gravitational attraction, the collisional cross section, which for small particles is just the geometrical cross section, $\pi(a_1 + a_2)^2 = \pi a_s^2$, is now increases, *i.e.*,

$$\sigma_{ij}^{\rm GF} = \pi a_s^2 \left(1 + \left(\frac{v_{\rm esc}}{\Delta v_{ij}}\right)^2\right), \tag{1.6}$$

with $v_{\rm esc}$ the escape velocity,

$$v_{\rm esc} = \sqrt{\frac{2G(m_i + m_j)}{a_s}}. \tag{1.7}$$

Assuming that $\Delta v > v_{\rm esc}$ and $a \propto m^{1/3}$, the gravitationally-enhanced collisional cross section starts to scale with the 4/3 power of mass, *i.e.*, $\sigma \propto m^{4/3}$, instead of the usual 2/3 power. Besides, if $\Delta v < v_{\rm esc}$ any fragmentation debris will be re-accreted. Gravitationally enhanced growth ($\Delta v < v_{\rm esc}$) therefore occurs in a runaway fashion, in which the most massive particles move away in mass from the lighter ones. The condition for runaway growth may be stated as

$$\frac{{\rm d}(m_1/m_2)}{{\rm d}t} > 0, \tag{1.8}$$

i.e., the most massive particle (m_1) moves away from the second-most-massive par-

[6] in fact the particle size where the dust-gas friction leads to the largest relative velocities depends on position in the disk, see § 1.2.1.

ticle m_2. If β determines the mass accretion rate, $\mathrm{d}m/\mathrm{d}t \propto m^\beta$ then $\beta > 1$ is required for runaway growth. Conversely, if $\beta < 1$ the growth is called 'ordinary' and when $\beta = 1$ the growth mode is 'neutral' (Lee 2000).

The condition $\beta > 1$ requires a dynamically cold disk ($\Delta v < v_{\rm esc}$ such that $\sigma \propto m^{4/3}$), meaning that the eccentricity and inclination of the planetesimals must be kept low. The runaway body must then transfer its energy through dynamical friction to the lower mass planetesimals and they must ultimately loose it by inelastic (non-catastrophic) collisions among themselves or by gas damping (Rafikov 2003; Goldreich et al. 2004b). Many works have simulated this growth stage using N-body simulations and other numerical methods (*e.g.,* Greenberg et al. 1978; Weidenschilling 1997; Inaba et al. 2001; Bromley & Kenyon 2006; Glaschke 2006; Kokubo & Ida 1996, 1998, 2000, 2002). Important concepts during the planetesimal accretion stage are *oligarchy* and *isolation mass*. Assuming that the protoplanets are cooled efficiently and stay in circular orbits, how big can they become? The gravitational sphere of influence of the planetary embryo is given by the Hill radius $R_{\rm H}$. Material within the embryo's Hill sphere is subject to its influence and will be accreted. The Hill radius can be found by equating the local angular velocity around the sun, Ω, with the rotational frequency around the big body, *i.e.,* $GM_\star/R^3 = GM/R_{\rm H}^3$, or

$$R_{\rm H} \sim \left(\frac{M}{M_\star}\right)^{1/3} R. \tag{1.9}$$

The total amount of mass is then easily found and is called the isolation mass, *i.e.,* $M_{\rm iso} \sim 2\pi R \Sigma_{\rm d} 2R_{\rm H}$ with $\Sigma_{\rm d}$ the surface density in planetesimals. Inserting Eq. (1.9) for $R_{\rm H}$ with $M = M_{\rm iso}$ and solving for $M_{\rm iso}$ by eliminating $R_{\rm H}$ gives

$$M_{\rm iso} \sim \frac{(4\pi)^{3/2}\Sigma_{\rm d}^{3/2}R^3}{M_\star^{1/2}} = 5.6\times10^{-4}\,M_\oplus \left(\frac{\Sigma_{\rm d}}{1\ {\rm g\ cm^{-2}}}\right)^{3/2}\left(\frac{R}{1\ {\rm AU}}\right)^3\left(\frac{M_\star}{M_\odot}\right)^{-1/2}. \tag{1.10}$$

(this estimate may be on the low side by a factor of a few; *cf.* Lissauer 1993.) In the Earth's accretion zone $\Sigma_{\rm d} \approx 10$ g cm^{-3} and $M_{\rm iso}$ is comparable to a lunar body, whereas in Jupiter's region $\Sigma_{\rm d} \sim 3$ g cm^{-3} (including ices) and $M_{\rm iso} \sim M_\oplus$. The general nomenclature for this system of runaway bodies accreting planetesimals from separate 'feeding zones' is oligarchy. Note the strong dependence on $\Sigma_{\rm d}$ and, especially, R, indicating that the runaway process in the outer solar system produces larger bodies.

Oligarchy ends when the protoplanets have grown large enough such that dynamical friction and subsequent energy dissipation among small bodies cannot keep pace with viscous heating between the larger bodies. This turning point is roughly reached if the mass in the oligarchs exceeds the mass in the small bodies. Interactions between oligarchs speed up their random motions until they become comparable to the escape speed, $v_{\rm esc}$. Then, the orbits of the oligarchs will cross, plunging the accretion process in utter chaos. Coagulation takes place on the timescale of Eq. (1.5) where $\rho_{\rm d} = \Sigma_{\rm d}/h$ with $h = \Delta v/\Omega$ the thickness of the layer in which the bodies

reside. Thus,

$$t_{\rm coag} \sim \frac{\rho_{\rm s} a}{\Sigma_{\rm d} \Omega} \tag{1.11}$$

which is on the order of $\sim 10^8$ yr for conditions at 1 AU. Of course, for gas giants to form, the time required to produce a $\sim 0.1\ M_\oplus$ 'seed body' able to accrete gas from the nebula must be shorter than the dissipation time of the gas itself! In the outer solar system $M_{\rm iso}$ is larger and here runaway accretion—happening on a much shorter timescale—may be sufficient. However, Pollack et al. (1996) found that gas is only accreted from the disk in significant quantities when its mass is $\sim 10\ M_\oplus$ or larger; before this time, solids still dominated the accretion. For these reasons, Jupiter formation may be a lengthy process, taking several 10^6 yr—a timescale which competes with the gas removal timescale. Moreover, in the outer solar system the escape velocity of the protoplanets may exceed the orbital escape velocity ΩR and much material may be ejected from the planetary system or end up in the Oort cloud.

This relatively long accretion timescale required to produce a $\sim 10\ M_\oplus$ core provide motivations to pursue a scenario in which the gas collapses due to a gravitational instability (Durisen et al. 2007, see § 1.2). Another way to speed-up accretion is by migration of the planetary embryo in a radial direction, such that multiple feeding zones of planetesimals are encountered (Alibert et al. 2005). Several migration mechanisms are possible. In type I migration the gravitational potential of planetary embryos exerts an asymmetric torque on the disk, which causes the embryo to migrate inwards. Tanaka et al. (2002), using detailed hydrodynamical calculations, estimate the migration timescale to be a mere 10^5 yr for earth-like planets. A more massive planet will clear a gap from the disk (which happens when its Hill radius is on the order of the scaleheight of the disk, $H_{\rm g}$); the planet in this type II migration mechanism then moves inwards on a viscous timescale ($\sim 10^5$ yr). Thus, disk-planet interactions are potentially responsible for fast, large-scale re-arrangement processes, which can severely 'shake-up' the planetary system.

In the inner solar system the embryos cannot easily be ejected from the solar system as $v_{\rm esc}$ is less than the Keplerian speed and will merge on the timescale of Eq. (1.11). The stochasticity in this phase determines the final outcome of a planetary system: the planet's masses and eccentricities but also their composition (*e.g.*, the presence of water, Chambers 2001). However, at this stage a lot of remaining 'small-stuff' material—quite significant because it will damp the orbits of the protoplanets—will remain, which ultimately must be accreted by the planets or ejected out of the solar system: the clean-up stage (Goldreich et al. 2004a). Second-generation dust (debris) is created out of fragmenting collisions between the remaining material. On these timescales (10^7 yr) gas will quickly dissipate from the debris disk. Then, fragmentation is the dominant collisional process and the resulting collisional cascade gives rise to a power-law size distribution. The smallest grains (micron-sizes) are removed either through Poynting-Robertson drag (loss of angular momentum due to asymmetric irradiation by the sun) or, for even smaller sizes, through blowout (Meyer et al. 2007).

However, as any $N \geq 3$ body system is unstable, the dynamical evolution of a

planetary system essentially never finishes. Long-term dynamics may ultimately determine the final outcome of planetary systems (Juric & Tremaine 2007). Of particular importance for the solar system may have been the 'late heavy bombardment', responsible for many of the impact craters observed on the moon, that occurred 3.6 Gyr ago. It has been hypothesized that the crossing of the 1:2 resonance between Jupiter and Saturn triggered this event (Tsiganis et al. 2005)—the so called NICE model. At the expense of a certain degree of fine-tuning it explains many of the orbital characteristics of the outer solar system (position and eccentricities of the Kuiper Belt and the major planets).

1.2 Important Concepts

1.2.1 The protoplanetary disk: structure

The gas-rich protoplanetary disk—sometimes also referred to as primordial disk—is the birthplace of planets. During its lifetime many diverse astrophysical processes operate. I will briefly review a few that are important in the context of this thesis, and focus in particular on the way dust particles interact with the gas. The first few paragraphs concern the gas disk and focus on the physical structure of the disk, *i.e.*, the density and temperature distribution and the relevance of turbulent processes. The later paragraphs address the role of the dust component: mechanisms through which particles obtain relative velocities, particle settling, and particle concentration mechanisms.

The gas disk

Clouds have (tiny) amounts of rotation and the instability that sheds the parent cloud of its support, creating the protostar, little affects the angular momentum. Thus, the gas from the outer shells does not fall onto the protostar but, rather, ends up in the disk. Although the amount of matter that ends up in the disk depends on the initial amount of angular momentum present in the core (*e.g.*, Hueso & Guillot 2005), the picture is clear: the large scale geometry of the protostar+disk system is axisymmetric. But what are the physical parameters of the disk, *i.e.*, its temperature and density structure? This requires us to solve the continuity and Navier-Stokes equations for a fluid:

$$\frac{\partial \rho_{\rm g}}{\partial t} + \nabla \cdot (\mathbf{v}\rho_{\rm g}) = 0; \tag{1.12a}$$

$$\frac{\partial \mathbf{v}}{\partial t} + (\mathbf{v}\cdot\nabla)\mathbf{v} = -\frac{1}{\rho_{\rm g}}\nabla P + \frac{1}{\rho_{\rm g}}\nabla\cdot\Pi + \nabla\Phi, \tag{1.12b}$$

where $\rho_{\rm g}$ is the (gas) density, P the pressure, Π the viscous stress tensor and Φ the gravitational potential. In the vertical (z) direction a stationary, isothermal structure (v_z, Π, $\partial\rho/\partial t$ and $\partial T/\partial z$ are all zero) may be assumed as a zeroth-order approximation. Then, if self-gravity can be neglected, the residual vertical force due to the stellar gravity, $\partial\Phi/\partial z = g_{\rm z} = (GM_\star/r^2)z/r = \Omega^2 z$ with G Newton's constant, $M_\star$ the stellar mass and Ω the local Keplerian orbital frequency, is balanced by the pres-

sure force $(\partial P/\partial z)/\rho_g = c_g^2(\partial\rho/\partial z)/\rho_g$, where c_g is the isothermal sound speed

$$c_g = \sqrt{\frac{k_B T}{\mu m_H}} \approx 1.0 \times 10^5 \text{ cm s}^{-1} \left(\frac{T}{300 \text{ K}}\right)^{1/2}. \tag{1.13}$$

Solving the hydrostatic equation for the density gives a Gaussian distribution

$$\rho_g(z) = \frac{\Sigma_g}{H_g\sqrt{2\pi}} \exp\left[-\frac{1}{2}\left(\frac{z}{H_g}\right)^2\right], \tag{1.14}$$

where Σ_g is the surface density ($\rho_g(z)$ integrated over the z-direction) and the disk scaleheight, H_g, is defined as

$$H_g(R) = \frac{c_g}{\Omega}. \tag{1.15}$$

If an optically thin disk is assumed, irradiated by the parent star as is the case in the solar system, the received flux at a distance R is $F \propto L/R^2$. Then, because $F \propto T^4$, the temperature scales as $T \propto R^{-1/2}$ and the sound speed as $c_g \propto R^{-1/4}$. For Keplerian disks, furthermore, $\Omega \propto R^{-3/2}$ results in a disk that is flared, *i.e.*, $H/R \propto R^{1/4}$ increases with radius (see Fg. 1.6). In reality, however, disks are not at all passive: a superheated surface layer is exposed to the most energetic stellar radiation and the midplane regions are only irradiated indirectly. The temperature of the disk midplane is, therefore, lower than 300 K at 1 AU. For a consistent description of the dust temperature and flaring structure the radiation and hydrodynamics must be calculated simultaneously (Chiang & Goldreich 1997; D'Alessio et al. 1998). These calculations nonetheless result in a flared disk and, although the isothermal assumption is strictly invalid, the relations above are useful first order estimates.

For the radial structure the radial velocity component v_R cannot be neglected because the disk evolves viscously. We thus express the viscous stress in terms of a viscosity, *e.g.*, $\Pi = (\rho_g\nu)\nabla \cdot \mathbf{v}$ where ν is the kinematic viscosity (in units of cm^2 s^{-1}). Moreover, under the thin disk approximation Eq. (1.12) can be integrated in the z-direction and expressed in terms of Σ_g rather than ρ_g. A straightforward, but somewhat tedious number of manipulations of the Euler and continuity equations then leads to (Pringle 1981)

$$\frac{\partial\Sigma_g}{\partial t} = \frac{3}{R}\frac{\partial}{\partial R}\left(\frac{1}{R\Omega}\frac{\partial}{\partial R}(R^2\Sigma_g\nu\Omega)\right). \tag{1.16}$$

For a Keplerian disk ($\Omega \propto R^{-3/2}$) this equation shows that under steady-state conditions $\Sigma_g\nu = \text{cnst}$, which reflects the mass flux, $\dot{M} = 3\pi\Sigma_g\nu$. From these considerations it is clear that the viscosity is a key parameter; the question only is which physical processes drive it. The problem is that the molecular viscosity, $\nu_m \sim c_g\ell_{mfp}$ with ℓ_{mfp} the mean free path of a gas molecule, is much too low to be responsible for the observed accretion rate $\dot{M}$. For example, a 1 AU surface density of 10^3 g cm^{-2}

results by Eq. (1.15) in a density $\rho_g \sim \Sigma_g/2H_g \sim 10^{-9}$ g cm^{-3}. This translates into a mean free path of $\ell_{mfp} \sim (2 \times 10^{-15}$ cm$^2 \rho_g/\mu m_H)^{-1} \sim 2$ cm where the prefactor of 2×10^{-15} cm^2 is the molecular cross section. Thus, the molecular viscosity is roughly $\nu_m \sim 10^5$ cm^2 s^{-1}, which would correspond to an accretion rate of only $\dot{M} \sim 10^{-17}\ M_\odot$ yr^{-1}. Another way to see that the molecular viscosity cannot drive the accretion, is to consider the viscous timescale,

$$t_{visc} = \frac{R^2}{\nu_m}, \tag{1.17}$$

which for $R = 1$ AU results in a value of $t_{visc} > 10^{13}$ yr.

MRI turbulence

The astonishing low molecular viscosity led to the understanding that large scale, *i.e.*, turbulent, processes govern the dynamics of accretion disks. This turbulent viscosity, ν_T, must arise from large-scale (L) input of energy, which, in a fashion described by Kolmogorov, cascades down to the smallest scale $\ell_s \ll L$, at which dissipation by the molecular viscosity takes over. This energy transport is often characterized in term of fluctuations — referred to as eddies — where an eddy of scale ℓ is associated with a (random) velocity v_ℓ and turn-over time of t_ℓ. According to Kolmogorov, the rate of energy dissipation ε is constant across the inertial range ($\ell_s \ll \ell \ll L$) . Thus, as $\varepsilon \sim v_\ell^2/t_\ell = v_\ell^3/\ell$ is constant, $v_\ell \propto l^{1/3}$. A common parameterization for the turbulence is, after Shakura & Sunyaev (1973),

$$\nu_T = \alpha c_g H_g = \alpha c_g^2/\Omega \approx L v_L, \tag{1.18}$$

where α is a dimensionless constant, and L and v_L are respectively the large eddy size and velocity scale. Thus, if $c_g \propto R^{-1/4}$ the viscosity is proportional to the radial distance R and a steady-state solution should have a surface density that scales as $\Sigma_g \propto R^{-1}$. An accretion rate of $10^{-8}\ M_\odot$ yr^{-1} results in an α-value of $\alpha \sim 10^{-2}$.

Most numerical simulations (Cuzzi et al. 1993; Dubrulle et al. 1995) fix the turn-over timescale of the largest eddies at $t_L = \Omega^{-1}$. Since $L = v_L t_L$ we thus get a large eddy velocity of $v_L \approx \alpha^{1/2} c_g$. The properties of the small eddies — ℓ_s, v_s and t_s — follow from the Reynolds number, $\mathrm{Re} = \nu_T/\nu_m$, which is typically $\gg$1. For example, $v_s \ell_s = \nu_m = v_L L/\mathrm{Re}$ combined with the Kolmogorov scaling, $v_\ell \propto \ell^{1/3}$, results in $\ell_s = \mathrm{Re}^{-3/4} L$. Similarly, $t_s = \mathrm{Re}^{-1/2} t_L$ and $v_s = \mathrm{Re}^{-1/4} v_L$.

The disk turbulent structure is of immense importance for the velocity field of the dust particles (see chapter 3). However, the question remains which physical processes generate the turbulence? Several instabilities are suggested, ranging from convection to gravitational instabilities, but one — the Magneto-Rotational Instability (MRI) — is perhaps the most likely candidate (Balbus & Hawley 1991; Hawley & Balbus 1991). The MRI requires a weakly magnetized, ionized disk. Numerical calculations indicate that the ensuing turbulence corresponds to $\alpha \sim 10^{-2}$. Thus, there is ample evidence — from these arguments on accretion rates and timescales, but also from meteorites (Cuzzi et al. 2005; Brownlee et al. 2006) — that protoplanetary

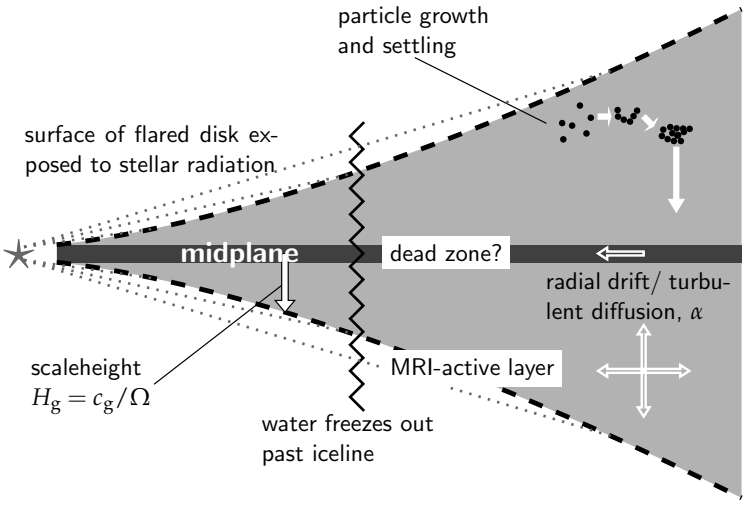

Fg. 1.6: Sketch of the physical structure of the protoplanetary disk. Figure not to scale.

nebulae are turbulent.

There is an important caveat, however. MRI-turbulence requires at least low levels of ionization. Although this may be evident in disk surface layers, where copious EUV and X-rays penetrate, the dense midplane regions are probably too dense, too well shielded, *i.e.,* too neutral for MRI to be operational. How far turbulence permeates the disk is uncertain. Sano & Stone (2002) find that the MRI operates when the magnetic Reynolds number, defined as $\mathrm{Re_M} = v_\mathrm{A}^2/\hat{\eta}\Omega$ where v_A is the Alfven speed and $\hat{\eta}$ the magnetic diffusivity, becomes larger than $\mathrm{Re_M} \gtrsim 1 - 30$. Regions where this criterion is not reached, *i.e.,* the midplane, are commonly referred to as the 'dead zone' (Gammie 1996) and will have a much reduced turbulence. The α-prescription offers some flexibility to deal with this uncertain quantity: just lower the value of the dimensionless constant α. Even then, turbulent motions will dominate the velocity field of small μm-size particles, until, for α as low as $10^{-6} - 10^{-5}$, systematic or thermal motions take over (see below). Another consequence of the disk stratification, *i.e.,* a dead zone amid accreting surface layers, is that the disk can no longer maintain steady state (Fleming & Stone 2003; Gammie & Johnson 2005). In this thesis, however, we always consider the simplifying assumption of a local environment that is characterized by one fixed but uncertain α-value.

Minimum Mass Solar Nebula

How is the surface density of the disk determined? From the arguments above simple estimates can be made. Assuming the gas disk is a few percent of the star's mass, extends over distances of 30 AU, and has a surface density structure that scales as $\Sigma_\mathrm{g} \propto R^{-1}$ (giving a constant $\dot{M}$ in the turbulent α model) we end up with a surface density of $\Sigma_\mathrm{g} \sim 10^2$ g cm^{-2} at 1 AU. Another way to estimate the disk mass and density distribution is from the mass and positions of the planets in the solar system. If one adds up the masses of the inner planets and the rocky cores of the gas giants

(these are the most uncertain) and account for the gas-dust mass ratio of $\sim$100, a disk mass of $\sim$0.013 $M_\odot$ is obtained. This is referred to as the Minimum Mass Solar Nebula (MMSN): the minimum amount of mass needed to form the planets. Moreover, a density distribution can be obtained by spreading out the mass in solids over annuli centered on the planets radius. These studies show that the surface density can best be approximated by a power-law of exponent $-3/2$ (Weidenschilling 1977b; Hayashi 1981), which translates into a surface density of $\rho_g = 1.7 \times 10^3$ g cm^{-2} at 1 AU and $\rho_g = 10$ g cm^{-2} at 30 AU. However, one must acknowledge that these are all *minimum*-mass models; the disk mass could have been much higher during planet formation with solids being thrown into the sun or ejected from the solar system by later processes. Furthermore, the current distribution will not reflect the initial distribution if large-scale re-arrangement processes (*e.g.*, planetary migration) were active in between. Therefore, MMSN models with different power-law exponents are considered; *e.g.*, $\Sigma \propto R^{-1}$ from the steady-state viscosity model (Takeuchi & Lin 2002) or $\Sigma \propto R^{-2.2}$ on the basis of the distribution of solids in the NICE model (Desch 2007). For these reasons MMSN models should be regarded with some caution, but they do serve as a useful beacon outlining the starting conditions of, *e.g.*, a coagulation model.

Gravitational instability

Are disks gravitationally stable? This can be assessed from the Toomre instability criterion, which asserts that instability sets in when the Toomre stability parameter $Q \lesssim 1$, where Q is given by

$$Q = \frac{c_g \Omega}{\pi G \Sigma} \sim 10^2 \left(\frac{T}{100\,\mathrm{K}}\right)^{1/2} \left(\frac{\Sigma_g}{10^3\,\mathrm{g\,cm^{-2}}}\right)^{-1} \left(\frac{R}{1\,\mathrm{AU}}\right)^{-3/2}, \tag{1.19}$$

which is roughly the ratio of stabilizing forces (pressure and rotation) *vs.* gravitational forces. Thus, it seems that the inner regions of the disk are gravitationally stable, unless an unusual amount of material can be compressed. In the outer regions the disk is somewhat more susceptible to become gravitationally-unstable but again it must be massive and also quite cool. However, there are many studies that suggest gaseous disks are, at least initially, (marginally) unstable, and simulations do result in the appearance of gravitationally-bound clumps — the proto-Jupiters (see *e.g.*, Boss 2000 for a classic example of this). This is the disk-instability model for (giant) planet formation and the main alternative to the core-accretion model, in which a rocky core is created first before the accretion of the gas (*e.g.*, Pollack et al. 1996; Hubickyj et al. 2005).

However, to form a planet this way more obstacles have to be overcome; in order to form a clump it has to cool on a timescale less than the orbital period; and, second, the clumps should be able to survive. It is unclear whether giant planets really do form via the disk-instability model; numerical simulations are sometimes ambiguous, *i.e.*, heavily dependent on the chosen assumptions (Durisen et al. 2007). Besides, observations of exoplanets and of the solar system show a strong correlation of planet formation with stellar metallicity (see Lissauer & Stevenson 2007), vindi-

cating the *core-accretion* model. However, the disk instability hypothesis has some attractive features (*e.g.*, it makes gas planets fast) and does produce sound, testable predictions.

Particle-gas interaction, Brownian motion

How do dust and other solid particles interact with the gas? One of the key concepts is the friction time, *i.e.*, the time required to slow down the motions of a particle by friction with the gas

$$\tau_\mathrm{f} = \frac{m v_\mathrm{pg}}{F_\mathrm{D}}, \tag{1.20}$$

where F_D is the drag force and v_pg the (averaged) particle velocity with respect to the gas. Equation (1.21) is merely the time required for the particle's momentum to be slowed down due to friction with the gas, *i.e.*, it is the time required to 'align' both motions. If $a < 9\ell_\mathrm{mfp}/4$, particles are in the free molecular regime in which the Epstein drag law is applicable, $F_\mathrm{D} = 4\pi a^2 \rho_\mathrm{g} c_\mathrm{g} v_\mathrm{pg}/3$, whereas for larger particle sizes a continuum approach applies and the Stokes drag law reads

$$F_\mathrm{D} = \frac{\pi}{2} \mathrm{C_D} a^2 \rho_\mathrm{g} v_\mathrm{pg}^2. \tag{1.21}$$

Here C_D is a drag coefficient that in turn depends on the Reynolds number of the particle $\mathrm{Re_p} = 2a v_\mathrm{pg}/\nu_\mathrm{m}$ (see, *e.g.*, Weidenschilling 1977a). However, in the protoplanetary disk small, micron size particles are always in the Epstein regime for which the friction time is

$$\tau_\mathrm{f} = \frac{3}{4 c_\mathrm{g} \rho_\mathrm{g}} \frac{m}{\pi a^2} \qquad (a \leq \frac{9}{4}\ell_\mathrm{mfp}). \tag{1.22}$$

For example, solid spheres with $\rho_\mathrm{s} = 3$ g cm^{-3} at a location of 1 AU in the MMSN model have friction times of 3 s for micron size particles and $\sim$1 h for mm-size particles. For $a > 4\ell_\mathrm{mfp}/9$ and $\mathrm{Re_p} < 1$ the drag coefficient C_D is proportional to $\mathrm{Re_p^{-1}}$; friction times are then enhanced by a factor $4a/9\ell_\mathrm{mfp}$ with respect to Eq. (1.22) but are still independent of the particle-gas velocity. In the protoplanetary disk, only very massive particles will have $\mathrm{Re_p} > 1$ for which the friction time becomes dependent on the particle-gas velocity.

In turbulence, it means that particles interact differently to eddies of different scales (or, rather, different turn-over times), which cumulatively contribute to providing the particles with a *relative* velocity with respect to the gas and with respect to each other solid particles. Computation of these turbulence-induced relative velocities is the subject of chapter 3. Here we discuss two other sources for relative velocities between particles: Brownian motion and radial drift.

Brownian motion is caused by the momentum transfer due to collisions with gas particles (Einstein 1905). As the gas molecules collide stochastically the particle

trajectory resembles a random walk, leading to an averaged relative velocity of

$$\Delta v_{\rm BM} = \sqrt{\frac{8k_{\rm B}T}{\pi m_\mu}}, \tag{1.23}$$

with m_μ the *reduced mass* of the particles, $m_\mu = m_1 m_2/(m_1+m_2)$. Thus, Brownian motions are important only if one of the masses is small: micron size (for which $\Delta v_{\rm BM} \sim$ mm s^{-1}) or smaller. Since velocities decrease with the $-3/2$ power of the size (of the smallest particle) Brownian motion is negligible for macroscopic particles. Another feature of Brownian motion is that relative velocities are independent of the gas density. Because relative velocities of small particles usually decrease with gas density—*e.g.*, in the case of turbulence and radial drift—the relative importance of Brownian motion increases with increasing density. For protoplanetary disks Brownian motion therefore initiates dust coagulation (Dullemond & Dominik 2005). For molecular clouds, on the other hand, Brownian motion is completely negligible.

Radial drift

Another source of relative motions emerges from the different nature of the gas and solids: whereas gas is (partially) pressure-supported, solids are not. The gas, therefore, rotates at velocities slightly below the Kepler velocity, *i.e.*, because pressure gradients are negative, force balance, $R\Omega_{\rm g}^2 = (\partial P/\partial r)/\rho_{\rm g} + R\Omega_{\rm K}^2$, results in a gas velocity $v = \Omega_{\rm g} R$ that lags the Keplerian velocity $v_{\rm K} = \Omega R$ by an amount $\eta v_{\rm K}$, *i.e.*, $\Omega_{\rm g} R = \Omega R - \eta v_{\rm K}$, with η a dimensionless parameter (Nakagawa et al. 1986)

$$\eta = \frac{1}{2\rho_{\rm g} R\Omega^2}\frac{\partial P}{\partial R} = \frac{1}{2}\frac{c_{\rm g}^2}{v_{\rm K}^2}\frac{\partial \ln \rho_{\rm g}}{\partial \ln r} \approx \frac{c_{\rm g}^2}{v_{\rm K}^2}, \tag{1.24}$$

For example, at 1 AU where $v_{\rm K} \approx 30$ km s^{-1} and $\eta \approx 10^{-3}$ the lag amounts to a velocity of $\Delta v \approx 33$ m s^{-1}. Solid particles, due to their inertia, are not influenced by these pressure forces and tend to move at Keplerian velocities, faster than the gas. The ensuing headwind then removes angular momentum from the particles, causing them to spiral into the sun. How much particles are affected depends on their size, or rather, the surface area-to-mass ratio. Particles that are very well coupled to the gas (*i.e.*, low $\tau_{\rm f}$) this effect is minimal. The same holds for large particles which, due to their large inertia, do not feel the gas at all. It is only in the intermediate regime for $\Omega\tau_{\rm f} \sim 1$ particles that radial drift is important, *i.e.*,

$$v_{\rm rd} = \frac{2\Omega\tau_f}{1+(\Omega\tau_{\rm f})^2}\eta v_{\rm K}, \tag{1.25}$$

(Weidenschilling 1977a) which peaks for particles that have $\Omega\tau_{\rm f} = 1$ at $v_{\rm rd} = \eta v_{\rm K}$. At 1 AU this corresponds to a velocity of ≈ 30 m s^{-1} or a consumption timescale (by the sun) of a little more than 100 yr! Assuming the particles can be modeled as solid spheres with $\rho^{(\rm s)}$ the internal density of the particle, the condition $\Omega\tau_{\rm f} = 1$

corresponds to a size of $a \sim \Sigma_g/\rho^{(s)}$ cm, *i.e.*, meter-sizes at 1 AU and cm-sizes in the outer solar system for a MMSN model. These timescale *and* velocity constraints are an enormous problem for any coagulation theory that involves incremental accretion. However, the other side of the medal is that radial drift motions also *concentrate* particles, since particles merely follow the pressure gradient; *i.e.*, particles will concentrate at any local pressure maximum (Kretke & Lin 2007). Applying this principle to the ice-line where the evaporation will create a pressure maximum, Brauer et al. (2008b) found a small 'window of opportunity' at which radial drift rates will disappear.

Dust settling and particle concentration

Apart from moving radially, particles of any size will feel the star's gravitational pull in the vertical direction, $g_z = GM_\star/R^2 = \Omega^2 R$, and settle to the midplane. By balancing g_z with the drag force one finds a terminal velocity of $v_z = g_z\tau_f = \Omega^2 z\tau_f$ and a settling timescale of $t_{settl} = (\Omega^2\tau_f)^{-1}$, which at 1 AU is a few times 10^5 yr for a 1 μm particle and $\sim 10^2$ yr for a mm-size particle. However, particle *diffusion* will halt the settling for small particles. The timescale for particles to diffuse over a scaleheight H_g is $t_{diff} \sim H_g^2/D_p$, where D_p is the particle diffusion viscosity. For small particles well coupled to the gas $D_p \sim \nu_T$ and the diffusion timescale can be written as $t_{diff} = 1/\alpha\Omega$. Thus, particles of friction times $\tau_f < \alpha/\Omega$ do not settle, while larger particles settle into a disk of scaleheight (Dubrulle et al. 1995)

$$\frac{h_p}{H_g} \sim \sqrt{\frac{\alpha}{\tau_f\Omega}}; \qquad \text{if} \quad \tau_f > \left(\frac{\alpha}{\Omega}\right) \tag{1.26}$$

where $h_p \leq H_g$ is the particle scaleheight. For very heavy particles, $\tau_f > t_L$, the particle diffusion coefficient D_p is reduced with respect to ν_T (the exact amount and dependence on τ_f are somewhat debated, see Youdin & Lithwick 2007; Carballido et al. 2008) and these particles settle into an even thinner disk.

A dust-dominated disk ($\rho_d > \rho_g$) forms when $h_p/H_g > \mathcal{R}_{gd}^{-1}$, where $\mathcal{R}_{gd} = 10^2$ is the cosmic gas-to-dust ratio by mass and where a monodisperse population of particles is assumed . Thus, $\rho_d > \rho_g$ requires $\tau_f\Omega > 10^4\alpha$. For example, for $\alpha = 10^{-6}$ (very weak turbulence) particles must have grown to cm-size before they settle into a dust-dominated layer. Alternatively, a dust-dominated layer is obtained (more easily) if the gas is removed, *e.g.*, by photoevaporation (Throop & Bally 2005). In a dust-dominated layer particles will again rotate at Keplerian velocities, preventing radial drift and being more susceptible for gravitational instabilities. However, with increasing stratification a new instability develops: the Kelvin-Helmholtz instability. This competition between mixing and buoyancy (which stabilizes mixing) is given mathematically by the Richardson number $\mathrm{Ri} \propto z/(\partial\rho_p/\partial z)$ (Youdin & Shu 2002). When Ri drops below a certain threshold, shear turbulence ensues. Shear turbulence prevents the particle layer from becoming gravitationally unstable, until particles are tens to hundreds of meters in size (Cuzzi et al. 1993). Although several instability mechanisms have been proposed they often require very specific conditions (Cuzzi & Weidenschilling 2006); turbulence (either global or shear), together with radial

drift motions prevent (small) particles from concentrating effectively.

Yet another particle concentration mechanism is the turbulence itself. Although throughout this thesis we implicitly assume that turbulence mixes particles effectively, this is only a zeroth-order approximation of the turbulent process. Instead, turbulence is capable of concentrating particles of a specific size. In this way Johansen et al. (2007) find that particles of $\tau_f \sim t_L$ (*i.e.*, m-sizes) become gravitationally-unstable in MRI-turbulence. However, it is unclear whether these boulders would not fragment under these conditions, because radial drift (relative) velocities peak at $\tau_f/t_L = \tau_f\Omega = 1$ (Eq. (1.25)). Likewise, much smaller particles ($\tau_f \sim t_s$: mm-sizes) can be concentrated (Cuzzi et al. 2001); these clumps may then slowly contract under the influence of gravity on a free-fall timescale (Cuzzi et al. 2008). This is an interesting scenario because the mm-scale corresponds to the sizes of the particles that dominate early meteorites: the chondrules (see § 1.2.3).

1.2.2 Dust microphysics: sticking, restructuring and fragmentation

Two material constants — the surface energy, γ, and the modulus of elasticity, $\mathcal{E}$ — determine the sticking behavior of solids. A brief overview of the microphysical processes involved in the collision of dust particles (or aggregates) is given below.

Surface tension is a well-known phenomenon in liquids, *e.g.*, water. The intramolecular forces (in water caused by the strong H-bonds) are responsible for keeping the liquid together. At the surface, however, the symmetry is broken and a tension is created. Energetically, the surface is in a higher energy state than the interior, because it lacks an (attractive) layer above the surface. Since the natural state is a state of lowest energy, surface tension thus the effect of reducing the surface area to a minimum. Therefore, rain drops tend to be spherical, only modified by the influence of gravity. To increase the area of a surface by an amount δA requires an amount of energy of $\gamma\delta A$, where γ is a measure of the surface tension, or the surface energy density.

In solid particles, too, molecular forces are present and they are likewise characterized by a surface energy density, γ. For example, if two (identical) bodies are connected by a surface area A, this requires an energy $2A\gamma$ to separate them to infinity. (The factor of two is because two bodies are involved.) The force required to separate two particles can then be estimated as $F \sim 2A\gamma/\delta$, where δ is the distance over which the bodies are in contact (see Fg. 1.7). For spheres $\delta \sim r^2/2a$ ($\delta \ll a$) where r is the radius of the contact region and $F \sim 4\pi\gamma a$.

A detailed study of contact breaking and formation requires another material property: the elasticity of the material, quantified by the elastic modulus $\mathcal{E}$. It gives the resistance of a material against compression. That is, to compress an object by a relative amount $\Delta x/x_0$, where x_0 is the length of the object and Δx the compression, requires a pressure $P = \mathcal{E}\Delta x/x_0$. Given a certain load (attractive force) the modulus of elasticity then determines the size of the contact area. In the case of two touching spheres the relevant displacement is δ/r and

$$\frac{\delta}{r} = \frac{\delta_1 + \delta_2}{r} = \frac{r}{2a_1} + \frac{r}{2a_2}; \quad (\delta \ll r \ll a_{1,2}). \tag{1.27}$$

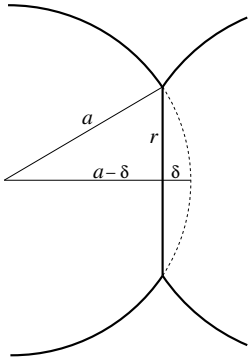

Fg. 1.7: Geometry of the contact area. a: radius of the aggregate; r: contact radius; δ: amount of compression.

From this expression it can be estimated that, in order to produce a contact area of πr^2, a pressure of $P \sim \mathcal{E}\delta/r \sim \mathcal{E}r/a$, or a force of $F \sim \pi\mathcal{E}r^3/a$, must be applied.

Because the deformation of the material is not one dimensional, the elastic modulus must be corrected by Poisson's ratio ν — the ratio of the transverse to axial strain of the material. The effective elastic modulus $\mathcal{E}^*$ follows from $1/\mathcal{E}^* = (1-\nu_1)^2/\mathcal{E}_1 + (1-\nu_2)^2/\mathcal{E}_2$. In the presence of an attractive force, furthermore, the force balance equation, which relates the external force F to the contact area r_0, becomes (Johnson 1987)

$$F = \frac{4\mathcal{E}^* r^3}{3a_\mu} - 4\sqrt{\pi\gamma\mathcal{E}^* r^3}, \tag{1.28}$$

where $a_\mu = a_1 a_2/(a_1 + a_2)$ is the reduced radius. The last term in Eq. (1.28) is zero for the case without an adhesive force ($\gamma = 0$), for which F corresponds within a factor of unity to the expression we previously obtained. For the case of a vanishing force the equilibrium contact radius becomes

$$r = r_e = \left(\frac{9\pi\gamma a_\mu^2}{\mathcal{E}^*}\right)^{1/3}. \tag{1.29}$$

In the tensile case (negative F), the contact radius r first decreases with respect to r_e. However, after a critical pulling force $-F > F_c = 3\pi\gamma a_\mu$ at a contact radius of $r = r_c$, no equilibrium is possible anymore. The particles then separate. Chokshi et al. (1993) calculate that the corresponding energy to break a contact is

$$E_{\mathrm{br}} \simeq 1.8 F_{\mathrm{c}}\delta_c = 43\left(\frac{\gamma^5 a_\mu^4}{(\mathcal{E}^*)^4}\right)^{1/3}, \tag{1.30}$$

where δ_c is the displacement at the critical contact radius. The expression in Eq. (1.30) is the energy required to break an existing contact, and also includes energy dissipation due to excitation of electric waves.

Apart from tensile motions, the grains can also move along the plane of the con-

COLLISIONAL REGIMES

Energy threshold (1)	Collisional outcome (2)	Growth stage (3)
$E < 5E_{\rm roll}$	no restructuring (hit-and stick)	fractal growth
$E > 5E_{\rm roll}$	start of visible restructuring	compaction+growth
$E \simeq N_c E_{\rm roll}$	maximum compression	compaction+bouncing
$E \simeq 3N_c E_{\rm br}$	start loosing monomers	erosion
$E \gtrsim 10N_c E_{\rm br}$	catastrophic destruction of aggregates	fragmentation

Table 1.1: Results of the Dominik & Tielens (1997) numerical collision experiments for aggregates. (1) Collisional energy E in comparison to the critical energy thresholds $E_{\rm br}$ and $E_{\rm roll}$. (2) Outcome of collisions. (3) Corresponding growth regime (indicative). The number of contact areas of an aggregate is denoted by $N_{\rm c}$.

tact surface. In this case, the grains are involved in rolling. Like contact breaking, a critical force is needed to initiate irreversible rolling (in contrast to elastic rolling). Dominik & Tielens (1997) derive the energy required to roll a contact over a distance πa_μ (*i.e.*, $90\,^\circ$ for equal size grains)

$$E_{\rm roll} = 6\pi\xi_{\rm crit} a_\mu \gamma, \tag{1.31}$$

where $\xi_{\rm crit}$ is the critical distance required to initiate the rolling motion, which Dominik & Tielens (1997) estimated to be on the order of the intra-atomic distance, $\xi_{\rm crit} \sim 1$ Å.

A qualitative picture for collisions involving aggregates then emerges from these critical energies in relation to the collision energy (see Table 1.1)

$$E = \frac{1}{2} m_\mu \left(\Delta v\right)^2, \tag{1.32}$$

where m_μ is the reduced mass. Collisions at energies that are both below $E < E_{\rm roll}$ and $E < E_{\rm br}$ are fully in the elastic regime: the contacts are not displaced. At higher energies, restructuring of the aggregate will occur. Porous aggregates can restructure by rolling of the constituent monomers, provided that the individual grains—monomers—are loosely bound. Thus, porous aggregates will restructure until a more compact and more stiff state is reached. In compact aggregates, on the other hand, the monomers have more neighbors and rolling is inhibited. Because the sound travel time for aggregates is often much shorter than the collisional timescale (Paszun & Dominik 2008b), the collisional energy is generally well distributed over the entire grain, which prevents breaking. However, at higher energies $E > N_{\rm c} E_{\rm br}$ (with $N_{\rm c}$ the total number of contacts) the particles will be disrupted.

Dominik & Tielens (1997) and, recently, Wada et al. (2007) have performed numerical experiments for aggregate collisions and confirmed this qualitative picture (see Table 1.1). However, the values for the critical energies derived by the theoretical study of Dominik & Tielens (1997) were not matched by collisional experiments (Poppe et al. 1999; Heim et al. 1999). In these, it was found that critical collisional

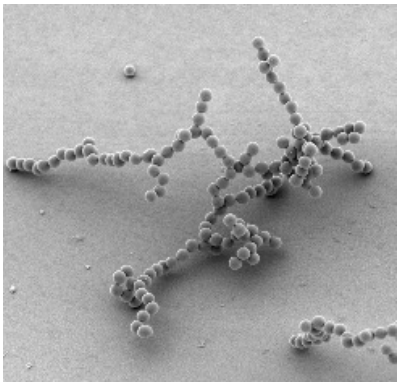

Fig. 1.8: Example of fractal aggregates produced by differential sedimentation in a laboratory experiment (Blum 2000). The fractal dimension is $D_\mathrm{f} = 1.8 \pm 0.1$. The size of the individual grains is 0.95 μm in radius.

thresholds are higher than the theoretical predictions. Clearly, Dominik & Tielens (1997) presents an idealized picture, *i.e.,* the monomers are perfect smooth spheres, whereas, in reality surface roughness and asperities will complicate the picture. For example, plastic deformation of these irregular features may explain the high sticking velocity measured experimentally (Paszun & Dominik 2008b). However, Blum & Wurm (2000) showed that their collision experiments are still in agreement with the framework outlined in Table 1.1 by re-adjusting the critical energy thresholds E_br and E_roll — several factors of 10 larger than the theoretical values. Over the last decade laboratory experiments have contributed significantly to the present physical picture of dust aggregation (see Blum & Wurm 2008 for a review). In this work we will use the results of these laboratory experiments for the two critical energies.

Fractal growth

In the regime where the collisional energy is less than a few times the rolling energy, *i.e.,* $E < 5E_\mathrm{roll}$, the colliding dust particles will stick at the point where they meet: 'hit-and-stick' growth. In many cases this growth represents fractal properties, *i.e.,* the relation between the number of grains in an aggregate N and the size a_out is then given by

$$N = k_\mathrm{f} \left(\frac{a_\mathrm{out}}{a_0} \right)^{D_\mathrm{f}} \qquad (1 \leq D_\mathrm{F} \leq 3), \tag{1.33}$$

where D_f is the fractal exponent, a_0 the monomer size and k_f a prefactor of order unity. Linear strings have $D_\mathrm{f} = 1$, $D_\mathrm{f} = 2$ for planar structures (*e.g.,* PAH molecules), and $D_\mathrm{f} = 3$ for homogeneous (compact) particles. However, in general the fractal exponent will have non-integer values (see Fg. 1.8 for a typical example of an aggregate formed by laboratory experiments). The fractal dimension of an aggregate depends on its growth history. Two specific modes are usually distinguished (see Fg. 1.9): growth by similar size particles (cluster-cluster coagulation or CCA) and growth by monomers (particle-cluster coagulation or PCA). The latter case leads to a fractal dimension of 3 in the limit of $N \gg 1$, whereas CCA typically has fractal dimensions of around two. Therefore, hit-and-stick growth of equal-size aggregates will lead to

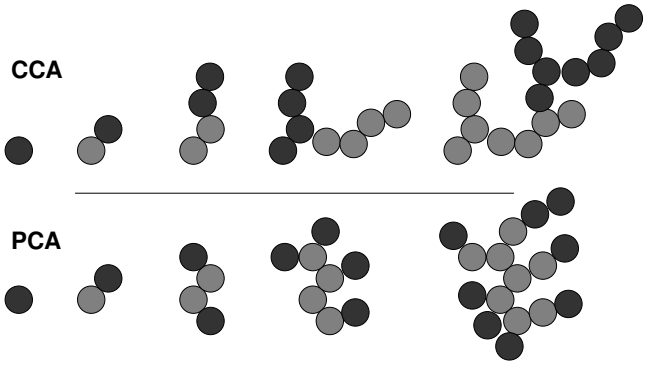

Fig. 1.9: Schematic illustration of cluster-cluster coagulation (CCA, *top*) *vs.* particle-cluster coagulation (PCA, *bottom*) in two dimensions. In PCA the incoming grains (*black*) collide with the cluster (*grey*) individually, whereas in CCA the incoming grains are also clustered, resulting in an overall more open (fluffy) structure.

very open (fluffy) structures.

Another concept related to the porosity of these fluffy aggregates is their *geometrical* size a. It is defined in terms of the angularly-averaged projected surface area of the aggregate A, *i.e.*, $A = \pi a^2$. It is this quantity that is of importance in the calculation of the drag force. Therefore, the size that must be used in expressions like Eq. (1.22) is a, and not the extremal or outer radius, $a_{\rm out}$. Similarly, A can be expressed as a fractal law like Eq. (1.33), $A \propto N^{\delta}$. Meakin & Donn (1988) find that δ approaches unity for large N; whereas the CCA calculation of Ossenkopf (1993) result in $\delta = 0.95$ (note that δ cannot be larger than unity as this would indicate that the geometrical area grows faster than mass).

1.2.3 The solar system: meteorites

Complementary to (high-resolution) observations of protoplanetary disks, the remnant solid bodies of our our planetary system provide valuable clues on the conditions of the solar system during planet formation, which could be applicable for other systems as well. Most interesting are the bodies that preserved their internal structure, *i.e.*, the ones that did not melt or were not involved in large-scale differentiation processes (like the Earth where the most dense material — iron — sunk to the core). From time-to-time meteorites fall on Earth and, if they remain intact, can be studied using modern laboratory equipment (see Fg. 1.10). Meteorites, especially chondritic meteorites, are therefore a means to provide observational constraints on scenarios regarding primary accretion: having formed within the first few million years after the origin of the solar system, in a disk that was still gas-rich, they are the real fossils of the solar system. The dominant component of these chondrites are chondrules: $\sim$100 μm to mm-size stony spherules composed primarily of the silicate minerals olivine and pyroxene. Here, I briefly sketch the background regarding chondrule and chondrite properties, mainly focusing on the physical picture. However, meteorites are renowned for their rich chemical complexity and for a more complete introduction readers are encouraged to browse more thorough works (*e.g.*, Lauretta & McSween 2006).

First of all, chondrites are very diverse. One of the reasons why this diversity appears is that they can be meticulously studied in laboratories. Thus, instead of

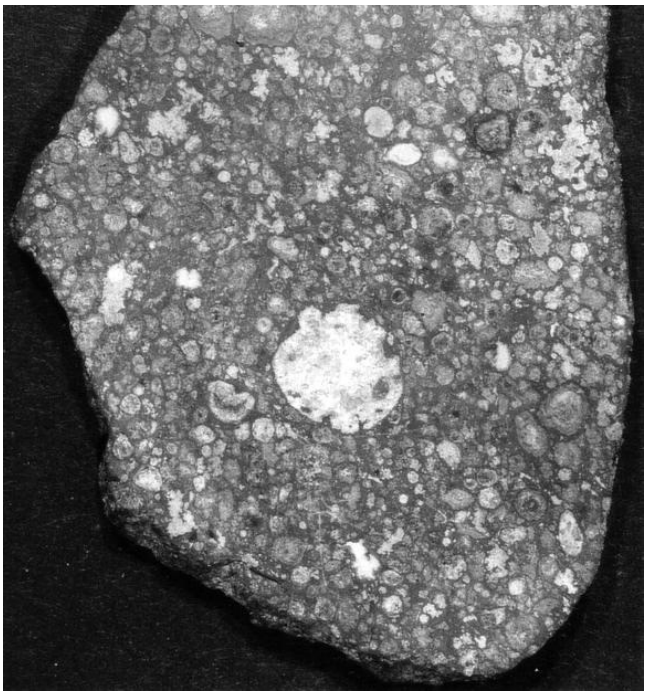

Fg. 1.10: The Allende carbonaceous chondrite which fell on Mexico, 1969. Most of the fragments seen here are chondrules: several 100 μm-size spherules embedded in a dark dusty matrix. The big white spot in the center of the image is a Calcium Aluminum Inclusion (CAI) of size $\sim$1 cm. It can be seen that the chondrules are mostly separated from each other, and are sometimes enshrouded by a rim of fine-grained dust material.

a single property like the size of a dust grain, or perhaps its porosity, laboratory measurements provide the full chemical state (*e.g.*, relative abundance of volatiles or isotopes). A cause for the diversity in chondrite properties are the variety of so called 'parent body processes' that the chondrules and matrix material endured *after* asteroid formation but which did not lead to its complete melting. Examples of these (geological) processes include: aqueous alteration (chemical reactions including water), abrasion (shaking up the asteroid), and metamorphism (change in mineralogy of the meteorite due to heating). Some chondrites endured more of these alteration effects than others, which explains part of their diversity. However, chondrites also show an intrinsic diversity in physical properties; *e.g.*, the relative proportion and mean size of chondrules varies between meteorite classes.

There are many different theories regarding the formation of chondrules. Chondrules show evidence of being melted, requiring temperatures of $\sim$1500 K for only a brief period of time (minutes or hours) . This seems best reconcilable with a 'shock heating' scenario in which the chondrule precursors could be dust particles (or aggregates of dust particles). In another class of theories chondrules are produced near the sun, and then transported throughout the solar system by an X-wind (Shu et al. 1994). One remarkable property of chondrules is that their sizes distribution within a given meteorite (class) is quite narrow, commonly within a factor of 10 and centered at $\sim$300 μm. This could reflect the property of their dusty precursors or was perhaps intrinsic to the shock-formation event. However, the (mean) size and chemical makeup of chondrules varies from meteorite to meteorite, which perhaps indicates

that the chondrule-producing processes that operated in the protoplanetary disks were different in space and time (Wood 2005). The question how chondrules formed is still vividly debated.

Calcium aluminum inclusions (CAIs) are another conspicuous component of chondrites that formed even earlier. Although much rarer, they are typically a factor of 10 larger than chondrules. Radio dating put their formation date at 4.5672 Gyr ago, which is conveniently referred to as the 'zero-time' of the solar system. After this point chondrites formed over a time span of a few million years. As chondrites formed out of these chondrules and CAIs, this would also indicate that planetesimal formation (or chondrite formation) was a relatively prolonged process, *i.e.,* happening over much of the life-span of the solar nebula.

Chondrites consist of another physical component in the form of micron size (silicate) dust particles. These are present throughout the chondrite in a matrix component or are found surrounding chondrules in the form of fine-grained rims (see Fg. 1.10). This configuration suggests that chondrules and dust are accreted together into the chondrites which implies that the matrix and rim material reflects conditions during the nebula phase, *i.e.,* when chondrules were still freely floating objects, (Metzler et al. 1992), although the precise interpretation is disputed (Trigo-Rodriguez et al. 2006). For instance, a positive correlation between the rim thickness and chondrule size is observed, which is in agreement with a scenario of sweep-up of dust in a turbulent nebula (Cuzzi 2004).

1.2.4 Coagulation: modeling

In the previous sections various physical processes have been discussed that are of importance for dust growth: the various sources of relative velocities, particle concentration, the nature and compositions of the particles and their relation to sticking forces; particle fragmentation. The challenge is to combine all these processes into one coherent evolution model. These models are referred to as coagulation models and it is instructive to provide a brief outline here.

In the case where a (gravitational) potential affects the particle motions — like, *e.g.,* in many cosmological simulations — N-body integration techniques may be used to calculate the temporal evolution of the system. However, if no potential is present the particles may be assumed to be ideally mixed and the distribution does not depend on spatial coordinates. The distribution function is then given by $f(m)$: the number density of particles in the interval $m, m + \mathrm{d}m$. To generalize, one may further sub-divide $f(m)$, adding other properties of the population. For example, $f(m, \phi)$ includes the filling factor ϕ of dust aggregates such that $f(m, \phi)\mathrm{d}m\mathrm{d}\phi$ is the number density of particles of mass $[m, m + \mathrm{d}m]$ and filling factor $[\phi, \phi + \mathrm{d}\phi]$. Using only the mass to characterize the particles, the collisional evolution of the distribution function $f(m)$ is given by the Smoluchowski equation

$$\frac{\partial f}{\partial m} = -f(m) \int K(m, m') f(m')\, \mathrm{d}m' + \frac{1}{2} \int K(m', m - m') f(m - m') f(m')\, \mathrm{d}m', \quad (1.34)$$

where the first term denotes the removal of particles of mass m due to coagulation with any other particles, and the second term represents the particles of mass m

created by collisions of a particle pair whose masses end up to be m (the factor of $1/2$ prevents double counting). The rate coefficient, $K(m, m')$, gives the probability of collision between a particle of mass m and m'. Equation (1.34) only considers sticking as a collisional outcome but a generalization to other physical processes (bouncing, fragmentation) is straightforward.

To calculate the collisional evolution, Eq. (1.34) has to be solved. Except for three very symmetric cases of the collision kernel — (i) $K = \text{cnst.}$, (ii) $K \propto m_i + m_j$, and (iii) $K \propto m_i m_j$ — this cannot be done analytically. Equation (1.34) is in fact a rather complex integro-differential equation, which is notoriously difficult to solve, even numerically. For example, mass conservation is easily violated when Eq. (1.34) is integrated directly. For this reason, most works involving dust coagulation do not explicitly solve the Smoluchowski equation but instead calculate the interaction rate $K(m_i, m_j) f(m_i) f(m_j)$ between the bins and then transfer this mass to the receiving bin (*e.g.*, Spaute et al. 1991).

In this thesis, however, we will take into account the internal structure as a second — and independent — parameter. Then, the Smoluchowski equation should be extended to a second dimension and it is less straightforward to calculate. This holds, in essence, for all grid-dependent techniques: more dimensions require more connections between the grid points. Although in two dimensions a successful integration of the Smoluchowski equation has been performed (Ossenkopf 1993), in this thesis we do not use the distribution function f to calculate the collisional evolution. Instead, a 'direct simulation Monte Carlo' (DSMC) technique is developed to follow the collisions between the particles individually. The distribution function is then obtained indirectly, after binning the particles, but is not used in the code itself.

The Monte Carlo method is a quite intuitive tool to solve coagulation problems as the probability of an event (a collision) is simply given through K. More specifically, the collision rate is $C_{ij} = K_{ij}/\mathcal{V}$ where $\mathcal{V}$ is the volume of the simulation and $C_{ij}\Delta t$ is the probability of a collision between the particles i and j in the (infinitesimal) time-interval Δt. Random numbers then determine which of the $N(N-1)/2$ (where N is the total number of particles involved in the simulation) collision events is the next. A more thorough introduction to the applied Monte Carlo technique is provided in § 2.3 or can be found in, *e.g.*, Gillespie (1975). The great advantage of the MC-simulation technique is that the collisional part of the model is naturally separated from the time-evolution part, contrary to the bin-techniques in which both parts are intertwined in the mass transfer. The main drawback of Monte Carlo models, however, are the limited numbers of particles that can be included, since the calculation and adjustment of the collision rates would otherwise strain computational resources. This will especially apply to distributions that are very broad or skewed, *e.g.*, where the massive particles dominate the total mass, whereas the smaller ones dominate the number. Suitable approximations in these cases should be sought.

1.3 This thesis

The emphasis of this thesis lies on coagulation of dust, either in the environment of protoplanetary disks (chapters 2, 4) or of molecular clouds (chapter 6). Here, the

challenge — and a major theme of the thesis — is to combine a physical model like that of § 1.2.2 with an accurate calculation of the collisional evolution of the system with time. In chapter 2 the framework of this model is outlined. Concepts of porosity, rephrased in terms of an enlargement factor, and Monte Carlo coagulation are introduced. The internal structure is included self-consistently, *i.e.*, not only are the outcomes of collisions determined by the internal structure but the internal structure is likewise affected by the collisions themselves. The results are then applied to the upper layers of the protoplanetary disks, with the primary aim of illustrating the new approach compared to conventional approaches.

As outlined in the preceding sections, turbulence is an important phenomenon in protoplanetary disks. It is the driving force behind the relative velocities of particles; therefore, an accurate description is of key importance for dust coagulation models. However, most models of dust coagulation are statistical — a full-blown hydrodynamic simulation would be too time consuming — and the effects of turbulence are included indirectly, usually with an analytic prescription of the relative velocities. Völk et al. (1980), in a pioneering work, presented a framework for the calculation of these velocity expressions, subsequently refined by Markiewicz et al. (1991). However, apart from specialized cases (Cuzzi & Hogan 2003) the expressions for the relative velocity, although analytic, were not cast in closed-form. It is the aim of chapter 3 to present such (approximate) closed-form expressions that can be easily implemented in coagulation models.

Being the dominant component of chondritic meteorites, chondrules must have played an important role in the primary accretion process. However, how were these tiny stony particles incorporated into big asteroids? In chapter 4 we look at the importance of the dust component of meteorites: are these μm-size particles responsible for sticking chondrule-size particles together? It is an appealing idea because the meteorite record shows that the dust component is scattered throughout the meteorite — in most cases the chondrules do not touch — *i.e.*, we may naturally expect that chondrules have swept up the dust (Cuzzi 2004). Could these chondrule-rimmed dust particles have facilitated the accretion process? In chapter 4 the feasibility of this model is thoroughly investigated.

Planet formation is above all a problem of scales. Models tracing the collisional evolution must therefore be able to handle a very large size-range: the journey from a 0.1 μm grain to planet Earth covers over 40 orders of magnitude in mass! In chapters 2, 4 and 6 we present Monte Carlo models that incorporate the internal structure in the collisional evolution. However, one drawback of MC-models is that particle collisions are usually treated one-by-one and is therefore best suited to situations where the size-distribution remains narrow. On the other hand, a wide size distribution, which may be obtained if fragmentation processes operate, is characterized by a multitude of collisions and is much harder to model. The aim of chapter 5 is to develop a solution to this problem, which we found in (physically) grouping the particles. The advantage of such an approach is that MC-simulations are no longer constrained to a physical limit in, *e.g.*, mass, and become applicable for runaway kernels as well. Chapter 5 is therefore predominantly a theoretical treatise which will find its way to future applications.

The final chapter forms the culmination of the new approach to the collisional evolution. Its collision model features many of the elements of the preceding chapters—the formulation of hit-and-stick growth and the grouping method—but is also based on the outcomes of state-of-the art numerical simulations (Paszun & Dominik 2008a), in which collisions between (small) aggregates are simulated. Collisional fragmentation is an integral part of the model. Here, we have decided to apply the model to the environment of molecular clouds, or rather, cores of molecular clouds, because the average size of dust aggregates in these environments is more comparable to the sizes studied in the numerical collision experiments. However, if dust particles are coated with ice—a more formidable sticking agent—orders of magnitude growth may again be expected. Within the context of this thesis, it is of special importance to contrast the collisional evolution in the pre-collapse phase with that of the protoplanetary disk.

2

Dust coagulation in protoplanetary disks: porosity matters[1]

— C. W. Ormel, M. Spaans, A. G. G. M. Tielens —

Sticking of colliding dust particles through van der Waals forces is the first stage in the grain growth process in protoplanetary disks, eventually leading to the formation of comets, asteroids and planets. A key aspect of the collisional evolution is the coupling between dust and gas motions, which depends on the internal structure (porosity) of aggregates. To quantify the importance of the internal structure on the collisional evolution of particles, and to create a new coagulation model to investigate the difference between porous and compact coagulation in the context of a turbulent protoplanetary disk. We have developed simple prescriptions for the collisional evolution of porosity of grain-aggregates in grain-grain collisions. Three regimes can then be distinguished: 'hit-and-stick' at low velocities, with an increase in porosity; compaction at intermediate velocities, with a decrease of porosity; and fragmentation at high velocities. This study has been restricted to physical regimes where fragmentation is unimportant. The temporal evolution has been followed using a Monte Carlo coagulation code. This collision model is applied to the conditions of the (gas dominated) protoplanetary disk, with an α parameter characterizing the turbulent viscosity. We can discern three different stages in the particle growth process. Initially, growth is driven by Brownian motion and the relatively low velocities involved lead to a rapid increase in porosity of the growing aggregate. The subsequent second stage is characterized by much higher,

[1]Originally published in *Astronomy & Astrophysics*, vol. 461, p. 215 (2007)

turbulent driven velocities and the particles compact. As they compact, their mass-to-surface area increases and eventually they enter the third stage, the settling out to the mid-plane. We find that when compared to standard, compact models of coagulation, porous growth delays the onset of settling, because the surface area-to-mass ratio is higher, a consequence of the build-up of porosity during the initial stages. As a result, particles grow orders of magnitudes larger in mass before they rain-out to the mid-plane. Depending on the precise value of α and on the position in the nebula, aggregates can grow to (porous) sizes of $\sim$10 cm in a few thousand years. We also find that collisional energies are higher than in the limited PCA/CCA fractal models, thereby allowing aggregates to restructure. It is concluded that the microphysics of collisions plays a key role in the growth process.

2.1 Introduction

Understanding the formation of planetary systems is one of the central themes of modern astrophysics. New stars form in molecular cloud cores when these cores contract under the influence of gravity. This contraction leads to the formation of a central object surrounded by a disk (Shu et al. 1987). Planets are generally thought to form in these disks, but neither the precise physical conditions required for, nor the processes involved in planetary body assemblage are well understood. Generally, it is thought that grain growth starts with the sticking of sub-micron-sized grains colliding at low velocities (Weidenschilling & Cuzzi 1993). The sticking is then driven by weak van der Waals interaction forces between the grains. Relative velocities may reflect Brownian motion or differences in coupling to turbulence in the disk. Eventually, when the grains have grown to $\sim$cm-sizes, they will settle to the mid-plane of the disk, forming a thin dust layer where further growth to planetesimal sizes can take place (Safronov 1969; Weidenschilling & Cuzzi 1993).

There is much observational support for the growth of dust grains in protoplanetary disks from sub-micron to millimeter size scales. In particular, the contrast of the 10 μm silicate emission feature relative to the local continuum shows that the grain size in the disk's photosphere—where these features originate—has increased from sub-micron sizes characteristic for interstellar dust, to the micron-sized range (van Boekel et al. 2003; Meeus et al. 2003; Przygodda et al. 2003; Kessler-Silacci et al. 2006). Furthermore, observations of the continuum (sub)millimeter emission—originating from the deeper layers of protoplanetary disks—show typical grain sizes in the range of millimeters, outside the range of interstellar grain sizes by many orders of magnitudes (Beckwith & Sargent 1991). Additional support for the importance of collisional grain growth follows from analytical studies of solar system dust. In particular, many interplanetary dust particles (IDPs) collected at stratospheric altitudes, consist of a large number of small grains assembled in a very open structure as expected for collisional aggregates (Brownlee 1979). These types of IDPs are thought to derive from comets and, indeed, comets may consist largely of such loosely bound aggregates. In addition, chondrules recovered from meteorites show dust rims which are generally attributed to collisional accretion processes in the so-

lar nebula before the meteorite and its parent body were assembled (Metzler et al. 1992; Cuzzi 2004).

The properties of the dust are of key importance to the evolution of protoplanetary disks. First and foremost, planet formation starts at the dust size and the dust characteristics at the smallest sizes will set the table for further growth. Second, the opacity is dominated by absorption and scattering by dust grains. Hence, the radiative transfer, temperature structure, as well as emission spectrum of protoplanetary disks are controlled by the characteristics of the dust (Beckwith et al. 2000; Bouwman et al. 2000). Third, in turn, the temperature structure will dominate the structure of the disk, including such aspects as flaring. Fourth, dust grains provide convenient surfaces that can promote chemical reactions. Specifically, ice mantles formed by accretion and reactions between simple precursor molecules are widespread in regions of star formation (Gibb et al. 2004; Boogert et al. 2004). In fact, grain surfaces may be catalytically active in the warm gas of the inner disks around protostars, converting CO into CH_4 (Kress & Tielens 2001).

Most early studies of the coagulation process and the characteristics of the resulting aggregates assumed hit-and-stick collisions where randomly colliding partners stick at the point of initial contact (Meakin 1988; Meakin & Donn 1988; Ossenkopf 1993). The structure of the aggregate then depends on whether the collision is between a cluster and a monomer (PCA) or between two clusters (CCA). The latter leads to very open and fluffy structures with fractal dimensions less than 2, while the former leads to more compact structures and a fractal dimension (for large aggregates) near 3. Ossenkopf (1993) also investigated the pre-fractal limit in which aggregates consist of $\lesssim 1000$ monomers. He provides simple analytical expressions for, *e.g.*, the geometrical and collisional cross-section in the case of PCA and CCA aggregation. These expressions include a structural parameter, x, which describes the openness (or fluffiness) of the particle. In this study we also introduce a structural parameter and confirm its importance in coagulation studies.

Over the last decade much insight has been gained in the structure of collisional aggregates through extensive, elegant, experimental studies (Blum et al. 2002; Blum 2004) supported by theoretical analysis (Chokshi et al. 1993; Dominik & Tielens 1997). These studies have revealed the importance of rolling of the constituent monomers for the resulting aggregate structure. At low collision velocities, the hit-and-stick assumption is well justified but at high collision velocities, aggregates will absorb much of the collision energy by restructuring to a more compact configuration. At very high velocities, collisions will lead to disruption, fragmentation, and a decrease in particle mass. The critical velocities separating these collisional regimes are related to material properties such as surface free energy and Young's modulus as well as monomer size and the size of the clusters.

While the porous and open structure of collisional aggregates is well recognized, their importance for the evolution of growing aggregates in a protoplanetary setting is largely ignored. Most theoretical studies represent growing aggregates either by an equivalent sphere (*e.g.*, Weidenschilling 1984a; Mizuno et al. 1988; Tanaka et al. 2005; Nomura & Nakagawa 2006) or adopt the fractal dimension linking mass and size characteristic for CCA or PCA growth (*e.g.*, Weidenschilling 1997; Suttner & Yorke

2001; Dullemond & Dominik 2005). Ossenkopf (1993) and Kempf et al. (1999) explicitly account for aggregates' internal structure in their numerical models, although, due to computational reasons, only a limited growth can be simulated. Indeed, the internal structure of collisional aggregates is the key to their subsequent growth. The coupling of aggregates to the turbulent motion of the gas is controlled by their surface area-to-mass ratio, while the relative velocity between the collision partners dictates in turn the restructuring of the resulting aggregate. Moreover, as a result of the growth process from sub-micron-sized monomers to cm-sized aggregates, the coupling to the gas velocity field may well change due to compaction. Indeed, compaction can be an important catalyst for aggregates to settle out in a mid-plane dust layer. Despite its importance for the collisional growth of aggregates in a protoplanetary environment, the evolution of porosity has not yet been theoretically investigated. The present chapter focuses precisely on this aspect of grain growth in protoplanetary disks.

This chapter is organized as follows. In § 2.2 a model is presented for the treatment of the porosity as a dynamic variable. This entails defining how porosity, or rather the openness of aggregates, is related to the surface area-to-mass ratio (§ 2.2.2) as well as quantifying how it is affected by collisions (§ 2.2.3). In § 2.3 a Monte Carlo model is presented to compute the collisional evolution, taking full account of the collisional aspect and all features of the porosity model. Section 2.4 then applies the model to the upper regions of the protoplanetary disks. Results from the porous model of this chapter are compared to traditional, compact models. In § 2.5 we discuss the differences of the new collision model with respect to PCA and CCA models of aggregation and also discuss our results from an observational perspective, before summarizing the main results in § 2.6.

2.2 Collision model

Dust grains are dynamically coupled to the turbulent motions of the gas and 'suspended' in the (slowly accreting) protoplanetary nebula. Upon collisions, these small dust grains can stick due to van der Waals forces, forming larger aggregates. Eventually, when these agglomerates have grown very large (∼cm-sized), they will decouple from the gas motions and settle in a thin disk at the mid-plane. Further collisional growth in the mid-plane can then lead to the formation of planetesimals (∼km-sized). Up to this point, growth is driven by weak van der Waals forces, but for km-sized planetesimals gravitational forces take over and rapid growth to a planet takes place. Here we focus on this process of small grains suspended in the nebula forming larger conglomerates. Coagulation is driven by the relative grain velocities. Velocities and the kinematics of dust in a turbulent nebula are discussed in § 2.2.1. The frictional coupling between dust and gas depends largely on the area-to-mass ratio of the grains and hence on the internal structure of the dust. Section 2.2.2 describes the relation between the area-to-mass ratio and the porosity of the dust agglomerates. In § 2.2.3, we discuss experimental and theoretical studies on the microphysics of dust coagulation and develop a simple model, given in the form of easily applicable recipes, which describes how the mass and porosity of the dust evolve

in collisions between two dust agglomerates. In § 2.2.4, finally, we compare these recipes in the fractal limit to the frequently used formulations of Particle-Cluster Aggregation (PCA) and Cluster-Cluster Aggregation (CCA).

2.2.1 The turbulent protoplanetary disk

For the characterization of the gas parameters of the protoplanetary disk we use the minimum-mass solar nebula (MMSN) model as described by Hayashi (1981) and Nakagawa et al. (1986). The surface gas density of the disk, Σ_g, is assumed to fall off as a -1.5 power-law with heliocentric radius (R) and the temperature scales as $R^{-1/2}$. The vertical structure of the disk is assumed isothermal, resulting in a density distribution which is Gaussian in the height above the mid-plane, z. The scaleheight of the disk, H_g, is an increasing function of radius, $H_g = c_g/\Omega \propto R^{5/4}$, with c_g the local isothermal sound speed and Ω the Keplerian rotation frequency. The thermal gas motions will induce relative (Brownian) velocities between dust particles with a mean rms-relative velocity of

$$\Delta v_{BM}(m_1, m_2) = \sqrt{\frac{8k_B T(m_1 + m_2)}{\pi m_1 m_2}}, \tag{2.1}$$

with m_1, m_2 the masses of the particles and k_B Boltzmann's constant. Except for low mass particles of size $\lesssim 10\ \mu$m, these velocities are negligibly small when compared to the relative velocities induced by the coupling with the turbulent gas. We assume that the turbulence is characterized by the Shakura & Sunyaev (1973) α-parameter,

$$\nu_T = \alpha c_g H_g = \alpha c_g^2/\Omega \approx v_L L = v_L^2 t_L, \tag{2.2}$$

with v_L, L and t_L, respectively, the velocity, the size and the turn-over time of the largest eddies. According to the standard (Kolmogorov) turbulence theory, turbulent energy is injected on the largest scales and transported to and eventually dissipated at the smallest eddies—characterized by turn-over time (or dissipation timescale), t_s, velocity, v_s, and scale size, ℓ_s, given by $\nu_m = v_s \ell_s$, with ν_m the molecular viscosity.[2] We can then define the Reynolds number as, $\mathrm{Re} = \nu_T/\nu_m$, giving $v_s = \mathrm{Re}^{-1/4} v_L$ and $t_s = \mathrm{Re}^{-1/2} t_L$. If t_L is assumed to be (of the order of) the Kepler time (Dubrulle & Valdettaro 1992), $t_L = 2\pi/\Omega^{-1}$, the turbulence is fully characterized by the α-parameter (see Fig. 2.1):

$$t_L = 2\pi\Omega^{-1}, \qquad t_s = \mathrm{Re}^{-1/2} t_L \tag{2.3a}$$

$$v_L = \alpha^{1/2} c_g, \qquad v_s = \mathrm{Re}^{-1/4} v_L \tag{2.3b}$$

$$L = \alpha^{1/2} H_g, \qquad \ell_s = \mathrm{Re}^{-3/4} L. \tag{2.3c}$$

This specification of turbulence is of importance, for, together with the friction times of two particles, it determines the (average root-mean-square) velocity be-

[2] $\nu_m = c_g \mu m_H / 2\rho_g \sigma_{mol}$ with μ and σ_{mol}, respectively, the mean molecular weight and mean molecular cross-section of the gas molecules.

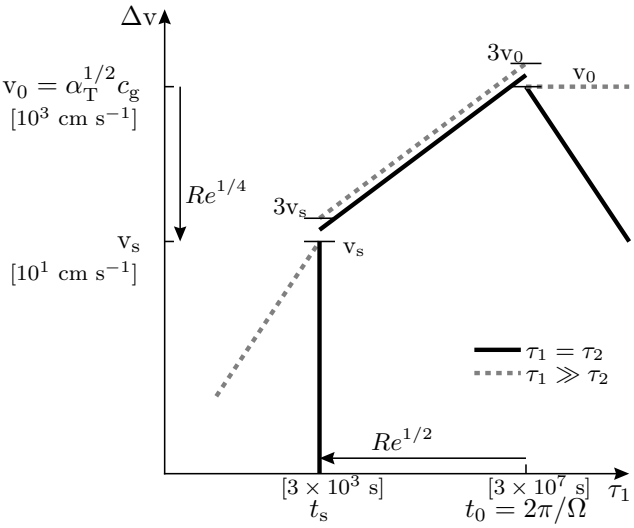

Fg. 2.1: Sketch of the turbulence induced relative velocities, Δv, as function of friction time, τ_1, for equal friction times, $\tau_1 = \tau_2$, (*solid line*) and different friction times $\tau_2 \ll \tau_2$ (*dashed line*) according to the analytic fits of Eqs. (2.5a, 2.5b) (after Weidenschilling 1984a). t_L and v_L are set by the global properties of the disk, while the range over which turbulence is important is determined by the Reynolds number, Re. Values between brackets denote typical values for $t_L = 1$ yr, $c_g = 10^5$ cm s^{-1} and $\alpha = 10^{-4}$.

tween the particles, Δv_{ij}, which in turn plays a crucial role in both the collision model of this section as well as in the time-evolution model of § 2.2.3. The relative velocities are a function of the friction time (τ_f) of the particles — the time it takes a particle to react to changes in the motion of the surrounding gas — which in the Epstein limit is[3]

$$\tau_f = \frac{3}{4 c_g \rho_g} \frac{m}{A}, \tag{2.4}$$

where ρ_g is the local mass density of the gas, m the mass of the particle and A its cross-section. In particular, if the friction time of a particle is much smaller than the turnover time of the smallest eddy ($\tau_f \ll t_s$), the particle is coupled to *all* eddies and flows with the gas. Therefore, grains with $\tau_f \ll t_s$ have highly correlated velocities. Eventually, however, due to growth and compaction, agglomerates will cross the Kolmogorov 'barrier' (*i.e.*, $\tau_f > t_s$) and are then insensitive to eddies with turnover times smaller than τ_f, since these eddies will have disappeared before they are capable of 'aligning' the particle's motion. At this point, grains can develop large relative motions (Fg. 2.1).

To calculate relative velocities accurately, contributions from all eddies have to be included. Völk et al. (1980) started quantifying these effects by dividing eddies into several classes and subsequently integrated over the full Kolmogorov power spectrum. With the exception of some special cases of the particle's friction times (Cuzzi & Hogan 2003) in which Δv can be expressed analytically, Δv between particles with different τ_f can be presented only numerically (Völk et al. 1980; Markiewicz et al.

[3]The Epstein limit holds for particles with sizes smaller than the mean-free-path of the gas, $a < \frac{9}{4}\ell_{mfp}$. If this limit is exceeded, friction times increase by a factor $\frac{4}{9} a/\ell_{mfp}$ and quadratically scale with radius (Whipple 1972; Weidenschilling 1977a; Schräpler & Henning 2004).

1991). Weidenschilling (1984a,b), however, has presented analytical fits, which have been frequently applied in subsequent coagulation models (*e.g.*, Suttner & Yorke 2001; Dullemond & Dominik 2005; Tanaka et al. 2005). For particle friction times, τ_1 and τ_2 ($\tau_1 \geq \tau_2$), less than t_L, these read,[4]

$$\Delta v_{12}\left(\tau_1,\tau_2\right) = \begin{cases} v_\mathrm{s}\dfrac{(\tau_1-\tau_2)}{t_\mathrm{s}} & \tau_1,\tau_2 < t_\mathrm{s} \\ v_\mathrm{s}\dfrac{3}{1+\tau_2/\tau_1}\sqrt{\dfrac{\tau_1}{t_\mathrm{s}}} & t_s < \tau_1 < t_\mathrm{L}, \end{cases} \tag{2.5a}$$

where τ_1 is the larger of the two friction times. If τ_1 exceeds t_L the relative velocities become,

$$\Delta v_{12} = \begin{cases} v_\mathrm{L} & \tau_2 < t_\mathrm{L} < \tau_1 \\ v_\mathrm{L}\dfrac{(\tau_1+\tau_2)t_\mathrm{L}}{2\tau_1\tau_2} & \tau_1,\tau_2 > t_\mathrm{L}. \end{cases} \tag{2.5b}$$

For example, in the regime where both friction times are small ($\tau_1,\tau_2 < t_\mathrm{s}$) the turbulence induced relative velocity is negligible when $\tau_2 \approx \tau_1$, but scales linearly with τ_1 when particle 2's mass-to-area ratio is much larger than that of particle 1 (Fg. 2.1). Thus, in the $\tau_1,\tau_2 < t_s$ regime particles with very different A/m-ratios will preferentially collide, because differential velocities are then highest. When one of the particles' friction time exceeds t_s the dependence on the absolute difference in τ_f vanishes and the relative velocities now scale with the square root of m/A of the largest τ_f. As can be seen in Fg. 2.1 relative velocities are rather insensitive to the precise ratio of the particles' friction times in this regime. (Because of the simplicity of the expressions for Δv in Eqs. (2.5a, 2.5b) the lines do not connect at $\tau_1 = t_s$ and $\tau_1 = t_\mathrm{L}$.) In the $\tau_\mathrm{f} > t_\mathrm{L}$ regime, (Eq. (2.5b) relative velocities would stop increasing and eventually become only a minor perturbation to the motion of the particle. These large τ_f regimes are, however, not reached in the early stages of coagulation considered in this chapter. Here, it is clear that the relative grain velocities are regulated by the area-to-mass ratio of the colliding grains which sets the friction timescale (Eq. (2.4) and hence the velocities (Eqs. 2.5a, 2.5b).

2.2.2 Porosity of agglomerates

For compact, solid particles,[5] the area-to-mass ratio scales linearly with the size. However, for porous aggregates the A/m ratio depends on the internal structure of the aggregates. In this section, we discuss how the internal structure of the aggregates affects collisions and, conversely, how collisions affect the aggregates' internal structure. The internal structure is modeled using the enlargement parameter. Here, we define an *enlargement parameter* ψ that is the ratio between its extended volume,

[4] Dullemond & Dominik (2005) note that the second expression in Eq. (2.5a) may not exceed v_L.

[5] The reader should note that the words 'particle', 'agglomerate' and 'aggregate' are frequently interchanged throughout this and other paragraphs.

V, and its compact volume, V^*, *i.e.*,

$$\psi = \frac{V}{V^*}, \qquad \psi \geq 1. \tag{2.6}$$

Here, V^* is the volume the material occupies in its compacted state, *i.e.*, without pores, and V the total (extended) volume of the particle. While V^* reflects the mass of the particle, V is related to the spatial extent of the aggregate. Here, V has been defined as the volume corresponding to the geometric cross-section of the aggregate (see Fg. 2.2). Figure 2.2 shows three aggregates of 1 000 monomers, such that V^* is the same, though with different degrees of compaction. The (from left to right) decreasing compaction translates to an increased geometric cross-section, A (outer circle), of the aggregates and hence to an increased ψ. Using the linearity between V^* and m and Eq. (2.6), two parameters, *e.g.*, m and ψ, determine A and, consequently, also determine the coupling with the gas (Eq. (2.4).

An enlargement factor of $\psi = 1$ thus corresponds to a particle in which the internal density is the same as the specific density of the material, $\rho_\mathrm{s} = m/V^*$. For aggregates, this limit is never reached, since pores contribute to the volume even in the most compact configuration. An enlargement factor of $\psi = 1$ can then only be achieved by melting the aggregates, a mechanism we will not consider in this work.[6] Since $\psi \geq 1$ we refer to ψ as the enlargement parameter or enlargement factor. ψ is related to the structural parameter, x, of Ossenkopf (1993), as $x \propto \psi^2$. Note the close relationship between ψ and porosity; a higher ψ means more open aggregates, *i.e.*, higher porosity. Therefore, we will also use this more familiar reference for ψ, but only in a qualitative sense.

Since our enlargement parameter, ψ, is defined in order to match the geometrical cross-section, A, of a particle, we refer to the resulting radii, $a(\psi)$, as geometrical. The other cross-section of importance in coagulation models is σ, the collisional cross-section. Ossenkopf (1993) has consequentially defined a 'toothing radius', a_tooth, such that $\sigma = \pi(a_{\mathrm{tooth},1} + a_{\mathrm{tooth},2})^2$ and provides expressions for a_tooth for PCA and CCA aggregates. σ is larger than A by a factor of order unity (see also Krause & Blum (2004)) and also depends slightly on the structure of the aggregates, *i.e.*, whether PCA or CCA. In this chapter, however, we are mainly concerned with obtaining a model for ψ and have therefore simply used a for the calculation of the collisional cross-section. Likewise, we have also ignored augmentations of σ due to effects such as, *e.g.*, charges and grain asymmetries (see again Ossenkopf 1993) and rotation of grains (Paszun & Dominik 2006).

The aggregates' internal structure has important consequences for the coagulation rate. The geometric cross-section scales, for example, as $\psi^{2/3}$. More subtle are the effects of ψ on relative velocities, which, as seen above, depend critically on the A/m-ratio of both aggregates. In coagulation models where grains are represented as compact bodies τ_f increases linearly with size ($A \propto m^{2/3}$; $\tau_\mathrm{f} \propto m^{1/3}$). However, in the initial stages of coagulation aggregates stick where they meet — a process characterized by a build-up of porous, fluffy structures, which can be described by frac-

[6] However, we have not put a lower limit to the porosity of the aggregates. Note also that the discussion in Ormel et al. (2007) regarding the definition of V^* is slightly erroneous.

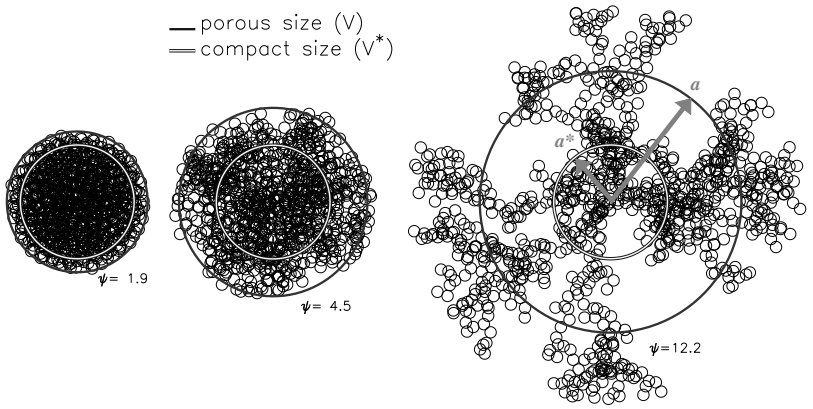

Fig. 2.2: Projections of fractal aggregates illustrating the relation between A, V and V^*. All fractals consist of 1 000 monomers and have consequently the same compact volume, V^* (*inner circle*). The black, *outer circle* gives the area, A, equal to the total projected surface area of the agglomerate. This area subsequently defines the volume, V (*e.g.*, $V \sim A^{3/2}$) and the enlargement factor, ψ, of the aggregate (Eq. (2.6)). Arrows denote the compact and porous radii, a^* and a.

tals. Meakin & Donn (1988) have computed the A/m ratio of an initially monodisperse population and found a profound flattening of this ratio as compared to compact models in which it decreases as $m^{-1/3}$. Often, in the 'hit-and-stick' regime the growth shows fractal behavior and the cross-section can be directly parameterized as a power-law, *i.e.*,

$$A \propto m^{\delta}, \qquad \tfrac{2}{3} \leq \delta \leq 1. \tag{2.7}$$

The lower limit $\delta = \frac{2}{3}$ corresponds to the growth of compact particles, whereas the upper limit of $\delta = 1$ denotes the aggregation of chains or planar structures. In the cluster-cluster coagulation (CCA) model of Ossenkopf (1993) $\delta = \delta_{\mathrm{CCA}} = 0.95$, a result that agrees well with the findings of Kempf et al. (1999), using N-particle simulations in the Brownian motion regime. More recent models, which also include rotation of aggregates (Paszun & Dominik 2006) also confirm this exponent. The scaling of friction time and enlargement factor with mass then become

$$\tau_{\mathrm{f}} \propto m^{1-\delta}, \qquad \psi \propto m^{\frac{3}{2}\delta-1}, \tag{2.8}$$

such that for compact aggregation models ($\delta = 2/3$) ψ stays constant. On the other hand, in models of cluster-cluster aggregation ($\delta \approx 1$), area scales roughly as mass and τ_{f} stays constant or is only weakly dependent on mass, while ψ increases monotonically. Thus, in CCA relative velocities are rather insensitive to growth. As a result, collisions are also less energetic in CCA models, *e.g.*, as compared to compact aggregation models.

The key to the coagulation process in protoplanetary disks is the coupling of the dust to the turbulent motions of the gas and the resulting velocity distribution. In essence, the enlargement parameter ψ provides a relationship between mass and surface area for growing aggregates which controls this gas-dust coupling. Equation (2.8) provides a relation for the evolution of ψ, but this relation is only valid in certain specific aggregation models, *e.g.,* CCA-coagulation, where similar, equally sized aggregates meet. In reality, however, collisions between particles of all kinds of sizes will occur, although, dependent on the parameters that determine Δv, some are just more probable than others. In the end, the growth of grains in protoplanetary disks is controlled by the individual collisions between two aggregates. Therefore, we have to provide prescriptions for the outcome of all possible collisional encounters, *i.e.,* all relevant combinations of m, ψ and Δv.

2.2.3 The collision model

We consider a collision between two particles with the aim of applying the results to a true coagulation model. Essentially, we have to provide a recipe for the enlargement factor, ψ, after the collision. Two relevant parameter sets enter into the new ψ: the progenitor masses and enlargement factors (*i.e.,* the (m_i, ψ_i) of the colliding particles). Moreover, the collision energy,

$$E = \frac{1}{2}\frac{m_1 m_2}{m_1 + m_2}(\Delta v)^2 = \tfrac{1}{2} m_\mu (\Delta v)^2, \tag{2.9}$$

with m_μ the reduced mass, is of key importance. At very low velocities, collisions between two aggregates will lead to sticking without internal restructuring, *i.e.,* the particles will stick where they make first contact. At moderate velocities, the internal structure of the resulting aggregate will adjust — dissipating a major fraction of the kinetic collision energy — resulting in a compaction of the aggregates. Finally, at very high collision velocities, the colliding aggregates will fragment into smaller units and this can lead to substantial erosion. Following the numerical model of Dominik & Tielens (1997) and the experimental studies by Blum & Wurm (2000), these collisional regimes are distinguished by the following critical (collision) energies:

- $E_{\rm restr} = 5E_{\rm roll}$, the energy needed for the onset of compaction;
- $E_{\rm max-c} \simeq N_{\rm c} \cdot E_{\rm roll}$, the energy at which aggregates are maximum compressed. Here, $N_{\rm c}$ is the total number of contact surfaces (between monomers) of the agglomerate. For a very open, fluffy agglomerate, $N_{\rm c} = N$. With increasing compaction the number of contacts will increase and for a cubic packing $N_{\rm c} = 3N$. Here, for simplicity, we will adopt $N_{\rm c} = N$.
- $E_{\rm frag} \simeq 3N_{\rm c} \cdot E_{\rm br}$, the energy needed for (the onset of) fragmentation of the agglomerate. Here $E_{\rm br}$ is the energy required to break a bond between two monomers. Its magnitude is of similar order as $E_{\rm roll}$.

For monomers of the same size $E_{\rm roll}$ is given by (Dominik & Tielens 1997; Blum & Wurm 2000)

$$E_{\rm roll} = 3\pi^2 \gamma a_0 \xi_{\rm crit} = \tfrac{1}{2}\pi a_0 F_{\rm roll}, \tag{2.10}$$

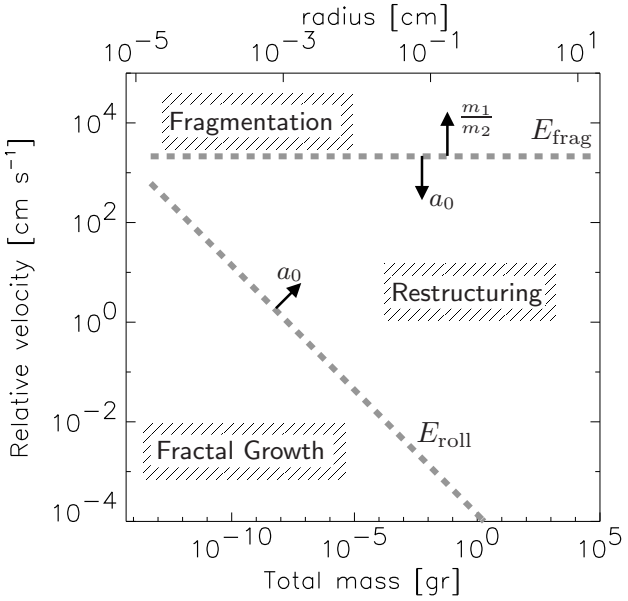

Fig. 2.3: The collision regimes as function of total particle mass and relative velocity. Thick *dashed lines* indicate the critical energies for the onset of rolling and fragmentation. Parameters are that of quartz particles ($\rho_{\rm s} = 3.0$ g cm^{-3}, $\gamma = 25.0$ ergs cm^{-2}, $a_0 = 0.1$ μm) and for the $E_{\rm frag}$ line we have assumed equal masses ($m_1 = m_2$) and $E_{\rm br} = E_{\rm roll}$. Arrows indicate how the critical energy lines shift with increasing monomer size and mass-ratio, m_1/m_2.

with a_0 the radius of the monomer, γ the specific surface adhesion energy and $\xi_{\rm crit}$ the yield displacement at which rolling commences. $F_{\rm roll}$, the rolling force, was measured by Heim et al. (1999) to be $F_{\rm roll} = (8.5 \pm 1.6) \times 10^{-5}$ dyn for uncoated SiO_2-spheres of surface energy density $\gamma = 14 \pm 2$ ergs cm^{-2}. We adopt this value for $F_{\rm roll}$ and assume proportionality with γ when applying it to other materials. The monomer size, a_0, is also an important model parameter directly affecting the outcome of the collision at a given mass; a smaller a_0 provides more contacts (for the same mass) and the agglomerate is more resistant to breakup. With these energy thresholds, three qualitatively different collision regimes can then be discerned (see Fg. 2.3):

(i) $E < E_{\rm restr}$: No internal restructuring. The particles stick where they meet ('hit-and-stick' growth) as in traditional, lattice-based, aggregation models (*e.g.*, Meakin 1988)—a process leading to fractal aggregates.

(ii) $E_{\rm restr} < E < E_{\rm frag}$: Restructuring (compaction) of aggregates.

(iii) $E > E_{\rm frag}$. Initially, loss of monomers, but for high energies complete fragmentation (*e.g.*, catastrophic collision). This phase requires a recipe for the mass distribution of the fragments. In this chapter, fragmenting collisions are avoided by, *e.g.*, 'choosing' moderate α and stopping coagulation for particles that reach a critical friction time (see § 2.4). Within these constraints, our results are therefore not compromised by ignoring the fragmentation issue.

From Fg. 2.3 it is clear that, when starting with small particles, growth will initially be in the fractal regime. This fractal growth will be followed by a period in which the collisions will promote the restructuring of the growing agglomerate. Fragmentation

becomes only important for velocities in excess of 10^3 cm s^{-1}. Since we assume that every contact can absorb a unit energy $E_{\rm roll}$, the $E_{\rm frag}$ line in Fg. 2.3 is independent of total mass. The $\Delta v \simeq 10^3$ cm s^{-1} limit translates to a critical value for the turbulent α parameter: $\alpha \lesssim 10^{-2}$. Within Fg. 2.3, the precise 'growth path' of the agglomerate will be controlled by evolution of the relative velocities and hence A/m or, equivalently, ψ. We will now construct recipes for ψ in, respectively, *i*) the fractal and *ii*) the compaction regime.

$E < E_{\rm restr}$: hit-and-stick

Besides the usual CCA and PCA formalisms, there have been a few attempts to give prescriptions for the evolving internal structure of aggregates in the hit-and-stick regime. Kostoglou & Konstandopoulos (2001) discuss a formalism for obtaining the new fractal dimension in terms of the sizes and fractal dimensions of the two colliding aggregates. One point is, however, that, apart from the fractal dimension, another parameter—the prefactor—is needed to fully describe the fractal, although it is usually of order unity. Ossenkopf (1993), like this study, introduces only one structural parameter and interpolates between the CCA and PCA limits. We will also follow this idea, but use a different interpolation mechanism.

We recognize that in the pure sticking regime most collisions are between evolved, fluffy aggregates, since the size distribution evolves progressively toward larger sizes. For low velocity-mass combinations (Fg. 2.3), where restructuring is unimportant, the collisional growth then resembles the CCA growth process the most. We therefore simply rewrite the fractal law in terms of the individual masses of the particles and keep the CCA exponent,

$$A = A_1 \left(\frac{m_1 + m_2}{m_1} \right)^{\delta_{\rm CCA}}, \qquad m_1 > m_2. \tag{2.11}$$

Although collisions between different particles are included in Eq. (2.11), we still adopt the CCA-characteristic exponent ($\delta_{\rm CCA} = 0.95$) to ensure that for the 'pure' CCA case ($m_1 = m_2$; $A_1 = A_2$) this prescription is in accordance with detailed numerical studies (Meakin & Donn 1988; Ossenkopf 1993; Kempf et al. 1999; Paszun & Dominik 2006). There is, however, a modification to Eq. (2.11) that must be made. The term in brackets in Eq. (2.11) determines the amount of increase in A in the fractal regime. Because fractal growth results from inefficient packing of voluminous objects, it is clear that this term must include parameters describing the spatial extent of the collision partners. These cannot, however, be given by the masses of the particles, since m (alone) does not reflect a spatial size. For example, if we would replace one of the aggregates by one of the same mass, but of lower porosity (*i.e.*, a more compact aggregate), its volume is obviously smaller and packing becomes more efficient. These effects, however, are not reflected in Eq. (2.11). For these reasons, we replace m by V in Eq. (2.11),

$$A = A_1 \left(\frac{V_1 + V_2}{V_1} \right)^{\delta_{\rm CCA}}, \qquad V_1 > V_2. \tag{2.12}$$

Note that for particles of the same internal density (porosity) Eq. (2.12) and Eq. (2.11) agree, such that Eq. (2.12) also can be seen as an extrapolation from the CCA case, but one that takes account of the different internal structures of the collision partners. Using the relation $A \propto V^{2/3}$ and Eq. (2.6), Eq. (2.12) can be re-written in terms of m and ψ only

$$\psi = \langle\psi\rangle_m \left(1 + \frac{m_2\psi_2}{m_1\psi_1}\right)^{\frac{3}{2}\delta_{\rm CCA}-1}, \tag{2.13}$$

with $\langle\psi\rangle_m$ the mass-averaged enlargement factor of the collision partners,

$$\langle\psi\rangle_m \equiv \frac{m_1\psi_1 + m_2\psi_2}{m_1 + m_2}. \tag{2.14}$$

In CCA coagulation ($m_1 = m_2$ and $\psi_1 = \psi_2$) we recover Eq. (2.8), but Eq. (2.13) now includes all collisions in the hit-and-stick regime. For example, if a large, fluffy aggregate sticks to a compact one, the enlargement factor of the newly formed aggregate is higher than the mass-averaged enlargement factor of the progenitor particles, $\langle\psi\rangle_m$, but smaller than that of the fluffy collision partner. In § 2.2.4, it will be shown, however, that the $\langle\psi\rangle_m$ term underestimates the porous growth when one of the particles is very small, *i.e.,* in PCA-like collisions. This is solved by adding to Eq. (2.13) a term that compensates for these cases and our final recipe then becomes

$$\psi = \langle\psi\rangle_m \left(1 + \frac{m_2\psi_2}{m_1\psi_1}\right)^{\frac{3}{2}\delta_{\rm CCA}-1} + \psi_{\rm add}, \tag{2.15}$$

where $\psi_{\rm add}$, a term important only for small m_2, is explained in § 2.2.4.

$E > E_{\rm restr.}$: compaction

In the compaction limit monomers are restructured at the expense of the porous volume of the aggregates. Following the theoretical study of Dominik & Tielens (1997) we will assume that the (relative) amount of compaction, $\Delta V_{\rm p}/V_{\rm p}$, scales linearly with collisional energy, *i.e.,* $\Delta V_{\rm p}/V_{\rm p} = -f_C = E/E_{\rm max-c} = -E/(N \cdot E_{\rm roll})$, where $V_p = V - V^*$ denotes the porous volume within the aggregate and N is the total number of monomers present.[7] Essentially, this implies that the collision energy is used to set individual monomers in an agglomerate rolling and that this rolling is only stopped when an additional contact is made, resulting in compaction. Recalling that $V = \psi V^*$ and $V_{\rm p} = V - V^* = (\psi - 1)V^*$ with V^* proportional to mass, we then find that the porous volume after colliding is

$$(V_1^* + V_2^*)(\psi - 1) = (1 - f_C)\left[V_1^*(\psi_1 - 1) + V_2^*(\psi_2 - 1)\right]. \tag{2.16}$$

[7]Note that we start compaction already at $E = E_{\rm roll}$ instead of $E = 5E_{\rm roll}$. We have found, however, that the simulations are insensitive to the precise energy at which compaction starts.

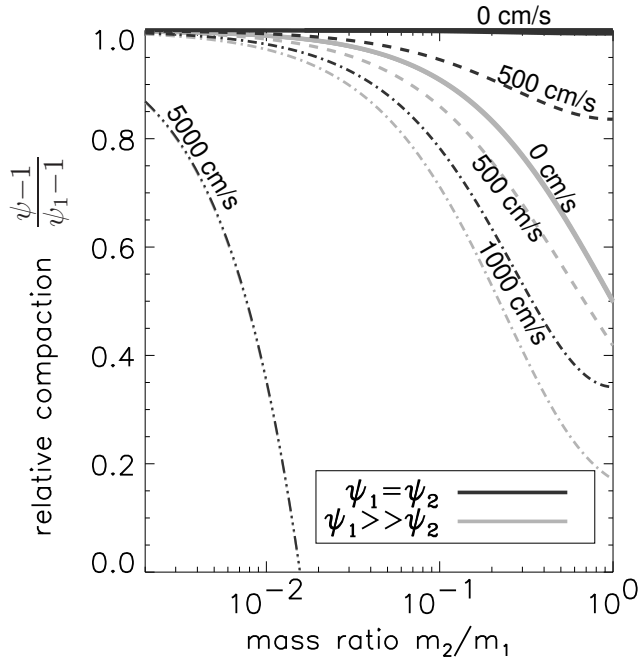

Fg. 2.4: Relative compaction as function of the mass ratio, m_2/m_1, at various collisional velocities. The expression on the y-axis measures the compaction relative to particle 1 and is a function of mass ratio, m_2/m_1, only (see Eq. (2.17). Here ψ_1 is the enlargement factor of the most massive aggregate, *i.e.*, $m_1 > m_2$, and plots are shown for $\psi_2 \ll \psi_1$ (*grey lines*) and $\psi_2 = \psi_1$ (*black lines*). At low mass ratios the curves converge.

And the new enlargement factor

$$\psi - 1 = (1 - f_C) \cdot \frac{1}{m_1 + m_2} \left(m_1(\psi_1 - 1) + m_2(\psi_2 - 1) \right) = (1 - f_C) \left(\langle \psi \rangle_m - 1 \right), \quad (2.17)$$

with $\langle \psi \rangle_m$ again the mass-averaged enlargement factor of the (two) collision partners (Eq. (2.14). We illustrate Eq. (2.17) in Fg. 2.4 for the limiting cases of equal porosity collisions ($\psi_1 = \psi_2$; black lines) and very porous *vs.* compact particle collisions ($\psi_1 \gg \psi_2$; grey lines). Higher mass-ratios give higher collision energies (higher m_μ) and hence more compaction. If velocities are low, ($\Delta v < 100$ cm s^{-1}) the net compaction occurs primarily through the $\langle \psi \rangle_m$ factor and the curves converge on the 0 cm s^{-1} (thick) line. Only when $\Delta v > 100$ cm s^{-1} does the f_C-factor start to become important. Collisions at velocities higher than 1 000 cm s^{-1} can result in fragmentation if the mass-ratios are similar. For low mass ratios the $\langle \psi \rangle_m$ is determined by ψ_1 (the highest mass) and there is little difference between the two limiting cases.

2.2.4 Porosity increase in the PCA and CCA limits

In the discussion on the ψ recipes in § 2.2.3 we have used the CCA fractal exponent ($\delta_{\rm CCA} = 0.95$) as the starting point and extrapolated this empirical relation to Eq. (2.13): a general recipe for all collisions in the 'hit-and-stick' regime. By definition, CCA-collisions are incorporated into this recipe and we may expect Eq. (2.13) also to account for collisions between aggregates having about the same size. The PCA model, where one monomer collides with an agglomerate, is the opposite ex-

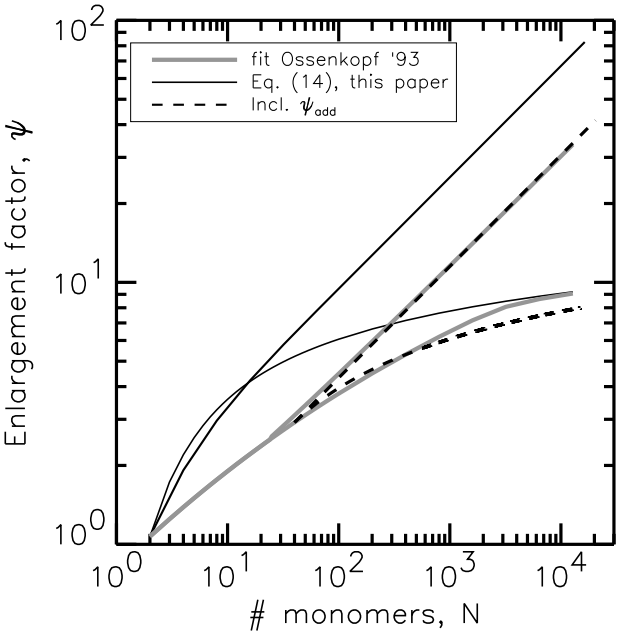

Fig. 2.5: The enlargement factor in the PCA and CCA limits as a function of the number of monomers (N) of the particle. The *thick grey curves* show the fits of Ossenkopf (1993) for CCA (*top*) and PCA (*bottom*) coagulation. The *solid curve* corresponds to the limiting cases of Eq. (2.13). The *dashed curves* show the same limits, but now the zero point lies at $N = 40$ (after which the PCA/CCA curves of Ossenkopf (1993) diverge in porosity) and includes the $\psi_{\rm add}$ correction term (Eq. (2.19).

treme. If we take the PCA-limit of Eq. (2.13), *i.e.*, $m_1 \gg m_2 \sim m_0$, with m_0 the monomer mass, the change in ψ after addition of a monomer becomes

$$\psi_{N+1} \approx \psi_N + \frac{N_2}{N}\left(\tfrac{3}{2}\delta_{\rm CCA}\psi_2 - \psi_N\right); \qquad N \gg N_2, \tag{2.18}$$

with $N = N_1 = m/m_0$ the number of monomers of the PCA agglomerate and $N_2 = 1$ for monomers. Thus, ψ_N goes to $\frac{3}{2}\delta_{\rm CCA}\psi_2 \approx 1.5$ in the PCA asymptotic limit ($N_2 = 1; \psi_2 = 1$).[8] The fact that an asymptotic limit is reached can be understood intuitively, since there must be a point at which the inward penetration of monomers into the center of the aggregate, which decreases ψ, starts to balance the porous growth due to hit-and-stick collisions at the surface. The asymptotic limit of $\psi \approx 1.5$, however, is much lower than typical PCA models indicate ($\psi \approx 10$) as is illustrated in Fg. 2.5, where the PCA/CCA limits of our model (solid lines) are compared to detailed numerical simulations of Ossenkopf (1993) (thick lines). Equation (2.13) thus underpredicts the porous growth for PCA-like collisions in which one of the particles is small; a result not too surprising since it originates from the CCA fractal law (Eq. (2.11)), which is constructed to apply only for similar (*i.e.*, equal-sized) particles. For these reasons we add to Eq. (2.13) a term that compensates the $-N_2\psi_N/N$ term in Eq. (2.18),

$$\psi_{\rm add} = B\frac{m_2}{m_1}\psi_1 \exp\left[-m_\mu/m_{\rm F}\right], \tag{2.19}$$

[8] Here we take $\psi_2 = 1$ as the enlargement factor of single monomers.

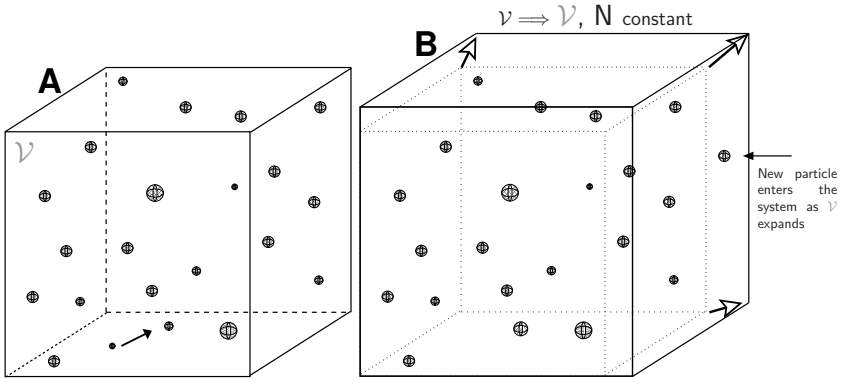

Fig. 2.6: Illustration of the adopted Monte Carlo technique. *(a)* N-particles are assumed to be uniformly distributed in a box of volume $\mathcal{V}$. The collision rate between particle i and j is $C_{ij} = \sigma_{ij}\Delta v_{ij}/\mathcal{V}$. A random number determines which two particles will collide. *(b)* After the collision the number of particles is restored by duplicating one of the remaining $N-1$ particles. Physically, this can be interpreted as an expansion of $\mathcal{V}$ (heavily exaggerated in this figure) to a volume at which $\mathcal{V}$ contains N-particles again. The hypothesis of this method is that the collisional evolution within $\mathcal{V}$ is representative for the coagulation of the total space under consideration.

where the exponential ensures $\psi_{\rm add}$ is unimportant for collisions between particles well above a certain mass-scale, $m_{\rm F}$. With $B = 1.0$ and $m_{\rm F} = 10\ m_0$ we find good correspondence with the results of Ossenkopf (1993). In Fg. 2.5 the new CCA and PCA limits are shown by the dashed curves, where we have shifted the 'zero point' from $N = 1$ to $N = 40$, i.e, the starting point for ψ after which we recursively apply Eq. (2.15). The transition toward fractal behavior emerges only after this point and we therefore directly take ψ from the results of Ossenkopf (1993) when $N \lesssim 40$.

Although, with Eq. (2.19) for $\psi_{\rm add}$, Eq. (2.15) does achieve the right PCA/CCA fractal limits, we do not claim they actually provide a model for ψ. The collision recipes are based on empirical findings and extrapolations from these. However, in contrast to the CCA and PCA limiting collisional growth models, where ψ can be directly parameterized in a single exponent, we recognize that the internal structure of the aggregates is changed during—and caused by—the collisional growth process. This is the main qualitative difference of our collision model captured in Eq. (2.15). This equation, together with Eq. (2.17), provides recipes for the collisional evolution of the enlargement factor, which can be easily incorporated into time-dependent coagulation models. We acknowledge this is an active area of research and future model efforts may well improve on the present formulation.

2.3 Monte Carlo Coagulation

2.3.1 Outline

To determine the implications the new collision model has for the solar nebula, *e.g.*, as compared to collision models where mass is the only parameter, it must be embedded in a coagulation model that evolves the particle distribution function, $f(\mathbf{x})$. $f(\mathbf{x},t)$ gives the number density of particles with a set of properties (parameters) $\{x_i\}$ at time t. In compact coagulation models all properties depend only on mass, so $f(\mathbf{x},t) = f(m,t)$. In the model described in § 2.2, however, the particle's enlargement factor has been included as an independent parameter such that f becomes a function of three variables, $f(\mathbf{x},t) = f(m,\psi,t)$. The coagulation equation which describes the evolution of $f(\mathbf{x})$ is

$$\begin{aligned}\frac{\partial f(\mathbf{x},t)}{\partial t} = & -f(\mathbf{x},t)\int \mathrm{d}\mathbf{x}' f(\mathbf{x}',t)K(\mathbf{x},\mathbf{x}') \\ & + \frac{1}{2}\int \mathrm{d}\mathbf{x}'\mathrm{d}\mathbf{x}'' f(\mathbf{x}',t)f(\mathbf{x}'',t)K(\mathbf{x}',\mathbf{x}'',t)\,\delta_{\mathrm{k}}\left(\mathbf{x}-\Gamma(\mathbf{x}',\mathbf{x}'')\right), \qquad (2.20)\end{aligned}$$

with $K = \sigma\Delta v$ the collision kernel, δ_{k} the Kronecker δ-function and Γ the collision function, which maps in the case of sticking $2n$ parameters (those of $\mathbf{x}'$ and $\mathbf{x}''$) to n, where n is the number of independent parameters with which a particle is characterized. Equation (2.20) of course is just an extension of the Smoluchowski equation[9] (Smoluchowski 1916) to more than one dimension. Applied to the formalism in § 2.2 it describes the loss of particles in state $\mathbf{x} = (m,\psi)$ due to collisions with any other particle (first term) and the gain of '$\mathbf{x}$-particles' that happen to be formed out of any suitable collision between two other particles (second term). Applied to the findings in § 2.2, Γ symbolizes the collision recipes with $\Gamma(m_1,\psi_1;m_2,\psi_2) = (m_1+m_2,\psi)$ and ψ is given by Eq. (2.15) or Eq. (2.17), dependent on the collisional energy.

One approach to implement coagulation is to numerically integrate the Smoluchowski equation. However, it is immediately clear that numerically integrating Eq. (2.20) becomes a daunting exercise. Integrating the ordinary (1-dimensional) Smoluchowski equation is already a non-trivial matter. Problems of near cancellation (the gain terms often equal the loss terms), mass conservation (systematic propagation of errors) and the problem concerning the determination of a time-step must all be tackled. (Dullemond & Dominik 2005 in their Appendix B give an overview of the subtleties involved.) The Γ-factor in Eq. (2.20) gives a further complication since there is no such thing as 'conservation of porosity' and the δ-factor cannot be easily integrated away. Although there is no fundamental reason against the binning method—see, *e.g.*, Ossenkopf (1993) who solves the Smoluchowski equation in two

[9] Which reads:

$$\frac{\partial f(m)}{\partial t} = -f(m)\int \mathrm{d}m'\; K(m,m')f(m') + \frac{1}{2}\int \mathrm{d}m'\; K(m',m-m')f(m')f(m-m'), \qquad (2.21)$$

describing losses of m due to all collisions with m (first term on right hand side) and gains in the distribution of m due to collisions between m' and $m-m'$ (second term), where the factor $\frac{1}{2}$ ensures collisions are not twice accounted for. Ossenkopf (1993) provides a general extension of the Smoluchowski equation including source and sink terms.

dimensions — these issues make the whole procedure quite elaborate. We felt that much of the simplicity of the collision model of § 2.2 would be 'buried' by numerical integration of a 2d-Smoluchowski equation and therefore have found it suitable to opt for an approach using direct Monte-Carlo simulation (DSMC) techniques.

The simplicity of using Monte-Carlo methods for coagulation problems is appealing. Basically, N-particles are distributed over a volume $\mathcal{V}$ (see Fg. 2.6a). The evolution then boils down to the determination of the two particles which are involved in the *next* collision. We hereafter assume that the particles are well mixed, *i.e.,* no potential is present, such that the determination of the next collision is governed by basic stochastic principles. Then the probability of a collision between particles i and j is given by the collision rate, $C_{ij} = K_{ij}/\mathcal{V}$ in which K_{ij} is the collision kernel. A random number determines which of the $\frac{1}{2}N(N-1)$ possible collisions will be the next. The collision then creates a new particle, after which the $\{C_{ij}\}$ must be updated and the procedure repeats itself.

The advantages of such an approach are obvious. Most striking perhaps is the 'physical character' of Monte-Carlo simulations. The growth-evolution of individual particles is directly traced and can be studied. The algorithm does not use the distribution function, f, in a direct way; it is obtained indirectly by binning the particles. Secondly, the above described method is exact, *i.e.,* no 'time *vs.* accuracy' considerations have to be made in choosing the time-step Δt; instead, Δt — the inter-collision time — is an outcome of the stochastic coagulation process as it is in nature. Furthermore, due to its stochastic nature, no Monte-Carlo simulation is the same. A series of (independent) runs gives at once a measure of the statistical spread in the distribution. Note that the fluctuations around the average are a combination of real stochastic noise and random noise, but it is qualitatively different from the Smoluchowski approach, which describes the evolution of the mean of all possible realizations and is therefore completely deterministic (Gillespie 1975). From a practical point of view the straightforwardness of the DSMC-method makes that there is no need for resorting to 'control parameters' like those required in the numerical-integration method.

The DSMC-method, however, has its limitations. It can be immediately seen, for instance, that when having started with N (say identical) particles of mass m_0 in a fixed volume, these will over time pile up in one agglomerate of $m_{\rm final} = Nm_0$. The accuracy then steadily decreases during the simulation (in MC-simulations the statistical error scales proportional to $N^{-1/2}$) and most of the computing time is spent in the first few (quite uninteresting) collisions. Consequently, to achieve orders of magnitude growth, the initial number of particles must be extremely large. And because the calculation of the $\{C_{ij}\}$ goes proportional to N^2 (every particle can collide with each other), it becomes clear that this method becomes impracticable. To counter the dependence on large initial particle numbers, one can also try to preserve the number of particles *during* the simulation. This can be done, for instance, by 'tossing-up' the particle-distribution when the number of particles reaches $N/2$ as described by Liffman (1991). A more natural approach perhaps, given by Smith & Matsoukas (1998), and adopted here, keeps the number of particles constant at each step; every time a collision takes place one of the remaining $N-1$ particles is randomly dupli-

cated such that the number of particles throughout the simulation stays the same. This procedure can graphically be represented as an increase in the simulated volume, $\mathcal{V}$ (see Fig. 2.6b), under the assumption that the collisional evolution outside of $\mathcal{V}$ progresses identically. Smith & Matsoukas (1998) have shown that the error in the coagulation-scheme now scales logarithmically with the extent of growth,— or growth factor (GF), defined here as the mean mass over the initial mean mass of the population — much improved over the constant-$\mathcal{V}$ case, where the error has a square-root dependence on GF. We might worry though about the consequences of the duplication mechanism. It causes a certain degree of 'inbreeding', which effects we cannot quantify directly. Smith & Matsoukas (1998) show it is unimportant for the constant or Brownian kernels used in their studies. However, these kernels are known to behave gently, *i.e.*, they are rather insensitive to irregular changes in the population since the variations in the K_{ij} are small. Perhaps, more erratic kernels are more sensitive to the 'duplication mechanism', but we might equally well attribute this sensitivity to the stochastic nature of the coagulation process. At any rate, these consequences are best quantified by running the code multiple times.

2.3.2 Implementation

In implementing the DSMC approach we follow the 'full conditioning method' of Gillespie (1975). This involves the calculation and updating of partial sums, C_i,

$$C_i \equiv \sum_{j=i+1}^{N} C_{ij}, \qquad i = 1, \ldots, N-1, \tag{2.22}$$

with $C_{ij} = K_{ij}/\mathcal{V} = \sigma_{ij}(a_i, a_j)\Delta v_{ij}(\tau_i, \tau_j)/\mathcal{V}(\kappa)$ (here κ is the total number of collisions since the start of the simulation). These $N-1$ quantities are stored in the memory of the computer. $C_{\rm tot} = \sum_i C_i$ is the total coagulation rate. The probability density function, $P(t, i, j)$, *i.e.*, the probability that the *next* collision will occur in time-interval $(t, t+dt)$ *and* involves particles i and j $(i < j)$ can then be written as (Gillespie 1975)

$$P(t,i,j) = C_{ij} \exp\left[-C_{\rm tot} t\right] = \Big(C_{\rm tot} \exp\left[-C_{\rm tot} t\right]\Big) \times \Big(C_i/C_{\rm tot}\Big) \times \Big(C_{ij}/C_i\Big). \tag{2.23}$$

Three random deviates, $\bar{r}_i \in [0,1]$, then determine successively: (i) the time it takes until the next collision takes place, $t = C_{\rm tot}^{-1} \ln(1/\bar{r}_1)$; (ii) the first particle (i) to collide, by summing over the C_i-s (starting with $i = 1$) until $\bar{r}_2 C_{\rm tot}$ is exceeded (this fixes i); and (iii) its collision partner (j) by summing the C_{ij}-s over the j-index (starting with $j = i+1$) until the value $\bar{r}_3 C_i$ is exceeded (Gillespie 1975, Eq. (19)). The outcome of the collision is evaluated using the relevant equations in § 2.2 and the new particle is stored in the i-slot. Another random number then determines which of the $N-1$ particles (excluding j) will be duplicated and this one is stored in the j-slot. Having created, removed and duplicated particles, all of the C_i-s need to be updated. This implies only the subtraction/addition of the C_{ij}-s that have changed, not the recomputation of Eq. (2.22). Moreover, the 'duplication procedure' entails a rescaling of the simulated volume, $\mathcal{V}$, such that the spatial density of solids, $\rho_{\rm d} = \sum_i m_i/\mathcal{V}(\kappa)$

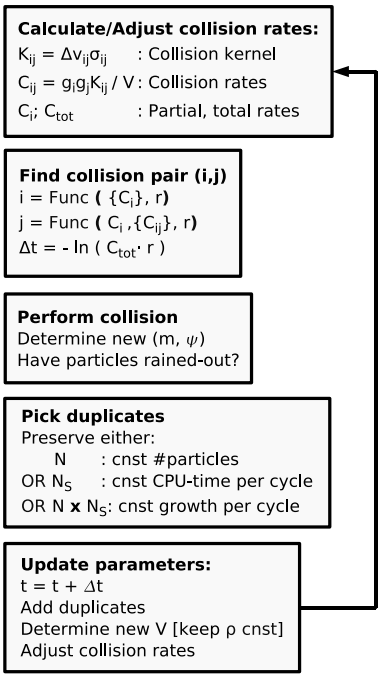

Fig. 2.7: Flow chart of the MC-coagulation method. One cycle corresponds to one collision. 'Func' like in i = Func($\{C_i\}, r$) indicates that i is a function of the C_i values and a random deviate, r. The procedure is further explained in the text.

remains constant. The algorithm can then be repeated. All these steps are order-N calculations at worst; most time-consuming are the determination of j (for which C_{ij} has to be calculated) and the update of the $\{C_i\}$. To achieve a given GF another factor N in computation time is needed,[10] bringing the total CPU-time proportional to N^2. These procedures are graphically summarized in Fig. 2.7.

It is possible, however, to save some CPU time by taking the duplicates together in the calculation of the collision rates. If there are $(g_i - 1)$ copies of particle i, it would be a waste of time to calculate the (same) rates g_i times. Rather, g_i can be absorbed in the calculation of the (combined) coagulation rate. $\tilde{C}_{ij} = g_i g_j C_{ij}$ is then the rate at which one of the i-particles collides with one of the j-particles ($i \neq j$) and $\tilde{C}_{ii} = \frac{1}{2} g_i (g_i - 1) C_{ii}$ between duplicates. The CPU time per step is now proportional to N_s, the total number of *distinct* particles, *i.e.,* excluding duplicates, with $\sum_{i=1}^{N_\mathrm{s}} g_i = N$. To think of it in biological terms: g_i gives the multiplicity of species i; N_s the total number of species; and N the total number of living creatures.

2.3.3 Tests

The Monte-Carlo coagulation model described above is tested with kernels that have an analytic solution. These are: (i) the constant kernel, $K_{ij} = 1$; and (ii) the linear kernel, $K_{ij} = \frac{1}{2}(m_i + m_j)$. The evolution of the mean mass of the distribution, $\langle m \rangle$

[10] Due to the duplication, the mean mass of the system increases with a factor $(N+1)/N$. The growth factor after κ steps then becomes $\mathrm{GF} = ((N+1)/N)^\kappa$. Thus, $\ln \mathrm{GF} = \kappa \ln(1 + N^{-1}) \approx \kappa/N$ if $N \gg 1$ and $\kappa \approx N \ln \mathrm{GF}$.

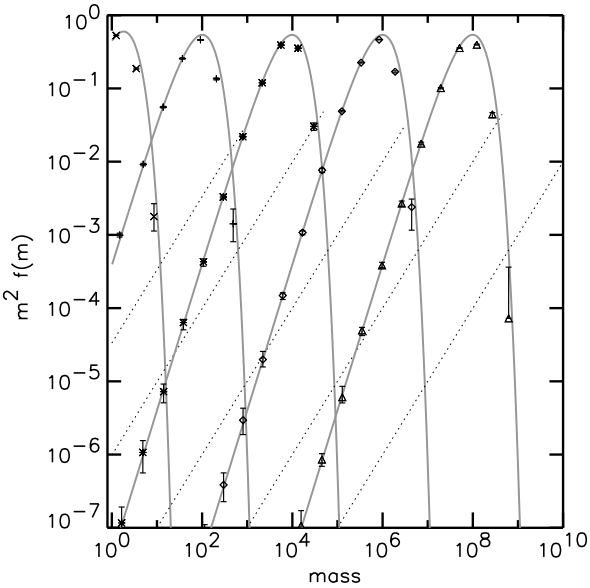

Fig. 2.8: Test of the Monte Carlo coagulation code — constant kernel ($K_{ij} = 1$), 20 000 particles. At (dimensionless) times $t = 1, 10^2, 10^4, 10^6, 10^8$ particles are binned and the distribution function f is computed (*symbols*). The analytical solutions at these times are overplotted by the *solid curves*. The error bars (hardly visible) show the spread averaged over 10 runs. The *dotted lines* show the distribution function if all the bins would be occupied by only 1 particle—it is an auxiliary line with slope 1 showing the lower limit of the (individual) distribution function.

for these kernels is[11] (Silk & Takahashi 1979; Tanaka & Nakazawa 1994)

$$\langle m \rangle = \begin{cases} m_0(1 + \frac{1}{2}t) & \text{constant kernel} \\ m_0 \exp\left[\frac{1}{2}t\right] & \text{linear kernel,} \end{cases} \tag{2.24}$$

where the distribution at $t = 0$ is monodisperse of mass m_0. Well-known coagulation models have either $K \propto m^{1/3}$ (Brownian coagulation) or $K \propto m^{2/3}$ (geometric area), but here, due to changes in ψ and Δv, we should be prepared for K to vary with time. Thus, it is important that the Monte-Carlo code passes both these tests. Initial conditions for these test cases are monodisperse with all relevant parameters put at 1 at $t = 0$ (i.e, $m_0 = 1$ and $f(t = 0) = 1$, $\rho_\mathrm{d} = 1$, $\rho_\mathrm{s} = 1$) and we do not take porosity into account ($\psi = 1$ always). At various times the particles are binned by mass and the distribution function $f(m)$ is determined by summing over the masses in the bin and dividing by the width of the bin (to get the spectrum) and the volume of the simulation (to get the density). Multiple runs of the simulation then provide the spread in f. Figures 2.8 and 2.9 present the results. On the y-axis $f(m)$ is multiplied by m^2 to show the mass-density per logarithmic bin. Analytical solutions (Tanaka & Nakazawa 1994) are overplotted by solid curves, while the dotted line shows the (hypothetical) distribution function if all the bins would be occupied by 1 particle. Thus, the dotted line corresponds to $m^2 f(m) = m^2/\mathcal{V}w_\mathrm{b} \approx m/\mathcal{V}$, because the widths of the bins, w_b, are also exponentially distributed. In a single simulation, the distribution function should lie above this (auxiliary) line and the vertical distance to this line is a measure for the number of particles in a bin.

[11] The mean mass of the population is inversely proportional to the number of particles per unit volume.

Figure 2.8 shows that the code passes the constant kernel test with flying colors. The spread in the data is limited, and it does not noticeably increase with time. The linear kernel (Fg. 2.9a), on the other hand, shows a different story. Here the mean mass, $\langle m \rangle$, as well as the peak mass, m_p — defined as the peak of the $m^2 f(m)$ size distribution — evolve exponentially with time. Note that the position of m_p only depends on the particles that contain most of the mass, while $\langle m \rangle$ is also sensitive to the total number of particles. Therefore, $\langle m \rangle$ lags m_p at any time and one can show that the gap between the two also increases exponentially with time. Inevitably, at some point in time, the theoretical value of the $m^2 f(m)$ mass-peak becomes larger than the total mass present inside $\mathcal{V}$. This corresponds to the crossing of the dotted line at, *e.g.*, $t \simeq 20$ in Fg. 2.9a. In other words, the duplication mechanism, needed to conserve N but which has the additional effect of enlarging $\mathcal{V}$, is incapable of keeping up with the exponential growth: 'runaway particles' could have formed, but the simulated volume $\mathcal{V}$ is just not large enough to take them into account. The postulate of the 'duplication mechanism' — the particle distribution evolves similarly in and outside $\mathcal{V}$ — then breaks down. The only way to avoid this effect is to enlarge $\mathcal{V}$ by having more particles in the simulation, *i.e.*, to improve the 'numerical resolution'. In Fg. 2.9b, we show the results, in which N_s, instead of N, is held constant (§ 2.3.2). In these simulations N increases with time, starting with $N = 20\,000$ and ends with more than a million particles. The distribution now represents more closely the theoretical curve. Growth factors of 14 orders of magnitude in mass ($\simeq$5 in size) can then be accurately simulated.

The drawback, however, is that the computation slows down as N increases, since the relative increase in the average mass is inversely proportional to N, *i.e.*, $\Delta\langle m \rangle / \langle m \rangle \propto N^{-1}$. These simulations therefore take much more CPU time. It is clear that a fundamental limit is reached, in which, given a certain CPU power, the calculation of the mass-distributions can only be achieved for a limited range. A way to overcome this problem is to collide multiple particles per event. In such an algorithm collisions are no longer between two particles but between two groups of particles. Although this approximates the collisional process, the coagulation can be accelerated by grouping especially small particles into a single unit. We will discuss the grouping algorithm and its implication in chapter 5. For the simulations in § 2.4, the product of N and N_s has been kept constant, which ensures a constant growth (in exponential terms) per cycle. We have fixed $\sqrt{N \times N_\mathrm{s}}$ at 20 000 but made sure that the numerical resolution issues as discussed here for the linear kernel, did not occur. Fortunately, realistic mass-distributions are not that broad as in the analytic, linear kernel; *e.g.*, the smaller particles are quickly removed due to Brownian coagulation.

In summary, we have built an efficient Monte Carlo code to follow coagulation. The advantage of this code (above other numerical methods) is that it is intuitive, simple to implement and expand, and that it takes full account of the stochastic nature of coagulation. Minor disadvantages are the N^2 dependence on CPU time, the somewhat artificial duplication procedure, and the resolution problems shown for the linear kernel at high m as the simulation progresses. We have addressed these concerns and developed methods suitable for the scope of this work. DSMC-coagulation methods are very appropriate to work in conjunction with multi-

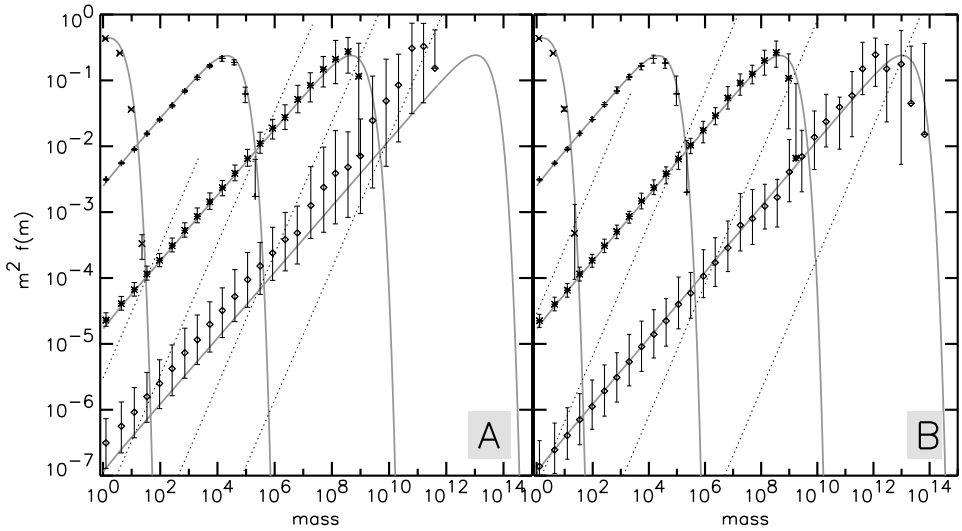

Fig. 2.9: Tests of the Monte Carlo coagulation code. Linear kernel, $K_{ij} = \frac{1}{2}(m_i + m_j)$. *(a)* fixed N ($N = 200\,000$). The distribution function f is computed at times $t = (1, 10, 20, 30)$. At $t = 30$ insufficient mass is present to provide a good fit to the analytical distribution. *(b)* fixed N_s . To obtain better correspondence with theory, the number of particles, N, is increased as the simulation progresses, such that more volume is sampled. N_s is fixed at 20 000 and N ends with over a million particles. The average corresponds well to the theory, yet the amount of CPU time is disproportionally larger at the later times.

parameter models. The collision model of § 2.2, with mass, m, and enlargement parameter, ψ, as variables, can now be put into an evolutionary setting.

2.4 Results

2.4.1 Application to a protoplanetary disk

The collision model of § 2.2 is embedded in the Monte Carlo code of the previous section and applied to the protoplanetary disk (§ 2.2.1). The coagulation is restricted to a turbulent environment in which particles are well mixed with the gas, yet do not fragment upon collision. For these reasons, we start out with a monodisperse population of sub-micron-sized grains (we choose them to be $a_0 = 0.1$ μm) present at $z = H_\mathrm{g}$, *i.e.*, at the scaleheight of the disk, where the density is a factor $\exp[-0.5]$ lower than at the mid-plane. Its collisional evolution within the gaseous nebula is followed until the point that systematic motions, *i.e.*, settling to the mid-plane, start to dominate. Thus, particles are either present and well mixed by turbulence, or have started to settle and are no longer in the region of interest. Settling is then modeled as a sudden phenomenon. The reality is, of course, a more gradual transition, but the discrete picture here is not a bad approximation, since the vertical structure is quickly established (Youdin & Chiang 2004). Settling occurs at the point when the friction

time of a particle has exceeded a critical friction time, $\tau_{\rm rain}$, such that the scaleheight of the particle, $h_{\rm p}(\tau_{\rm f})$, becomes smaller than that of the gas, *i.e.*, $h_{\rm p}(\tau_{\rm f}) < H_{\rm g}$. If self-gravity is neglected (valid in the gaseous nebula) and Schmidt numbers, Sc, are close to unity,[12] then $h_{\rm p}$ can be obtained by equating the particle diffusion timescale, $t_{\rm diff} = h_{\rm p}^2/\nu_{\rm T}$, with the particle settling timescale, $t_{\rm settl} = (\Omega^2\tau_{\rm f})^{-1}$, *i.e.*, $h_{\rm p}(\tau_{\rm f}) = H_{\rm g}\sqrt{\alpha/\Omega\tau_{\rm f}}$ (*cf.* Schräpler & Henning 2004; Youdin 2005). The critical friction time is then

$$\tau_{\rm f} = \frac{\rho_{\rm s}}{c_{\rm g}\rho_{\rm g}}\frac{a^*}{\psi^{2/3}} = \tau_{\rm rain} = \frac{\alpha}{\Omega}, \tag{2.25}$$

with a^* the compact size of particles (see Fg. 2.2). As expected, higher values of α and higher gas densities (lower $\tau_{\rm f}$) delay the onset of settling in the sense that the particle has to grow further in size before it arrives at the critical friction time. Alternatively, increasing ψ also delays settling.

In the code, settling is implemented as a 'rain-out': the particle is removed from the simulation and the spatial dust density decreases. The evolution of these 'rain-out particles' during settling is not traced anymore. The focus stays on the particles that remain in the layers above the mid-plane. Their evolution is followed for 10^7 yr.

The α parameter is one of the major uncertainties concerning the characterization of protoplanetary disks. One of the prime candidates for turbulence is the magneto-rotational instability (Hawley & Balbus 1991; Balbus & Hawley 1991), which seems to be most robust in well-ionized regions, *i.e.*, in the upper layers of the disk. Another way to characterize α is to relate it to the observed accretion rate, dM/dt, (Cuzzi et al. 2005) and then values in the range of $10^{-4} \lesssim \alpha \lesssim 10^{-2}$ seem plausible. Yet, despite its uncertainty, α appears in key expressions as, *e.g.*, Δv_{ij} and $\tau_{\rm rain}$. Therefore, models are run that cover a large range in α: $\alpha = 10^{-6} - 10^{-2}$. Furthermore, we divide the runs in two categories, which reflect the spatial position in the solar nebula. The 'inner' models correspond to conditions at 1 AU where the monomers are quartz with internal density $\rho_{\rm s} = 3.0$ g cm^{-3} and surface energy density of $\gamma = 25$ ergs cm^{-2}. The 'outer' models correspond to conditions at 5 AU, where the coagulation is that of ices ($\rho_{\rm s} = 1$ g cm^{-3} and $\gamma = 300$ ergs cm^{-2}) and with an enhanced surface density of a factor 4.2 over the minimum solar nebula (Nakagawa et al. 1986). For comparison, we also run compact models for the $\alpha = 10^{-4}$ runs. Compact models (denoted by the C-suffix in Table 2.1) are models where the internal structure does not evolve, *i.e.*, $\psi = 1$ by definition. An overview of all the models is given in Table 2.1.

2.4.2 Particle growth and compaction

In Fg. 2.10 mass distributions are shown at various times during their collisional evolution. On the y-axis the mass function is plotted in terms of $m \cdot a^* \cdot f(a^*)$, which shows the mass-density, *i.e.*, the mass of grains of compact size a^* in logarithmic bins. The panels compare the results of compact coagulation (Fg. 2.10a,b) with those of porous coagulation (Fg. 2.10c,d) for a turbulent strength parameter of $\alpha = 10^{-4}$. The

[12] The Schmidt number measures the ratio of the gas to particle diffusivity; it is supposed to be close to unity if $\tau_{\rm f} < t_{\rm L}$ (Schräpler & Henning 2004).

MODEL RUNS

Model-id[a]	Model Parameters			Notes
	R [b]	α	δ	
(1)	(2)	(3)	(4)	(5)
R1Ta4-P	1 AU	10^{-4}	0.95	default model
R1Ta2-P	1 AU	10^{-2}	0.95	increased turbulence
R1Ta6-P	1 AU	10^{-6}	0.95	decreased turbulence
R1Ta4-C	1 AU	10^{-4}	2/3	compact model
R5Ta4-P	5 AU	10^{-4}	0.95	default model at 5AU
R5Ta2-P	5 AU	10^{-2}	0.95	increased turbulence
R5Ta6-P	5 AU	10^{-4}	0.95	decreased turbulence
R5Ta4-C	5 AU	10^{-6}	2/3	compact model

Table 2.1: Overview of all the runs. (1) Reference name. Names are intended to be mnemonic. 'Rx' stands for radius at x AU. Ta, denotes the strength of the turbulence, *e.g.,* Ta4 stands for $\alpha = 10^{-4}$. Finally, the suffix denotes whether models are porous (P) or compact (C). (2) Heliocentric radius. At 1 AU quartz particles coagulate: $\rho_g/\rho_d = 240$, $\gamma = 25$ ergs cm^{-2}, $\rho_s = 3.0$ g cm^{-3}; at 5 AU coagulation is between ices: $\gamma = 370$ ergs cm^{-2}, $\rho_s = 1.0$ g cm^{-3}, $\rho_g/\rho_d = 57$. The gas parameters correspond to a minimum mass solar nebula model (see § 2.2.1). (3) Turbulent-α parameter. (4) Fractal growth parameter. (5) Notes.

coagulation is calculated at 1 AU (quartz; Fg. 2.10a,c) and at 5 AU (ices, Fg. 2.10b,d). In Fg. 2.11 the $\alpha = 10^{-4}$ model at 1 AU is compared to other α models at 1 AU (see Table 2.1). In Fg. 2.13 averages of the size distributions of Fgs. 2.10a,c are shown explicitly with time. Here $\langle a \rangle_m$ is the mass-weighted size,

$$\langle a \rangle_m = \frac{1}{\sum_i m_i} \sum_i m_i a_i, \tag{2.26}$$

of the population. Thus, while $\langle a \rangle$ gives the average particle size, $\langle a \rangle_m$ corresponds to the (average) size to which a unit of mass is confined. Because of this weighting, $\langle a \rangle_m \geq \langle a \rangle$, with the equality valid only for monodisperse distributions.

The porosity evolution is also displayed in Fg. 2.12, where we plot the ratio of $\langle a \rangle_m$ to $\langle a^* \rangle_m$. $\langle a^* \rangle_m$ is defined analogously to Eq. (2.26), but then for the compact particle size. $\langle a \rangle_m / \langle a^* \rangle_m$ then gives the mass-weighted averaged enhancement of the geometrical radius of the particles (see, Fg. 2.2) . In the case of monodisperse populations or runaway growth one size dominates the average and the ratio is directly related to $\langle \psi \rangle_m$ as $\langle a \rangle_m / \langle a \rangle_m = \langle \psi \rangle_m^{1/3}$ This ratio is plotted *vs.* $\langle a^* \rangle_m$ in Fg. 2.12 for various models. It shows the build-up of porosity during the fractal stage, the stabilization during the compaction stage, up to the stage where the particles rain-out. In Fg. 2.12 the average sizes of some of these rain-out particles are indicated by the detached crosses. Note that (for illustrative reasons) the x-axis for these particles corresponds to porous size, a, rather than compact size, a^*. Properties of the 'rain-out' population are given in Table 2.2. In Fg. 2.12 the temporal stage is indicated by numbered ticks.

The evolution of the mass-distribution (Fgs. 2.10, 2.11, 2.13) can be divided into

RAIN-OUT PARAMETERS

model	$\langle a \rangle$	$\langle m \rangle$	$\langle \psi \rangle$	$\langle a/a^* \rangle$	$\langle t_{\rm rain} \rangle$	$\langle t_{99\%} \rangle$
	cm	gr			yr	yr
(1)	(2)	(3)	(4)	(5)	(6)	(7)
R1Ta4-P	2.1 ± 0.1	1.4 ± 0.1	$(8.6 \pm 0.2) \times 10^1$	4.4 ± 0.0	$(4.7 \pm 0.2) \times 10^3$	$(4.5 \pm 1.0) \times 10^4$
R1Ta4-C	2.4×10^{-2}	$(1.9 \pm 0.2) \times 10^{-4}$	1	1	$(2.6 \pm 0.1) \times 10^3$	$(4.4 \pm 0.3) \times 10^4$
R5Ta4-P	0.72 ± 0.04	$(1.4 \pm 0.1) \times 10^{-2}$	$(1.1 \pm 0.1) \times 10^2$	4.8 ± 0.1	$(1.9 \pm 0.1) \times 10^4$	$(2.2 \pm 0.3) \times 10^5$
R5Ta4-C	6.7×10^{-3}	1.2×10^{-6}	1	1	$(8.1 \pm 0.3) \times 10^3$	$(2.1 \pm 0.1) \times 10^5$
R1Ta2-P	7.8 ± 0.7	$(1.6 \pm 0.3) \times 10^3$	(3.9 ± 1.1)	1.6 ± 0.1	$(2.6 \pm 0.3) \times 10^2$	$(4.0 \pm 19) \times 10^{5\,a}$
R5Ta2-P	24 ± 2	$(1.7 \pm 0.3) \times 10^3$	$(3.6 \pm 0.1) \times 10^1$	3.3	$(1.4 \pm 0.1) \times 10^3$	$(4.5 \pm 4.6) \times 10^{3\,a}$
R1Ta6-P	2.1×10^{-2}	1.3×10^{-6}	$(8.7 \pm 0.1) \times 10^1$	4.4	$(1.3 \pm 0.1) \times 10^3$	2.3×10^6
R5Ta6-P	1.3×10^{-3}	$(4.6 \pm 0.1) \times 10^{-10}$	$(2.0 \pm 0.0) \times 10^1$	2.7	61 ± 7.2	1.1×10^5

Table 2.2: Properties of the particle distribution at rain-out. Entries denote: (1) model-id (see Table 2.1); (2) size at rain-out; (3) mass at rain-out; (4) enlargement factor at rain-out; (5) size enhancement at rain-out; (6) time at which first rain-out occurs; (7) time-interval over which 99% of the mass has rained-out. Values have been averaged over the 50 runs with the error bars reflecting the variations between the 50 runs of the simulation. (The spread is only given when the rms-value exceeds the second significant digit.) [a]Some simulations did not achieve a 99% rain-out of the density, so that $t_{99\%} > 10^7$ yr. This caused the large spread.

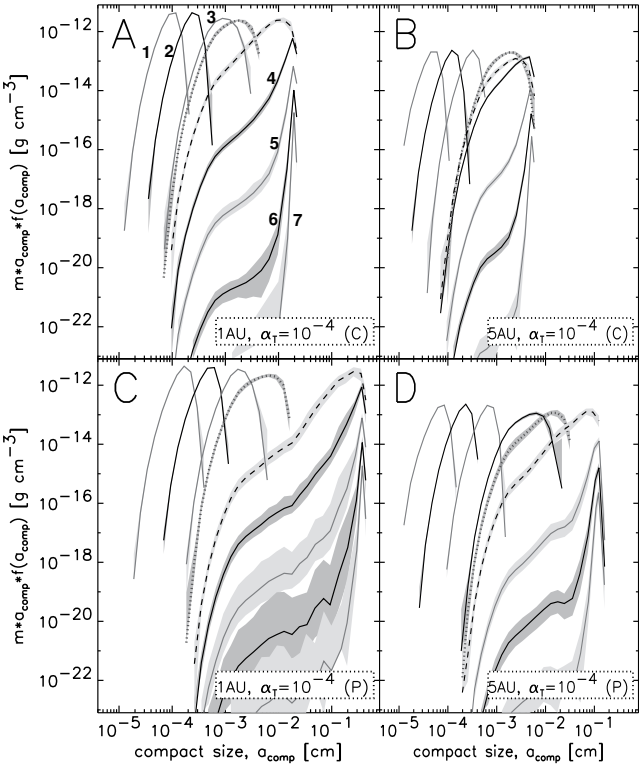

Fig. 2.10: The mass function plotted at various times for the $\alpha = 10^{-4}$ models. The panels compare the coagulation of the compact models ($\psi = 1$, *top* panels) with those where porosity effects are included (*bottom* panels). *Left* (right) panels show the coagulation of quartz (ice) particles at 1 AU (5 AU). Each plot shows the mass function at every logarithmic interval in time from $t = 10$ yr until $t = 10^7$ yr. Greyscales indicate the spread in the 50 realizations of the simulation. *See page 244 for a larger, full-color version of this figure.*

three stages. Initially, since particles start out as grains with sizes of 0.1 μm, Brownian motion dominates. The size-distribution is therefore rather narrow, because the Brownian collision kernel favors the lighter particles. Quickly ($\sim 10^2$ yr), however, turbulent velocities become dominant and relative velocities are now highest for the more massive (high τ_f) particles. Once the first compaction event occurs (dotted line) τ_f enters the regime in which it becomes (at least) proportional to size and the pace of coagulation strongly accelerates toward larger sizes. These findings correspond well with the simple analytical model of Blum (2004), where in his Fg. 5 the Brownian motion driven growth is also followed by a stage in which the growth is exponential. This evolution could be called 'run-away', were it not for the fact that (in our case) the particle distribution is truncated at $\tau_{\rm rain}$ (Eq. (2.25). The distribution at the first rain-out event is shown by the dashed line. Thereafter, the mass function collapses and evolves to a monodisperse population, close to the rain-out size (Fgs. 2.10,2.13). Two causes conspire to make these particles favored: first, large particles can only be (efficiently) removed by a collision with a similar-sized particle (and no longer by a larger particle since these have disappeared); second, in the $\alpha = 10^{-4}$ models friction times are always in the $\tau_f < t_s$ regime and relative velocities between similar-sized particles are suppressed. For these reasons, particles in the $\alpha = 10^{-4}$ models near rain-out deplete the smaller particles faster than they deplete themselves, and the size distribution evolves again to monodispersity. Note, however, that this behav-

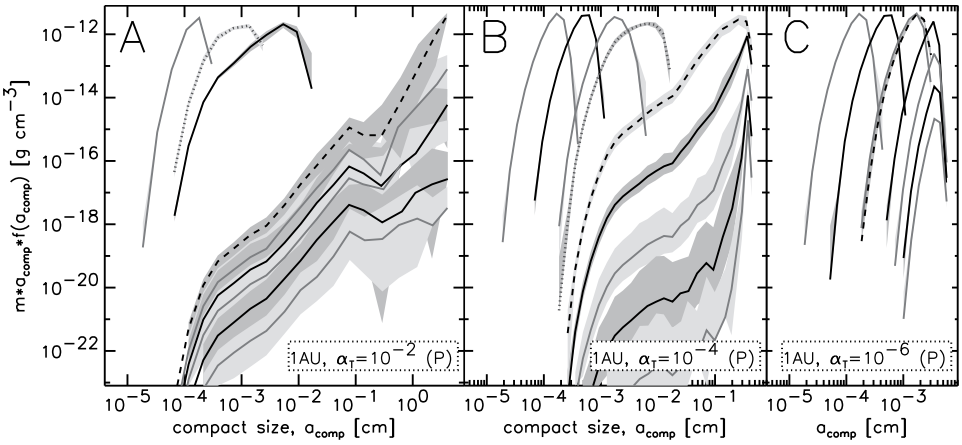

Fig. 2.11: Effects of turbulence on the coagulation. Panels show the collisional evolution at 1 AU of the porous models, yet with α values of 10^{-2} *(a)*, 10^{-4} *(b)* and 10^{-6} *(c)*. The scaling of the axis is the same throughout the panels. In the $\alpha = 10^{-2}$ models the spread in the runs is very large, causing the error bars to overlap. In the $\alpha = 10^{-6}$ model the particles rain-out without compacting.

ior is essentially caused by the imposed presence of a sharp cut-off size due to the rain-out criterion. In reality, a more smooth transition can be expected.

Although the qualitative trends between the porous and compact models are essentially the same—fractal growth, compaction and run-away growth, rain-out and depletion—it is unambiguously clear that the porous models evolve to larger particles, as is also seen in Table 2.2 in which the values for the rain-out particles are tabulated. The size difference at rain-out is $\sim$2 order of magnitude in size and $\sim$4 orders of magnitude in mass. Particles only rain-out at $\tau_{\rm rain}$ and in the porous models particles have to grow much further before the critical friction time is reached (Eq. (2.25). The inclusion of porosity in the coagulation models thus allows particles (when $\alpha > 10^{-4}$) to grow to cm/dm sizes in the gaseous nebula, *i.e.,* before settling to the mid-plane.

Apart from determining the size at which particles rain-out, α also determines the pace of coagulation. In the $\alpha = 10^{-2}$ models (Fg. 2.11a) coagulation is rapid. Also, a large degree of stochasticity is seen among different models. In the $\alpha = 10^{-6}$ models, on the other hand, the turbulent velocities are very small and the support against gravity is weak, such that that rain-out happens before any compaction takes place. These models are most reminiscent of the 'laminar nebula', where systematic (*i.e.,* settling) velocities dominate and are therefore most prone to gravitational instability effects (Hubbard & Blackman 2006). The comparison between the various α-models is perhaps best seen in the 'evolution tracks' of Fgs. 2.12. They show that initially all porous models follow the same (fractal) curve, until the moment compaction occurs. In the 1 AU, $\alpha = 10^{-2}$ model a significant compaction of aggregates can clearly be observed (descending line). After $t > 10^3$ yr, this is followed by a slight increase

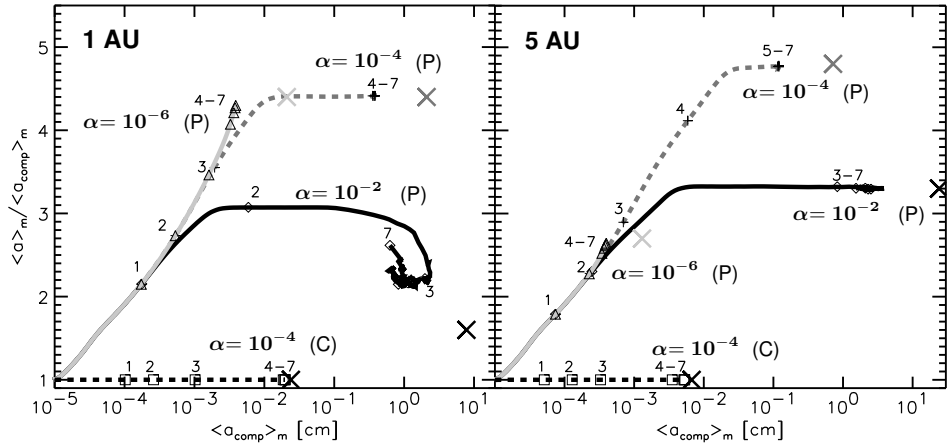

Fig. 2.12: Evolution curves of various models. In these panels the enlargement factor is characterized by the ratio of the mass-weighted porous size, $\langle a \rangle_m$, over the mass-weighted compact size, $\langle a_{\rm comp} \rangle_m$, ($\langle a^* \rangle_m$ in the text), against $\langle a_{\rm comp} \rangle_m$. Rising curves correspond to an increase of porosity due to fractal growth, and horizontal or declining curves indicate compaction. Numbers give the temporal stage of the coagulation (*i.e.*, $t = 10^i$). The detached, crosses indicate the average *porous sizes* (x-axis) and the size enhancement of the rain-out particles (y-axis).

in $\langle a \rangle_m / \langle a_{\rm comp} \rangle_m$; apparently due to the heavy rain-out, most collisions are again in the fractal regime.

Comparing the coagulation of the two materials studied here, *i.e.*, quartz for the 1 AU models and ice for the 5 AU models, one sees similarities in their collisional evolution (see also Fg. 2.13). It seems, however, that the coagulation at 5 AU is somewhat slower. This can be explained naturally because of the lower density, but also perhaps because compaction is more difficult to achieve due to the higher surface density (γ) of ices. Although the differences are subtle, one can see, *e.g.*, in Fg. 2.12 that the curves of the $\alpha = 10^{-4}, 10^{-2}$ porous models level-off at higher $\langle a \rangle_m$-to-$\langle a \rangle$ ratio than the corresponding 1 AU curves, indicating compaction is achieved 'easier' at 1 AU. Also, at $\alpha = 10^{-2}$ the 1 AU particles that rain-out are strongly compacted (an even higher α would have led to fragmentation), while the rain-out particles at 5 AU do not compact considerably before rain-out (see also Table 2.2). Thus, the larger surface energy (γ) of ices translates into a higher rolling energy and, subsequently, to decreased compaction.

2.5 Discussion

It now becomes clear that the internal structure of particles, represented here by the enlargement parameter ψ, is a variable of key importance in models of dust-aggregation. To illustrate this point further, Fg. 2.14 compares the 'evolution curve' of our (default $\alpha = 10^{-4}$, 1 AU) model with those of compact, PCA and CCA aggregation (grey curves). The superimposed black curve connects the (m, ψ) values of the

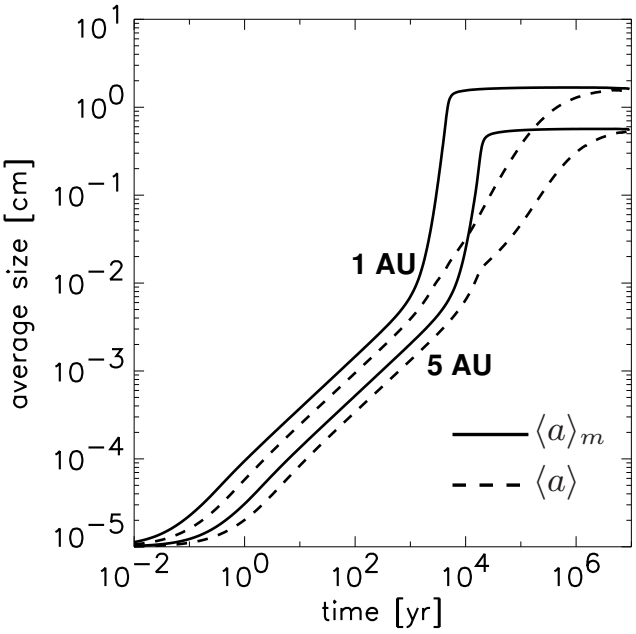

Fig. 2.13: Evolution of the size distribution with time. The mass-weighted size, $\langle a \rangle_m$ (solid line), and the mean size, $\langle a \rangle$ (*dashed curve*), are calculated for the default models ($\alpha = 10^{-4}$) at 1 AU (top lines) and 5 AU (*bottom curves*). The data are averaged over the 50 simulation runs. After $t \gtrsim 10^3$ yr the coagulation drives most of the mass into the largest particles.

most massive particle resulting from the collision model. The small, erratic structure in this curve corresponds to the fact that the particles fluctuate stochastically during the simulation. Furthermore, since we compare single particles here, instead of a (weighted) mean of the distribution as, *e.g.*, in Fig. 2.12, a fixed point in the figure corresponds to one particular friction time and lines of equal friction times lie parallel to the dashed lines indicating $\tau_\mathrm{f} = \tau_\mathrm{rain}$ and $\tau_\mathrm{f} = t_\mathrm{s}$. For the specific choice of $\alpha = 10^{-4}$ we see that τ_rain comes prior to t_s and velocities therefore remain modest. Still, in our collision model the coagulation will reach a point, indicated by a cross in Fig. 2.14, at which some collisions, having the right mass ratio and relative velocity, are energetic enough to cause compaction ($E > E_\mathrm{roll}$), which effectively halts any further increase in porosity. However, due to the earlier extensive build-up of porosity in the fractal regime, the particle distribution now evolves to larger sizes as compared to the compact models (Fg. 2.10), causing the rain-out masses to be orders of magnitudes higher (Table 2.2). Thus, a major part of the growth takes place in the nebula phase. Large, porous particles are quickly produced, stay in the nebula mixed with the gas and only settle when they are sufficiently compacted, *e.g.*, by energetic collisions (this chapter) or shocks (see below).

The curve of our model, with its characteristic bending point due to compaction, is a direct result of treating porosity as a dynamic variable that is altered by the collisional process. In all other models in Fg. 2.14, on the other hand, compaction is not incorporated, resulting in straight lines when the growth is in the fractal regime. In the PCA/CCA fractal models compaction is of course *a priori* ruled-out. However, the pre-assumed absence of compaction in the PCA/CCA models is consistent with the low collision energies in these limiting cases. In CCA, friction times barely grow

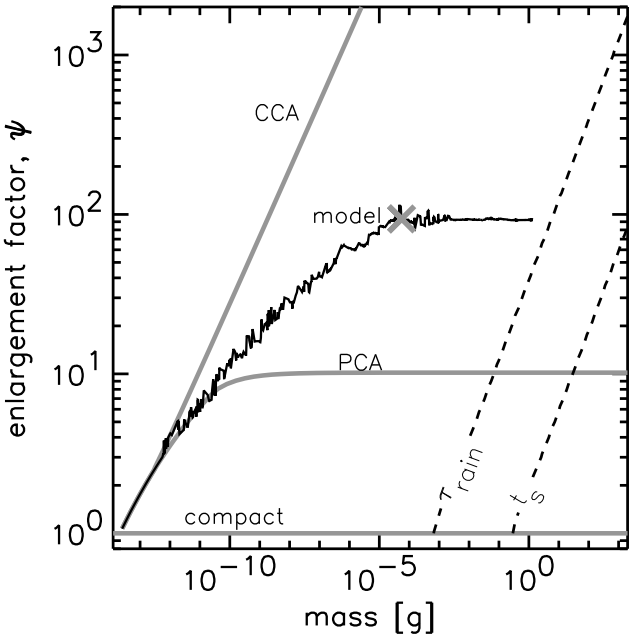

Fig. 2.14: The m-ψ relation for several aggregation models. Plotted is $\psi(m)$ for: the most massive particle in one of the R1Ta4-P models (*black curve*); the PCA, CCA aggregation models, discussed in § 2.2.4, (*grey curves*); and compact ($\psi = 1$) models. The *dashed lines* indicate points of equal friction times, $\tau_{\rm rain} \approx 500$ s and $t_{\rm s} \approx 1\,600$ s. The *cross* shows the point at which the model experiences the first compaction event.

($\tau_{\rm f} \propto m^{0.05}$), the $t_{\rm s}$ 'threshold' is not reached and relative velocities vanish for similar particles. In PCA, on the other hand, relative velocities are higher, but the collision energy is now suppressed by the reduced mass. Thus, if the coagulation process would (for some reason) be restricted to these limiting growth modes, aggregates will not restructure. Fig. 2.14 shows how this affects the overall coagulation process. It shows, *e.g.*, that compact grains rain-out at $\sim 10^{-4}$ g, 'PCA grains' at $\sim 10^{-2}$ g, porosity-evolving particles of our model at ~ 1 g, and 'CCA particles' will grow forever! It is clear that the porosity evolution of collisional agglomerates is of decisive influence on the coagulation process. Modeling the porosity evolution in combination with a microphysical collision model is therefore a key requirement for a full understanding of the first stages of planet formation.

To quantify the effects of coagulation on the appearance of the disk, we have calculated optical depths to the mid-plane in the MMSN. As a first order approximation, the vertical structure is to be taken of constant density and extends over one scaleheight. We assume that this layer is represented by the particles of our simulation and that the rain-out particles (which we do not follow) are below it, *i.e.*, at the mid-plane regions of the disk. The geometrical optical depth (*i.e.*, at visible/UV-wavelengths) *to* the mid-plane is then calculated as

$$\tau_{\rm geom} = H_{\rm g} \int {\rm d}m \, f(m) \pi a^2. \tag{2.27}$$

Results are given in Fig. 2.15 for the 1 AU and 5 AU models. In Fig. 2.15a it is seen that the $\alpha = 10^{-6}$ models stay optically thick for most of the disk's evolution. Note

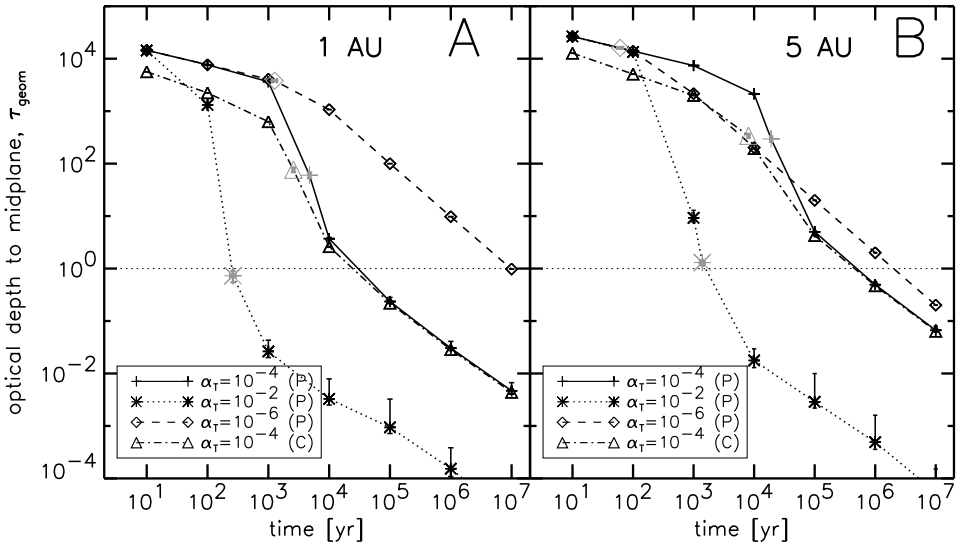

Fg. 2.15: Geometrical optical depth to the mid-plane as function of time for the 1 AU models (*left*) and the 5 AU models (*right*). The optical depth is computed at every logarithmic interval in time and also at the point where particles rain-out (grey symbol). For illustrative purposes the points are connected by lines. Error bars denote the spread throughout the 50 runs of each model.

also that the $\alpha = 10^{-4}$ porous models (solid lines) and the $\alpha = 10^{-4}$ compact models (dashed-dotted line) do not deviate much in $\tau_{\rm geom}$. This shows again the dual effects of porosity on the population: it increases the geometrical cross-section, yet it also speeds up the coagulation, causing more mass to be 'locked' inside large particles. At 5 AU (Fg. 2.15b), the timescales are longer and the disks only becomes optically thin after $\sim 10^6$ yr when $\alpha \lesssim 10^{-4}$. In the $\alpha = 10^{-2}$ models, evolution to optical thinness is very fast at both radii. It is clear that, within the frame-work of these models, the inner regions of protoplanetary disks are rapidly depleted of small grains unless $\alpha \sim 10^{-6}$ or less.

There is a further serious issue hidden here. All our models show a rapid decline of the (sub-)micron size population on a timescale of $\sim 10^3$ yr. This is a well-known problem in models for grain coagulation in protoplanetary environments: the densities are high enough for coagulation to proceed rapidly (Dullemond & Dominik 2005). Furthermore, the turbulence induced relative velocities promote collisions between particles with different friction times, *i.e.*, between small and larger particles. In contrast, observations reveal the presence of copious amounts of small grains in the disk-photospheres of isolated Herbig AeBe stars and T-Tauri stars, pointing toward the presence of small grains on timescales of some 10^6 yr (van Boekel et al. 2004, 2005; Meeus et al. 2003; Natta et al. 2007). This discrepancy implies a continuous replenishment of (sub)micron-sized grains. In particular, it may reflect the importance of vaporization and condensation processes continuously forming fresh,

small grains. Likely, this vaporization and condensation would be localized in the hot and dense, inner regions of the disk and these grains would then have to be transported upwards and outwards to the disk photosphere through diffusion processes. The high degree of crystallinity of silicates in the inner few AU of protoplanetary disks also points toward the importance of condensation processes in these environments (van Boekel et al. 2004). Likewise, the presence of crystalline silicates in the cold outer regions of protoplanetary disks has been attributed to large scale mixing of materials in these environments (Bockelée-Morvan et al. 2002; Gail 2004). Alternatively, the replenishment of small grains is through collisional fragmentation. These energetic collisions could take place either in the gaseous nebula due to high relative velocities driven by a high α, or in the mid-plane regions with the subsequent upwards diffusion of small grains. While it might be difficult to sustain $\alpha \gtrsim 10^{-2}$ over a prolonged period of time, fragmentation in the mid-plane regions seems viable since more massive particles will reside here. Furthermore, if the mid-plane becomes dust-dominated ($\rho_{\rm d} > \rho_{\rm g}$), shear-turbulence will develop, further augmenting the collisional energies (Cuzzi et al. 1993).

Further constraints on the collisional growth of grains in protoplanetary disks are provided by the solar system record; specifically, the chondrules and Ca-Al-rich Inclusions (CAI), which dominate the composition of primitive meteorites. These millimeter-size igneous spherules are high-temperature components that formed during transient heating events in the early solar system. We realize that the cm-sized fluff-balls formed in our porous coagulation models are in the right mass-range of these meteorite components. It is tempting to identify these fluff-balls as the precursors to the chondrules and CAIs. We might then envision a model where the collisional evolution is terminated by the flash-heating event, for example a shock or lightning, which leads to melting and the formation of a chondrule and subsequent immediate settling. During the settling phase the chondrule may acquire a dust rim by sweeping up small dust grains or other unprocessed fluff-balls still suspended in the nebula (Cuzzi 2004). One key point to recognize here is that chondrules show a spread in age of a few million years (Wood 2005), which indicates that the collisional grain growth process takes place over a much longer timescale than our models would predict (see above).

In this study we have focused on the agglomeration driven by random motions—either Brownian or turbulent—high up in the nebula. Growth is then presumed to be terminated once the aggregate has compacted enough to settle. At that point, the aggregate will drop-down about one scaleheight after which further growth must occur for further settling to continue. In reality, instead of the simple two-component picture of nebula and mid-plane presented in this work, the nebula will acquire a stratified appearance (Dubrulle et al. 1995), where larger particles with higher friction times have smaller scaleheights. Collisional evolution models should be able to include this stratified nature of the disk. This stratification also extends in the radial direction due to radial drift motions and turbulent diffusion. Incorporation of these motions into the Monte Carlo code will be challenging. We expect that the study presented here can serve as the basis for incorporating realistic grain growth in hydrodynamical models, likely in the form of well-selected 'collision-recipes'. An

obvious step would be to include collisions that exceed the $E_{\rm frag}$ limit in the collision model. Note, for example, that in the Dominik & Tielens (1997) terminology what we have called 'fragmentation' should in fact be sub-divided in a continuous range of aggregate disruptions. At first monomers will be lost and only if $E \gg E_{\rm frag}$ are aggregates completely shattered. Other extensions to the model are to allow for a distribution of monomer sizes and to use monomers of different chemical composition. Both will affect the critical energy for restructuring, $E_{\rm roll}$. However, with an increasing number of parameters characterizing the collision, it is worthwhile to verify experimentally — either through laboratory experiments or through detailed numerical calculations — which are of prime importance.

2.6 Conclusions

We have presented a model that incorporates the internal structure of aggregates as a variable in coagulation models. We used the enlargement parameter ψ to represent the internal structure. It is seen that the internal structure is key to the collisional evolution, since it crucially affects the dust-gas coupling. However, in the model presented in § 2.2 ψ is not a static variable. It is altered by the collisional process and we have constructed simple recipes to include this aspect in coagulation models.

Next, we have applied the new collision model to the collisional evolution of the turbulent protoplanetary disk, until particles rain-out to the mid-plane. Our main conclusions are:

1. With the treatment of porosity as a variable, three different regimes can be distinguished: fractal growth, compaction and fragmentation (Blum 2004) . These regimes are also reflected in the collisional evolution of the size distribution: fractal growth (mostly Brownian motion), compaction (growth accelerates) and rain-out.
2. The collisional evolution of our porosity-evolving model is quantitatively different from PCA/CCA aggregation models in which porosity can be parameterized by a fixed exponent. Therefore, a microphysical collision model is a key requirement for coagulation models.
3. Due to the porous evolution, particles up to dm-sizes can be suspended in the gaseous nebula, orders of magnitude larger in mass than in models of compact coagulation. Therefore, chondrule precursors could have had their origin in regions above the mid-plane.
4. If $\alpha < 10^{-2}$, no fragmentation occurs in the gaseous nebula. Therefore, if $10^{-6} < \alpha < 10^{-2}$, the inner nebula will become optically thin on timescales of $\sim 10^4$ yr, unless an influx of small grains takes place.

Acknowledgment. C.W.O. likes to show his appreciation to Carsten Dominik and Dominik Paszun for extensive discussion on the manuscript. These greatly helped to improve the quality of the chapter, especially regarding § 2.2. We appreciate the suggestion of Carsten Dominik to include Fgs. 2.2 and 2.13 and Dominik Paszun for useful assistance with creating Fg. 2.2. Finally, we appreciate Jürgen Blum for providing a thorough and helpful review.

3

Closed-form expressions for particle relative velocities induced by turbulence[1]

— C. W. Ormel, J. N. Cuzzi—

We present complete, closed-form expressions for random relative velocities between colliding particles of arbitrary size in nebula turbulence. These results are exact for very small particles (those with stopping times much shorter than the large eddy overturn time) and are also surprisingly accurate in complete generality (that is, also apply for particles with stopping times comparable to, or much longer than, the large eddy overturn time). We note that some previous studies may have adopted previous simple expressions, which we find to be in error regarding the size dependence in the large particle regime.

3.1 Introduction and outline

Gas in astrophysical environments is often in a turbulent state of motion, constantly affected by temporally and spatially varying accelerations from eddies having a variety of scales. A particle, due to its inertia, does not instantaneously follow the gas motions but requires a certain time in order to align with the gas motion. The particle's interaction with the gas is captured in the definition of the *stopping time* of the particle (sometimes also referred to as friction time),

$$\tau_{\rm f} = \frac{3}{4 c_{\rm g} \rho_{\rm g}} \frac{m}{A}, \tag{3.1}$$

[1]Originally published in *Astronomy & Astrophysics*, vol. 466, p. 431 (2007)

where c_g and ρ_g are, respectively, the sound speed and the volume mass density of the gas, and m and A the mass and projected surface area of the particle. Due to this inertial lag, a particle develops a relative velocity with respect to the gas. In addition, these lags also cause particles to acquire relative velocities among themselves.

While the general problem of calculating these relative velocities has received considerable attention in the basic fluid dynamics community (see Cuzzi & Hogan (2003) for references; henceforth CH03), the formalism most frequently used in the astrophysics community was developed by Völk et al. (1980) and Markiewicz et al. (1991) (henceforth MMV). In these works the final results are given in terms of integrals that were not *solved* analytically. Some workers have used simple fits to these numerical results in their models of dust coagulation; however, simple closed-form expressions for particle-particle relative velocities would help streamline these models (*e.g.*, Suttner & Yorke 2001; Dullemond & Dominik 2005; Nomura & Nakagawa 2006; Ormel et al. 2007). Recently, CH03 obtained closed-form expressions from the MMV model for particle velocities in inertial space v_p, for particle-gas relative velocities v_{pg}, and for relative velocities between two identical particles v_{pp}, but did not extend their results to the general case of two particles of different stopping times. Moreover, CH03 stressed the validity of their analytical results for particles with stopping times much shorter than the large eddy turnover time. In this chapter we generalize the approach and results of CH03 to obtain closed-form expressions for relative velocities between particles of arbitrary, and unequal, size. In § 3.2 we define important quantities and review previous work. In § 3.3 we present two independent approaches for obtaining the desired closed-form solutions. In § 3.4 we give our conclusions and a summary.

3.2 Definitions and previous work

Nebula gas turbulence is generally described as being composed of eddies having a range of spatial scales ℓ and spatial frequencies $k = 1/\ell$, with an energy spectrum $E(k) \propto k^{-5/3}$ and total energy $v_g^2/2$ per unit mass providing the normalization condition

$$\frac{v_g^2}{2} = \int_{k_L}^{k_s} E(k)\mathrm{d}k, \tag{3.2}$$

from which $E(k) = v_g^2/3k_L\ (k/k_L)^{-5/3}$. The largest, or integral scale, eddies have spatial scale $L = 1/k_L$, and the smallest, or Kolmogorov scale, eddies have spatial scale $\ell_s = 1/k_s$. The form of $E(k)$ given above is the inertial range expression most often assumed, with $E(k) = 0$ for $k > k_s$ or $k < k_L$. Völk et al. (1980) used a spectrum $P(k) = 2E(k)$ and stipulated no smallest scale ℓ_s for the turbulence, but Weidenschilling (1984a) and MMV noted that a finite value for $\ell_s > 0$ had profound effects on the particle velocities, especially the relative velocities v_{pp} for small particles. Each eddy wavenumber k has a characteristic velocity $v(k) = \sqrt{2kE(k)}$ and overturn time $t_k = \ell/v(k) = (kv(k))^{-1}$. Our standard definition of the particle *Stokes number* is $\mathrm{St} = \tau_f/t_L$, where t_L is the overturn time of the largest eddy, generally taken to

be the local orbit period. The local turbulent intensity is described by its Reynolds number, Re, defined as the ratio between the turbulent and the molecular kinematic viscosities, $\mathrm{Re} = \nu_\mathrm{T}/\nu$. The values for ℓ, v and t at the integral scale then follow from Re, *e.g.*, $\ell_\mathrm{s} = \mathrm{Re}^{-3/4}L$ and $t_\mathrm{s} = \mathrm{Re}^{-1/2}t_\mathrm{L}$. These expressions bring Re into the final expressions for particle velocities as a limit on certain integrals (*cf.* CH03 for more detail). In the notation of astrophysical 'α-models', $\mathrm{Re} = \alpha c_\mathrm{g} H_\mathrm{g}/\nu = \alpha c_\mathrm{g}^2/\nu\Omega$ where c_g, H_g, and ν are the sound speed, vertical scale height, and kinematic viscosity of the nebula gas and Ω is the orbital frequency.

Völk et al. (1980) introduced the concept of 'eddy classes'. Class I eddies vary slowly enough that a particle, upon entering a class I eddy, will forget its initial motion and align itself to the gas motions of the eddy before the eddy decays or the particle leaves the eddy. Class II eddies, on the other hand, have fluctuation times shorter than the particle's stopping time τ_f, and fluctuate too rapidly to provide more than a small perturbation on the particle. The timescale on which an eddy decays is given by t_k, while the eddy-crossing timescale is $t_\mathrm{cross} \approx \ell/v_\mathrm{rel} = (kv_\mathrm{rel}(k))^{-1}$, with v_rel the relative velocity between a grain and an eddy. For an eddy to be of class I both t_k and t_cross must be larger than the particle's stopping time. The boundary between these classes occurs at $k = k^*$ (or at $t_k = t^*$) which can be defined as (Völk et al. 1980, MMV):

$$\frac{1}{\tau_\mathrm{f}} = \frac{1}{t^*} + \frac{1}{t_\mathrm{cross}} = \frac{1}{t^*} + k^* v_\mathrm{rel}(k^*). \tag{3.3}$$

It is important to realize that k^* (or t^*) is a function of stopping time τ_f, that is, the boundary separating the two classes is different for each particle. The different treatment for the two eddy classes $k < k^*$ and $k > k^*$ forms the core of the derivation of the turbulence-induced particle velocities.

All turbulent velocities in this chapter are statistical, root-mean-square, averaged quantities. The average inertial space particle velocity v_p is given by Eq. (6) of MMV.

$$v_\mathrm{p}^2 = \int_{k_\mathrm{L}}^{\max(k^*,k_\mathrm{L})} 2E(k)\left(1 - K^2\right)\mathrm{d}k + \int_{\max(k^*,k_\mathrm{L})}^{k_\mathrm{s}} 2E(k)\,(1-K)\,[g(\chi) + Kh(\chi)]\,\mathrm{d}k, \tag{3.4}$$

in which $K = \tau_\mathrm{f}/(\tau_\mathrm{f} + t_k)$. The K^2 term in the first integral results from the more recently preferred '$n = 1$' gas velocity autocorrelation function (MMV and CH03). The functions $g(\chi) = \chi^{-1}\tan^{-1}(\chi)$ and $h(\chi) = 1/(1+\chi^2)$ with $\chi = Kt_k k v_\mathrm{rel}$ were first obtained by Völk et al. (1980).

CH03 noted that, for very small particles with $\tau_\mathrm{f} \ll t_\mathrm{L}$ or $\mathrm{St} \ll 1$, the second integral becomes negligible, leaving only the first integral which is analytically solvable and for which the upper limit can be extended to k_s with negligible error. Here, to generalize the approach of CH03 to particles of *arbitrary* size, we approximate $h(\chi) = g(\chi) = 1$ for *all* particle sizes (see CH03 § 2.2.3 for supporting logic). Numerical calculations of $h(\chi)$ and $g(\chi)$ validate this approximation to order unity (see App. 3.A), and we gain further confidence in it from *a posteriori* comparison with ex-

act numerical model results. The general expression for $v_{\rm p}^2$ is then the same as in the $\tau_{\rm f} \ll t_{\rm L}$ regime, and the same analytical result is obtained, *i.e.*, CH03,

$$v_{\rm p}^2 = \int_{k_{\rm L}}^{k_{\rm s}} {\rm d}k\, 2E(k) \left(1 - K^2\right) = v_{\rm g}^2 \left(1 - \frac{{\rm St}^2(1 - {\rm Re}^{-1/2})}{({\rm St}+1)({\rm St}+{\rm Re}^{-1/2})}\right). \tag{3.5}$$

CH03 did not give this explicit result for $v_{\rm p}$, but merely noted that it was straightforward to derive it from their Eq. (19) for $v_{\rm pg}$ and the general relationship $v_{\rm pg}^2 = v_{\rm p}^2 - v_{\rm g}^2$; however we will use it explicitly here.

Comparison of the predictions of this simple expression with detailed numerical results (MMV, CH03) show that it is indeed a good approximation for arbitrary St. A more accurate approximation to Eq. (3.4), in which the g and h functions are approximated as power-laws in k^*/k, is outlined in App. 3.A. Unless ${\rm St} \ll 1$, we can neglect the Reynolds number term in Eq. (3.5) and obtain $v_{\rm p} = v_{\rm g}/\sqrt{1+{\rm St}}$, a well known result (Völk et al. 1980; Cuzzi et al. 1993; Schräpler & Henning 2004) which describes the diffusivity of large particles in turbulence.

3.3 Results

3.3.1 k-space approach

MMV (their Eq. (7)) expressed the relative velocities $v_{\rm p1p2}$ between particles of different stopping times t_1 and t_2 as

$$v_{\rm p1p2}^2 = v_{\rm p1}^2 + v_{\rm p2}^2 - 2\overline{v_{\rm p1} v_{\rm p2}} \equiv \Delta v_{12}^2. \tag{3.6}$$

Having already derived $v_{{\rm p}i}^2$ ($i = 1, 2$) above, we can determine Δv_{12} by evaluating the cross term $\overline{v_{\rm p1} v_{\rm p2}}$; this chapter presents analytical solutions of this problem obtained in two separate ways. In this subsection we retain the wavenumber dependence; in § 3.3.2 we transform to time variables. In Eq. (8) of MMV the cross term is given as a sum over the two particle sizes involved, which we separate here, writing $\Delta v_{12}^2 = v_{\rm p1}^2 + v_{\rm p2}^2 - (v_{\rm c1}^2 + v_{\rm c2}^2)$, where

$$v_{{\rm c}i}^2 = \frac{2t_i}{t_1+t_2}\left(\int_{k_{\rm L}}^{\min(k_1^*,k_2^*)} E(k){\rm d}k - \int_{k_{\rm L}}^{\min(k_1^*,k_2^*)} E(k)\left(\frac{1}{1+t_k/t_i}\right)^2 {\rm d}k\right). \tag{3.7}$$

Changing variable to $x = k/k_{\rm L}$, substituting for $E(k)$, and converting stopping time t_i to Stokes number ${\rm St}_i = t_i/t_{\rm L}$:

$$v_{{\rm c}i}^2 = \frac{2v_{\rm g}^2 t_i}{3(t_1+t_2)}\left[\int_1^{x_1^*} x^{-5/3}{\rm d}x - \int_1^{x_1^*} \frac{{\rm St}_i^2 {\rm d}x}{x^{5/3}({\rm St}_i + x^{-2/3})^2}\right], \tag{3.8}$$

where we have taken, without loss of generality, $k_1^* \le k_2^*$. The first integral is trivial and the second integral can be solved exactly as in Eqs. (17–19) of CH03. In evalu-

ating the specific value of the integrals above, we need a closed form for the upper limit $x_1^* = k_1^*/k_\mathrm{L}$. A simple prescription is readily found by inspection of Fg. 3 of CH03: $x_1^* = k_1^*/k_\mathrm{L} = 0.5\mathrm{St}_1^{-3/2} + 1$. That is, the boundary eddy for particles with stopping time t_1 is that for which $t_k \sim t_1$ until $t_1 > t_\mathrm{L}$, beyond which it remains constant. This is merely a convenient mathematical shorthand to keep everything in closed form. Then, repeating the analytical solution of CH03 (Eqs. (17–19)) we obtain

$$v_{ci}^2 = v_\mathrm{g}^2 \frac{t_i}{(t_1+t_2)} \left[(1 - x_1^{*-2/3}) - \left(\frac{\mathrm{St}_i}{1+\mathrm{St}_i} - \frac{\mathrm{St}_i}{1+\mathrm{St}_i x_1^{*2/3}} \right) \right]. \tag{3.9}$$

This solution for the cross term is easily combined with Eq. (3.5) to obtain expressions for particle-particle relative velocities Δv_{12}^2. Further manipulation of these expressions may be possible, but the important point here is that Δv_{12} can be expressed in closed form as function of St_1, St_2, v_g, and Re. With a few minutes of algebra, simpler expressions can be found in the limiting regimes of interest ($\mathrm{St}_1 \ll 1, \gg 1$, *etc.*) which agree well with those which we present in the next section, for analytical solutions obtained in the time domain instead of the wavenumber domain, and where an analytical solution for the boundary $k^*(t^*)$ is used rather than the form for x_1^* adopted above. It should be recalled that, for *very* small particles $\tau_\mathrm{f} < t_\mathrm{s}$, x_1^* has an upper limit of $k_\mathrm{s}/k_\mathrm{L} = \mathrm{Re}^{3/4}$ (see, *e.g.*, CH03, Fg. 3).

3.3.2 t-space approach

The integrals expressing $v_{\mathrm{p}i}^2$ and v_{ci}^2 are transformed into a simpler form by changing variables from k to t_k. Since $t_k = 1/kv(k) = \left(k\sqrt{2kE(k)}\right)^{-1}$ and $E(k) = Ak^{-5/3}$ for a Kolmogorov power spectrum (where A is the normalization factor), we obtain that $E(k)\mathrm{d}k = \frac{3}{2}\sqrt{2}A^{3/2}\mathrm{d}t_k$. Now, $A = \frac{1}{3}v_\mathrm{g}^2 k_\mathrm{L}^{2/3}$ from the normalization of the turbulent spectrum (Eq. (3.2)), $k_\mathrm{L} = (v_\mathrm{L} t_\mathrm{L})^{-1}$ with v_L the velocity of the largest eddy, and $v_\mathrm{L}^2 = \frac{2}{3}v_\mathrm{g}^2$ also by normalizing the power spectrum (see CH03). We then end up with

$$E(k)\ \mathrm{d}k = \frac{1}{2}\frac{v_\mathrm{g}^2}{t_\mathrm{L}}\mathrm{d}t_k, \tag{3.10}$$

which can be substituted into all the integrals, putting them into a simpler form. For instance, Eq. (3.5) becomes for particle i

$$v_{\mathrm{p}i}^2 = \frac{v_\mathrm{g}^2}{t_\mathrm{L}} \int_{t_\mathrm{s}}^{t_\mathrm{L}} 1 - \left(\frac{t_i}{t_i + t_k} \right)^2 \mathrm{d}t_k = \frac{v_\mathrm{g}^2}{t_\mathrm{L}} \left[t_k + \frac{t_i^2}{t_i + t_k} \right]_{t_\mathrm{s}}^{t_\mathrm{L}}. \tag{3.11}$$

Similarly, the cross term becomes

$$v_{ci}^2 = \frac{v_\mathrm{g}^2}{t_\mathrm{L}} \frac{2t_i}{t_1+t_2} \int_{t_{12}^*}^{t_\mathrm{L}} 1 - \left(\frac{t_i}{t_i + t_k} \right)^2 \mathrm{d}t_k \ = \frac{v_\mathrm{g}^2}{t_\mathrm{L}} \frac{2t_i}{t_1+t_2} \left[t_k + \frac{t_i^2}{t_i + t_k} \right]_{t_{12}^*}^{t_\mathrm{L}} \tag{3.12}$$

With $t_{12}^* = \texttt{max}(t_1^*, t_2^*)$ and $t_\mathrm{s} \le t_{12}^* \le t_\mathrm{L}$ since t^* refers to an eddy's turn-over time. We now solve for Δv_{12}^2 by splitting the integral in Eq. (3.11) at t_{12}^* and subtracting the corresponding v_{ci} terms from Eq. (3.12) to get

$$\Delta v_{12}^2 = \frac{v_\mathrm{g}^2}{t_\mathrm{L}} \left(\left[t_k + \frac{t_1^2}{t_1+t_k} \right]_{t_\mathrm{s}}^{t_{12}^*} + \left[t_k + \frac{t_1^2}{t_1+t_k} \right]_{t_{12}^*}^{t_\mathrm{L}} - \frac{2t_1}{t_1+t_2} \left[t_k + \frac{t_1^2}{t_1+t_k} \right]_{t_{12}^*}^{t_\mathrm{L}} + (1 \leftrightarrow 2) \right), \tag{3.13}$$

where the $(1 \leftrightarrow 2)$ notation indicates interchange between particles 1 and 2. With further manipulation and cancellation of terms, the previous expression simplifies slightly to

$$\begin{aligned} \Delta v_{12}^2 &= \frac{v_\mathrm{g}^2}{t_\mathrm{L}} \left(\left[t_k + \frac{t_1^2}{t_1+t_k} \right]_{t_\mathrm{s}}^{t_{12}^*} + \frac{t_2-t_1}{t_1+t_2} \left[\frac{t_1^2}{t_1+t_k} \right]_{t_{12}^*}^{t_\mathrm{L}} + (1 \leftrightarrow 2) \right) \\ &= \Delta v_\mathrm{II}^2 + \Delta v_\mathrm{I}^2 \end{aligned} \tag{3.14}$$

This is perhaps the most concise way to write the expressions for Δv_{12}^2. The first term we call Δv_II^2 since this term involves class II (fast) eddies. If $t_{12}^* = t_\mathrm{L}$ (heavy particles) all eddies are fast and only this term remains. Conversely, if $t_{12}^* = t_\mathrm{s}$ (small particles) the contribution from Δv_II vanishes and the second term, Δv_I, determines relative velocities. In the intermediate regime, $t_\mathrm{s} < t_{12}^* < t_\mathrm{L}$, both terms contribute. Written in terms of the Stokes numbers these terms becomes

$$\begin{aligned} \Delta v_\mathrm{I}^2 &\equiv \frac{v_\mathrm{g}^2}{t_\mathrm{L}} \frac{t_2-t_1}{t_1+t_2} \left[\frac{t_1^2}{t_1+t_k} \right]_{t_{12}^*}^{t_\mathrm{L}} + (1 \leftrightarrow 2) \\ &= v_\mathrm{g}^2 \frac{\mathrm{St}_1 - \mathrm{St}_2}{\mathrm{St}_1 + \mathrm{St}_2} \left(\frac{\mathrm{St}_1^2}{\mathrm{St}_{12}^* + \mathrm{St}_1} - \frac{\mathrm{St}_1^2}{1+\mathrm{St}_1} - (1 \leftrightarrow 2) \right) \end{aligned} \tag{3.15a}$$

$$\begin{aligned} \Delta v_\mathrm{II}^2 &\equiv \frac{v_\mathrm{g}^2}{t_\mathrm{L}} \left[t_k + \frac{t_1^2}{t_1+t_k} \right]_{t_\mathrm{s}}^{t_{12}^*} + (1 \leftrightarrow 2) \\ &= v_\mathrm{g}^2 \left((\mathrm{St}_{12}^* - \mathrm{Re}^{-1/2}) + \frac{\mathrm{St}_1^2}{\mathrm{St}_1 + \mathrm{St}_{12}^*} - \frac{\mathrm{St}_1^2}{\mathrm{St}_1 + \mathrm{Re}^{-1/2}} + (1 \leftrightarrow 2) \right) \end{aligned} \tag{3.15b}$$

Note again that since $t_\mathrm{s} \le t_{12}^* \le t_\mathrm{L}$ we also have that $\mathrm{Re}^{-1/2} \le \mathrm{St}_{12}^* \le 1$. Below, we will first solve for St_{12}^*, and then consider solutions for Δv_{12} in various limiting cases of the particle stopping times.

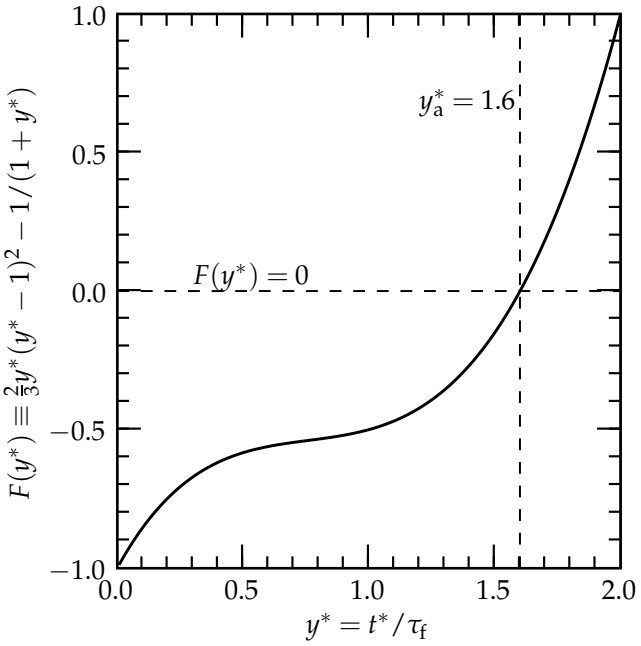

Fig. 3.1: The function $\frac{2}{3}y^*(y^*-1)^2 - 1/(1+y^*)$. If $\tau_f \ll t_L$ and $v_{sys} = 0$ (no systematic velocity drifts; see § 3.3.3) this equation is equal to zero and we find a solution $y^* = t^*/\tau_f \approx y_a^* = 1.6$. On the other hand, for $\tau_f \sim t_L$, the RHS of Eq. (3.18d) is ≈ -0.5 and $y^* \approx 1$.

Solving for t^*

The relative velocity between a particle with stopping time τ_f and an eddy k, is given by Völk et al. (1980), Eq. (15):

$$v_{rel}^2(k) = v_{sys}^2 + 2\int_{k_L}^{k} E(k') \left(\frac{\tau_f}{\tau_f + t_k}\right)^2 \mathrm{d}k'. \tag{3.16}$$

v_{sys} is any systematic velocity component not driven by turbulence—such as due to pressure-gradient driven azimuthal headwind, the ensuing radial drift, or vertical settling under solar gravity. We can integrate this equation in the same fashion as Eq. (3.12) and arrive at

$$v_{rel}^2(k^*) = v_{sys}^2 + \frac{v_g^2}{t_L}\left[\frac{\tau_f^2}{\tau_f + t_k}\right]_{t_L}^{t^*} = v_{sys}^2 + \frac{v_g^2 \tau_f}{t_L}\left(\frac{1}{1+y^*} - \frac{1}{1+y_L}\right), \tag{3.17}$$

in which $y = t_k/\tau_f$. Also, using the definition for t_k (see text above Eq. (3.10)), k^* can be expressed as $(k^*)^2 = (2A)^{-3/2} t^{*-3} = \frac{3}{2} v_g^{-2} t_L t^{*-3}$. Inserting the expressions for k^* and v_{rel}^2 into Eq. (3.3), assuming that $v_{sys} = 0$ for simplicity (see however § 3.3.3), we obtain:

$$\frac{1}{k^*}\left(\frac{1}{\tau_f} - \frac{1}{t^*}\right) = v_{rel} \Rightarrow \tag{3.18a}$$

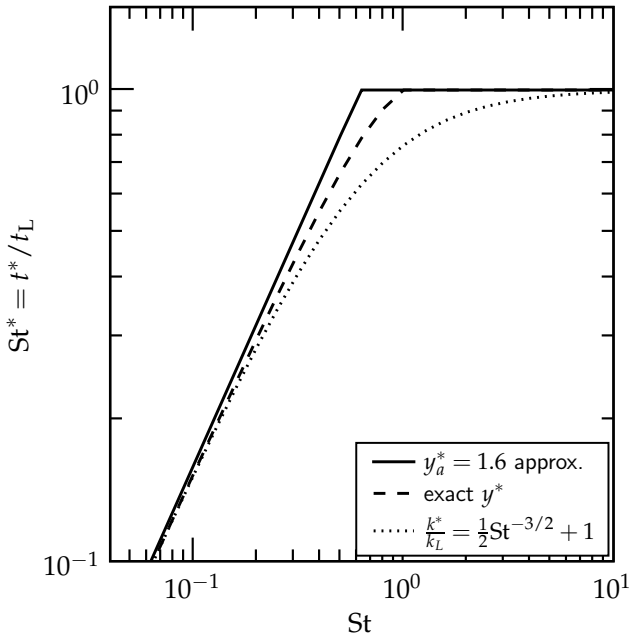

Fig. 3.2: Three different assumptions for t^* (or the related k^*) are shown here.

$$t^* \left(\frac{t^*}{\tau_\mathrm{f}} - \frac{t^*}{t^*} \right)^2 = (2A)^{-3/2} v_\mathrm{rel}^2 \Rightarrow \tag{3.18b}$$

$$t^* \left(y^* - 1 \right)^2 = \tfrac{3}{2}\tau_\mathrm{f} \left(\frac{1}{1+y^*} - \frac{1}{1+y_\mathrm{L}} \right) \Rightarrow \tag{3.18c}$$

$$\tfrac{2}{3} y^* \left(y^* - 1 \right)^2 - \frac{1}{1+y^*} = -\frac{1}{1+y_\mathrm{L}}, \tag{3.18d}$$

where we have defined $y^* = t^*/\tau_\mathrm{f}$ and $y_\mathrm{L} = t_\mathrm{L}/\tau_\mathrm{f} = \mathrm{St}^{-1}$. The LHS of Eq. (3.18d) is plotted in Fg. 3.1. If $y_\mathrm{L} \gg 1$ for small particles, the RHS of Eq. (3.18d) is negligible and the numerical solution for y^* becomes $y^* \approx y_a^* = 1.6$, or $t^* \approx 1.6\tau_\mathrm{f}$. On the other hand, when τ_f nears t_L, the $-1/(1+y_\mathrm{L})$ term causes the RHS of Eq. (3.18d) to drop to -0.5, and $y^* \to 1$. For $\tau_\mathrm{f} > t_\mathrm{L}$ we always have that $t^* = t_\mathrm{L}$; *i.e.,* for such a particle all eddies are of class 2. In Fg. 3.2 we compare the exact solution (dashed line) for t^* with the $t^* \approx y_a^* \tau_\mathrm{f} = 1.6\tau_\mathrm{f}$ approximation (solid curve; in both cases $t^* \leq t_\mathrm{L}$ is simply enforced), and the empirical function $k^*/k_\mathrm{L} = 1 + \frac{1}{2}\mathrm{St}^{-3/2}$ (dotted line; see § 3.3.1).

The exact solution for Δv_{12} (Eq. (3.14)) is given in Fg. 3.3 both for $t_1 \gg t_2$ (solid curve) and for particles of equal stopping times (dashed curve). A Reynolds number of $\mathrm{Re} = 10^8$ has been adopted.

3.3.3 The role of v_sys: eddy-crossing effects

Systematic velocities v_sys due to vertical settling, and pressure-gradient headwinds and drifts, will occur (*e.g.,* Nakagawa et al. 1986). Because particles drift through

eddies, their transit time is affected (because $v_{\rm rel}$ is larger) and the boundary between class I and II eddies shifts. Cuzzi et al. (1993) include this effect, due to vertical settling, in their model of particle diffusion (their Eq. (43)). The model presented here offers a generalized way of treating this effect, which we will only sketch here.

Repeating the procedure outlined in § 3.3.2 but retaining the $v_{\rm sys}$ term in $v_{\rm rel}$ (Eq. (3.17)), we end up with Eq. (3.18d) including a correction term

$$\tfrac{2}{3}y^*\left(y^*-1\right)^2-\frac{1}{1+y^*}\equiv F(y^*)=-\frac{\mathrm{St}}{1+\mathrm{St}}+\frac{1}{\mathrm{St}}\frac{v_{\rm sys}^2}{v_g^2}, \tag{3.19}$$

where we have substituted $\mathrm{St}=1/y_{\rm L}$. The correction term can be roughly constrained using an estimate of the systematic drift velocity $v_{\rm sys}\sim(\mathrm{St}/(\mathrm{St}+1))\beta v_K$, where $v_{\rm K}$ is the Keplerian velocity at distance R from the Sun, Ω is the orbit frequency, and $\beta=(H_{\rm g}/R)^2$ is a radial pressure gradient parameter; also we take $v_{\rm g}=\alpha^{1/2}c_{\rm g}$ (see, *e.g.*, Nakagawa et al. 1986 or Cuzzi & Weidenschilling 2006). Then

$$\frac{v_{\rm sys}}{v_{\rm g}}=\frac{\mathrm{St}}{\mathrm{St}+1}\frac{\beta v_K}{\alpha^{1/2}c_{\rm g}}=\frac{\mathrm{St}}{\mathrm{St}+1}\frac{\beta R\Omega}{\alpha^{1/2}H_{\rm g}\Omega}=\frac{\mathrm{St}}{\mathrm{St}+1}\frac{\beta}{\alpha^{1/2}\beta^{1/2}}=\frac{\mathrm{St}}{\mathrm{St}+1}\left(\frac{\beta}{\alpha}\right)^{1/2}, \tag{3.20}$$

and Eq. (3.19) becomes,

$$F(y^*)=\frac{\mathrm{St}}{1+\mathrm{St}}\left(\frac{\beta/\alpha}{1+\mathrm{St}}-1\right). \tag{3.21}$$

Normally $\beta\sim2\times10^{-3}$ is assumed (Nakagawa et al. 1986; Cuzzi et al. 1993), but its real value, and that of α, are not well known. Equation (3.21) shows that for a given value of St, $F(y^*)$ increases with increasing β/α. Consequently, $y^*=t^*/\tau_{\rm f}$ is also higher (see Fg. 3.1). The boundary between the class I and II eddies therefore shifts to higher values of t^*, that is, there are less class I eddies for high β/α and the $\mathrm{St}^*=1$ upper limit (when $t^*=t_{\rm L}$) is reached at lower Stokes numbers. Inserting the definition of $F(y^*)$ (LHS of Eq. (3.19)) into Eq. (3.21) with $y^*=t_{\rm L}/\tau_{\rm f}=\mathrm{St}^{-1}$ and solving for St, we find that the Stokes number at which $\mathrm{St}^*=1$ occurs at

$$\mathrm{St}_{\mathrm{St}^*=1}=\left(1+\sqrt{\frac{3\beta}{2\alpha}}\right)^{-1/2}. \tag{3.22}$$

For example, for $\beta/\alpha=1$, St^* reaches its upper limit at $\mathrm{St}\approx0.67$.

In the small particle regime ($\mathrm{St}\ll1$), however, the exact value of β/α is unimportant since $F(y^*)$ is always close to zero, and the $y_{\rm a}^*$ approximation is justified. It is only for $\beta/\alpha\gtrsim\mathrm{St}^{-1}$ that the RHS of Eq. (3.21) starts to becomes significant and $y^*>y_{\rm a}^*$. This is the weakly-turbulent or non-turbulent regime where class II eddies dominate even for small particles. In practise, however, it means that eddy crossing effects are important only if turbulence is very weak and we will not treat them

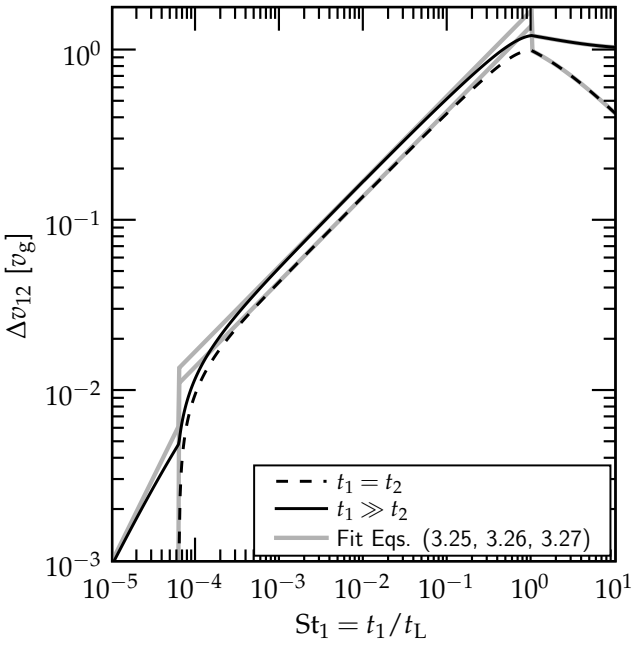

Fig. 3.3: Exact solution to Eq. (3.14) for Δv_{12} in the case of identical particles (*dashed curve*) and $t_1 \gg t_2$ (*solid curve*) for a Reynold number of 10^8. The dotted curves are approximations to Eq. (3.14) given by Eqs. (3.24, 3.25, 3.26).

further in this chapter.

3.3.4 Limiting solutions

As intuition-building examples we obtain simple, closed-form expressions for Δv_{12}^2 in various limiting regimes from the t-space solutions; similar results are easily obtained from the k-space solutions (§ 3.3.1). Without loss of generality we take particle 1 to have the largest stopping time, *i.e.*, $t_1 \geq t_2$ and $t_{12}^* = t_1^*$. Moreover, we assume that $t_s \ll t_L$; *i.e.*, $\mathrm{Re}^{1/2} \gg 1$ and there is an extended inertial range of eddies. Recall again that $\mathrm{St}_{12}^* = \mathrm{Re}^{-1/2}$ for $t_1 < t_s/y_a^*$, and that St_{12}^* will not exceed 1.

Tightly coupled particles, $t_1, t_2 < t_s$

In this limit all eddies are of class I and $\Delta v_{12}^2 \to \Delta v_I^2$. For each particle, the second term on the RHS of Eq. (3.15a) is negligible; thus

$$\Delta v_{12}^2 = v_g^2 \frac{\mathrm{St}_1 - \mathrm{St}_2}{\mathrm{St}_1 + \mathrm{St}_2} \left(\frac{\mathrm{St}_1^2}{\mathrm{St}_1 + \mathrm{Re}^{-1/2}} - \frac{\mathrm{St}_2^2}{\mathrm{St}_2 + \mathrm{Re}^{-1/2}} \right). \tag{3.23}$$

In the very small particle regime ($t_1 \ll t_s$), $\mathrm{St}_i \ll t_s/t_L = \mathrm{Re}^{-1/2}$ and

$$\Delta v_{12}^2 = v_g^2 \frac{t_L}{t_s} (\mathrm{St}_1 - \mathrm{St}_2)^2 . \tag{3.24}$$

Since $v_g^2 = \frac{3}{2} v_s^2 \mathrm{Re}^{1/2} = \frac{3}{2} v_s^2 t_L / t_s$, this expression transforms directly to $\Delta v_{12} = \sqrt{3/2}(t_1 - t_2) v_s / t_s$, in good agreement with the heuristic, although physically motivated, expression $\Delta v_{12} = v_s (t_1 - t_2)/t_s$ of Weidenschilling (1984a).

Intermediate regime, $t_s \leq t_1 \leq t_L$.

If t_1 (the stopping time of the larger particle) approaches the Kolmogorov scale, two changes occur. First, the $\mathrm{St}_1^2/(\mathrm{St}_{12}^* + \mathrm{St}_1)$ term in Eq. (3.15a) now becomes linear with St_1, since St_{12}^* grows proportional to St_1 (the second term is still negligible throughout most of this regime). Relative velocities therefore increase as the square-root of stopping time. Second, class II eddies also contribute to Δv_{12}^2 (Eq. (3.15b)). This contribution scales also with St_1, but is significantly larger and does not disappear when $t_1 = t_2$. From a physical point of view, class II eddies act as small, random kicks to the particle trajectory, while two particles captured by a class I eddy are subject to the same, systematic, change in motion. Class II eddies are therefore much more effective in generating velocity differences for similar-sized particles.

In the 'fully intermediate regime,' *i.e.*, $t_s \ll t_1 \ll t_L$, we can also ignore the $\mathrm{Re}^{-1/2}$ terms in Eq. (3.15b). In addition, the $t^*/\tau_f = y_a^*$ approximation holds. Upon writing $\mathrm{St}_2 = \epsilon \mathrm{St}_1$, Eqs. (3.15a, 3.15b) become linear with St_1 and we can write Δv_{12}^2 as (see App. 3.B)

$$\Delta v_{12}^2 = v_g^2 \left[2y_a - (1+\epsilon) + \frac{2}{1+\epsilon} \left(\frac{1}{1+y_a} + \frac{\epsilon^3}{y_a + \epsilon} \right) \right] \mathrm{St}_1, \tag{3.25}$$

where $\epsilon \leq 1$ is the ratio between the stopping times and $y_a = 1.6$. For $t_1 \gg t_2$ we then find that $\Delta v_{12}^2 \approx 3.0 v_g^2 \mathrm{St}_1$, while for equal particles the numerical factor goes down to 2.0. Written in terms of stopping times the relative velocities become, $\Delta v_{12} = [1.7 \div 2.1] v_L \sqrt{t_1/t_L}$. This also compares well with Weidenschilling (1984a) fits for this regime (who gives prefactors of 2.1 and 3.0, respectively). Note, however, that our full expressions for Δv (Eqs. 3.14, 3.15a, 3.15b) also capture the behavior near the t_s and t_L 'turning points' (see Fg. 3.3).

Heavy particles, $t_1 > t_L$

If $t_1 > t_L$, $\mathrm{St}_{12}^* = 1$ and there is no contribution from class I eddies (Eq. (3.15a)). Also, we can neglect the $\mathrm{Re}^{-1/2}$ terms in Eq. (3.15b) and the relative velocities simply become

$$\Delta v_{12}^2 = \Delta v_{II}^2 = v_g^2 \left(\frac{1}{1+\mathrm{St}_1} + \frac{1}{1+\mathrm{St}_2} \right). \tag{3.26}$$

This result can, of course, directly be obtained from the v_{pi} terms (Eq. (3.11)) since the cross-term vanishes in this regime. For small St_2 relative velocities are still $\sim v_g$; however, if both Stokes numbers are large, the relative velocity decreases roughly with the square root of the smallest particle stopping time. Note that the linear fit of Weidenschilling (1984a) in this regime (his Eq. (15)) is inappropriate (see, however, Völk et al. 1980; Weidenschilling 1988; Weidenschilling & Cuzzi 1993; Cuzzi et al.

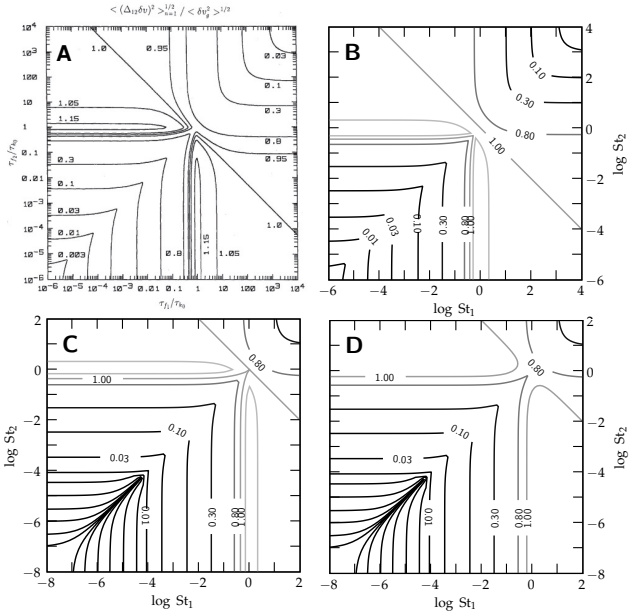

Fig. 3.4: Contour plots of particle-particle, turbulence induced, relative velocities Δv_{12} normalized to $v_{\rm g}$. *(a)* Numerical results of Markiewicz et al. (1991), without inner scale (Re $\to \infty$). *(b)* Analogous result from our closed-form expressions with the fixed $y^* \approx y^*_{\rm a} = 1.6$ approximation (§ 3.3.2). *(c)* Like *(b)*, but with an exact solution for y^* and with Re $= 10^8$. *(d)* Using the CH03 formula for k^*, $k^*/k_L = 0.5{\rm St}^* + 1$, and also with Re $= 10^8$. Contours are drawn twice per logarithmic decade (at $\Delta v_{12}/v_{\rm g} = 3 \times 10^i$ and at 10^i) with an additional contour at 0.8 and 1.15. *See page 245 for a larger, full-color version of this figure.*

1993 in which a square-root fall off is advocated). Since an explicit, closed-form solution to the Völk et al. (1980) and MMV expressions for Δv_{12} has not previously been available, many dust coagulation models (*e.g.*, Suttner & Yorke 2001; Dullemond & Dominik 2005; Ormel et al. 2007) have relied on the Weidenschilling (1984a) fits to calculate relative velocities. Turbulent motions and relative velocities for particles in the $\tau_{\rm f} > t_{\rm L}$ regime have therefore been underestimated in these calculations. However, concerning these works, we also think no major conclusions have been affected, since the error is introduced only for large dust particles, that is, if the system is already well evolved.

3.3.5 Contour plots

Following Völk et al. (1980) and MMV we also present our results as contour plots. Figure 3.4a shows, for comparison, the results of MMV, obtained by numerical evaluation of the integrals involved without an inner turbulent scale (Re $\to \infty$). The next three panels of Fg. 3.4 show the result using our closed-form expressions derived from Eq. (3.14). In Fg. 3.4b, the y^*_a approximation has been used and, like Fg. 2 of MMV (Fg. 3.4a), the inner scale of the turbulence is extended to infinity so that Eqs. (3.25, 3.26) apply. Somewhat systematically higher values for Δv_{12} when compared to MMV can be explained by the CH03 approximation for $v_{\rm p}$ (see Eq. (3.5)) but these discrepancies are less than $\sim$10%. In Fg. 3.4c and Fg. 3.4d we show the contour plots corresponding to the other formulations for k^* (see Fg. 3.2), *i.e.*, the exact solution for y^* (Fg. 3.4c) and the CH03 empirical approximation (Fg. 3.4d). The differences between these three methods for determining k^* differ around the St $= 1$ point (see

Fig. 3.2) and are reflected in the contour plots. For St ≈ 1, Fig. 3.4c compares best to the numerical result of MMV, but no significant errors are made when using the y_a^* approximation or the CH03 formula for k^*.

In Fig. 3.4c and Fig. 3.4d, a Reynolds number of Re $= 10^8$ has been adopted. For St $< 10^{-4}$, therefore, velocities are greatly suppressed since only class I eddies remain to generate relative velocities and relative velocities disappear completely for equal friction times. Also, the contours are much closer spaced since in this limit the velocity Δv_{12} is proportional to St (see Eq. (3.23)).

3.4 Conclusions

We have extended and, essentially, completed the work of Cuzzi & Hogan (2003), who derived explicit, closed-form expressions for particle velocities in turbulence based on the physics originally developed by Völk et al. (1980) and Markiewicz et al. (1991). Within the framework of this physics, the only approximations used here are in Eq. (3.5) for the particle velocities (where *a posteriori* comparisons with exact numerical solutions indicate the approximation is well justified) and in Eqs. (3.17) *et seq* where the systematic velocity $v_{\rm sys}$ is neglected to simplify calculating the boundary between eddy classes (generalizing this step should be straightforward, however). The full analytic expression for Δv_{12} is given by Eq. (3.14) (or by the sum of Eqs. (3.15a, 3.15b)), but more simple, explicit expressions apply in restricted regimes (provided Re$^{1/2} \gg 1$):

- Equation (3.24), in the very small particle limit ($t_1 \ll t_{\rm s}$);
- Equation (3.25), in the 'fully intermediate' regime, *i.e.*, for $t_{\rm s} \ll t_1 \ll t_{\rm L}$;
- Equation (3.26), for $t_1 \geq t_{\rm L}$.

Near the $t_1 = t_{\rm s}$ and $t_1 = t_{\rm L}$ turning points the behavior is more complex (see Fg. 3.3) and for accurate analytical approximations one has to revert to the full expressions for Δv given by Eqs. (3.14, 3.15a, 3.15b).

Acknowledgment. The authors thank Robert Hogan for computational assistance in creating Fg. 3.5 and the referee, H. Völk, for positive feedback. C.W.O. acknowledges support from the Netherlands Organisation for Scientific Research (NWO) that made this work possible. J.N.C.'s contributions were supported by a grant from NASA's Planetary Geology and Geophysics Program.

3.A A more accurate closed-form solution for $v_{\rm p}$ and all related velocities, using power-law approximations to the functions g and h

In § 3.2 the very simple approximation $g(\chi) = h(\chi) = 1$ was introduced for all stokes numbers St and eddy scales k. It proves to be quite adequate for most purposes; however, as noted in § 3.3.5, small inaccuracies remain at the 10% level because the approximation overestimates the contributions of fast eddies to $v_{\rm p}^2$ and other velocity components. Figure 3.5 shows the detailed behavior of the functions g and h for

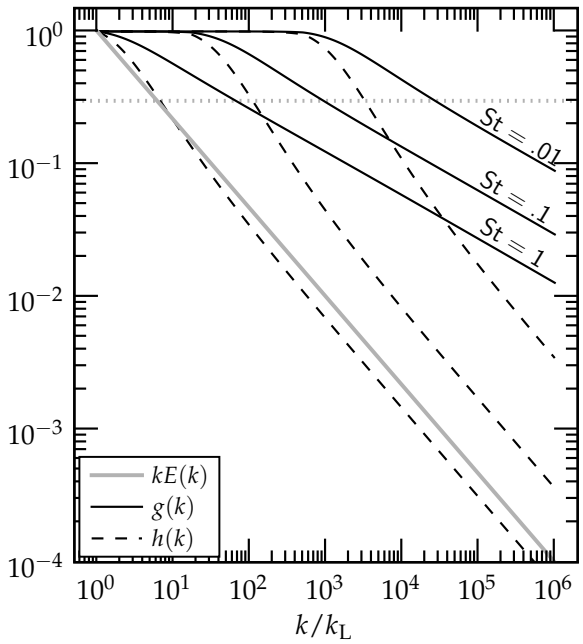

Fig. 3.5: The functions g (*black solid curves*) and h (*black dashed curves*) plotted for three different Stokes numbers at a Reynolds number of 10^8. After $k > k^*$ the functions show power-law behavior. The power spectrum (weighted by k) is plotted by the *grey solid line*. Below the *dotted line* the g and h functions deviate significantly from the unity approximation. However, the same holds for the weighting function $kE(k)$.

$\mathrm{Re} = 10^8$ for Stokes numbers of St = 0.01, 0.1, and 1.0. The inflection point for all three values of St is at $k = k^*$ (recall that $k^*/k_\mathrm{L} \approx 1 + \frac{1}{2}\mathrm{St}^{-3/2}$). For $k > k^*$, the functions are well approximated by power-laws of $-1/3$ and $-3/4$, respectively, *i.e.*, $g(k) = (k/k^*)^{-1/3}$ and $h(k) = (k/k^*)^{-3/4}$. The success of the approximation of § 3.2 is due to the fact that the power in the weighting function $kE(k)$ (solid grey line; we multiply with k since we compare logarithmically) decreases rapidly with increasing k; thus by the time the assumption $g(k) = h(k) = 1$ becomes really bad, the relative contribution of successive terms has become small. For small St, the weighted contribution of eddy power has already become very small even before $k \sim k^*$ (the logic of CH03). For $\mathrm{St} = 1$ or larger, the weighting function has dropped by nearly an order of magnitude by the time $h(k)$ (the faster-decreasing function) has dropped to 0.3 (dotted line), and this seems to account for the success of our simple assumption.

This behavior can be understood from the definition of $\chi = Kt_k k v_\mathrm{rel}$. For $k \gg k^*$, $K \approx 1$ and $v_\mathrm{rel} \lesssim v_\mathrm{g}$ are both constant. Then, because $t_k \propto k^{-2/3}$, χ scales as $\chi \propto k^{1/3}$ and becomes large at large k. Since $g(\chi) = \arctan(\chi)/\chi \propto \chi^{-1}$ for large χ, we get that $g(k) \propto k^{-1/3}$. Similarly, $h(\chi) \propto k^{-2/3}$, which is a bit shallower than the $-3/4$ exponent observed over most regions of interest (Fig 3.5). While the $-2/3$ exponent is reached at large k, the $-3/4$ exponent seems more appropriate at intermediate k. Yet, in our subsequent analysis, we will use the large-k limit for this exponent ($-2/3$) because it simplifies the math. Thus, we approximate the g and h behavior as follows: unity for $k < k^*$, and power laws in k/k^* with exponents of $-1/3$ and

$-2/3$ for $k > k^*$. Then Eq. (3.4) becomes

$$v_\mathrm{p}^2 = \int_{k_\mathrm{L}}^{k^*} 2E(k)\left(1-K^2\right)\mathrm{d}k + \int_{k^*}^{k_\mathrm{s}} 2E(k)\,(1-K)\left[\left(\frac{k}{k^*}\right)^{-1/3} + K\left(\frac{k}{k^*}\right)^{-2/3}\right]\mathrm{d}k. \tag{3.27}$$

Where we have that $k_\mathrm{s} \leq k^* \leq k_\mathrm{L}$ such that in the case of very small or very large particles one of the integrals vanishes (§ 3.3.2). Since the approximation $g = h = 1$ still holds for $k < k^*$ (or for $t > t^*$) the velocities resulting due to class 1 eddies (Eq. (3.15a)) are not affected; the new approximation only affects Eq. (3.15b). By writing $K = \mathrm{St}/(\mathrm{St} + x^{-2/3})$, $E(k) = E_\mathrm{L}(k/k_\mathrm{L})^{-5/3} \propto x^{-5/3}$ with $x = k/k_\mathrm{L}$ the solution to Eq. (3.27) involves integrals of the form

$$\int x^{-5/3+p}\left(\frac{\mathrm{St}}{\mathrm{St}+x^{-2/3}}\right)^{n=[1,2]}\mathrm{d}x \tag{3.28}$$

with $n = 2$ for the K^2 term and $p = -1/3$ or $-2/3$. These integrals can be solved analytically. Going to 't-space', however, gives somewhat cleaner solutions and we will from here on follow that approach and show how it affects relative velocities, *i.e.*, Δv_II. After the change of variables ($t_k/t^* = (k/k^*)^{-2/3}$) the second term of Eq. (3.27) becomes

$$\frac{v_g^2}{t_\mathrm{L}}\int_{t_\mathrm{s}}^{t^*}(1-K)\left(\frac{t_k}{t^*}\right)^{1/2} + (1-K)K\left(\frac{t_k}{t^*}\right)\mathrm{d}t_k. \tag{3.29}$$

We now introduce the dimensionless variable $y = t_k/\tau_\mathrm{f}$ (*cf.* Eq. (3.17)). Then $t_k/t^* = y/y^*$ with $y^* = t^*/\tau_\mathrm{f}$. Also $K = 1/(1+y)$ and $1-K = y/(1+y)$ and Eq. (3.29) becomes

$$\frac{v_g^2\tau_\mathrm{f}}{t_\mathrm{L}}\int_{t_\mathrm{s}/\tau_\mathrm{f}}^{t^*/\tau_\mathrm{f}}(y^*)^{-1/2}\frac{y^{3/2}}{1+y} + (y^*)^{-1}\frac{y^2}{(1+y)^2}\mathrm{d}y = \frac{v_g^2\tau_\mathrm{f}}{t_\mathrm{L}}\left\{(y^*)^{-1/2}\Big[I_h(y)\Big]_{t_\mathrm{s}/\tau_\mathrm{f}}^{t^*/\tau_\mathrm{f}} + (y^*)^{-1}\Big[I_g(y)\Big]_{t_\mathrm{s}/\tau_\mathrm{f}}^{t^*/\tau_\mathrm{f}}\right\} \tag{3.30}$$

in which the functions $I_h(y)$ and $I_g(y)$ are defined as

$$I_h(y) \equiv \int_0^y \frac{z^{3/2}}{1+z}\mathrm{d}z = \left(\frac{2}{3}y - 2\right)\sqrt{y} + 2\arctan(\sqrt{y}) \tag{3.31a}$$

$$I_g(y) \equiv \int_0^y \frac{z^2}{(1+z)^2}\mathrm{d}z = \frac{(2+y)y}{1+y} - 2\log(1+y) \tag{3.31b}$$

The expressions for Δv_II now consist of several contributions. First, $I_h(y)$ and $I_g(y)$ are evaluated at both the upper (y^*) and lower (y_s) limits. This must be done for both particles 1 and 2, because the Δv_II term (Eq. (3.15b)) has separate contributions

from each particle. For the particle of highest friction time (say this is t_1) the power-law approximation for g and h holds over the range $\Delta v_{\rm II}$ is calculated, *i.e.*, $\tau_{\rm f} \leq t_{1k} \leq t_{12}^* = t_1^*$. However, for the second particle the power-law approximation only holds for $t_{2k} \leq t_2^*$, while for the remaining range over which the integral in $\Delta v_{\rm II}$ is evaluated, *i.e.*, $t_2^* \leq t_{2k} \leq t_1^*$, the $g = h = 1$ approximation applies.

This gives us several terms that contribute to $\Delta v_{\rm II}$. Collecting these terms, the new expression for $\Delta v_{\rm II}$ becomes

$$\Delta v_{\rm II} = \frac{v_g^2}{t_{\rm L}} \left\{ t_1 \left(\frac{t_1^*}{t_1}\right)^{-1/2} \Big[I_h(y) \Big]_{t_{\rm s}/t_1}^{t_1^*/t_1} + t_1 \left(\frac{t_1^*}{t_1}\right)^{-1} \Big[I_g(y) \Big]_{t_{\rm s}/t_1}^{t_1^*/t_1} + (1 \leftrightarrow 2) \right.$$
$$\left. + \left[t_k + \frac{t_2^2}{t_2 + t_k} \right]_{t_2^*}^{t_1^*} \right\}, \qquad (t_1 \geq t_2). \tag{3.32}$$

Although still fully analytical, this more accurate expression for $\Delta v_{\rm II}$ is also more complicated and we did not present it in the main body of the chapter. Equation (3.32) is useful, however, for readers whose applications demand this higher level of accuracy.

3.B Derivation of Eq. (3.25)

We consider the limiting case of $t_{\rm s} \ll t_1 \ll t_{\rm L}$. The y_a^* approximation for ${\rm St}_{12}^*$ then holds, *i.e.*, ${\rm St}_{21}^* \approx y_a^* {\rm St}_1$ with $y_a = 1.6$. We will now argue that we can neglect the ${\rm Re}^{-1/2}$ terms in Eq. (3.15b). For particle 1 this is obvious since ${\rm St}_1 \gg {\rm Re}^{-1/2}$. The last term (where ${\rm Re}^{-1/2}$ is in the denominator) then becomes simply $-{\rm St}_1$. However, for the interchange term a similar approximation

$$\frac{{\rm St}_2^2}{{\rm St}_2 + {\rm Re}^{-1/2}} \approx {\rm St}_2, \tag{3.33}$$

is not that obvious since we have not put a constraint on ${\rm St}_2$. For example, if ${\rm St}_2 \ll {\rm Re}^{-1/2}$ the ${\rm Re}^{-1/2}$ term dominates the denominator. However, in that case this term *and* its approximation are small anyway compared to $-{\rm St}_1$, such that by making the approximation in Eq. (3.33) our final result is not affected. Similarly, if ${\rm St}_2 \sim {\rm Re}^{-1/2}$, Eq. (3.33) (which goes to $\sim \frac{1}{2}{\rm Re}^{-1/2}$) or its approximation ($\sim {\rm Re}^{-1/2}$) are insignificant since ${\rm St}_1 \gg {\rm Re}^{-1/2}$. Only if $\epsilon \sim 1$, *i.e.*, ${\rm St}_2 \gg {\rm Re}^{-1/2}$, does the ${\rm St}_2$ term matter, but then the approximation in Eq. (3.33) is well justified. All terms in Eq. (3.15b) are then linear in Stokes and we can reduce it to

$$\frac{\Delta v_{\rm II}^2}{v_{\rm g}^2} = \left(2y_{\rm a}^* - (1-\epsilon) + \frac{1}{1+y_{\rm a}^*} + \frac{\epsilon^2}{\epsilon + y_{\rm a}^*} \right) {\rm St}_1, \tag{3.34}$$

with $\epsilon = \mathrm{St}_2/\mathrm{St}_1 \leq 1$. Similarly, Eq. (3.15a) becomes

$$\frac{\Delta v_\mathrm{I}^2}{v_\mathrm{g}^2} = \frac{1-\epsilon}{1+\epsilon}\left(\frac{1}{y_a^*+1} - \frac{\epsilon^2}{y_a^*+\epsilon}\right)\mathrm{St}_1. \tag{3.35}$$

Combining these expressions and collecting the $1/(1+y_a^*)$ and $\epsilon^2/(y_a^*+\epsilon)$ terms then gives Eq. (3.25).

4

Co-accretion of chondrules and dust in the solar nebula[1]

—C. W. Ormel, J. N. Cuzzi, A. G. G. M. Tielens—

We present a mechanism for chondrules to stick together by means of compaction of a porous dust rim they sweep up as they move through the dusty nebula gas. It is shown that dust aggregates formed out of micron-sized grains stick to chondrules, forming a porous dust rim. When chondrules collide, this dust can be compacted by means of rolling motions within the porous dust layer. This mechanism dissipates the collisional energy, compacting the rim and allowing chondrules to stick. The structure of the obtained chondrule-dust agglomerates (referred to as compounds) then consists of three phases: chondrules, porous dust, and dust that has been compacted by collisions. Subsequently, these compounds accrete their own dust and collide with other compounds. The evolution of the compound size distribution and the relative importance of the phases is calculated by a Monte Carlo code. Growth ends, and a simulation is terminated when all the dust in the compounds has been compacted. Numerous runs are performed, reflecting the uncertainty in the physical conditions at the chondrule formation time. It is found that compounds can grow by 1-2 orders of magnitudes in radius, upto dm-sizes when turbulence levels are low. However, relative velocities associated with radial drift form a barrier for further growth. Earlier findings that the dust sweep-up by chondrules is proportional to their sizes are confirmed. We contrast two scenarios regarding how this dust evolved further towards the densely packed rims seen in chondrites.

[1]Originally published in *The Astrophysical Journal*, vol. 679, p. 1588 (2008)

4.1 Introduction

Protoplanetary nebulae have been studied in increasing detail from visual to microwave wavelengths (Meyer et al. 2007; Watson et al. 2007), and hundreds of extrasolar planetary systems have been discovered, but the 'primary accretion' stage of the planetary formation process — that which leads from interstellar grains to planetesimals large enough to decouple from the nebula gas (asteroid- and comet-nucleus size objects) — remains obscure. In this particle size range, coupled particle-gas dynamics dominates the evolution, as reviewed recently by Cuzzi et al. (2005), Cuzzi & Weidenschilling (2006), and Dominik et al. (2007). The main processes which have been hypothesized for primary accretion include (i) incremental growth by sticking of small grains to each other and to larger particles, (ii) various kinds of instabilities occurring in a particle-rich midplane region, and (iii) formation of planetesimals from dense zones of particles that form in turbulence due to vorticity or pressure effects.

A critical but unknown nebula question in this stage is whether turbulence is present, and if so, what its intensity is (Stone et al. 2000; Gammie & Johnson 2005). If the nebula is nonturbulent, particles of all sizes can settle into a dense layer near the midplane where incremental growth is fairly robust for expected, but still poorly known and therefore somewhat ad-hoc, sticking properties (Weidenschilling & Cuzzi 1993; Cuzzi et al. 1993; Weidenschilling 1997, 2000, 2004). This is because the dense particle layer drives the entrained gas to corotate, and relative velocities between equal-size particles would largely vanish. The high local mass density ensures that growth is rapid (Weidenschilling 2000) — perhaps too rapid (Cuzzi et al. 2005). Various instabilities in such a layer, mostly gravitational, have been studied for decades (Goldreich & Ward 1973; Sekiya 1998; Youdin & Shu 2002; Youdin & Goodman 2005), but these are precluded if the nebula is even weakly turbulent (Cuzzi & Weidenschilling 2006).

Astronomical and planetary observations seem to be most naturally reconciled with turbulent nebulae (Dullemond & Dominik 2005; Cuzzi et al. 2005; Brownlee et al. 2006; Zolensky et al. 2006; Ciesla & Cuzzi 2007). A number of studies indicate that turbulence excites meter-size particles to relative velocities at which they probably disrupt each other (Weidenschilling 1988; Benz 2000; Sirono 2004; Langkowski et al. 2008), posing a barrier to further growth. However, some recent studies suggest that turbulence itself can concentrate particles of different sizes, in different ways, and trigger rapid planetesimal formation (Cuzzi et al. 2001, 2007; Rice et al. 2006; Johansen et al. 2007). Thus, in spite of the ongoing uncertainty in just how turbulence may be maintained (Stone et al. 2000; Mukhopadhyay 2006), it is sensible to consider its effect in model studies. This collisional disruption limit, combined with the rapid inward drift of m-size particles by which they are 'lost' from the local region, led to the concept of a 'm-size barrier' or bottleneck to growth; once large particles exceed this barrier, relative velocities become lower, allowing them to grow further and to drift less rapidly out of the accreted region. Our studies were initially motivated by a desire to see if growth into loose fractal clusters and subsequent packing could allow the m-size barrier to be crossed.

In the conceptually simplest models, growth occurs by simple sticking of parti-

cles (Weidenschilling 1997, 2000, 2004; Blum 2004). While it goes against our earth-bound intuition that macroscopic particles can stick to each other, some microgravity and earth-based experiments show that, while bouncing transpires at intermediate velocities, sticking prevails for both low (less than a meter/second) and high (for $13 - 25$ m s^{-1}) relative velocities (Blum & Wurm 2000; Blum & Schräpler 2004; Wurm et al. 2005; Marshall et al. 2005; Dominik et al. 2007). Other experiments indicate that certain solids (water and methanol ice, organic material) are 'stickier' than others (silicates) (Bridges et al. 1996). However, no significant amount of these especially sticky materials has been found in primitive meteorites. Still, entire chondrites (and by inference entire parent bodies) are composed of small silicate objects that seem to have been gently assembled and compacted, at least initially (Metzler et al. 1992; Brearley 1996; Cuzzi & Weidenschilling 2006); how did this happen? The meteorite record (discussed in more detail below) shows that many mm-sized solid objects are encased in rims of micron and submicron-sized mineral grains. One obvious possibility is that these rims form by nebula accretion of grains onto the underlying core particles (Nagahara 1984; Metzler et al. 1992; Paque & Cuzzi 1997; Hua et al. 2002; Zega & Buseck 2003). In § 4.2 we show that this dust accretion may be expected to occur fractally, leading to porous structures. Collisions easily crush this structure, in the process dissipating kinetic energy and allowing colliding particles to stick (Blum & Wurm 2008).

Recent reviews of the relevant properties of chondrites are provided by Brearley & Jones (1998), Scott & Krot (2005a) and Weisberg et al. (2006). Chondrites are dominated by mm-sized silicate chondrules, which were melted in the nebula (Brearley & Jones 1998; Jones et al. 2000, 2005; Lauretta & McSween 2006), but are found in meteorites to be embedded in a fine-grained matrix. Formation of chondrules (and chondrites) occurred over a period of several Myr (Scott & Krot 2005a; Kita et al. 2005; Russell et al. 2006; Kleine et al. 2006). Chondrites can be divided into three broad classes — ordinary, carbonaceous and enstatite — with each class being further subdivided into more than a dozen groups reflecting chemical, mineralogical and isotopic differences. For example, CM carbonaceous chondrites contain abundant matrix that has been affected by aqueous alteration, while Ordinary Chondrites contain very little matrix and have generally incurred only limited aqueous alteration. Violent collisional processes occurred after primary accretion which affected the contents and appearance of most meteorites, and to best understand the primary accretion process one must look back through this stage where possible to the rare, unbrecciated subset of rocks and rock fragments called 'primary texture' (Metzler et al. 1992; Brearley 1993).

The dust in chondrites is found to have two physically defined components: rims and inter-chondrule matrix (Huss et al. 1981; Scott et al. 1988; Brearley 1996; Brearley & Jones 1998). Fine-grained rims are clearly associated with individual chondrules and other macroscopic particles in microscopic images, and usually even stay attached to the chondrules when they are disaggregated from the host rock (Paque & Cuzzi 1997). Some studies report that the composition of these fine-grained rims is uniform across a wide range of underlying mineral types, including more refractory (higher-temperature) oxides which formed much earlier (Brearley 1993; Hua et al.

2002) and some find dramatic variations between the composition of rims on adjacent chondrules (Taylor et al. 1983; Scott et al. 1984). Generally, the chondrules cooled completely before accreting these fine dust grains (Brearley 1993). Interchondrule matrix, more generally dispersed between all the macroscopic components of the rock, is also made of fine-grained material. The grain sizes in fine-grained rims are noticeably smaller than the ubiquitously enveloping matrix, even though the compositions of the rims and matrix are very similar or identical (Ashworth 1977; Brearley 1993, 1996; Zolensky et al. 1993). It has been reported that the rim porosity is also smaller than that of the surrounding matrix (Ashworth 1977; Trigo-Rodriguez et al. 2006). The relative abundance of rim and matrix material to chondrule material varies from one meteorite class to another (Scott et al. 1988); however, the rim mass (or thickness) is often found to be proportional to the mass (or radius) of the underlying chondrule (Metzler et al. 1992; Paque & Cuzzi 1997).

Several different model efforts have attempted to explain some of these properties in the context of nebula sweep-up or accretion of the fine-grained rims by chondrules and their like. Morfill et al. (1998) hypothesized that if a particle had a speed relative to the gas which was proportional to its radius, and if the chondrules in a region sweep up all the local dust in a one-stage event (no ongoing replenishment of dust), the observed rim-core correlation would be obtained. Cuzzi (2004) showed that chondrule-size particles in turbulence plausibly exhibit just the appropriate (near-linear) dependence of relative velocity on size, even though most particles obey a square-root dependence on radius. Cuzzi (2004) relied on collisional outcomes proposed by Dominik & Tielens (1997) for porous aggregates of fine grains, and suggested that for particles much larger than chondrules, the velocity relative to the gas increases to a point where they enter an erosional regime.

On the other hand, Sears et al. (1993) and Trigo-Rodriguez et al. (2006) question whether fine-grained rims are nebula accretion products at all. Trigo-Rodriguez et al. (2006) point out in particular that the fine-grained rims in CM chondrites, such as discussed by Metzler et al. (1992), have a porosity of 10-20%, much lower than the high-porosity structures formed by, *e.g.*, Blum & Wurm (2000) or Blum & Schräpler (2004). Less is known quantitatively about the porosity of fine-grained rims in other chondrite types, although Ashworth (1977) states that rim porosities are less than 6-15% in ordinary chondrites. The alternate that Trigo-Rodriguez et al. (2006) and Sears et al. (1993) prefer, while they differ in the details, is that the fine-grained rims seen in CM chondrites, in particular, are created on the parent body from a generic enveloping matrix, by some combination of compaction and pervasive aqueous alteration. This suggestion might make it harder to explain why the grain size is smaller than in the nearby enveloping matrix. Nevertheless, the discussion shows that the porosity of fine-grain rims is an important diagnostic of their origin.

In this chapter, we develop a detailed collision model to study the rimming and accretion processes of chondrules simultaneously and, in a statistical study, quantify the growth that can be obtained under a wide range of (uncertain) nebular conditions. Our model treats multiple components: solid 'chondrules,' submicron grains and their very porous nebula aggregates, porous accretion rims formed by direct accretion of monomers and aggregates onto chondrules, compact rims formed by

collisional compression of pre-existing porous rims, and compound objects formed by sticking of rimmed objects, which themselves might become rimmed in dust. Our collisional outcomes use physical guidelines set by laboratory and theoretical models (Dominik & Tielens 1997; Blum & Wurm 2000; Blum & Schräpler 2004; Langkowski et al. 2008). We use quantitatively correct closed form relative velocity expressions for particles in turbulence of varying intensity (Ormel & Cuzzi 2007), which capture the increase in relative velocity as particles grow by accretion of other particles. We use a Monte Carlo approach to calculate the probability of different outcomes, over a wide range of nebula parameters (level of turbulence, gas and solid density). We assess (i) the extent to which fine-grained rims can dissipate collisional energy and allow growth by sticking to proceed, and (ii) the extent to which these dissipative collisions compact initially porous dust rims into lower porosity states. We leave for future study the physics of disruptive collisions and the details of vertically varying particle density and turbulent intensity, such as might occur if the global turbulent intensity is vanishingly small (Cuzzi et al. 1993; Sekiya 1998; Dobrovolskis et al. 1999; Weidenschilling 1997).

This chapter is organized as follows. In § 4.2 the collision model is discussed. Here we outline the three distinct components with which we model the compound objects that result out of accretion of dust on chondrule surfaces and collisions with other chondrules. We also introduce the different sources of relative velocities particles can obtain in the nebula, and calculate the timescales involved in the various accretion processes. We end this discussion with a brief summary of the envisioned collisional scenario. Section 4.3 briefly reviews the Monte Carlo code with which the coagulation is solved. Section 4.4 presents the results of our work. First, a few individual models are addressed in detail, before we present the results of a parameter study in which many uncertain (mostly nebula-related) parameters are varied. In § 4.5 we discuss the effects of a particle dominated environment caused by settling of compounds on the growth of compounds. We also discuss several observational implications, emphasizing in particular the relation between the dust in our model to the fine-grained rims seen around chondrules in meteorites. We summarize our results in § 5.4.

4.2 Model

4.2.1 Outline

The central theme of this chapter is to model the process of dust accretion onto chondrule surfaces and explore whether compaction of this dust during inter-chondrule collisions acts as a sticking agent, with which significant growth can be achieved. For dust aggregates this compaction mechanism is well known (Dominik & Tielens 1997; Blum & Wurm 2000; Wada et al. 2007): by restructuring of the constituent grains the excess collisional energy is dissipated. For dust-rimmed chondrules we argue the situation is analogous, except that part of the aggregate's interior is now replaced by a chondrule. The prerequisite for such a scenario is the presence of a reservoir of dust that is accreted fractally by the chondrules, preserving its fluffy structure. Here, we follow the Morfill et al. (1998) 'closed box' scenario in which a fixed amount of

dust is injected instantaneously to the chondrule population. The compound objects (or, simply, compounds) thus obtained are modeled to consist of three phases: chondrules, compact (*i.e.,* restructured) dust, and porous (*i.e.,* fractally accreted) dust. The restructuring mechanism also holds for collisions between compounds, again at the expense of the porous phase. In this way a coagulation process is initiated by which chondrules are accreted into large compounds. This coagulation is only stopped when the compounds run out of porous dust, such that the collisional energy can no longer be dissipated; at this stage, all the free-floating dust has been accreted and no more porous dust remains.

The environment in which these processes take place is a key ingredient that enters the coagulation model. A violent, low dust density environment leads to high velocity collisions which quickly pack down the porous rim, limiting its capability to allow further sticking, while even higher velocities will lead to break-up of compounds. On the other hand, if (relative) velocities are modest and remain so during the phase in which compounds accrete other compounds and porous dust, this could lead to significant growth. In this work we use various sources for relative velocities: thermal, turbulent and systematic. The relative velocity is further determined by the internal structure (density) of the compounds, which affects their coupling to the gas. The internal structure of compounds is reflected in the definition of the 'geometric size': the size that corresponds to the effective aerodynamic cross section. The evolution of the internal structure during the accretion process is therefore of key importance: *i.e.,* do collisions follow 'hit-and-stick' behavior in which growth proceeds fractally, or do collisions keep the filling factor constant.

4.2.2 The turbulent nebula

Disk physical structure and model components

The start of the model is defined as the point at which populations of chondrules and dust interact. Before this point, the two populations were either spatially isolated or one did not exist. This chapter is not concerned with the history of the two populations — specifically, we avoid the nagging chondrule formation question — but merely define the zero time of the model ($t = 0$) as the point where the two populations mix. Of course, the history of the two populations determines to a large extent the conditions that prevail at the start of the model, *e.g.,* the size of the dust particles. We take 1 μm as the monomer size (*i.e.,* the smallest constituent size of a dust grain), which roughly corresponds to the sizes of the fine grains observed in chondrites (Ashworth 1977). These grains may have formed by condensation onto seed grains (Chiang 2004) and could have aggregated into larger (fluffy) dust particles before they interact with the chondrules. For instance, if dust condenses out in a region of (recently formed) chondrules (Wasson & Trigo-Rodriguez 2004; Scott & Krot 2005b), the size distribution will be dominated by monomers. However, if chondrules encounter a dust cloud only after a certain time since its formation ($\sim 10^2 - 10^3$ yr), larger aggregates are expected to have formed through monomer collisions. In this work, though, the size of the dust aggregates ($a_{\rm dust}$) is simply treated as a free model parameter (§ 4.2.4).

Both solid components find themselves in the gas-dominated protoplanetary disk.

GAS AND DUST PARAMETERS

(1)	(2)	(3)	(4)
gas density*	ρ_g	28/2.4/0.16	10^{-11} g cm^{-3}
sound speed	c_g	10./7.6/5.6	10^4 cm s^{-1}
mean free path (gas)	ℓ_{mfp}	6.9/82/1230	cm
temperature	T	280/162/89	K
pressure parameter	η	1.6/2.7/4.9	$\times 10^{-3}$
large eddy turn-over time	$t_L = \Omega^{-1}$	0.16/0.82/5.0	yr
turbulent strength parameter*	α	10^{-4}	
inner eddy turn-over time*	t_s	1.3/12/131	10^3 s
gas-chondrule ratio*	$\mathcal{R}_{gc}$	100	
gas-dust ratio*	$\mathcal{R}_{cd}$	100	
chondrule mean size	a_c	300	μm
monomer dust size	a_0	1	μm
fractal growth parameter	δ	0.95	
surface energy density dust*	γ	19	erg cm^{-2}

Table 4.1: Parameters characterizing the gas (upper rows) and dust/chondrules (bottom rows). Gas parameters correspond to a minimum mass solar nebula (MMSN) model of total gas mass of 2.5×10^{-2} M$_\odot$ inside 10 AU with power law exponents of, respectively, -1.0 and -0.5, for the surface density and temperature structure as function of radius (Takeuchi & Lin 2002). Columns denote: (1) parameter description; (2) symbol, $\mathcal{R}_{gc} = \rho_g/\rho_c$ and $\mathcal{R}_{cd} = \rho_c/\rho_d$; (3) corresponding value with multiple values denoting conditions at 1, 3 and 10 AU, respectively (3 AU is the default); (4) unit. Parameters indicated by $\star$ are variables (default model values are given).

We use a minimum mass solar nebula (MMSN) model (Hayashi 1981) to determine the gas parameters (Table 4.1, after Takeuchi & Lin 2002). At $R = 3$ AU this corresponds to a spatial density of $\rho_g = 2.4 \times 10^{-11}$ g cm^{-3}, a thermal speed of $c_g = 7.6 \times 10^4$ cm s^{-1} and a mean free path of $\ell_{mfp} = 82$ cm. Studies of chondrule formation indicate, however, that gas densities may be much higher (*e.g.*, Desch & Connolly 2002; Cuzzi & Alexander 2006) and we will therefore treat ρ_g as a free parameter, denoting with ρ_X the density enhancement over MMSN. We further assume the gas surface density (Σ) and temperature (T) profiles are power-laws of heliocentric radius (R) and fix the exponents at -1.0 and -0.5, respectively. This choice is consistent with a steady disk in which $\dot{\Sigma} = 0$ and an accretion flow, $\dot{M}$, independent of radius.[2] The gas-to-chondrule and the chondrule-to-dust density ratios,

$$\mathcal{R}_{gc} = \rho_g/\rho_c; \text{ and } \mathcal{R}_{cd} = \rho_c/\rho_d, \tag{4.1}$$

are free parameters; for example, $\mathcal{R}_{cd} = 1$ means that chondrules and dust are present in equal proportion (as observed in some meteorite groups, Huss et al. 2005) and $\mathcal{R}_{gc} = 100$ is the standard gas to solids ratio. In our model chondrules follow a log-normal size distribution, for which we take parameters of 300 μm (the mean)

[2]Provided the α-turbulence model (Eq. (4.2)) is assumed and boundary conditions are neglected (see, *e.g.*, Pringle 1981).

and a (log-normal) width parameter of 0.5 (see, *e.g.*, Rubin & Keil 1984; Nelson & Rubin 2002). This makes the mean, mass-weighted size of the chondrule population, $\langle a \rangle_m = 720$ μm. Note that the initial distribution is not necessarily equivalent to the distribution that ends up in meteorites, or the distribution extracted from meteorites by the thin section method (Eisenhour 1996). An overview of all parameters characterizing the gas and solids is given in Table 4.1.

We assume that the gas in the disk is in a turbulent state of motion. After Shakura & Sunyaev (1973), the turbulent viscosity is parameterized as

$$\nu_{\rm T} = \alpha c_{\rm g} H_{\rm g} = \alpha c_{\rm g}^2 / \Omega, \tag{4.2}$$

where $H_{\rm g}$ is the scaleheight of the gas disk, Ω the local (Keplerian) rotation velocity, and α a scale parameter that determines the strength of the turbulence (Shakura & Sunyaev 1973). Values for α are very uncertain. If the magneto-rotational instability is active it may be up to 10^{-3} (Balbus & Hawley 1991; Hawley & Balbus 1991); however in regions of low ionization it can be much lower (Gammie 1996; Sano et al. 2000). The extent of the turbulence is determined by the Reynolds number, Re, defined as ${\rm Re} = \nu_{\rm T}/\nu_{\rm m}$, with $\nu_{\rm m}$ the molecular viscosity, $\nu_{\rm m} = c_{\rm g}\ell_{\rm mfp}/2$ (Cuzzi et al. 1993). The turbulent spectrum consists of eddies characterized by a scale (ℓ), velocity (v), and turn-over time (t), between an outer (or integral) scale L and an inner (or Kolmogorov) scale $\ell_{\rm s}$. Following previous works, $t_{\rm L}$, the largest eddy turn-over time, is taken equal to the inverse orbital frequency, $t_{\rm L} = 1/\Omega$, and $v_{\rm L} = \alpha^{1/2} c_{\rm g}$ (*e.g.*, Dubrulle et al. 1995; Cuzzi et al. 2001; Schräpler & Henning 2004). The eddy properties at the turbulence inner scale then follow from the Reynolds number:

$$t_{\rm s} = {\rm Re}^{-1/2} t_{\rm L}; \qquad \ell_{\rm s} = {\rm Re}^{-4/3} L; \qquad v_{\rm s} = {\rm Re}^{-1/4} v_{\rm L}. \tag{4.3}$$

Thermal motions

When gas molecules collide with a larger (dust) particle momentum is transferred, changing the motion of the dust particle. These kicks occur stochastically, resulting in a velocity behavior known as Brownian motion. The ensuing velocity difference between two particles of mass m_1 and m_2 is highest for low masses and high temperatures,

$$\Delta v_{\rm BM} = \sqrt{\frac{8 k_{\rm B} T (m_1 + m_2)}{\pi m_1 m_2}}, \tag{4.4}$$

where $k_{\rm B}$ is Boltzmann's constant. For micron-sized particles Brownian velocities are a few mm/s; but since $\Delta v_{\rm BM}$ decreases with the $-3/2$ power of the size of the smallest particle, it quickly becomes negligible for larger particles.

Systematic motions

The key parameter that determines the coupling of solids to the gas is the friction time, $\tau_{\rm f}$. In the Epstein regime the size of the particle, a, is small with respect to the

mean-free-path of gas molecules, $\ell_{\rm mfp}$, and the friction time is given by

$$\tau_{\rm f} = \tau_{\rm f}^{\rm Ep} = \frac{3}{4 c_{\rm g} \rho_{\rm g}} \frac{m}{\pi a^2}. \qquad (a \leq \tfrac{9}{4}\ell_{\rm mfp}) \tag{4.5}$$

For solid 1 μm-grains the friction time is $\tau_{\rm f} \sim 10^2/\rho_X$ s for the default nebula parameters of 3 AU (Table 4.1), while for an $a \sim 300$ μm chondrule it takes $\sim 10/\rho_X$ hours before the traces of its initial motion are 'erased.' Note that Eq. (4.5) defines a as the geometrical radius of the particle, *i.e.,* the radius corresponding to the angularly-averaged projected surface area of the particle. If the particle is a fluffy aggregate its friction time is therefore much less than a compact-equivalent with the same mass. If significant growth takes place, particles will no longer obey the Epstein drag law; friction times are then enhanced with respect to $\tau_{\rm f}^{\rm Ep}$, *i.e.,*

$$\tau_{\rm f}^{\rm St} = \frac{4a}{9\ell_{\rm mfp}} \frac{1}{{\rm Re_p} C} \tau_{\rm f}^{\rm Ep}. \qquad (a \geq \tfrac{9}{4}\ell_{\rm mfp}) \tag{4.6}$$

Here, ${\rm Re_p} = 2a v_{\rm pg}/\nu_{\rm m}$ is the *particle* Reynolds number, which determines the constant C,[3] and $v_{\rm pg}$ the particle-gas velocity. Within the physical conditions of the simulations in § 4.4 the particle Reynolds number stays below ${\rm Re_p} = 1$, for which $C = {\rm Re_p}^{-1}$ (Weidenschilling 1977a). Friction times are then independent of $v_{\rm pg}$.

One of the well-known problems in the planet-formation field is the strong inward radial drift particles of a specific size experience, *e.g.,* meter-sized particles at $\sim$AU radii or cm-sized at $\sim$100 AU radii (see Brauer et al. (2007) for a recent review). This inward radial drift is caused by the existence of gas pressure gradients, resulting in a gas velocity that is somewhat less than Keplerian by a difference of magnitude $\eta v_{\rm K}$ (Weidenschilling 1977a; Nakagawa et al. 1986) with η the dimensionless pressure parameter, defined as

$$\eta \equiv -\frac{1}{2R\Omega^2} \frac{1}{\rho_{\rm g}} \frac{\partial P}{\partial R} \approx c_{\rm g}^2/v_{\rm K}^2. \tag{4.7}$$

However, particles do not experience this pressure term and instead attempt to move at Keplerian velocities, faster than the gas. The ensuing drag force removes angular momentum from the particle resulting in a radial velocity of (Weidenschilling 1977a)[4]

$$v_{\rm rd} = -\frac{2{\rm St}}{1 + {\rm St}^2} \eta v_{\rm K}, \tag{4.8}$$

[3] Compared to, *e.g.,* Weidenschilling (1977a) the definition of C has been scaled down by a factor of 24. That factor is already present in Eq. (4.6).

[4] In Eq. (4.8) we have not accounted for collective effects when the particle density is comparable to or higher than the gas density. Equation (4.8) then changes (Nakagawa et al. 1986). Angular momentum exchange between the dust and gas dominated layers (Youdin & Chiang 2004) is another process to be accounted for, but its significance is relatively modest (Brauer et al. 2007).

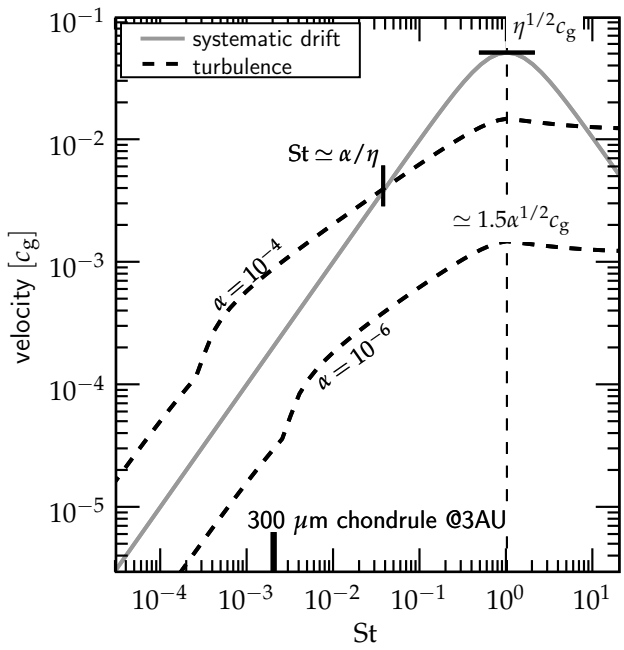

Fig. 4.1: Comparison of systematic and turbulent velocities as function of particle Stokes number. Plotted are radial velocities (Eq. (4.8), solid grey curve) and turbulent velocities with $\varepsilon = 0$ (Eq. (4.10), dashed curves). Note the change in slope between the linear and the square-root turbulent velocity regime which happens at St $\simeq \mathrm{Re}^{-1/2}$. Turbulent velocities dominate over systematic velocities for St $\lesssim \alpha/\eta$ (provided this is $\gtrsim \mathrm{Re}^{-1/2}$). The Stokes number corresponding to a 300 μm-sized chondrule at the default nebular conditions of 3 AU (see Table 4.1) is also indicated. All velocities peak at St $= 1$ (light-dashed vertical curve).

where we have defined $\mathrm{St} = \tau_\mathrm{f}\Omega$. This systematic radial drift velocity peaks at $\mathrm{St} = 1$. Chondrule-sized particles, however, are generally sufficiently well coupled to the gas ($\mathrm{St} \ll 1$) so that radial motions are low in most physical conditions; turbulent-induced motions then dominate (unless α is really low). However, when particles grow in size, systematic motions may take over from turbulent velocities (see Fig. 4.1).

Turbulent motions

For a Kolmogorov spectrum, turbulence leads to mean (large scale) velocity fluctuations of $v_\mathrm{g} = (3/2)^{1/2} v_\mathrm{L} = (3/2)^{1/2}\alpha^{1/2} c_\mathrm{g}$ (Cuzzi & Hogan 2003). Due to their inertia, solids do not instantaneously follow these fluctuations but require a time τ_f before their motions align. This leads to a net relative motion, v_pg, between the gas and the solid particle of (Cuzzi & Hogan 2003)

$$v_\mathrm{pg} = v_\mathrm{g} \sqrt{\frac{\mathrm{St}^2(\mathrm{Re}^{1/2} - 1)}{(\mathrm{St}+1)(\mathrm{St}\mathrm{Re}^{1/2}+1)}}, \tag{4.9}$$

where the Stokes number, St, is the ratio between the friction time and the large eddy turn-over time, *i.e.*, $\mathrm{St} = \tau_\mathrm{f}/t_\mathrm{L} = \tau_\mathrm{f}\Omega$.[5] The limiting expressions of Eq. (4.9), $v_\mathrm{pg} = \mathrm{St} v_\mathrm{g}$ for $\mathrm{St} \ll 1$ and $v_\mathrm{pg} = v_\mathrm{g}$ for $\mathrm{St} \gg 1$, respectively, correspond to the cases of particles that are well coupled (small particles) and poorly coupled (larger

[5] $\mathrm{St} = \tau_\mathrm{f}/t_\mathrm{L}$ is the formal definition for the Stokes number. In the α-turbulence model $t_\mathrm{L} = \Omega^{-1}$ and the definitions for St in equations (4.8) and (4.9) coincide.

particles) to the gas.

The calculation of particle-particle relative velocities does not follow directly from the $v_{\rm pg}$'s since particle velocities can become very incoherent in turbulence (*e.g.*, $\Delta v_{12} \neq |v_{1\rm g} - v_{2\rm g}|$). Consider, for example, two small particles entrained in the same eddy. If their motions are aligned, no relative velocity is present; it is only within a time $\tau_{\rm f}$ after being caught in the eddy that these particles have the chance to develop relative motions, provided their friction times differ (*i.e.*, $\tau_1 \neq \tau_2$). The problem of finding suitable (*i.e.*, closed-form) expressions for Δv_{12} is important since these are key to any model of dust coagulation (*e.g.*, Weidenschilling 1997; Suttner & Yorke 2001; Dullemond & Dominik 2005; Nomura & Nakagawa 2006) including this work. Following earlier works of Völk et al. (1980), Weidenschilling (1984a), Markiewicz et al. (1991) and Cuzzi & Hogan (2003), Ormel & Cuzzi (2007) have presented closed-form analytical expressions for Δv_{12} (with a margin of error of $\sim$10%) in terms of the Stokes number of the particles:

$$\left(\frac{\Delta v_{12}}{v_{\rm g}}\right)^2 = \begin{cases} {\rm Re}^{1/2}\left({\rm St}_1 - {\rm St}_2\right)^2 & \text{for } \tau_1 < t_{\rm s} \\ \left[2y_{\rm a}^* - (1+\varepsilon) + \frac{2}{1+\varepsilon}\left(\frac{1}{1+y_{\rm a}^*} + \frac{\varepsilon^3}{y_{\rm a}^*+\varepsilon}\right)\right]{\rm St}_1 & \text{for } 5t_{\rm s} \simeq \tau_1 \lesssim t_{\rm L} \\ \left(\frac{1}{1+{\rm St}_1} + \frac{1}{1+{\rm St}_2}\right) & \text{for } \tau_1 \geq t_{\rm L} \end{cases} \quad (4.10)$$

In these expressions τ_1 (or ${\rm St}_1$) always corresponds to the particle of the largest friction time and $\varepsilon = \tau_2/\tau_1 \leq 1$. Near the $\tau_1 = t_{\rm s}$ turning point the expression for Δv_{12} is somewhat more complex (see Ormel & Cuzzi 2007). The term $y_{\rm a}^*$ is a numerical constant of value $y_{\rm a}^* \simeq 1.60$ if $\tau_1 \ll t_{\rm L}$; however, when $\tau_1 \simeq t_{\rm L}$ it becomes a function of τ_1 and drops to unity at $\tau_1 = t_{\rm L}$. In that case we approximate $y_{\rm a}^*$ by an interpolation function. In Fg. 4.1 Δv_{12} is plotted for two values of α in the limit of ${\rm St} = {\rm St}_1 \gg {\rm St}_2$ (dashed curves). The three regimes of Equation (4.10) are clearly distinguishable: the linear regime for $\tau_{\rm f} \lesssim t_{\rm s}$ (or ${\rm St} \lesssim {\rm Re}^{-1/2}$; small particles); the square-root regime, $t_{\rm s} \lesssim \tau_{\rm f} \lesssim t_{\rm L}$; and the high Stokes regime, ${\rm St} \geq 1$, where particles decouple from the gas. Small particles like chondrules have Stokes number ${\rm St} \ll 1$; whether they fall into the linear or square-root velocity regime depends on their sizes in relation to the gas parameters (*e.g.*, $\alpha, \rho_{\rm g}$) of the disk.

Figure 4.1 also shows the systematic drift velocity (Eq. (4.8), solid curve). If one assumes that ${\rm St}_2 \ll {\rm St}_1$ the radial drift curve also gives the relative velocity a particle with ${\rm St} = {\rm St}_1$ has with a much smaller particle. Actually, for ${\rm St}_1 \leq 1$ turbulent and systematic drift relative velocities (Eqs. (4.8) and (4.10)) depend only weakly on ${\rm St}_2$ (the lower Stokes number); the curves in Fg. 4.1 can therefore be interpreted as the typical relative velocity a particle of a given Stokes number has with particles of similar or lower Stokes numbers. Figure 4.1 shows that for very small particles ($\tau_{\rm f} \ll t_{\rm s}$ or ${\rm St} \ll {\rm Re}^{-1/2}$) turbulent velocities only dominate when $\alpha \gtrsim 10^{-5}$. Then, when turbulent velocities flatten out in the square-root regime, the radial drift motion may catch up with the point of intersection lying at ${\rm St} \simeq \alpha/\eta$, provided α is not either too low or too high. For any model with $\alpha \lesssim \eta$ radial drift motions will eventually dominate: a regime of high relative velocities ($\sim$10 m s^{-1}) is therefore unavoidable.

COMPOUND PHASES

Phase	Specific density	Mass fraction[a]	Filling factor
chondrule	$\rho_{\rm c}^{(\rm s)} = 3$ g cm^{-3}	$(1 - f_{\rm d})$	$\phi_{\rm c} = 1$
compact dust	$\rho_{\rm d}^{(\rm s)} = 3$ g cm^{-3}	$f_{\rm d}(1 - f_{\rm p})$	$\phi_{\rm cd} = 0.33$
porous dust	$\rho_{\rm d}^{(\rm s)} = 3$ g cm^{-3}	$f_{\rm d} f_{\rm p}$	$\phi_{\rm pd} \lesssim 0.15$

Table 4.2: Material properties of compounds phases. [a]Mass fraction with respect to entire compound (sum equals 1); $f_{\rm d}$ = mass fraction in dust; $f_{\rm p}$ = porous mass fraction of the dust.

4.2.3 Collisions between dust-rimmed chondrules

Theoretical studies and laboratory experiments have shown that the outcome of grain-grain or aggregate-aggregate collisions depends on its ratio of the kinetic energy to a critical energy (Dominik & Tielens 1997; Blum & Wurm 2000). Specifically, porous dust is accreted when chondrules sweep up dust grains, or aggregates of dust grains, at collisional energies (E) that stay below the energy threshold for restructuring, $5E_{\rm roll,}$ where $E_{\rm roll}$ is the energy required to roll one contact area over the surface of the grain. This can lead to a very open structure of filling factors ($\phi_{\rm pd}$) that are lower than the filling factors obtained in particle-cluster aggregation, $\phi_{\rm PCA} \simeq 0.15$ (see below). As outlined in § 4.2.1, the absence of restructuring during dust sweep-up is crucial since the resulting porous structure can then be compacted in more energetic collisions — the collision of compounds — promoting further growth. In compound collisions, $E > E_{\rm roll}$ and the dust within the compound will restructure, dissipating a unit of $\sim E_{\rm roll}$ for each dust grain that is involved in the rolling motion. The porous dust that is involved in restructuring compacts to a higher filling factor, $\phi_{\rm cd}$.

Compounds can then be represented as a three phase structure: chondrules, compact dust and porous dust. Two numbers, the dust fraction $f_{\rm d}$ and the porous dust fraction $f_{\rm p}$, quantify the relative importance of each phase within a compound (see Table 4.2). The internal structure of each phase is further characterized by its filling factor, ϕ. A schematic picture of the structure is given in Fg. 4.2.

Collisional compaction

The accreted dust mantles surrounding chondrules can have a very porous and fractal structure. Typically, grains in these rims will be bonded to two other grains in large string-like structures. When two rimmed chondrules collide, contact will be established between two (or a limited number of pairs of) grains and these grains will bear the full brunt of the collision. Once the force on these grains exceeds the critical rolling force, they start to roll (restructuring). The rolling of these grains may enable contact formation between more pairs of grains, thereby promoting compaction and at the same time reducing the force per contact. Compaction will stop when the force on newly made contacts drops below the rolling force. Compaction may also stop because the resulting structure is too rigid to allow for further rolling, *i.e.*, the rolling grain made contact with too many grains. Since forces are propagated through such compacted structures, this means that none of the grains involved ex-

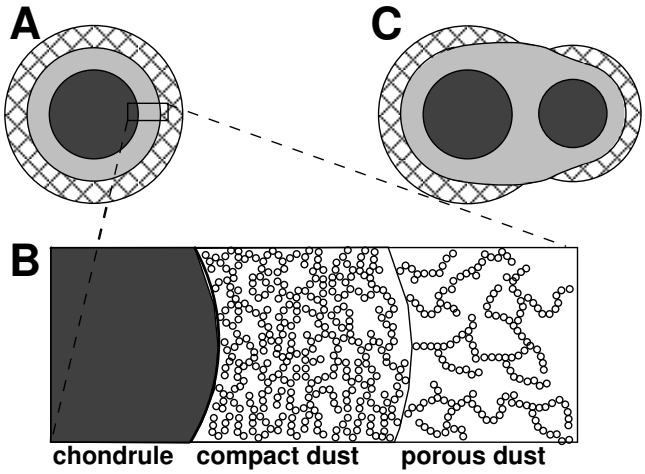

Fg. 4.2: *(a)* Schematic representation of the three-phase model of dust-rimmed chondrules: chondrule (*dark grey*), compact dust (*light grey*) and porous dust (*pattern*). The inset *(b)* shows the substructure of the dust that consists of micron-sized monomers. *(c)* If chondrules collide, the collision energy is dissipated by transferring dust from the porous to the compact dust phase. Figure not to scale.

periences a force exceeding the rolling force. The compression of the contact area in a collision between two monomers will give rise to an elastic repulsion force slowing down and eventually reversing the collision. The absolute value of the repulsive force will be set by the kinetic energy of the collision; in the Hertzian limit the sum of the forces on the individual contacts scales with the remaining kinetic energy to the 3/5th power. For colliding aggregates, rolling of the contacting monomers provides an additional energy dissipation channel. But once the resulting structure is too rigid to enable further rolling, compression of the individual contact areas will provide the repulsion required to slow down and possibly even reverse the collision if the collision is energetic enough. The collision partners then bounce.

Blum & Schräpler (2004) have designed experiments to measure the compaction of dust cakes under uniaxial compression. These dust cakes were grown through a Particle-Cluster-Aggregation (PCA) method by deposition of individual 1.5 μm diameter monomers at low velocities where rolling is not a factor and growth occurs through a hit-and-stick process. The volume filling factor of the resulting aggregates was measured to be 0.15, in good agreement with numerical simulations of this process (Ossenkopf 1993; Watson et al. 1997). At this volume filling factor, the typical coordination number, *i.e.*, the number of neighbors with which the monomer is in contact, is calculated to be 2 (Ridgway & Tarbuck 1967). These dust cakes were exposed to a unidirectional pressure in a static experiment. Figure 4.3 shows the resulting volume filling factor as a function of the applied unidirectional pressure (Blum & Schräpler 2004). The results show that compaction is initiated at an applied pressure of $\sim 10^4$ dyn cm^{-2}. If we assume that the number of monomers per unit area being pressed on is given by,

$$N/A = \left(\pi a_0^2 \phi^{2/3}\right)^{-1} \sim 2 \times 10^8 \text{ cm}^{-2} \tag{4.11}$$

with a_0 the radius of the monomer, the force on an individual monomer becomes $\sim 5 \times 10^{-5}$ dyn. This is very close to the rolling force of 7×10^{-5} dyn Blum &

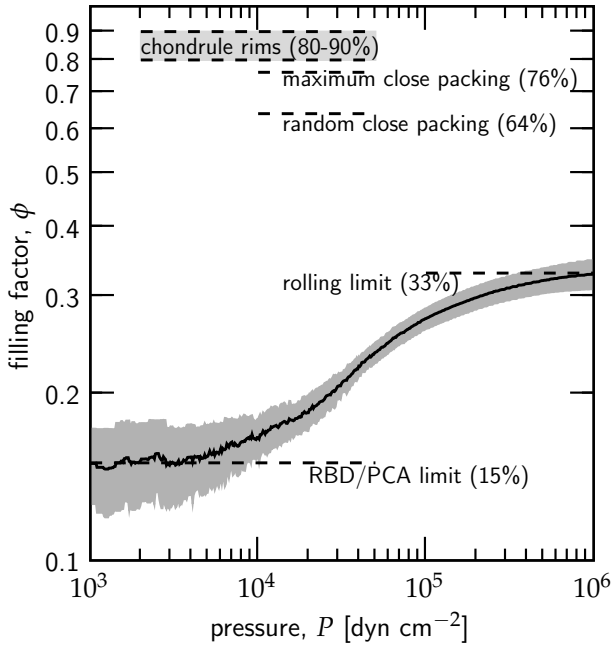

Fg. 4.3: (*solid curve*) Compression of PCA aggregates, obtained by static compression of 'dust cakes' created by random ballistic deposition of $a_0 = 0.75\,\mu$m SiO_2 spheres (Blum & Schräpler 2004; Blum et al. 2006). The uncertainty in the measurements is denoted by the grey area. Values for ϕ for several amounts of packing configurations are shown. (Data on the compression curve experiments kindly provided by Jürgen Blum.)

Schräpler (2004) extrapolated from the measurements by Heim et al. (1999). As the dust cake compacts and the average coordination number increases, the structure becomes more rigid and resistant to further compression (under these conditions, see below). Finally, at a pressure of $\sim 10^6$ dyn cm^{-2} the structure is dense enough for rolling motions to be inhibited. This corresponds to an average coordination number of 3.9 and a filling factor of 0.33 (Fg. 4.3).

The conditions in the protoplanetary disk under which dust rims are formed by grain accretion and under which they evolve through collisions with other rimmed grains differ from those in these laboratory studies. First, the initial structure of the dust rims accreted on the chondrule surface may differ from PCA. Although low velocity collisions are expected, the monomers may collide preferentially among each other before colliding with a chondrule. In that case the resulting structure is referred to as Cluster-Cluster Aggregation (CCA), a process that leads to much lower filling factors than PCA. Whether PCA or CCA is preferred depends on the relative abundance of dust and chondrules and their relative velocities. So, the filling factor of the porous dust component may start lower than the experimental one in Fg. 4.3. However, since this process is directly tied to the rolling force experienced by the monomers that make contact, we expect that this difference in initial structure will have no influence on the critical pressure required for the onset of compaction. We expect, likewise, that uniaxial compression of dust rims grown by CCA will stall at 0.33 filling factor since this is again a property of the resulting structure; *e.g.*, at these kinds of volume filling factors, monomers in the dust rims will have been organized in 'stabilizing' structures.

However, under nebular conditions continuous impacts will arise from random

CRITICAL ENERGIES

Expression	Breaking	Rolling
Theoretical [a]	$E_{\rm br} = A_{\rm br}\gamma^{5/3}a_\mu^{4/3}/\mathcal{E}^{\star 2/3}$	$E_{\rm roll} = A_{\rm roll}\xi_{\rm crit}a_\mu\gamma$
DT97 Prefactors[a]	$A_{\rm br} \simeq 9.6$	$A_{\rm roll} \simeq 59$
Measured energies[b]	$E_{\rm br} = 1.3\times10^{-8}$ erg	$E_{\rm roll} = 1.7\times10^{-8}$ erg
Empirical prefactors[c]	$A_{\rm br} = 2.8\times10^{3}$	$A_{\rm roll} = 1.8\times10^{3}$

Table 4.3: Comparison between predicted and measured critical energies for breakup and rolling. *Notes.* [a]Theoretically derived expressions for $E_{\rm br}, E_{\rm roll}$ from Chokshi et al. (1993) (for the breakup energy) and Dominik & Tielens (1997) (for rolling) and corresponding pre-factors, $A_{\rm br}, A_{\rm roll}$. We define $\xi_{\rm crit} = 10^{-8}$ cm. [b]Values adopted from Blum & Wurm (2000) for parameters of $a_0 = 2a_\mu = 9.5\times10^{-5}$ cm, $\gamma = 19\,{\rm erg\,cm^{-2}}$ and $\mathcal{E}^\star = 3.7\times10^{11}\,{\rm dyn\,cm^{-2}}$. The original measurements were performed by Poppe et al. (1999) (for the breakup energy) and Heim et al. (1999) (for the rolling energy). [c]Empirically derived prefactors from the theoretical expressions with the measured values for $E_{\rm br}$ and $E_{\rm roll}$.

directions; it is therefore likely that collisional compaction under these conditions will result in higher volume filling factors than the unidirectional compression experiments would indicate, possibly even as high as 0.5 (the value of $\phi = 0.64$ characterizes for Random Close Packing, RCP). We note that Blum & Schräpler (2004) and Blum et al. (2006) in their compression studies did approach RCP when applying an omnidirectional pressure of $\sim10^9\,{\rm dyn\,cm^{-2}}$. Note, however, that omnidirectional pressure is not achieved in collisions between two bodies in an open environment; *i.e.*, the dust has the chance to spread perpendicular to the direction of compression, and the obtained high volume filling factor may not be generally attainable. Indeed, for $\phi > 0.33$ rolling motion become impeded and we do expect that in order to 'crush' the dust (rims) to RCP values much higher pressures are required. Studies indicate pressures of $\sim10^{10}\,{\rm dyn\,cm^{-2}}$ in order to reach RCP (Martin et al. 2003; Tanwongwan et al. 2005). This second stage of compaction would correspond to a very different collision regime characterized by much higher energies. Adopting the Hertzian limit, we expect that this higher pressure, *c.q.* force in the contact area corresponds to a impact energy which is higher by a factor $(10^9/10^6)^{5/3}$ or a collision velocity higher by a factor $10^{5/2}$ over the velocity/energy required to initiate compaction. In this study, while acknowledging that higher filling factors are plausible, we have for simplicity assumed that $\phi = 0.33$ is the limiting value.

Acquisition of a porous dust layer

Two critical energies—the breakup and rolling energy—regulate the behavior of the dust (porous accretion/compaction) upon collision: (Chokshi et al. 1993; Dominik & Tielens 1997; Blum & Wurm 2000)

$$E_{\rm br} = A_{\rm br}\frac{\gamma^{5/3}a_\mu^{4/3}}{\mathcal{E}^{\star 2/3}}; \tag{4.12a}$$

$$E_{\rm roll} = 6\pi^2\xi_{\rm crit}a_\mu\gamma = A_{\rm roll}\xi_{\rm crit}a_\mu\gamma, \tag{4.12b}$$

where $a_\mu = a_1 a_2/(a_1 + a_2)$ is the reduced radius of the collision partners, γ the surface energy density of the material and $\mathcal{E}^\star$ Young's elastic modulus (assuming the same materials collide). Also, $\xi_{\rm crit}$ in the $E_{\rm roll}$ expression is some critical distance used to initiate rolling which Dominik & Tielens (1997) assumed to be on the order of the atomic size, $\xi_{\rm crit} = 10^{-8}$ cm. Using these definitions the constants $A_{\rm br}$ and $A_{\rm roll}$ are dimensionless. Blum & Wurm (2000) have experimentally determined the breakup and rolling energies (see Table 4.3) and found these to be higher than the Dominik & Tielens (1997) theoretical predictions. However, apart from a scale factor, the Blum & Wurm (2000) experiments agreed well with the Dominik & Tielens (1997) model; that is, collisions can be separated into the regimes of perfect sticking, restructuring and fragmentation. We therefore apply the mechanism put forward by Dominik & Tielens (1997) but use pre-factors ($A_{\rm br}, A_{\rm roll}$) from the experimental results (last row of Table 4.3). Note that for micron-sized particles the rolling and breakup energy are similar.

When two particles meet, direct sticking occurs if the collision energy, E, is dissipated at the first point of contact; *i.e.*, $E \leq E_{\rm st}$, where $E_{\rm st}$ is related to the breakup energy as $E_{\rm st} = 0.22 E_{\rm br}$ (Dominik & Tielens 1997). Writing $E = \frac{1}{2} m_\mu (\Delta v)^2$ with $m_\mu = m_1 m_2/(m_1 + m_2)$ the reduced mass and Δv the relative velocity, the criterion $E \leq E_{\rm st}$ translates into a threshold velocity of

$$
\begin{aligned}
v_{\rm st} = \sqrt{\frac{2E_{\rm st}}{m_\mu}} &= \sqrt{0.45 A_{\rm br}} \frac{\gamma^{\frac{5}{6}} a_\mu^{\frac{4}{6}}}{(\mathcal{E}^\star)^{\frac{1}{3}} m_\mu^{\frac{1}{2}}} = 0.33 A_{\rm br}^{\frac{1}{2}} \left(\rho_{\rm d}^{(\rm s)}\right)^{-\frac{1}{2}} \gamma^{\frac{5}{6}} N_\mu^{-\frac{1}{2}} a_\mu^{\frac{2}{3}} a_0^{-\frac{3}{2}} (\mathcal{E}^\star)^{-\frac{1}{3}} \\
&= 35 \text{ cm s}^{-1} \, N_\mu^{-\frac{1}{2}} \left(\frac{a_\mu}{a_0}\right)^{\frac{2}{3}} \left(\frac{a_0}{\mu\text{m}}\right)^{-\frac{5}{6}} \left(\frac{\rho_{\rm d}^{(\rm s)}}{3 \text{ g cm}^{-3}}\right)^{-\frac{1}{2}} \\
&\quad \times \left(\frac{\gamma}{19 \text{ erg cm}^{-2}}\right)^{\frac{5}{6}} \left(\frac{\mathcal{E}^\star}{3.7 \times 10^{11} \text{ dyn cm}^{-2}}\right)^{-\frac{1}{3}},
\end{aligned}
\tag{4.13}
$$

where we have assumed that like materials meet (*i.e.*, same $\gamma, \mathcal{E}^\star$) , and where the reduced mass has been parameterized as $m_\mu = N_\mu m_0$ with $m_0 = 4\pi\rho_{\rm d}^{(\rm s)} a_0^3/3$ the mass of the (smallest) grain. Thus, $N_\mu = 1/2$ for equal-size particles and $N_\mu = 1$ for very different size particles. Equation (4.13) shows that micron-sized silicate particles have no problem to stick to each other at velocities of $\sim$10 cm s^{-1}. This also holds for collisions between μm-sized grains and chondrules since it is the reduced size a_μ that enters the equation. However, at higher velocities the grains will bounce off.

In collisions between chondrules ($a_0 \sim 300$ μm) the sticking velocity falls below $\sim$cm s^{-1}, lower than the velocities between chondrules for most values of α (see Fg. 4.1). Also, for chondrules, the assumption of a smooth, spherical surface on which the physics behind Eq. (4.12a) is based breaks down. Although surface roughness increase the sticking capabilities for μm-sized grains (Poppe et al. 2000), the asperities in chondrules are probably too large to favor sticking. However, we now expect the previously accreted porous dust layer to act as the sticking mecha-

nism through a dynamic restructuring and compaction of the constituent grains.

Another important collision is between a chondrule (or compound) and a dust grain or dust aggregate. Here, the criterion for sticking *without restructuring* is $E \leq 5E_{\rm roll}$ (Dominik & Tielens 1997). This translates into a velocity of (using the same substitutions as above)

$$v_{\rm st,aggr} = \sqrt{\frac{10E_{\rm roll}}{m_\mu}} = 1.6 \times 10^2 \text{ cm s}^{-1}\, N_\mu^{-1/2} \left(\frac{a_\mu}{a_0}\right)^{1/2} \left(\frac{a_0}{1\ \mu\text{m}}\right)^{-1} \tag{4.14}$$

$$\times \left(\frac{\rho_{\rm d}^{(\rm s)}}{3 \text{ g cm}^{-3}}\right)^{-1/2} \left(\frac{\gamma}{19 \text{ erg g}^{-1}}\right)^{-1/2}, \tag{4.15}$$

in which now $N_\mu > 1$ roughly corresponds to the number of grains in the aggregate. Thus, at moderately low velocities small aggregates will hit-and-stick, preserving their porous structure. This 'hit-and-stick' behavior will also be referred to as 'fractal accretion.' However, when aggregates become large or α is high (*e.g.*, $\alpha \geq 10^{-3}$ and $\rho_X = 1$; Fg. 4.1) some compaction is likely to occur. However, in this study we have ignored this effect (for reasons of computational efficiency) and simply assumed that all dust accretion occurs fractally. Although invalid in a violent collisional environment, the consequences of this assumption are marginal as the porous dust on the chondrule surface is quickly compacted by colliding chondrules in any case.

Collisions between dust-chondrules compounds

Hatzes et al. (1991) studied collisions between cm-sized particles and found that sticking forces increased significantly when a frosty layer was present. While they attribute this enhanced sticking to interlocking of jagged surface structures, this effect probably reflects energy dissipation due to restructuring. In the case of chondrules, rimmed by a layer of fluffy dust, the situation is analogous: the fluffy structure allows the collisional energy to be dissipated away. Assuming that each monomer (of mass m_0, size a_0 and internal density $\rho_{\rm d}^{(\rm s)}$) in the porous dust layer is capable of absorbing an energy $E_{\rm roll}$, $E/E_{\rm roll}$ monomers are needed to dissipate the total collision energy. Expressed in terms of mass, a porous mass fraction of at least $f_{\rm comp}$ must be available, with $f_{\rm comp}$ the ratio of the required mass in porous dust to the total mass of the collision partners,

$$f_{\rm comp} = \frac{m_0 E/E_{\rm roll}}{m_1 + m_2} = \frac{4\pi}{3A_{\rm roll}\xi_{\rm crit}} \rho_{\rm d}^{(\rm s)} a_0^2 \gamma^{-1} \left(\frac{m_\mu^2}{m_1 m_2}\right) (\Delta v)^2 \tag{4.16}$$

$$= 3.7 \times 10^{-2} \left(\frac{m_\mu^2}{m_1 m_2}\right) \left(\frac{a_0}{\mu\text{m}}\right)^2 \left(\frac{\Delta v}{10 \text{ cm s}^{-1}}\right)^2 \left(\frac{\rho_{\rm d}^{(\rm s)}}{3 \text{ g cm}^{-3}}\right) \left(\frac{\gamma}{19 \text{ erg cm}^{-2}}\right)^{-1}.$$

This equation reveals a few important results. First, $f_{\rm comp}$ decreases with smaller dust grains (smaller a_0); although more monomers are required to dissipate the same collision energy, the total mass of the monomers that restructures is less. Also, the

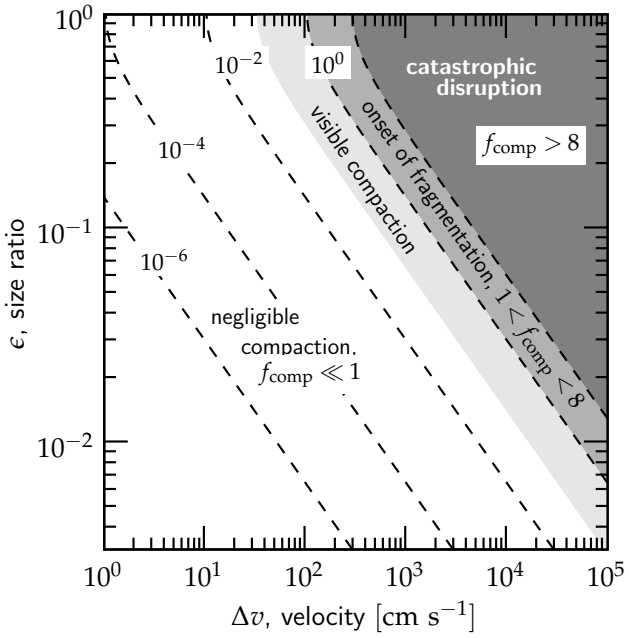

Fig. 4.4: Contours of $f_{\rm comp}$ (*dashed curves*) — the fraction of the (combined) compound mass that must be involved in restructuring to dissipate away the collisional energy to stick the compounds (Eq. (4.16)) — as function of collision velocity (x-axis) and size ratio (y-axis). Equal internal densities are assumed, $\rho_1 = \rho_2 = 3$ g cm^{-3} and $a_0 = 1$ μm The criterion for sticking is $f_{\rm comp} \leq \langle f_{\rm d} f_{\rm p} \rangle_m$ (see text). For low velocities or size-ratio's compaction is insignificant. Collisions with $f_{\rm comp} \gtrsim \langle f_{\rm d} f_{\rm p} \rangle_m$ compact all their dust. When $f_{\rm comp} \gtrsim 8$ complete destruction occurs (see § 4.2.3).

dependence on velocity is rather steep; at very low velocities the amount of compacted material is negligibly low ($f_{\rm comp} \ll 1$), while visible compaction happens in a quite restricted velocity band (see Fig. 4.4). Another important point is the mass-dependence in Eq. (4.16). The value of $f_{\rm comp}$ does not depend on the absolute masses of the particles involved, but, through the $m_\mu^2 / m_1 m_2$ factor, rather on the *mass-ratio* of the collision partners. Thus, a collision between particles of very unequal size has a lower $f_{\rm comp}$ than equally-sized particles colliding at the same velocity and, therefore, a higher probability to stick (see Fig. 4.4). This is of course due to the reduced mass that enters the collision energy.

Collisional recipe

We will now quantify how the collisions affect the structural parameters of the compound, *i.e.*, the $f_{\rm d}$ and $f_{\rm p}$ quantities. Equation (4.16) gives the mass fraction of the collision partners that must be compacted, which, for sticking, must be less than the mass fraction available in porous dust ($f_{\rm d} f_{\rm p}$), averaged over the collision partners, *i.e.*, $\langle f_{\rm d} f_{\rm p} \rangle_m = (m_1 f_{\rm d,1} f_{\rm p,1} + m_2 f_{\rm d,2} f_{\rm p,2}) / (m_1 + m_2)$. If $f_{\rm comp} \leq \langle f_{\rm d} f_{\rm p} \rangle_m$ enough porous dust is present to absorb the collisional energy and the two compounds stick. A fraction $f_{\rm comp}$ is then transferred from the porous to the compact phase. If $f_{\rm comp} > \langle f_{\rm p} f_{\rm d} \rangle_m$, however, restructuring cannot dissipate all the collisional energy. As mentioned before, we do not include other energy dissipation channels but simply consider all collisions in which $f_{\rm comp} > \langle f_{\rm d} f_{\rm p} \rangle_m$ to result in bouncing; $f_{\rm p}$ is then set to 0 for both particles. This means fragmentation of compounds or erosion of the porous rim are neglected (but see below: role of fragmentation).

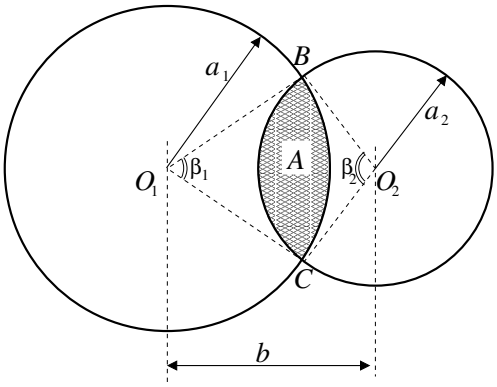

Fg. 4.5: Projection of two compounds colliding at an impact parameter b. The ratio of the shaded region (A) relative to the cross section of each compound (πa_i^2) determines the fraction of the porous dust that can be used during the collision, *i.e.*, $f_{\mathrm{geo},i} = A/\pi a_i^2$. A is obtained by subtracting the kite O_1BO_2C from the two circular sectors spanned up by β_1 and β_2 (Eq. (4.17)).

A further restriction to the amount of dust that can be compacted is made when we account for the geometry of the collision. Then, only a fraction (f_{geo}) of the compound (and of its dust) is involved in being compacted and dissipating energy. We estimate f_{geo} from the intersection between the particles' trajectories. This intersection actually is one between a cylinder and a sphere, but here we approximate it as a 2d intersection between two circles which meet at an impact parameter b. The area of the intersection, A, can be calculated by elementary geometry as (see Fg. 4.5)

$$A(a_1,a_2,b) = 2a_1^2 \arccos\left(\frac{b^2+a_1^2-a_2^2}{2ba_1}\right) + 2a_2^2 \arccos\left(\frac{b^2+a_2^2-a_1^2}{2ba_2}\right) - \sqrt{(-b+a_1+a_2)(b+a_1-a_2)(b-a_1+a_2)(b+a_1+a_2)}, \quad (4.17)$$

from which $f_{\mathrm{geo},i}$ for each particle is calculated as $f_{\mathrm{geo},i} = A/\pi a_i^2$. Equation (4.17) is valid for impact parameters of $|a_1 - a_2| < b < a_1 + a_2$. For $b \leq |a_1 - a_2|$ the intersection equals the projected area of the smaller particle, while $A = 0$ for $b \geq a_1 + a_2$. The total mass-fraction of the particles that participates is $(m_1 f_{\mathrm{d1}} f_{\mathrm{p1}} f_{\mathrm{geo},1} + m_2 f_{\mathrm{d2}} f_{\mathrm{p2}} f_{\mathrm{geo},2})/(m_1+m_2)$ and this has to be greater than f_{comp} for sticking. Note, however, that inclusion of the f_{geo} factor might be too restrictive: since the sound speed inside aggregates ($\sim$30 m s^{-1}; Paszun & Dominik 2008b) is usually much higher than Δv, the energy will be quickly transferred along movable structures. For completeness we therefore consider both extremes: f_{geo} determined from Eq. (4.17) and $f_{\mathrm{geo}} = 1$.

When the collision results in sticking, the total dust and porous dust fractions are calculated as follows,

$$f_{\mathrm{d}} = \frac{f_{d1}m_1 + f_{d2}m_2}{m_1+m_2}; \quad (4.18a)$$

$$f_{\mathrm{p}} = \frac{f_{d1}f_{p1}m_1 + f_{d2}f_{p2}m_2 - f_{\mathrm{comp}}(m_1+m_2)}{f_{\mathrm{d}}(m_1+m_2)}. \quad (4.18b)$$

For example, in Eq. (4.18b) the three terms in the numerator denote, respectively, the mass in porous dust of particle 1, the porous dust mass of particle 2, and the porous mass transferred to the compact dust phase. In order to get the relative amount of porous dust this is divided by the new total dust mass (calculated in Eq. (4.18a)) of the compound. If the collision results in a bounce, $f_{\rm d}$ stays the same for both particles and $f_{\rm p}$ is reduced by a factor $1 - f_{\rm geo}$.

Role of fragmentation

As the above formulas for $f_{\rm d}$ and $f_{\rm geo}$ suggest, fragmentation is not included in the collision model. The large number of particles produced by a fragmenting collision is especially problematic in the context of a Monte Carlo program, where the number of particles is limited (see § 4.3). However, the results of Dominik & Tielens (1997) provide insight into the stage at which fragmentation becomes important. They found that the onset of fragmentation starts at $E \simeq 0.3 N_{\rm c} E_{\rm br}$ with catastrophic disruption at energies of $\simeq 10 N_{\rm c} E_{\rm br}$, where $N_{\rm c}$ is the total number of contacts (roughly equal to the number of monomers, N) in an aggregate. Recalling that $E_{\rm br} \sim E_{\rm roll}$ the catastrophic fragmentation limit corresponds to $f_{\rm comp} \sim 8$ in terms of Eq. (4.16). The corresponding curve in Fg. 4.4 then shows that fragmentation becomes important at velocities above a few 10^2 cm s^{-1} (for equal sized particles; as the mass disparity increases the fragmentation velocity increases). The m/s transition for the onset of fragmentation is in agreement with previous studies (Blum & Münch 1993; Blum & Wurm 2000) but compact structures at high filling factor may require more effort to fragment than their fluffy counterparts (D. Paszun 2007, priv. comm.). From Fg. 4.1 the critical velocity can be translated into a Stokes number. We will *a posteriori* check to determine in which models fragmentation is expected to play a dominant role.

4.2.4 Evolution of the internal structure

The aerodynamic properties of the compounds, which determine their coupling to the gas, alter with accretion of dust and mutual collisions between compounds. These properties are quantified in the friction time, $\tau_{\rm f}$ (see Eq. (4.5)), of the particles—essentially a measure of its mass-to-surface area ratio, $m/\pi a^2$. It is an important parameter since lower friction times mean lower relative velocity between the particles (§ 4.2.2), and low relative velocities between compounds, in turn, imply potential to grow large.

Through the adopted three phase model of compounds (§ 4.2.3) the total geometrical volume, $V_{\rm geo}$, defined by a, can be reduced to its three components: (i) chondrule, (ii) compact dust, and (iii) porous dust, *i.e.*,

$$\frac{4\pi}{3} a^3 \equiv V = V_{\rm c} + V_{\rm cd} + V_{\rm pd}. \tag{4.19}$$

In § 4.2.3 the filling factors of the chondrule and compact dust phases have been fixed at 1 and 0.33, respectively, so that V_i for these phases linearly corresponds to the mass inside these phases. However, for the porous dust phase, this does not have to be the case: the dust fluff-balls that are accreted can be of different size and

porosity. Besides, if the compound accretion process itself proceeds fractally, the porous phase becomes a mixture of porous dust and voids created by the hit-and-stick packing of the compounds. This could lead to a much reduced filling factor of the porous phase (see § 4.2.4).

With these issues in mind we discuss the three accretion modes that are at work and outline the implications for the internal structure of dust and compounds. In a largely chronological order these are: (i) dust-dust, (ii) chondrule-dust, and (iii) compound-compound accretion.

Dust-dust aggregation

If the dust distribution initially consists of monomers of size a_0, the number density of dust particles is likely to be much larger than that of chondrules. Therefore, monomers probably form aggregates *before* they are themselves accreted by chondrules or compounds. Provided the collisional energies involved stay below $5E_{\rm roll}$ (see § 4.2.3), the dust aggregates will hit-and-stick, leading to fractal growth (Meakin & Donn 1988; Blum et al. 2000). In addition, if this collision is between similar-size aggregates, the outcome is referred to as CCA. In that case fractal aggregates form with a surface area that grows faster with mass than in the compact case, i.e, $\pi a_{\rm dust}^2 \propto m^\delta$, or, $V \propto m^{3\delta/2}$ with $\delta = 0.95$ (Ossenkopf 1993; Paszun & Dominik 2006) as compared to $V \propto m^{1/3}$ (or $\delta = 2/3$) for compact growth. Using the relation $V = V_0 N^{3\delta/2}$, where V_0 denotes the volume of a single monomer and N the number of monomers the aggregate contains, the filling factor evolves as

$$\phi_{\rm dust} = \frac{NV_0}{V} = \left(\frac{V}{V_0}\right)^{2/3\delta-1} = \left(\frac{a_{\rm dust}}{a_0}\right)^{2/\delta-3} = N^{1-3\delta/2}. \tag{4.20}$$

We consider two mechanisms through which dust aggregates can form: (i) Brownian motion and (ii) differential velocities due to turbulence. For simplicity, equal particle sizes are assumed at all times. The timescales involved are determined by the particle number density ($n_{\rm d}$), size ($a_{\rm dust}$) and relative velocities (Δv) between the particles, *i.e.*,

$$t_{\rm dd} = (n_{\rm d}\sigma\Delta v)^{-1} = \frac{1}{3}\frac{\rho_{\rm d}^{(\rm s)}}{\rho_{\rm d}}\frac{a_{\rm dust}\phi}{\Delta v}, \tag{4.21}$$

in which we have used $n_{\rm d} = \rho_{\rm d}/m$, $\sigma = \pi(a_1 + a_2)^2 = 4\pi a_{\rm dust}^2$ for the collisional cross section, and $m = 4\pi a_{\rm dust}^3 \phi \rho_{\rm d}^{(\rm s)}/3$ for the mass of a dust aggregate, with $\rho_{\rm d}^{(\rm s)}$ the specific material density of the dust. The relative velocities in the case of Brownian motion and turbulence read, respectively,

$$\Delta v^{\rm BM} = \sqrt{\frac{8k_{\rm B}T}{\pi m_\mu}} = \frac{2}{\pi}\sqrt{\frac{3k_{\rm B}T}{\rho_{\rm d}^{(\rm s)}}}a_{\rm dust}^{-3/2}\phi^{-1/2}; \tag{4.22a}$$

$$\Delta v^{\mathrm{T}} = \frac{v_{\mathrm{s}}}{t_{\mathrm{s}}} \frac{\rho_{\mathrm{d}}^{(\mathrm{s})}}{c_{\mathrm{g}} \rho_{\mathrm{g}}} a_{\mathrm{dust}} \phi, \tag{4.22b}$$

If $\tau_{\mathrm{f}} < t_{\mathrm{s}}$, turbulent relative velocities are in fact determined by the spread within their friction times (see § 4.2.2) and a numerical factor of, *e.g.*, 0.1 in front of Eq. (4.22b) can be inserted if the particle distribution is monodisperse. This expression is further reduced by writing $v_{\mathrm{s}}/t_{\mathrm{s}} = \mathrm{Re}^{1/4} \alpha^{1/2} c_{\mathrm{g}} \Omega$. For Brownian motion, the timescale t_{dd} then becomes

$$t_{\mathrm{dd}}^{\mathrm{BM}} = \frac{\pi (\rho_{\mathrm{d}}^{(s)})^{3/2} \mathcal{R}_{\mathrm{gd}}}{6 \rho_{\mathrm{g}} \sqrt{3 k_B T}} \phi^{3/2} a^{5/2} \approx 1.4 \times 10^2 \text{ yr } \rho_{\mathrm{X}}^{-1} \phi^{3/2} \left(\frac{a_{\mathrm{dust}}}{1\ \mu\mathrm{m}} \right)^{5/2}, \tag{4.23a}$$

and for turbulence,

$$t_{\mathrm{dd}}^{\mathrm{T}} \approx \frac{10}{3} \mathcal{R}_{\mathrm{gd}} \mathrm{Re}^{-1/4} \alpha^{-1/2} \Omega^{-1} \approx 6 \times 10^2 \text{ yr } \rho_{\mathrm{X}}^{-1/4} \left(\frac{\alpha}{10^{-4}} \right)^{-3/4}, \tag{4.23b}$$

where the expressions are evaluated for the default parameters of the $R = 3$ AU model (Table 4.1) with $\mathcal{R}_{\mathrm{gd}} = \mathcal{R}_{\mathrm{gc}} \mathcal{R}_{\mathrm{cd}} = 100$ the gas to dust mass ratio, and where the factor of 10 in Eq. (4.23b) follows from the considerations given above. For turbulence the increase in geometrical area due to the fractal growth is exactly canceled by the decreased τ_{f} so that the timescales for turbulence become independent of size and ϕ and growth progresses exponentially; for Brownian motion the growth of aggregates (in mass) is proportional to t^2 (Blum 2004).

Equations (4.23a) and (4.23b) show that aggregate formation is initiated by Brownian motion. Turbulence can take over at high α but the dust is then also quickly swept up by chondrules. At high gas densities aggregates can grow large.

Dust-chondrule/compound accretion

The size of the dust aggregates at which they are accreted by chondrules/compounds (a_{dust}) depends on the dust-chondrule accretion time t_{dc} in relation to t_{dd}. The timescale, t_{dc}, for a dust particle to encounter a chondrule of size a_{c}, is

$$t_{\mathrm{dc}} = \frac{1}{n_{\mathrm{c}} \pi a_{\mathrm{c}}^2 \Delta v} = \frac{4 \rho_{\mathrm{c}}^{(s)} a_{\mathrm{c}}}{3 \rho_{\mathrm{c}} \Delta v} = \frac{4 \mathcal{R}_{\mathrm{gc}}}{3 \mathrm{Re}^{1/4} \alpha^{1/2} \Omega} \approx 240 \text{ yr } \rho_{\mathrm{X}}^{-1/4} \left(\frac{\alpha}{10^{-4}} \right)^{-3/4}, \tag{4.24}$$

where a monodisperse distribution of chondrules that dominates the cross section ($a_{\mathrm{c}} \gg a_{\mathrm{dust}}$) and the velocity field is assumed, and $\mathcal{R}_{\mathrm{gc}} = 100$. Equation (4.24) again assumes the relation $\Delta v \sim v_{\mathrm{s}} \tau_{\mathrm{c}}/t_{\mathrm{s}}$, although chondrules might also fall in the square-root part of the velocity regime (§ 4.2.2). Equations (4.23b) and (4.24) show that in turbulence the dust is preferentially swept up by chondrules. On the other hand, in Brownian motion, velocities are always determined by the smallest particle (the dust); the grains therefore simply collide with particles that dominate the total cross-section. Thus, if turbulence dominates the velocity field for the grains and $\mathcal{R}_{\mathrm{cd}} \sim 1$, chondrules will sweep up the dust before significant aggregation takes place and $a_{\mathrm{dust}} \sim a_0$; contrarily, if Brownian motion dominates (or when $\tau_{\mathrm{c}} \gg t_{\mathrm{s}}$),

the monomers will first collide with each other before being accreted by chondrules.

The question that remains is what this means for the porosity of the rim. Assuming a hit-and-stick process, in which the accreting dust particles are all of equal size and much smaller than the chondrule/compound, the structure of the rim will resemble that of PCA. Thus, if the dust particles are solid monomers the filling factor of the rim indeed equals $\phi_{\rm PCA}$. On the other hand, if the accreting dust particles are fluffy aggregates, but still smaller than the chondrule, the resulting filling factor of the rim will be less than $\phi_{\rm PCA}$. The precise filling factor will be determined by the amount of interlocking between the aggregates but as a crude upper limit the aggregated may be approximated as a homogeneous porous sphere such that the packing process of the dust aggregates is PCA. Then, the filling factor of the porous dust, $\phi_{\rm pd}$, is just the product of $\phi_{\rm PCA}$ (caused by hit-and-stick packing) and the porosity the dust aggregates already contain ($\phi_{\rm dust}$), *i.e.*, $\phi_{\rm pd} = \phi_{\rm PCA}\phi_{\rm dust}$.

In yet another collisional growth scenario we envision that chondrules are mixed into a dust region *after* this dust has aggregated into dust balls but *before* the dust balls are compacted (Ormel et al. 2007). In any case we assume here that the dust consists of porous aggregates and parameterize its filling factor by the $\phi_{\rm pd} = \phi_{\rm PCA}\phi_{\rm dust}$ relation. Using Eq. (4.20), $a_{\rm dust}$ is the parameter that regulates the fluffiness of the dust accretion process and we run models at different values of $a_{\rm dust}$ to test its importance and sensitivity.

Compound-compound accretion

The timescale for chondrule-chondrule accretion, $t_{\rm cc}$, is similar to the dust-chondrule timescale, Eq. (4.24). During the collision, a fraction of the porous dust is lost to the compact dust phase. Since the porous phase filling factor is always less than that of the compact phase there is always a net loss in geometrical volume when two compounds collides, *i.e.*, $V < V_1 + V_2$. This, we call the 'conservative approach' (no fractal accretion of compounds). Alternatively, collisions of compounds (consisting of one or more dust-rimmed chondrules) may be in the hit-and-stick regime. This would occur if the impact energy is absorbed locally and is not communicated to other parts of the compound. In that case the compound packing proceeds fractally. Ormel et al. (2007) provide an expression for the growth of V in the hit-and-stick case for particles of different size, derived by an interpolation from the PCA and CCA limiting cases, *i.e.*,

$$V = V_1 \left(1 + \frac{V_2}{V_1}\right)^{\frac{3}{2}\delta}, \tag{4.25}$$

where V_1 is the volume of the largest of the two particles that meet and $\delta \simeq 0.95$. The growth of the porous phase $V_{\rm pd}$ then results from the gain in V through Eq. (4.19). The porous phase is then a mixture of porous dust and voids and the geometrical volume becomes a balance between hit-and-stick packing of chondrules (increasing V) and compaction of porous dust (decreasing V). This, contrary to the conservative approach in which the total volume always decreases at collision.

For example, if $V_2 = \frac{1}{10}V_1$, Eq. (4.25) shows a volume $0.045V_1$ is added to the

porous phase, decreasing its filling factor. It then depends on $f_{\rm comp}$ how the net growth of the porous phase turns out. In the initial stages of coagulation $f_{\rm comp}$ is often very low and, therefore, fractal accretion of compounds can become very important in enhancing the geometrical volume of the compounds.

Although fractal accretion of compounds increases the volume of the porous phase, no mass is transferred to it. It is only the filling factor that is affected, in its turn affecting the aerodynamic properties of the compound. Eventually, due to compaction, all models run out of porous dust and the dust inside the final objects—whether fractal accretion is involved or not—has the same filling factor $\phi_{\rm cd} = 0.33$. The lower filling factor of the porous phase during the collision process merely reflects the voids between the chondrules that are created in the models with fractal accretion. As velocities increase, however, the fractal structure must collapse. We suspect, furthermore, that structures of very low filling factor are too weak to survive the more violent collisions (see, *e.g.,* Paraskov et al. 2007).

4.2.5 Collisional scenario

We have proposed a model where chondrules—in the presence of dust particles—acquire rims of fine-grained dust, which help them stick together, and discussed various collisional scenarios for this growth process. Here we briefly summarize the envisioned scenario from a chronological viewpoint, and emphasize the (free) parameters the model contains.

At the start of our simulation ($t = 0$) a population of chondrules encounters a reservoir of dust particles of characteristic size $a_{\rm dust}$ (see § 4.2.4). The physical conditions of the disk (*e.g.,* gas density ρ_X, turbulent strength α; see § 4.2.2) determine the relative velocities between the chondrules/compounds. Another important parameter is the spatial density of dust ($\rho_{\rm d}$) or, rather, the dust to chondrule density ratio, $\mathcal{R}_{\rm cd}$, since this determines the thickness of the rims. These, and other physical conditions at the start of the simulation determine the subsequent accretion process. First, chondrules start to accrete the dust aggregates (see § 4.2.4), resulting in a porous rim of filling factor, $\phi_{\rm pd}$. When rimmed chondrules collide, part of this porous structure collapses to $\phi_{\rm cd} = 0.33$ filling factor through the initiation of rolling motions. This dissipates the collisional energy and, if enough porous dust is present by the criterion of Eq. (4.16), the two chondrules stick and a compound is created. In this way compounds are created and many chondrules can be stuck together until the accretion process is terminated when both the amount of free-floating dust and the porous dust inside the compounds have become insignificant. The end product is an inert population of compact-dust rimmed chondrules and compounds that only bounces. Collisional fragmentation is not explicitly included in the model, but we can *a posteriori* compare the velocities with a critical threshold ($\sim$m s^{-1}) to verify its importance.

4.3 Monte Carlo coagulation

The physical model of chondrule accretion contains many free (*i.e.,* unknown) parameters. In a statistical study of compound coagulation, we will sample these free

parameters at discrete intervals such that a grid of models is created (see § 4.4). In this section we briefly describe the Monte Carlo coagulation code used to calculate the collisional evolution of the compounds.

Compounds are characterized by four numbers—*e.g.*, m, f_d and f_p to determine the mass inside each phase, and ϕ_pd for the filling factor of the porous phase. Therefore, a Monte Carlo code, rather than the multi-variate Smoluchowski equation, is the obvious way to solve the collisional evolution. In our code we do not keep track of the individual positions of each constituent unit (the monomers) within a compound as in *e.g.,* Kempf et al. (1999) but identify each compound by these four numbers. In this way we have a good characterization of the internal structure of the compound, although the precise internal structure cannot be retrieved.

The code we use is called *event driven*; *i.e.,* the timestep Δt defines the time between two consecutive events (Gillespie 1975; Spouge 1985; Liffman 1991). Here, events are collisions between two compounds (see below for the dust). The collision rate C_{ij} gives the probability of a collision—$C_{ij}\Delta t$ is the probability of collision in the next (infinitesimal) timestep Δt involving compounds i and j, *i.e.,*

$$C_{ij} = \frac{\sigma_{ij}\Delta v_{ij}}{\mathcal{V}}; \quad \text{and} \quad C_\mathrm{tot} = \sum_i^N \sum_{j>i}^N C_{ij}, \tag{4.26}$$

in which σ_{ij} is the collision cross section[6] between particles i and j, Δv_{ij} the relative velocity between the two compounds, and N the total number of particles in the simulation. The volume of the simulation, $\mathcal{V}$, is determined from the spatial density in chondrules, the constant ρ_c, and the total mass in chondrules, *i.e.,* $\mathcal{V} = \sum_{i=1}^N m_i(1 - f_{\mathrm{d},i})/\rho_\mathrm{c}$. From these quantities the timestep is defined by $\Delta t = -C_\mathrm{tot}^{-1} \ln \bar{r}$, with $\bar{r}$ a random deviate. The particles that are involved in the collisions are also determined randomly, weighted by their collision rates C_{ij}. Then, using the recipes outlined in § 4.2, the outcome of the collision—sticking or bouncing—is determined. In either case, the parameters of the new or modified compounds are re-computed. (In the case of bouncing the change is reflected in a smaller size, a, due to the compaction.) Subsequently, the new collision rates of the particles (*i.e.,* the $\{C_{ik}\}$ and, if the second particle due to bouncing is still present, the $\{C_{jk}\}$ for $k = 1 \ldots N$ and $k \neq i, j$) are re-computed. These updates of the collision rates are the most CPU-intensive part of the code. With it one cycle is completed, after which a new stepsize Δt is determined and the steps repeat themselves.

Equation (4.26) involves the total relative velocity between the particles. To calculate Δv_{ij} we use thermal, turbulent and systematic velocities (Eqs. (4.4), (4.8) and (4.10)), adding them up in quadrature. Strictly speaking, the zero-dimensional nature of the MC-model is inconsistent with dispersal of particles (particles do not have a positions); however, when the drift is modest the change in the physical environment is negligible and we can still use the MC-approach. For the radial drift this

[6] In general one must distinguish between the collisional cross section (which gives the reaction rate of the two species) and the geometrical cross section (which is the average projected area of the particle that determines the coupling to the gas). Here we will simply equate them as in $\sigma_{ij} = \pi(a_i + a_j)^2$ and ignore the small discrepancy (see Krause & Blum 2004).

assumption applies only when the total drift is small compared to the initial location of the particle, *i.e.*, $\Delta R \ll R$, such that the same physical conditions apply throughout the simulation. We will *a posteriori* check whether radial drift is significant.

Apart from collisions between compounds, we also keep track of dust accretion. This is, however, not implemented in a Monte Carlo fashion: it would have made the code very slow since the tiny dust particles far outnumber the chondrules. Instead, we catalogue the cumulative dust mass that is accreted by the compounds over the timesteps; *i.e.*, for compound i we increase the amount by $\pi a_i^2 \Delta v_{i\mathrm{d}} \rho_{\mathrm{d}}(t) \Delta t$. Only when this mass exceeds a certain fraction (say $f_{\mathrm{upd}} = 10^{-3}$) of the total mass of the compound, this quantity is added as porous dust to the compound and the $f_{\mathrm{d}}, f_{\mathrm{p}}$ parameters as well as the collision rates are updated (Eq. (4.26)). Although this procedure makes the program still a bit slow at the initial stage of the simulation, it is definitely much faster than updating all $\frac{1}{2}N(N-1)$ collision rates at *every* timestep. The (decreasing) amount of free-floating dust, $\rho_{\mathrm{d}}(t)$, is computed in this way. We have examined the sensitivity of this mechanism on f_{upd} and found that $f_{\mathrm{upd}} = 10^{-3}$ is accurate, while much more efficient (faster) than, *e.g.*, 10^{-5}.

The strong point of the MC code is that it can deal with many structural parameters and that it is transparent and straightforward; the weak point, however, is its low numerical resolution. Given the complexity of the model and the large number of models we intend to run, the number of particles (N) we use in the simulations is a few thousands at most. To prevent the resolution from deteriorating (a collision resulting in sticking decreases N by one) we artificially stabilize the total particle number by a procedure called *duplication*. In this process, one particle is randomly chosen and duplicated from the existing population (Smith & Matsoukas 1998). Subsequently, $\mathcal{V}$ is increased proportionately such that the total density in chondrules, ρ_{c}, stays constant. This procedure is called the constant-N algorithm—an algorithm far superior in terms of accuracy to the constant $\mathcal{V}$ algorithm (Smith & Matsoukas 1998), and we have previously shown that it is able to calculate large orders of growth, especially when the size distribution is narrow (Ormel et al. 2007). Through the duplication mechanism, furthermore, a distinction can be made between 'duplicates' and 'distinct species,' and it is actually the latter that we keep constant, such that the total number of compounds involved can be much larger than a few thousands, also improving the efficiency of the model.

4.4 Results

In our models we generally recognize three stages in the growth process: hit-and-stick dust accretion (increasing the porosity), compound accretion (*i.e.*, growth), and compaction with accompanied stalling of the growth. The balance between these phases controls the size of the resulting compounds, while their relative importance and 'timing' are determined by the adopted model parameters. In § 4.4.1 we discuss two illustrative cases, focusing on the temporal stages during their evolution. Then, in § 4.4.2 we investigate the sensitivity of the other parameters by means of a parameter study.

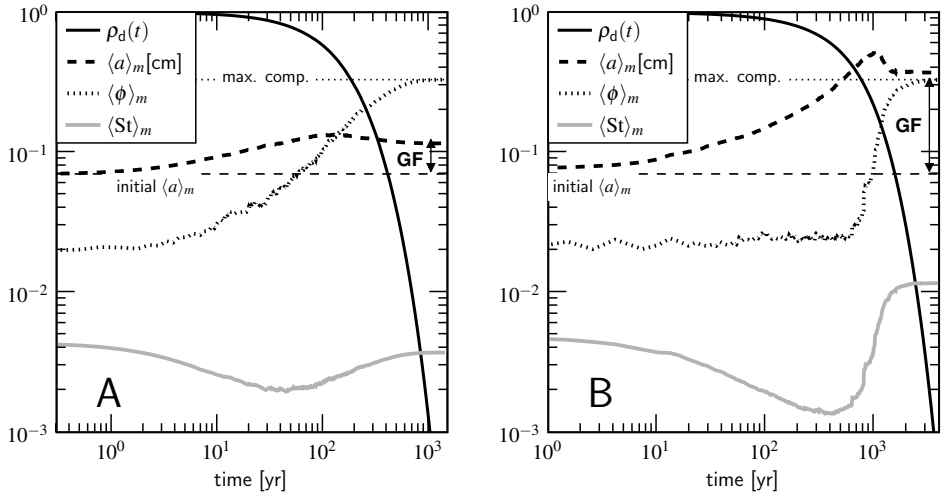

Fig. 4.6: *(a)* A run of the compound accretion model with $\alpha = 10^{-4}$, $\rho_X = 1$, $a_{\rm dust} = 10$ μm, $\gamma = 19$ erg cm^{-2}, $R = 3$ AU, $\mathcal{R}_{\rm gc} = 100$ and $\mathcal{R}_{\rm cd} = 1$ (the default model). Plotted as function of time are: the normalized density of free floating dust (*solid black curve*; the initial dust density is $\rho_{\rm dust}(t = 0) = 2.4 \times 10^{-13}$ g cm^{-3}); the mass-averaged size of the population (dashed-line); the mass-averaged filling factor of the dust within the compounds (*dotted curve*); and the mass-averaged Stokes number of the population (*solid grey curve*). Shown is also the definition of the growth factor, *GF*. All quantities share the same *y*-axis. *(b)* Like *(a)* but with $\alpha = 10^{-6}$.

4.4.1 Individual model runs

Figures 4.6 and 4.7 show detailed results for two individual runs of the simulation with (default) parameters of gas density $\rho_X = 1$, $a_{\rm dust} = 10$ μm, $\mathcal{R}_{\rm gc} = 100$ and $\mathcal{R}_{\rm cd} = 1$, $\gamma = 19$ erg cm^{-2} at a distance of 3 AU (see Table 4.1). In these figures panels A correspond to a model with $\alpha = 10^{-4}$, while $\alpha = 10^{-6}$ in panels B. In Fg. 4.6 several (mass-averaged) quantities are shown as function of time, while in Fg. 4.7 the size distributions of compounds are shown at three points during their evolution: (i) $t = 0$ (the initial size distribution of chondrules); (ii) the time at which 50% of the dust is accreted; and (iii) the time at which a negligible amount of porous dust remains (the final distribution). The negligible criterion is met when both the *porous* dust mass within all compounds as well as the density of free-floating dust are less than 0.1% of the initial dust mass.

In Fg. 4.6 we make use of mass-weighted averages. For example, the mass-weighted average size of the population is defined as

$$\langle a\rangle_m = \frac{\sum_i m_i a_i}{\sum_i m_i}, \tag{4.27}$$

where the summation is over all particles of the simulation. It gives the mean size in which most of the mass of the population resides, and is more appropriate to de-

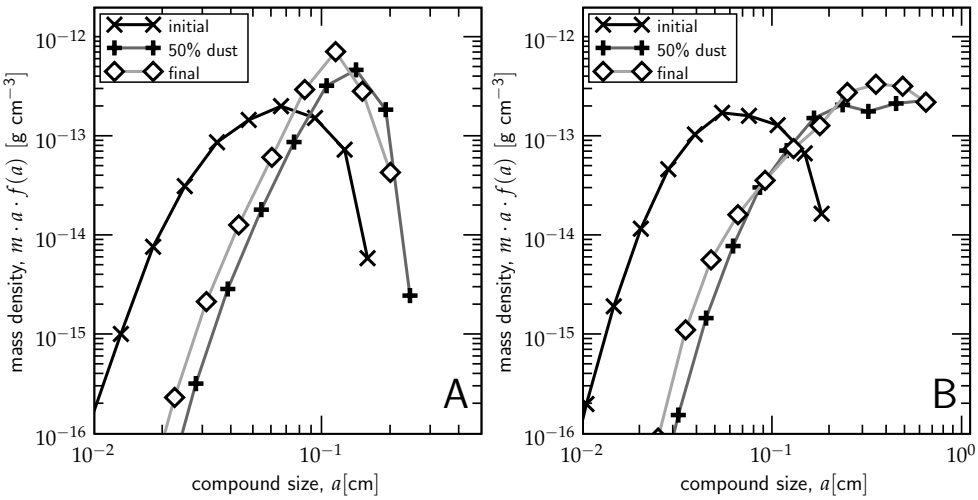

Fig. 4.7: Size distributions of compounds corresponding to the runs in Fig. 4.6 for the $\alpha = 10^{-4}$ model *(a)* and the $\alpha = 10^{-6}$ model *(b)*. Shown are the initial distribution (*crosses*), the distribution at the time where 50% of the dust has been accreted (*plus-signs*) and the final distribution (*diamonds*). Note that compaction has the effect of shifting the distribution to the left.

scribe the population than the average size, $\langle a \rangle$. In particular, adding a large number of small particles with negligible mass (density) to the population, decreases $\langle a \rangle$ but leaves $\langle a \rangle_m$ unaffected. In the following the prefix 'mw-' is used as an abbreviation for 'mass-weighted average of the distribution.'

Figure 4.6a shows that dust is accreted on timescales of a few 10^2 yr, which agrees well with previous studies (Cuzzi 2004). This causes the size distribution (Fg. 4.7) to shift towards larger sizes: the accretion of porous dust particles at low filling factor significantly increases the geometrical size of the compounds. The dotted curve in Fg. 4.6a shows the mw-filling factor of the accreted dust. At the start of the simulation this equals $\phi_{\rm pd} = \phi_{\rm dust}\phi_{\rm PCA}$; however, collisions are energetic enough to compact the porous dust on a global scale. The decrease in friction time (solid grey curve), caused by the accretion of porous dust, therefore is only modest. (Note that even accretion of $\phi = \phi_{\rm cd} = 33\%$ dust on chondrules would cause the friction time to decrease). Consequently, the sticking rate never increases much beyond $\sim$50%. After $\sim 10^2$ yr the accretion of porous dust cannot keep pace with the compaction and sticking fails, resulting in a decrease of the compounds geometrical size (dashed curve). This results in a 'retrograde motion' of the final size distribution curve in Fg. 4.7a. In the $\alpha = 10^{-6}$ model (Fg. 4.6b) the collision velocities are much lower and, different from the $\alpha = 10^{-4}$ model, the porous dust does not experience compaction for a long time. The sticking rate then increases to almost 100%. However, depletion of dust triggers the end of the growth phase; growth is quickly terminated by the mutually enforcing processes of rim compaction and increasing velocities. From these panels it is clear that much growth can be achieved when relative velocities are

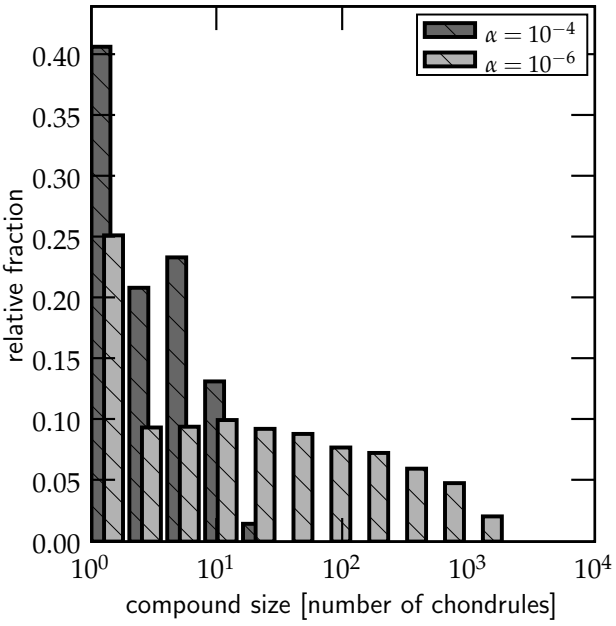

Fg. 4.8: Relative fraction of dust accreted by compounds of different size for the $\alpha = 10^{-4}$ and $\alpha = 10^{-6}$ simulations. The compounds are placed in bins according to the number of chondrules they contain. The bins are exponentially distributed by factors of two. The histogram shows the distribution of the dust over the compound sizes (in terms of number of chondrules inside the compound) at the time of the dust accretion. Single chondrules (first bin) accrete a significant fraction of the dust.

kept low during the dust and chondrule accretion.

Although the Monte Carlo code does not keep track of the position or size distribution of chondrules within compounds, we can still extract useful statistical information from the model runs. One such statistic is the distribution of the dust over compounds of different size: is the dust primarily accreted by individual chondrules or by large compounds containing many chondrules? The results are presented in the histogram of Fg. 4.8. The $x-$axis denotes the number of chondrules a compound contains (N) and is divided into logarithmic bins of base 2, *i.e.,* the first bin corresponds to single-chondrule compounds, the second to compounds that contain 2 or 3 chondrules, the third to $4-7$ chondrules, etc. The $y-$axis gives the relative fraction of the dust that first accretes onto a chondrule or compound with size in each bin; that is, Fg. 4.8 only reflects the dust accretion history and does not include the subsequent re-distribution of dust due to coalescence of compounds (which would shift the dust-rimmed chondrules to a larger compound bin). The relatively high level of the first bin (single-chondrule compounds) reflects dust accretion during the early phase of the simulation where individual chondrules provide a high surface area and the density of free-floating dust is highest. In simulations with strong turbulence this fraction becomes very high: the dust is then accreted by single chondrules only. But even in the case of low α single chondrules are responsible for a significant share of the dust sweep-up, as the $\alpha = 10^{-6}$ results show. Besides, larger compounds also have a larger surface to spread this dust over; rims created by dust accretion are therefore thickest on chondrules.

FREE MODEL PARAMETERS

(1)	(2)	(3)	(4)	(5)
turbulent strength	α		5	$[10^{-7}—10^{-3}]$
size of dust aggregates	$a_{\rm dust}$	cm	3	$[10^{-4}—10^{-2}]$
gas density[a]	ρ_X	g cm^{-3}	3	[1—100]
nebula location	R	AU	3	[1, 3, 10]
gas-chondrule ratio	$\mathcal{R}_{\rm gc}$		2	[10, 100]
chondrule-dust ratio	$\mathcal{R}_{\rm cd}$		2	[1, 10]
dust composition[b]	γ	ergs cm^{-2}	2	[19, 370]
compaction mode[c]	$f_{\rm geo}$		2	[X, 1]
fractal accretion of compounds[d]			2	[yes, no]

Table 4.4: List of free model parameters. Columns denote: (1) parameter description; (2) symbol; (3) unit; (4) number of grid points per parameter; (5) parameter range, with a grid point at every factor of 10, unless otherwise indicated. See also Table 4.1 for other (fixed) parameters. *Notes.* [a]Gas density over MMSN model at 3 AU. [b]Energy surface density, γ. The high γ model corresponds to ice as the sticking agent (10 AU models only). [c]$f_{\rm geo} = {}'{\rm X}'$: $f_{\rm geo}$ is computed after the procedure outlined in § 4.2.3; $f_{\rm geo} = 1$: use $f_{\rm geo} = 1$ always. [d]Whether a hit-and-stick packing model for compounds (leading to a fractal structure, § 4.2.4) is adopted or not.

4.4.2 Parameter study

Figure 4.9 presents the results of the parameter study. The free parameters (Table 4.4) are distributed over a grid such that each grid point corresponds to a unique model. In total a few thousand distinct models are run. Each model is run a few times to account for stochastic effects in their results (typically ∼10% or so). For each free parameter the models are ordered by the grid-values of the parameter, corresponding to the panels in Fg. 4.9. Two output values are shown: the ratio of final mw-radius to initial mw-radius, or growth factor (crosses) and the time at which the dust is depleted and the simulation terminated, or simulation time (diamonds) (they share the same y-axis; for clarity the timescale error-bars are slightly offset in the x-direction). The symbols denote the logarithmic averages of all models at the grid-values and the error bars indicate the range in which 50% of the models fall. This spread can be huge since it is primarily determined by the spread in the other parameters (and therefore nowhere close to Gaussian). The same holds for the averages: these can be arbitrarily scaled up or down by giving more weight to extreme models in the parameter study.

However, the value of Fg. 4.9 lies not in its absolute numbers but in the trends that emerge from the parameter variation. The lines indicate this trend and their slopes are given in each panel. From these, it is seen that timescales are primarily determined by turbulent α (velocities), nebula location R (densities) and the chondrule density (Fg. 4.9e). Parameters that favor large growth of compounds are low α (Fg. 4.9a), high gas densities (Fg. 4.9c), low chondrule-to-dust ratios (Fg. 4.9f), and high surface energy densities (Fg. 4.9g). Growth is favored in these models due to the moderate relative velocities (Fg. 4.9a,c) or better sticking capabilities (Fg. 4.9f,g). Other parameters are sometimes surprisingly irrelevant. For example, the depen-

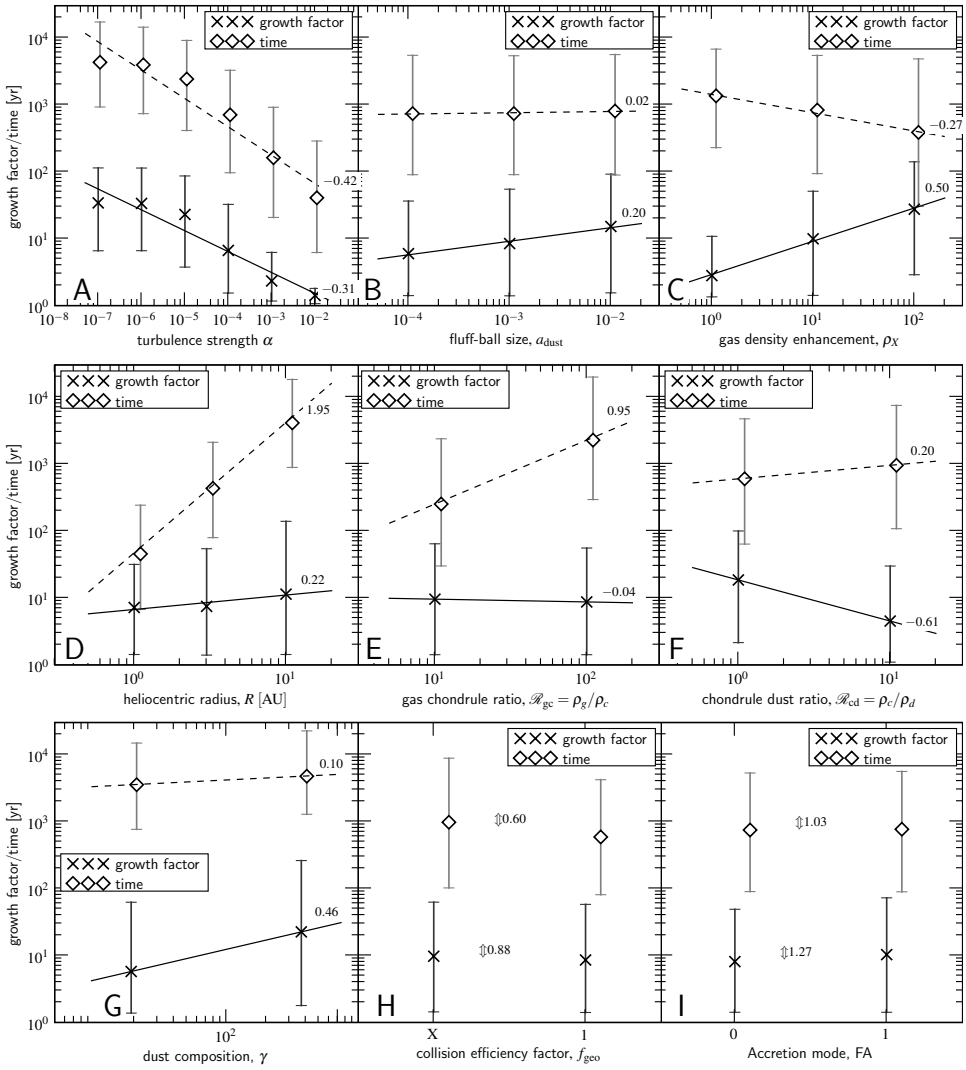

Fig. 4.9: Results of the parameter study. Each panel sorts the data according to a free parameter (x-axis), from which the logarithmic mean and variance are calculated. Two output values are shown on the same y-axis: growth factor (*crosses*) and simulation time (*diamonds*). The lines show the trend in variation of the parameter and the 'best-fit' power-law exponent is given. *(g)* Data from $R = 10$ AU models only, comparing silicate dust ($\gamma = 19$ erg cm^{-2}) with ice ($\gamma = 370$ erg cm^{-2}). *(h)* $f_{\rm geo} = \mathrm{X}$ indicates $f_{\rm geo}$ is a free parameter calculated after Eq. (4.17), while $f_{\rm geo} = 1$ indicates it is 1 always. *(i)* 0 and 1 denote, respectively, that fractal accretion of compounds is turned off or on. In these latter two panels the numerical factor next to the ⇕ gives the ratio in growth factor and timescale between the two modes (not the power-law exponent).

dence on the size of the dust fluff-balls, $a_{\rm dust}$, defining their porosity (Eq. (4.20)), is only modest (Fg. 4.9b), and also the latter two panels do not show clear trends. Figure 4.9h,i directly give the ratio between the two data points, instead of the exponent of the power-law fit. Figure 4.9h shows the effects of taking the geometry of the collision into account. Here, $f_{\rm geo} = {\rm X}$ where $0 < {\rm X} \leq 1$ means that $f_{\rm geo}$ is determined by the geometry of the collision as discussed in § 4.2.3, whereas $f_{\rm geo} = 1$ indicates that all dust is available for compaction. However, allowing for a lower $f_{\rm geo}$ also reduces the maximum amount of dust that is compacted. Apparently, these two effects largely compensate. A similar insensitivity is shown in Fg. 4.9i: whether we allow for fractal accretion of compounds ('1') or not ('0') does not, on average, make a difference. Note, however, that the values shown in the panels are averages; in some individual simulations we do see a notable increase when fractal accretion is turned on. Figure 4.9a shows that the positive correlation between growth factor and decreasing α breaks down for values below $\alpha < 10^{-5}$: the growth flattens out and reaches a constant level. The reason is that for low values of α, and, subsequently, large compounds, radial drift motions quickly take over from turbulent motions such that the evolution becomes insensitive to α. The high radial drift obtained when particles approach the ${\rm St} = 1$ regime forms a barrier for further growth. Low α combined with high gas densities delay this transition since compounds are now much better coupled to the gas (lower Stokes numbers) meaning much growth early on. Yet, Stokes numbers inevitably grow to values near unity, and in most cases the resulting $\eta v_{\rm K}$ drift velocities (Eq. (4.8)) stall growth below 1 meter.

Figure 4.9d shows that growth depends only modestly on nebula radius, R. Here, the positive correlation with growth factor is a bias resulting from the high γ 'ice models' (Fg. 4.9g) — ice promotes sticking — that are only present at $R = 10$ AU. Thus, despite the fact that almost all nebula parameters scale with R, their combined effect does not result in a clear trend that favors growth. For example, larger nebula radii mean lower densities and higher Stokes number, increasing the velocity in the initial stages, but this is offset by a (slightly) lower sound speed, and the better sticking agents that are available.

In Fg. 4.10 all models are combined in a scatter plot of total (mass-weighted) radial drift against the final mw-size obtained in the simulation. The few models that cluster around the meter size are all ice models ($\gamma = 370$ and $R = 10$ AU, indicated by triangles). Some of them do manage to cross the $\langle {\rm St} \rangle_m = 1$ barrier (at 10 AU and $\rho_X = 1$ this already happens at a few centimeters) but do not make the jump to planetesimal sizes. In models that during their growth drift less than $\Delta R \sim R$ the local assumption is justified; for models that drift over several AU-distances, however, the approximation we used in the calculation of the collisional evolution, *i.e.*, that the physical conditions stay the same, breaks down. Note, however, that the drift distances in Fg. 4.10 are upper limits: radial drift slows down with decreasing R due to a better coupling to the gas, or may diminish when collective effects become important (see § 4.5.1).

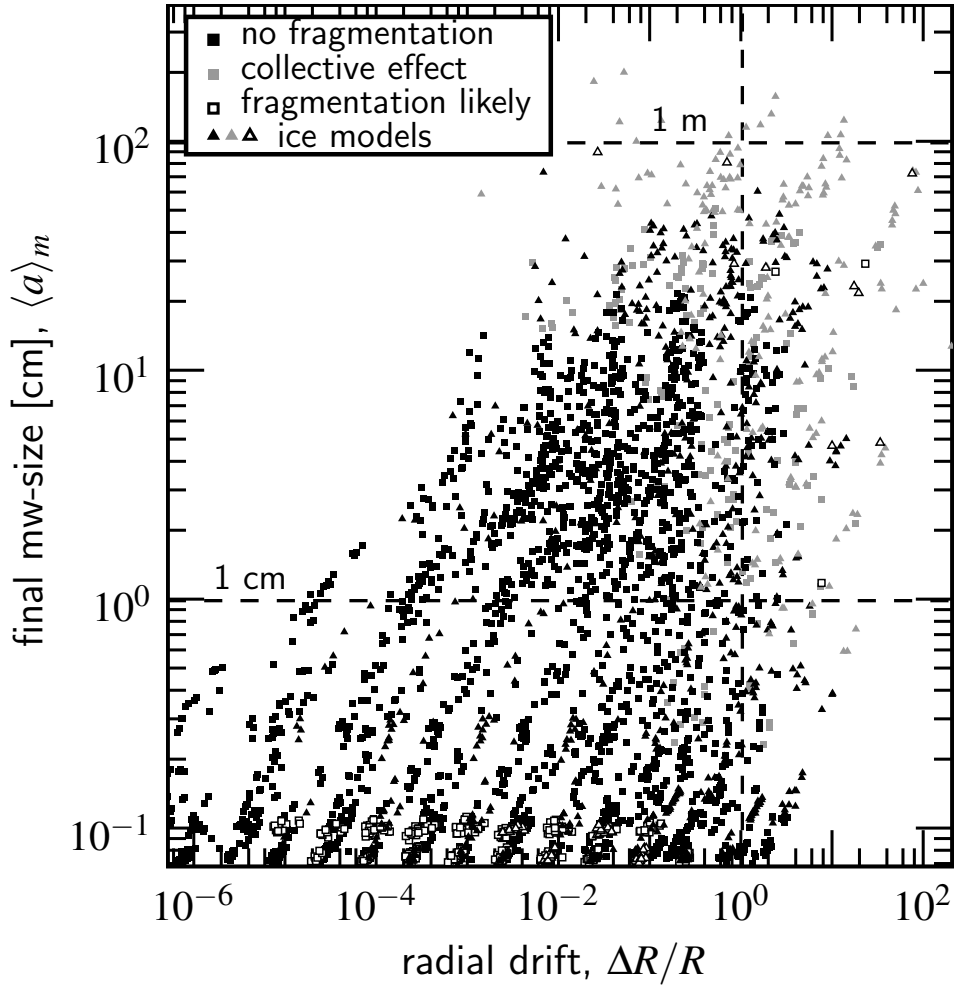

Fig. 4.10: Scatter plot of the fractional inward radial drift covered during the aggregation process ($\Delta R/R$, x-axis) against the final mass-averaged size of the compounds ($\langle a \rangle_m$, y-axis). The results of all model runs are shown. Models are separated into the low-velocity regime ($\Delta v \lesssim 10^2$ cm s^{-1}, *black squares*) and the high velocity regime ($\Delta v \gtrsim 10^2$ cm s^{-1}, *open squares*). *Triangles* denote 'ice models' ($\gamma = 370$ at $R = 10$ AU). In the models shown by grey squares (or triangles) the collective effect could have prevented high drift velocities but this is not incorporated in the present models. The *vertical dashed line* corresponds to a drift of 1 AU. The *dashed horizontal lines* indicate compound sizes of 1 cm and 1 m, respectively.

4.4.3 Importance of fragmentation

The models neglect the possibility that high velocity collisions will fragment, rather than merely compact or bounce, compounds. In § 4.2.3 it was estimated that at $\sim$m s^{-1} velocities, fragmentation becomes likely, starting with erosion, followed

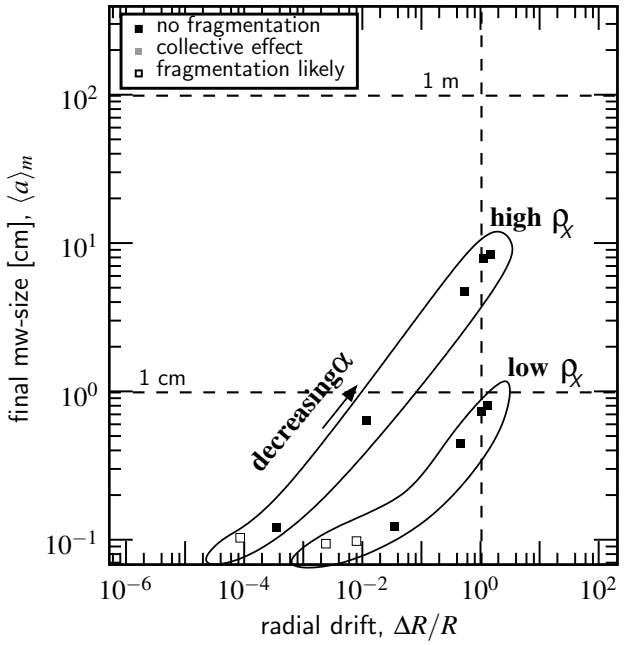

Fig. 4.11: A selection of 12 models from the scatter plot of Fg. 4.10, indicating systematic trends. Compared to Fg. 4.10 results are limited to: $a_{\rm dust} = 10^{-3}$, $\rho_X = 1$ or 10, $\mathcal{R}_{\rm gd} = 100$, $\mathcal{R}_{\rm cd} = 1$, $R = 3$ AU, $f_{\rm geo} = {\rm X}$ (local compaction), and no fractal accretion of compounds. See Table 4.5 for quantitative results.

by catastrophic disruption of the compound. This threshold can now be compared to the maximum velocities attained at a particular Stokes number (see Fg. 4.1), *i.e.*, $\sim\eta^{1/2}c_{\rm g}{\rm St}$ and $\sim\alpha^{1/2}c_{\rm g}{\rm St}^{1/2}$ for the systematic drift and turbulent velocities, respectively. Inserting the final mw-Stokes number into these expressions, we obtain a criterion that tells us whether fragmentation is of importance. As the critical velocities we take 2 m s^{-1} for turbulence and 6 m s^{-1} for radial drift (see Fg. 4.4). It can be shown that for systematic velocities scaling proportional to size the collisional energy peaks at size ratios of $\epsilon \sim 0.5$, which, according to Fg. 4.4, corresponds to a fragmentation velocity of $\sim$3 m s^{-1}, or a $\sim$6 m s^{-1} radial drift velocity for the largest particle. For ice models (triangles) the fragmentation threshold is increased by another factor of four, reflecting their higher γ. In Fg. 4.10 the models that have crossed the threshold velocity are indicated by an open square, whereas black squares indicate velocities that stay below the threshold. The grey squares are models in which collective effects could have had a significant reduction in relative velocities and drift rates, due to concentration of compounds near the midplane (see below, § 4.5.1). However, these subtleties are presently *not* taken into account in the simulation and it remains unclear whether fragmentation is an important phenomenon in models for which settling is important.

For most models in Fg. 4.10 fragmentation is not a serious concern. This is a natural result as compaction precedes fragmentation and growth stalls before reaching the fragmentation threshold. However, for large, fluffy compounds the compaction is more pronounced, resulting in a significant decrease in surface area-to-mass ratio, increasing the Stokes, and thereby possibly breaching the threshold for fragmenta-

DETAILED RESULTS

α	ρ_X	$\langle a \rangle_m$ [cm]	$\langle \mathrm{St} \rangle_m$	$\rho_\mathrm{p}/\rho_g^\mathrm{mid}$	Δv^turb [cm s^{-1}]	Δv^sys [cm s^{-1}]	$\Delta v^\mathrm{sys,CE}$ [cm s^{-1}]
(1)	(2)	(3)	(4)	(5)	(6)	(7)	(8)
10^{-7}	10	8.5	2.6×10^{-2}	4.9	5.9	358.6	10.3
10^{-6}	10	8.0	2.5×10^{-2}	1.5	18.0	336.9	54.6
10^{-5}	10	4.8	1.5×10^{-2}	0.4	44.3	204.4	108.2
10^{-7}	1	0.8	2.5×10^{-2}	4.8	5.8	345.0	10.2
10^{-6}	1	0.7	2.3×10^{-2}	1.4	17.4	316.7	53.4
10^{-4}	10	0.6	2.0×10^{-3}	0.0	51.2	27.4	25.1
10^{-5}	1	0.5	1.4×10^{-2}	0.4	42.8	190.9	103.8
10^{-3}	10	0.1	3.9×10^{-4}	0.0	71.4	5.3	5.2
10^{-4}	1	0.1	4.0×10^{-3}	0.1	71.9	53.9	47.9
10^{-3}	1	0.1	3.3×10^{-3}	0.0	206.7	44.5	42.8
10^{-2}	1	0.1	3.2×10^{-3}	0.0	641.7	42.9	42.0
10^{-2}	10	0.1	3.5×10^{-4}	0.0	212.3	4.7	4.6

Table 4.5: Detailed results from 12 selected models (see text), ordered after final mw-size, col. (3). The columns denote: (1) turbulent-α; (2) gas-density enhancement (restricted to 1 or 10); (3) final mw-size; (4) final mw-Stokes number; (5) final midplane dust-gas density ratio would settling have been included; (6) turbulent velocity contribution, $\alpha^{1/2}\mathrm{St}^{1/2}c_\mathrm{g}$; (7) systematic drift after Eq. (4.8); (8) systematic drift due to collective effects after Eq. (4.28) with col. (4) for St.

tion. Also note the fragmentation models (open symbols) at the bottom of Fg. 4.10: in these the fragmentation threshold was already exceeded at the start of the simulation.

Figure 4.11 shows a small subset of models from Fg. 4.10 that takes away the redundancy (caused by less influential parameters) and focuses on the more plausible scenarios. More specifically, Fg. 4.11 shows models limited to the following parameters: $\mathcal{R}_\mathrm{gc} = 100$, $\mathcal{R}_\mathrm{cd} = 1.0$, $a_\mathrm{dust} = 10^{-3}$ cm, $\rho_X = 1$ or 10, $R = 3$ AU, $\gamma = 19$ erg cm^{-2}; furthermore, we assume only local compaction ($f_\mathrm{geo} = \mathrm{X}$) and assume collisions between compounds are not in the hit-and-stick regime (§ 4.2.4). Only 12 models are then shown with the only free parameters being α (all 6 distinct values) and ρ_X (2 values). Table 4.5 shows various output values corresponding to the 'top ten' models of Fg. 4.11, ordered after final mw-size; for example, the maximum velocities due to systematic and turbulent motions. This shows that for these low-α models systematic drift velocities (col. (7)) quickly become dominant over turbulent motions (col. (8)).

4.5 Discussion

4.5.1 Collective effects in a settled layer

Despite the ability of the chondrule-sticking model to tweak many parameters to optimize the growth, compounds never achieve planetesimal sizes. Ultimately, m/s

or higher velocities are unavoidable in any model due to the radial drift; that is, compounds inevitably reach (and have to cross) the $\mathrm{St} = 1$ bottleneck at which their radial drift velocities peak. The studied accretion mechanism — chondrule sticking by compaction of initially fluffy dust — is simply too weak to grow past the $\mathrm{St} = 1$ bottleneck.

There is one issue, however, that is unaccounted for within the framework in which the simulations are performed: if the turbulence is weak enough, in addition to moving radially, compounds can also settle into a dense layer at the midplane as their Stokes numbers increase. When the density of solids at the midplane exceeds the gas density, the gas is dragged with the particles (instead of the other way around), resulting in gas velocities that tend to become closer to Keplerian, which subsequently diminishes the radial drift and relative velocities of particles. Nakagawa et al. (1986) have solved the equations of motion in such a two-fluid medium analytically for a single particle size (or Stokes number); the radial drift velocity now becomes (instead of Eq. (4.8))

$$v_{\mathrm{rd}} = \frac{2\mathrm{St}}{\mathrm{St}^2 + (1 + \rho_{\mathrm{p}}(z)/\rho_{\mathrm{g}})^2} \eta v_{\mathrm{K}}, \tag{4.28}$$

where $\rho_{\mathrm{p}}(z)$ is the total density of particles at a height z above the midplane. For a generalized solution over a particle size distribution see Weidenschilling (1997) or Tanaka et al. (2005). Thus, in a dust-dominated layer the radial drift of individual particles depends through $\rho_{\mathrm{p}}(z)$ on the density of all other particles: a collective effect. The particle concentration can be found by balancing the gravitationally induced settling rate with the diffusion rate of a particle, assuming a steady-state distribution. The scaleheight of the resulting particle distribution, h_{p}, can be calculated as (Dubrulle et al. 1995)

$$h_{\mathrm{p}} = \frac{H_{\mathrm{g}}}{\sqrt{1 + \mathcal{S}}}, \tag{4.29}$$

where $\mathcal{S} = \mathrm{St}/\alpha$. Under conditions of initial cosmic abundances, in order to reach $\rho_{\mathrm{p}} \sim \rho_{\mathrm{g}}$ the particles must settle into a layer of thickness one-hundredth of the gas scaleheight, requiring $\mathcal{S} > 10^4$ (Cuzzi et al. 2005). This may occur for chondrules in very low-α environments, or, at moderate α, only for large compounds during their growth and settling stage. In Table 4.5 we have calculated the density enhancement ($\rho_{\mathrm{p}}/\rho_{\mathrm{g}}$, col. (5)) and the corresponding velocities ($\Delta v^{\mathrm{sys,CE}}$, col. (8)) for a few selected models at the end of their simulation, where we fixed most parameters at their default 3 AU values, except for α and ρ_X. Note that in the context of our current model setup collective effects are purely hypothetical (we treat $\rho_g/\rho_c = \mathcal{R}_{\mathrm{gc}}$ as a constant); the columns of Table 4.5 therefore merely provide an indication of what could be expected had settling-effects been included. In these calculations we have used the mass-averaged Stokes number of the population (col. (4) of Table 4.5) as the Stokes number that enters equations (4.28) and (4.29). The last two columns of Table 4.5 show that collective effects ($\rho_{\mathrm{p}}/\rho_{\mathrm{g}} > 1$) quickly reduce the radial drift. In a future study, we intend to investigate the effects of the particle concentration on the

compounds' growth.

There is yet another subtlety involved when collective effects (*i.e.*, a dust-dominated midplane) become important. This is the Kelvin-Helmholtz instability (Weidenschilling 1980), caused by the shear between the two fluids now moving at a relative velocity of ΔV, the azimuthal velocity difference between the gas in the particle-dominated and the gas-dominated layer. For shear turbulence the turbulent viscosity is $\nu_T \sim (\Delta V)^2/\Omega \mathrm{Re}^{*2}$ (Cuzzi et al. 1993), where Re^* is a critical Reynolds number at which the flow starts to become turbulent, which Dobrovolskis et al. (1999) found to be $\mathrm{Re}^* \sim 20 - 30$. Also, the large eddy turnover frequency in shear turbulence (Ω_e) can become much larger than Ω, depending on the thickness of the shear layer (see Weidenschilling 2006 for how Ω_e depends on the particle density structure, $\rho_\mathrm{p}(z)$). Equating $\nu_\mathrm{T} \sim (\Delta V)^2/\Omega \mathrm{Re}^{*2}$ with $(v_\mathrm{L}^\mathrm{sh})^2/\Omega_\mathrm{e}$ then provides the expression for the shear turbulent (large eddy) velocity, v_L^sh,

$$v_\mathrm{L}^\mathrm{sh} \sim \left(\frac{\Omega_\mathrm{e}}{\Omega}\right)^{1/2} \frac{\Delta V}{\mathrm{Re}^*} \approx 0.033 \left(\frac{\Omega_\mathrm{e}}{\Omega}\right)^{1/2} \Delta V \lesssim 0.18 \eta^{1/2} c_\mathrm{g}, \tag{4.30}$$

where the upper limit assumes $(\Omega_\mathrm{e}/\Omega) \sim \mathrm{Re}^* = 30$ and $\Delta V = \eta v_\mathrm{k} = \eta^{1/2} c_\mathrm{g}$. This corresponds to the situation where the shear layer is thin (meter-size or larger particles; the shear layer cannot become thinner than the Eckman layer, see Cuzzi et al. 1993). In that case, setting $v_\mathrm{L}^\mathrm{sh} = \alpha_\mathrm{sh}^{1/2} c_\mathrm{g}$ the equivalent α value for shear turbulence becomes $\alpha_\mathrm{sh} \sim 3 \times 10^{-5}$. This is an upper limit; for smaller particles, or a size-distribution of particles, both Ω_e and ΔV are lower and α_sh decreases as well. Shear turbulence may therefore be much more conducive to compound growth.

Future studies must show whether these effects enable growth to planetesimal sizes. Recently, Johansen et al. (2007) have suggested that concentration of meter-size particles ($\mathrm{St} \sim 1$) in certain azimuthally-oriented near-midplane high pressure zones, which form between large turbulent eddies, might lead to gravitationally bound clumps with the mass of planetesimal size objects. The results from Johansen et al. (2007) were most pronounced when the turbulent intensities were moderately high (this leads to the largest radial pressure contrast), suggesting values of $\alpha \sim 10^{-3}$. However, our results suggest that it is difficult to grow a population of meter-size boulders in the first place under such conditions. The maximum growth (in terms of Stokes number) our models achieve for $\alpha = 10^{-3}$ is $\mathrm{St} \sim 5 \times 10^{-3}$ at 3 AU (essentially no growth at all: just dust-rimmed chondrules). 10 AU ice models do somewhat better: $\mathrm{St} \sim 7.4 \times 10^{-2}$. Even if they can form, a population of meter-sized boulders may be difficult to maintain if these originated from dust-coated, solid chondrules as modeled in this chapter. In § 4.2.3 we estimated that fragmentation occurred at a critical velocity of $\sim 10^2$ cm s^{-1}, 30 times smaller than the expected value of $\mathrm{St} = 1$ particles for $\alpha = 10^{-3}$. This translates into a specific kinetic energy for disruption of $Q^* = 10^4$ erg g^{-1}, much lower than the critical Q^* Johansen et al. (2007) adopt (for aggregates of solid basalt objects, as taken from Benz 2000). Thus, our results indicate that it may be difficult for the instability described by Johansen et al. (2007) to become viable in the turbulent inner (ice-free) nebula.

In the outer solar system, however, conditions may be more favorable to growth

in a turbulent environment. First, if ice acts as the sticking agent Q^* may be over an order of magnitude larger, reflecting the scaling with the surface energy density parameter, γ. Second, if chondrule formation is not common the particles grow directly from aggregates of tiny grains to larger aggregates and therefore contain roughly twice as much mass in small grains as dust-rimmed solid chondrules. Moreover, Stokes numbers for the same particles increase with larger heliocentric radii (R) due to the lower gas densities. Therefore, at large R the $\mathrm{St} \sim 1$ regime is reached at smaller sizes (centimeters), which may be somewhat more difficult to disrupt (*i.e.*, higher Q^*) than m-size bodies (Housen & Holsapple 1990; Benz 2000). (In our simple estimate of Q^* we do not have a size dependence, though.) Still, it is hard to see that $\gtrsim 10$ m s^{-1} velocity collisions between equally-sized particles, even under these most favorable conditions, will not result in disruption; but this should of course really be tested by experiments.

On the other hand, it also seems sensible to pursue incremental growth scenarios which take place in quiescent (or low-α) nebulae. Due to the relatively low effective α-values for shear turbulence derived above, it is the radial drift motions that will provide the limits to growth. However, even a modest reduction of radial drift motion by a few factors due to collective effects may already be sufficient to prevent catastrophic collisions as particles reach $\mathrm{St} = 1$ (see, Cuzzi et al. 1993; Weidenschilling 2006). Recall that fragmentation is easiest for nearly equal-size particles, which collide at very low velocities due to their systematic, nonturbulent motions. Moreover, the compound size distribution, which is a function of height, also determines whether collisions are beneficial to the growth; for example, if the size distribution is nearly monodisperse this will certainly favor growth in the nonturbulent cases. Since all these effects will vary with height, however, it is difficult to predict how these effects will unfold, and which parameters are key. Clearly, additional modeling is needed, where we may even combine these two different modes of turbulence since it is quite natural to expect that different physical processes operate at different heights (Ciesla 2007). However, incremental growth in the dense, particle-dominated midplanes of nonturbulent models then proceeds extremely rapidly (Cuzzi et al. 1993; Weidenschilling 2000) which is contrary to the evidence from meteorites and asteroids (see Cuzzi et al. 2005 or Cuzzi & Weidenschilling 2006 for a discussion).

4.5.2 Dust rim and matrix

Figure 4.12 provides an illustration of the internal structure of the objects obtained at the end of our simulation. In Fg. 4.12 it is assumed that each chondrule (black circles) is surrounded by a dust rim at least $\sim$40% of the chondrule's mass, corresponding to the amount of dust accreted by individual chondrules (see Fg. 4.8). This translates into an outer rim radius that is a factor of 1.3 larger than that of the chondrule and is reflected in the inter-chondrule spacing of Fg. 4.12. For the remainder the chondrules are positioned at random. (Note that Fg. 4.12 does not follow directly from the Monte Carlo collision model since we do not keep track of the positions of chondrules within compounds and cannot 'reconstruct' a compound.) Furthermore, we have assumed the initial chondrule size distribution holds, but accounted for the

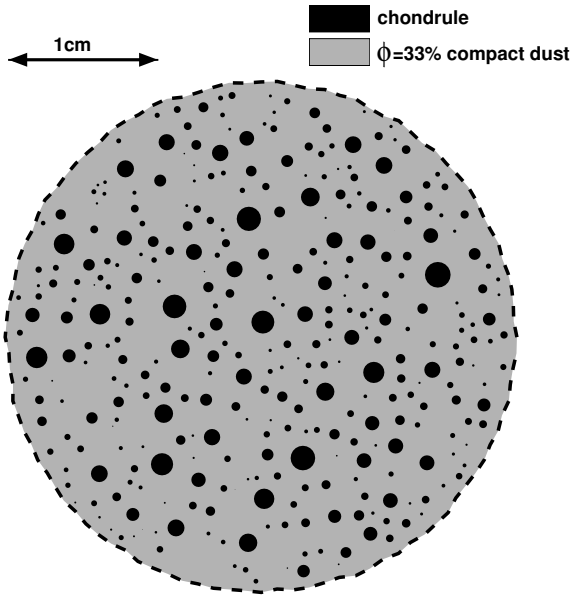

Fig. 4.12: A sketch of a cross-cut through a compound at the final state of our model. The compound contains two phases, present in equal proportion by mass: chondrules (*black*) and $\phi = 0.33$ compact dust (*grey*). The cross-cut introduces a selection effect and shifts the chondrule size distribution to bigger chondrules. The chondrules are placed at random but a certain distance between the chondrules is preserved (see text).

bias a cross cut introduces to the observed structure (Eisenhour 1996). The chondrule size distribution is therefore skewed towards larger chondrules.

However, the picture of a uniform 67% porosity dust phase between chondrules contrasts with the meteoritic record. Here, the dust is compacted to a much larger extent and — at least in the pristine CM chondrites but in others as well — can be divided into two distinct components: the fine-grained, low porosity (10-20%; Trigo-Rodriguez et al. 2006) rim that surrounds chondrules and the interstitial matrix material. Figure 4.12, however, does not show this fine structure as the physical processes responsible for it were not modeled. Yet, the observed fact that chondrules in chondrites are separated by dust and not clustered together supports the main idea of this work: that dust is accreted by chondrule-sized and perhaps somewhat larger particles (compounds) but not, *e.g.,* by planetesimals. How then did the rim-matrix distinction originate? Two scenarios can be envisioned: (i) a period of nebula dust sweep-up and compaction; or (ii) shock waves in the parent body.

The first scenario concerns a moderately intense turbulent environment (*i.e.,* high α) in which chondrules are largely unable to stick, so that most of the dust is accreted by individual chondrules. These bouncing chondrules quickly compact each other's rims, while grazing collisions may also result in dust being partially stripped away or eroded from the rims. Presumably, a steady-state between rim accretion and erosion is established, where some of the dust is firmly attached to each chondrule and compacted, while another, more fluffy, component is continuously eroded off and reaccreted to the chondrule surfaces. Any of this latter, loosely bound phase which remains attached to chondrules at the point they are accreted to their parent planetesimal would be easily stripped away in the abrasive environment of the accreting

planetesimal to become 'matrix.'

Alternatively, a much more gentle collisional environment may be considered in which big compounds form very quickly, and then continue to grow to planetesimal sizes. The dust is then primarily accreted by compounds, though, as we have argued in § 4.4.1, a significant proportion of the dust is always accreted by individual chondrules. As collisional energies stay low no identifiable rims are formed; and any rim signature might anyway easily abrade off on the parent planetesimal. In this scenario, the fine-grained dust rims might result from later processes on the parent body. Specifically, it has been suggested that shock waves through these planetesimals (caused, for example, by violent collisions with other planetesimals) will compact the dust (Trigo-Rodriguez et al. 2006). In the Trigo-Rodriguez et al. (2006) model the highest compaction of the dust takes place near the solid chondrule surface. Thus, it is only during the planetesimal stage that rims become distinguishable from the matrix.

There are a number of constraints the rim formation mechanisms must satisfy. For instance, collisions must be energetic enough to compact the rims significantly to explain the high filling factors observed in chondrites. In the nebula formation scenario, therefore, more energetic collisions are required than provided by the model we present here. From the arguments given at the end of § 4.2.3, we can estimate the velocities required to compact the accretion rims into nearly random closely packed configurations to be $10^{5/2}$ higher than the sticking velocity (Eq. (4.13)), or $v \sim 0.1$ km s^{-1}. Clearly, other compaction processes are needed than can be provided by collisions in turbulence, even between compounds approaching $\mathrm{St} = 1$ in size. One possibility, given the preference for melting of chondrules by Mach 7 shock waves (Desch & Connolly 2002; Hood et al. 2005), is that the plausibly more numerous, more prevalent, weaker shocks which are consequently experienced even more routinely by particles, would provide this range of collisional velocities for chondrule-size particles and their fractal aggregates (Ciesla 2006). Another constraint is the rim-matrix distinction. In the parent body shock scenario it must therefore be shown that this distinction unambiguously results from these shocks. Trigo-Rodriguez et al. (2006) provide a qualitative idea on how this mechanism operates, and it would be desirable for this hypothesis to be backed-up more quantitatively by, *e.g.*, sophisticated numerical simulation.

Yet a third observational constraint is the linear correlation between chondrule radius and rim thickness (Metzler et al. 1992; Paque & Cuzzi 1997). Figure 4.13 illustrates this point in the context of our accretion model. In Fg. 4.13a the chondrule-mass (m_c, x-axis) is plotted against the rim mass (m_rim, y-axis) for the two models discussed in detail in § 4.4.1: crosses for the $\alpha = 10^{-6}$ model and circles for the $\alpha = 10^{-4}$ model. (In Fg. 4.13a the $\alpha = 10^{-6}$ points are arbitrarily offset vertically by a factor of 10^3 for reasons of clarity.) The parameter m_rim is defined as dust that is accreted by individual chondrules, before they become incorporated into a compound. The m_c-m_rim relation is shown for 200 chondrules, randomly selected from the initial distribution. The dashed lines show the best fit having slopes of 0.93 and 0.91, respectively. The near-linear trend of m_rim with chondrule mass is obvious but the spread is large, as seen in actual chondrites (Metzler et al. 1992). Figure 4.13b

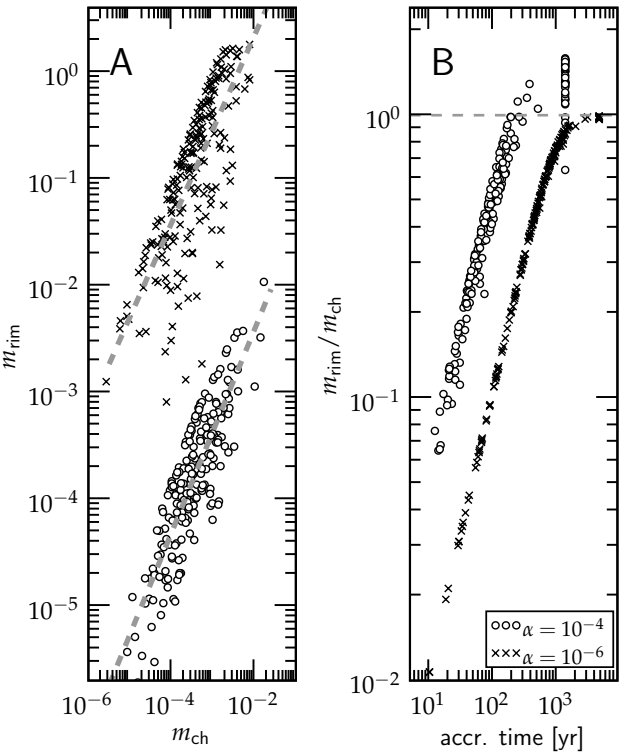

Fig. 4.13: (*symbols*) Model predictions for the thickness of the chondrule dust rim. The amount of dust accreted before the chondrule's incorporation into a compound determines the dust rim mass ($m_{\rm rim}$). *(a)* Scatter plot of chondrule mass $m_{\rm c}$ against $m_{\rm rim}$ for 200 chondrules, chosen randomly at the conclusion of the run. Two models are shown: $\alpha = 10^{-4}$ and $\alpha = 10^{-6}$ with the latter population being shifted by a factor of 10^3 for clarity. The least-squares power-law fits are given by the *dashed lines*, which have exponents of 0.93 and 0.91, respectively. *(b)* Dust-chondrule mass ratio (y-axis) at the time of its accretion into a compound (x-axis).

shows the accretion history of these compounds: the mass ratio, $m_{\rm rim}/m_{\rm c}$, is plotted (y-axis) against the time at which the chondrule is swept up by a compound. The '$\alpha = 10^{-4}$ chondrules' lie to the left of the '$\alpha = 10^{-6}$ chondrules,' reflecting their shorter collision times. The initially linear trend breaks down at later times as the density of free-floating dust decreases. Although many processes contribute to the spread in the data points of Fg. 4.6a — for example, differences in velocity field (linear/square-root regime) during the simulation and the bouncing history of chondrules — the stochasticity in the chondrule-compound accretion time is the main contributor. Note also the pile-up of particles in the $\alpha = 10^{-4}$ model near $t \sim 10^3$ yr, the final time of the simulation: these are the chondrules that remained single during the entire simulation.

The relation of rim thickness with chondrule size can be naturally understood as the outcome of a nebula accretion process (Morfill et al. 1998; Cuzzi 2004; Fg. 4.13). The observed linear relationship in chondrites therefore suggests this relationship should somehow have survived further processing. As dust rim accretion in the violent collisional environment differs from the non-fragmentation environment in which our simulations are performed, it still remains to be shown that the linear relationship is maintained after fragmentation/erosion sets in. Alternatively, if the imprints of nebula dust-accretion are destroyed during parent body accretion, a different mechanism must explain the observed relationship.

Future work—*e.g.*, experimental work on rim-chondrule size ratios and more advanced theoretical models—must determine which of the two scenarios described above is more likely. Dust fragmentation and additional compaction mechanisms may be included into the present model. Increasingly energetic collisions (when compounds grow towards the $\mathrm{St} = 1$ barrier) may disrupt compound objects without stripping the rims entirely off of individual chondrules, and in doing so may compact the surviving fine grained rims further than the $\phi_{\mathrm{cd}} = 0.33$ limit we have adopted in this study. Also, size distributions in the fine-grained component might also allow a greater degree of packing than in our models and Blum & Schräpler (2004) expect, in which the grains are all monodisperse.

4.6 Summary

We have investigated a chondrule-dust aggregation mechanism in which the fine-grained dust acts as the glue that allows chondrules to stick. We argue that the energy in collisions is sufficient to compress directly accreted material, which initially has a porous 'fairy-castle' structure, into a more compact state having a porosity that is roughly 67% (based on compaction measurements by Blum & Schräpler 2004 and theoretical arguments). We have applied this model to a variety of questions regarding the meteoritic record: the relation of individual chondrules to their fine-grained dust rims, the internal structure of the chondrites, and the ability of growth by sticking to surpass the meter-size barrier. This study only starts to address these questions; more sophisticated models are needed to answer detailed questions on the structure of the meteorites.

We find that porous accretion rims do indeed cushion collisions and facilitates growth to compound objects containing many rimmed chondrules, but this growth is limited to $30 - 100$ cm radius objects under the most favorable conditions. This is because the chondrule component sweeps up all the local dust in a short time ($10^2 - 10^4$ yr, depending on nebular location) and these compounds experience higher relative velocities during their growth stage. Subsequent collisions merely pack the existing rims down further, so that the system ultimately reaches a dead-end steady state where collisions only result in bouncing, or possibly disruption. Other conclusions from this study are:

1. Compound growth works best in a quiescent environment (high gas density, low α values). In a more violent collisional environment ($\alpha \sim 10^{-3} - 10^{-2}$) it is difficult to accrete dust fractally on chondrules surfaces and the energetic collisions between compounds quickly compact the remainder such that collisional growth is quickly terminated.
2. The importance of the other parameters on the accretion process is mostly minor. The radial location does not affect the final growth of the compounds, although timescales are longer at larger R. Ice, rather than silicate, as the sticking agent will lead to bigger compounds (but we note icy grains do not dominate the meteoritic record).
3. In no single model do compounds grow to planetesimal sizes. Either turbulent or systematic velocities are too high for the porous dissipation mechanism, the

St $= 1$ size being the bottleneck; but we may have over-estimated the systematic velocities in this study by not accounting for particle collective effects in low turbulence nebulae.

4. We anticipate that the dust accreted by individual chondrules — before chondrules coagulate into compounds — will finally end up as the chondrule rim. In strong turbulent models this fraction is very high, but it remains significant (tens of percents) even in the collisionally gentle models.
5. However, at the current state of the art of this model, fine-grained accretion rims have a porosity significantly larger than seen in actual rims. Other compaction processes are not hard to envision, such as higher velocity collisions by larger mass compound objects, or nebula shock waves (peripheral to those energetic enough to melt chondrules). These remain to be modeled.
6. When we define the rim as the dust swept up by individual chondrules, we find very good agreement with the nearly linear (average) correlation between rim thickness and underlying chondrule radius seen in CM and CV chondrites (Metzler et al. 1992; Paque & Cuzzi 1997).

Future work will focus on two aspects of our coagulation model:

1. An improvement of the collisional physics, *i.e.,* including fragmentation as a collisional outcome for velocities above $\sim$m s^{-1}; and a refinement of the characterization of the compound structure, *e.g.,* to allow dust to compact to higher filling factors.
2. Inclusion of a proper description of the vertical structure of the nebula, *i.e.,* taking account of phenomena such as settling, collective effects, and shear turbulence. Especially, the transition from global- (α) to shear-turbulence is important, and in future work we will address this critical junction.

Acknowledgment. We thank Jürgen Blum, Carsten Dominik, Alan Rubin, Marco Spaans and John Wasson for helpful conversations. C.W.O. acknowledges a grant from the Netherlands Organisation for Scientific Research (NWO). J.N.C.'s contributions were supported by a grant from NASA's Origins of Solar Systems program. We thank the anonymous referee for comments that helped clarifying this chapter.

5

Monte Carlo simulation of particle interactions at high dynamic range: Advancing beyond the Googol[1]

—C. W. Ormel, M. Spaans—

We present a method which extends Monte Carlo studies to situations that require a large dynamic range in particle number. The underlying idea is that, in order to calculate the collisional evolution of a system, some particle interactions are more important than others and require more resolution, while the behavior of the less important, usually of smaller mass, particles can be considered collectively. In this approximation groups of identical particles, sharing the same mass and structural parameters, operate as one unit. The amount of grouping is determined by the zoom factor — a free parameter that determines on which particles the computational effort is focused. Two methods for choosing the zoom factors are discussed: the 'equal mass method,' in which the groups trace the mass density of the distribution, and the 'distribution method,' which additionally follows fluctuations in the distribution. Both methods achieve excellent correspondence with analytic solutions to the Smoluchowski coagulation equation. The grouping method is furthermore applied to simulations involving runaway kernels, where the particle interaction rate is a strong function of particle mass, and to situations that include catastrophic fragmentation. For the runaway simulations previous predictions for the decrease of the runaway timescale with the initial number of particles

[1]Originally published in *The Astrophysical Journal*, vol. 684, p. 1291 (2008)

$\mathcal{N}$ are reconfirmed, extending $\mathcal{N}$ to 10^{160}. Astrophysical applications include modeling of dust coagulation, planetesimal accretion, and the dynamical evolution of stars in large globular clusters. The proposed method is a powerful tool to compute the evolution of any system where the particles interact through discrete events, with the particle properties characterized by structural parameters.

5.1 Introduction

In the field of natural sciences the dynamical evolution of a population is often determined by interactions that operate at short range, *e.g.,* when the members come into contact, but which do otherwise not influence each other. The dynamical evolution of the system is then regulated by discrete events and the system can be described statistically. The most direct interaction is, of course, the merging of two bodies that come into contact. Examples are numerous. In the Earth's atmosphere water vapor condenses on cloud droplets (tiny water drops), which merge to form rain drops. In biology, the size distribution of many species of animals can be found by assuming animal groups merge when they make contact. The distribution is then determined by a power-law, which seems to agree with observations of, *e.g.,* schools of tuna fish or herds of African buffaloes (Bonabeau et al. 1999). Similarly, a power-law emerges when bigger organisms are assumed to feed on smaller ones (Camacho & Solé 2001). In astrophysics, too, coagulation processes appear. The transition of the dust component in protoplanetary disks — from (sub)micron grains to planets — covers a huge dynamic range: many tens of orders of magnitude in mass. Due to small molecular forces, micron-sized grains will stick when they meet (Blum 2004). How sticking continues as particles grow to macroscopic proportions ($\sim$cm or larger) is still unclear but once the km-size is reached gravity will dominate the accretion process (Lissauer 1993; Goldreich et al. 2004b). Another example where coagulation is of importance are dense stellar systems. Although stellar densities are usually too low for collisions to be likely on a Hubble timescale, it has been shown that mechanisms, *e.g.,* mass-segregation or equipartition, conspire to make stellar collisions feasible (Freitag et al. 2006). The coagulation process, excluding fragmentation and injection, is described mathematically by the Smoluchowski equation (Smoluchowski 1916), which in the continuous limit reads

$$\frac{\partial f(m)}{\partial t} = -f(m)\int f(m')K(m,m')\mathrm{d}m' + \frac{1}{2}\int f(m-m')f(m')K(m-m',m)\mathrm{d}m', \tag{5.1}$$

where the terms on the RHS denote, respectively, the loss and gain terms of particles of mass m. The distribution function, $f(m)$, gives the number density of particles (*e.g.,* dust grains, stars, *etc.*) of mass m; *i.e.,*

$$f(m)\cdot \mathrm{d}m = \text{number density of particles in mass-interval } (m, m+\mathrm{d}m). \tag{5.2}$$

MOMENTS

Kernel	K_{ij}	$M_0(t)$	$M_1(t)$	$M_2(t)$
constant	1	$(1+\frac{1}{2}t)^{-1}$	1	$1+t$
sum	$\frac{1}{2}(m_i+m_j)$	$\exp[-\frac{1}{2}t]$	1	$\exp[t]$
product	$m_i m_j$	$1-\frac{1}{2}t$	1	$(1-t)^{-1}$

Table 5.1: Moment expressions for the classical analytic kernels: M_0 describes the particle density, M_1 the mass density (which is conserved), and M_2 is related to the mass peak, m_p, of the distribution. The initial distribution at $t=0$ is monodisperse, $f(m, t=0)=\delta(m-1)$. The numerical factor of $1/2$ in the sum kernel causes its evolution to coincide with the other kernels at small t. The expressions for the product kernel, $K=m_i m_j$ become invalid after the formation of the gel, at $t=1$. The mean mass $\langle m\rangle$ and peak mass m_p are related to the moments as $\langle m\rangle = M_1/M_0$ and $m_\mathrm{p}=M_2/M_1$.

Given that the initial conditions of the distribution, *i.e.*, $f(m, t=0)$ are specified, the coagulation is fully determined by the coagulation kernel, $K(m,m')$, which is the product of the cross section of collision and the relative velocity of the particles, $K(m,m')=\sigma(m,m')\Delta v(m,m')$. It gives the rate coefficient (in units of $\mathrm{cm}^3\ \mathrm{s}^{-1}$) for the collision between two particles of mass m and m'. For only three distinct cases of K does Eq. (5.1) have a, closed form, analytic solution (Tanaka & Nakazawa 1994). These are:

1. The constant kernel, $K=$ cnst.;
2. The additive (or sum) kernel, $K\propto(m_i+m_j)$; and
3. The product kernel, $K\propto m_i m_j$;

These three kernels each show their own characteristic behavior. This can be seen by considering the moments of the distribution

$$M_\mathrm{p}(t)=\int_0^\infty m^p f(m,t)\,\mathrm{d}m. \tag{5.3}$$

Multiplying the Smoluchowski equation by m^p and integrating over m yields the moment equation (Leyvraz 2003; Estrada & Cuzzi 2008)

$$\frac{\mathrm{d}M_\mathrm{p}}{\mathrm{d}t}=\frac{1}{2}\int_0^\infty K(m,m')f(m,t)f(m',t)\left[(m+m')^p-m^p-m'^p\right]\mathrm{d}m\,\mathrm{d}m', \tag{5.4}$$

from which $M_\mathrm{p}(t)$ can be found. In Table 5.1 the zeroth, first and second moments as function of time for monodisperse initial conditions are given for the three classes of kernels. The first moment M_1, the mass density, is conserved. The zeroth moment, M_0, describes the (decreasing) particle density; it therefore defines the mean mass of the population, $\langle m\rangle = M_1/M_0$. The second moment, M_2, is of considerable importance for our study as it traces the mass distribution on a logarithmic scale, *i.e.*, $mf(m)\mathrm{d}m = m^2 f(m)\mathrm{d}\log m$. We therefore define the peak mass as $m_\mathrm{p}=M_2(t)/M_1(t)$. For most continuous distributions m_p corresponds to the particle sizes that (together) dominate the total mass of the population.

These three kernels are each representative of a very distinct growth behavior. In the constant kernel growth is orderly, not only do $\langle m \rangle$ and m_p evolve linearly with time, their ratio, which indicates the (relative) spread in the distribution, stays constant as well. This relative narrowness of the distribution means that this kernel can be relatively easily simulated by numerical methods. The situation for the sum kernel, however, is different. Initially, ($t \ll 1$) it evolves similarly to the constant kernel, but after $t \sim 1$ it starts to grow exponentially. The exponential nature of the growth not only holds for $\langle m \rangle$ or m_p but also holds for the spread in the distribution, $m_\mathrm{p}/\langle m \rangle \sim \exp[\frac{1}{2}t]$ (see Fg. 5.1).

The third class of kernels are the runaway kernels, of which $K_{ij} = m_i m_j$ is its analytic representative. From Table 5.1 a peculiarity can be noted: the moment expressions do not make sense after a certain amount of time: the mean density will become negative after $t = 2$, whereas $M_2(t)$ becomes infinite at $t = 1$. The reason for this behavior is that at $t = 1$ a runaway particle of mass $m_R(t)$ is created that separates from the rest of the distribution. In theoretical studies of coagulation this particle is called the 'gel' and $m_R(t)$ becomes infinite at precisely $t = 1$. In physical situations, where the total mass in the system is finite, $m_R(t)$ grows continuously with time but nevertheless separates from the distribution. This discontinuity in the distribution is also the reason why the moment expressions become invalid after $t = 1$.

In systems where small number statistics (one runaway particle) become important the assumptions underlying the Smoluchowski equation become invalid. Coagulation is more accurately described by the stochastic coagulation equation which assigns a probability that the system is in a specific state $\{n_k\}(t)$, with $\{n_k\}$ the discrete particle numbers for the mass bins k. The Smoluchowski equation only follows when certain assumptions are made, like $\langle n_i n_j \rangle = \langle n_i \rangle \langle n_j \rangle$, which break down when i and j are statistically correlated (Gillespie 1975). Clearly, Eq. (5.1) is dangerous when it is used to describe the coagulation process — a process that is inherently discrete.

In many situations of physical interest $K = \sigma \Delta v$ cannot be expressed in the simple forms above where analytic solutions are available. If K can be expressed in terms of a simple mass-scaling behavior of the form $K \propto (\mathrm{mass})^\beta$, then semi-analytic solutions are available (Silk & Takahashi 1979). However, in many physical situations β will not be constant over the whole mass range under consideration. For example, in studies of dust coagulation in protoplanetary disks, relative velocities can be divided into several 'regimes,' each with a different velocity behavior (*e.g.*, Ormel & Cuzzi 2007). Another example, is the enhancement of the collisional cross section by gravitational focusing, *i.e.*,

$$\sigma = \pi R_\mathrm{s}^2 \left(1 + \frac{2G(m_i + m_j)}{R_\mathrm{s}(\Delta v_{ij})^2} \right), \tag{5.5}$$

where R_s is the sum of the radii of the bodies and G is Newton's gravitational constant. Equation (5.5) displays a natural break in the scaling of σ versus mass: *i.e.*, $\sigma \propto m^{2/3}$ at low masses vs. $\sigma \propto m^{4/3}$ at high masses. The break happens at the

point where the relative velocity of the particles starts to become less than the escape velocity $v_{\rm esc} = \sqrt{2G(m_i + m_j)/R_{\rm s}}$ of the biggest body, $\Delta v_{ij}/v_{\rm esc} < 1$.

So in most situations a numerical approach to the coagulation problem is required. Most directly, Eq. (5.1) can be integrated numerically. This entails dividing up the mass-axis into discrete bins and applying Eq. (5.1) to all of these bins. However, this is a rather elaborate procedure as, *e.g.*, mass conservation is not intrinsically conserved, and most works have actually avoided to explicitly use the Smoluchowski equation. For example, Spaute et al. (1991) and Inaba et al. (1999) use a (fixed) binning method that assumes the mass inside a bin is distributed as a power-law; coagulation is then an interchange of mass between the various bins. Recently, Brauer et al. (2008a) have modified a matrix method, the Podolak algorithm (see also Kovetz & Olund 1969), which distributes the mass of a coagulation event evenly between its two nearest grid points. Wetherill (1990) and Inaba et al. (1999) use a method where the mass is divided over a discrete number of 'batches,' each characterized by a single mass. Interactions with other batches and with themselves cause the batches to grow, *i.e.*, move up the mass scale. This representation of intrinsically discrete quantities is especially useful in the case of non-continuous distributions (runaway kernels).

Bin size techniques are generally one-dimensional, *i.e.*, the quantities that enter Eq. (5.1) (cross sections, velocities) depend on mass only. This approximation may neglect *variables* that play a pivotal role in the coagulation process. For example, a charge distribution on grains (Marshall & Cuzzi 2001; Konopka et al. 2005) is difficult to include in this way. A more subtle example concerns the coagulation of dust particles in disks. Here, collisions affect the internal structure of the particles such that their porosity is not constant, which affects their aerodynamic properties and hence their collisional evolution. Ossenkopf (1993) has extended the Smoluchowski formalism to solve the two-dimensional distribution function for the collisional evolution of dust aggregates, using their fluffiness as the second variable. However, it is clear that the increased number of connections between the bins, caused by the higher dimensionality of the problem, makes the procedure more elaborate, and slower—impractical, perhaps, for three or more dimensions.

In these cases one has to resort to Monte Carlo (MC) simulations. A good description of how a direct-simulation MC method is implemented is outlined by Gillespie (1975) which we briefly summarize below (§ 5.2.1). In MC methods $K(m, m')$ determines the probability that an event (here, the collision between the particles) takes place. For multi-dimensional models it is probably the preferred method. Besides, the MC method as described by Gillespie (1975) provides an exact description of the stochastic coagulation process, and will also accurately describe runaway kernels. However, in MC simulations one is limited to the finite number of particles that can be followed. It is therefore best suited for distributions that remain relatively narrow, such that a modest number of particles gives a good knowledge of the distribution function f. On the other hand, when the distribution is wide a large number of particles must be present in order to obtain a good characterization of f; the required particle numbers then severely limit the applicability of the code.

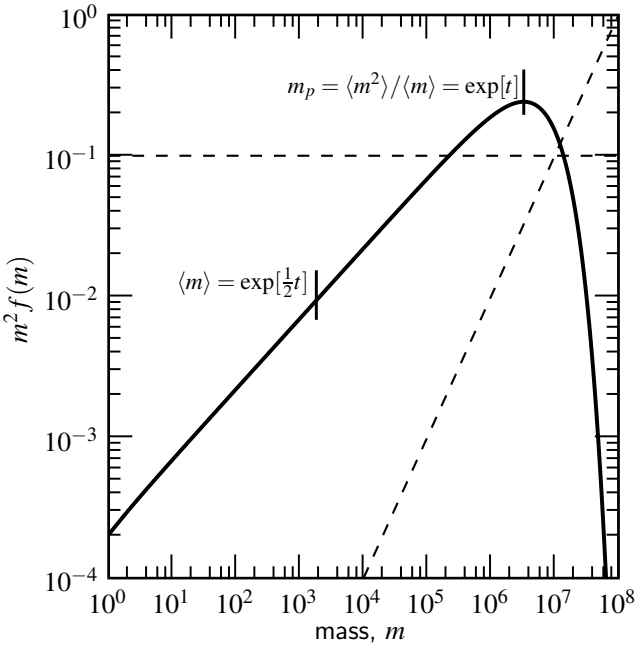

Fig. 5.1: (*solid curves*) The $m^2 f(m)$ mass function of the sum kernel ($K_{ij} = \frac{1}{2}(m_i + m_j)$) at $t = 15$. At this time the mass function has achieved self-similarity. The mean mass, $\langle m \rangle$, and peak mass, m_p, are indicated. *Dashed lines* of logarithmic slopes 0 and 1, respectively, trace areas of equal mass- and number density per logarithmic unit of mass. Because of the $f(m) \propto m^{-3/2}$ falloff towards small masses, the small particles dominate by number, yet most of the mass resides in the large particles (around $m = m_\mathrm{p}$).

These effects can best be illustrated in the case of the sum kernel. In Fg. 5.1 we have plotted the theoretical value of $m^2 f(m)$ at $t = 15$ (Tanaka & Nakazawa 1994) corresponding to $K_{ij} = \frac{1}{2}(m_i + m_j)$, and an initial monodisperse distribution of mass $m_0 = 1$ and $f(m, t = 0) = \delta(m - m_0)$. At $t = 15$ the distribution has reached self-similarity and the shape is the characteristic one for the sum kernel. In Fg. 5.1 $m^2 f(m)$ is plotted showing (per logarithmic mass interval) the mass density distribution. Because of the $m^{-3/2}$ falloff of $f(m)$ with mass in the low-m tail of the distribution, the smaller ($m \sim m_0$) particles dominate by number, although it is the larger particles that contain most of the mass. If, for example, the total simulated mass is M_tot, there are $\sim M_\mathrm{tot}/m_\mathrm{p}$ particles representing the mass peak, and $\sim M_\mathrm{tot}/\langle m \rangle$ particles in total. The fraction of m_p particles then decreases with increasing m_p as $\langle m \rangle / m_\mathrm{p} \propto m_\mathrm{p}^{-1/2}$. This behavior inevitably causes computational problems since a few massive particles remain in comparison to a huge number of small particles, while both regimes must be included in order to obtain a good characterization of $f(m)$. With increasing m_p, a point is reached at which there are simply not enough particles to resolve the complete distribution.

In short, the dynamic range for these kinds of simulations is too large to tackle with conventional MC methods; more particles are required, but this is impossible due to computational constraints. To overcome these problems—*i.e.*, to extend MC methods to situations that require high dynamic range—we introduce the assumption that one simulation particle can represent multiple physical particles: the grouping method. Section 5.2.2 introduces the grouping method. First the framework of a MC simulation is described in § 5.2.1, then § 5.2.2-§ 5.2.4 outline the grouping

method in detail. In § 5.3 the new method is tested against the analytic solution of the sum kernel (§ 5.3.1) and the product kernel (§ 5.3.2). In § 5.3.3, we consider a class of runaway kernels and test the assumption that the runaway timescale goes down with the size of the simulation (keeping the physical quantities such as the initial mass density constant). Next, in § 5.3.4 we present steady-state distributions that result from fragmentation of the largest particles. We briefly summarize our findings and discuss astrophysical applications in § 5.4.

5.2 The grouping algorithm

Before introducing the grouping method (§ 5.2.2) we first briefly outline the main features of a direct simulation Monte Carlo code.

5.2.1 The Monte Carlo code

The direct simulation Monte Carlo method in its simplest form consists of three steps (Gillespie 1975):

1. calculation/update of the collision rates, $\{C_{ij}\}$;
2. selection the collision by random numbers: which particles collide and the timestep involved;
3. execution of the collision: removal of the collision partners and addition of the new particle(s).

A Monte Carlo simulation starts with the calculation of the collision rates between the particles, $C_{ij} = K_{ij}/\mathcal{V}$ where $\mathcal{V}$ is the simulated volume and $1 \leq i, j \leq N_\mathrm{p}$. Here, N_p is the number of particles in the simulation and C_{ij}, the collision rate, is related to the probability of collision, such that $C_{ij}\Delta t$ is the probability that particles i and j collide in the next infinitesimal time Δt. In total there are $N_\mathrm{p}(N_\mathrm{p}-1)/2$ collision rates. A trick which saves memory requirements (although it increases CPU-time) is to store only the partial rates, $C_i = \sum_j^{N_\mathrm{p}} C_{ij}$. The total collision rate is $C_\mathrm{tot} = \sum_i^{N_\mathrm{p}} C_i$. In step 2 three random deviates ($\bar{r}$) determine the time interval to the next collision, and the particles involved (i and j). As described by Gillespie (1975) the time increment Δt is found from the total collision rate, $\Delta t = -C_\mathrm{tot}^{-1} \ln \bar{r}$, whereas the particles that are involved are found from sampling the $\{C_i\}$ and $\{C_{ij}\}$. Step 3 computes the new properties of the particles that result from the collision. The fact that in MC methods these steps are separated shows its advantages when introducing multiple variables; by including multiple variables, the outline of the program, *i.e.*, steps 1–3, will remain the same. Finally, the $(N_\mathrm{p}-1)$ collision rates associated with the newly created particle need to be re-calculated (step 1), after which the $\{C_i\}$ are updated. The steps then repeat themselves in a new cycle.

Constant-V vs constant-N simulations

Because each collision that results in coagulation reduces the particle number by one, all particles will have coalesced into one body after N_p steps. This is the constant-$\mathcal{V}$ algorithm: the simulated volume $\mathcal{V}$ and total mass stays the same. However, in

many cases this is not the intended behavior: the volume $\mathcal{V}$ occupied by the initial number of particles in the simulation, $\mathcal{N} = N_{\rm p}(0)$, is only a small sample of the total volume under consideration. Although $\mathcal{V}$ may start out as a volume large enough to represent the particle population, after sufficient coagulation (and decreasing particle numbers) it loses this property: a larger volume is needed in order to get the desired sampling. However, increasing the initial number of particles $\mathcal{N}$ is no solution, since the number of collision rates becomes quickly impractical.

A natural solution to prevent the statistical deterioration due to the decreasing particle numbers is to keep the numbers constant: the constant-N algorithm. Here, the number of (simulated) particles is artificially kept constant by *duplicating* a particle after each coagulation event. Thus, mass is added to the system, which physically translates into an expansion of the simulated volume, because the volume density stays the same. As described in Smith & Matsoukas (1998) the new particle is taken randomly from the existing (simulated) distribution and is therefore called a duplicate. Smith & Matsoukas (1998) have shown that the error introduced due to the duplication scales logarithmically with $\langle m \rangle(t)/m_0$, which is a measure of the amount of growth. This is much improved compared to the constant-$\mathcal{V}$ method in which the reduced number of particles causes the error to scale as the square-root of the growth. In principle, this method allows for indefinite growth. Fundamentally, the assumption is that the simulated volume (containing $N_{\rm p}$ particles) at all times stays representative of the parent distribution (containing $\gg N_{\rm p}$ particles). We test whether the Smith & Matsoukas (1998) duplication mechanism also holds in systems where the growth occurs over many orders of magnitude.

On the other hand, in situations where runaway growth occurs, the collisional evolution will depend on the initial number of particles present in the system, even if locally the same physical conditions apply, *i.e.,* for the same density (Wetherill 1990; Malyshkin & Goodman 2001). Clearly, a constant-N simulation is not the proper way to treat these kernels; we will always use a constant-$\mathcal{V}$ algorithm when treating these kernels. It is challenging to test simulations in which $\mathcal{N} = N_{\rm p}(0)$ becomes truly astronomical. Here, too, the grouping method will be applied.

The species formalism

A natural way to deal with the existence of a large number of *identical* particles, *e.g.,* resulting from monodisperse initial conditions or through the duplication mechanism in constant-N simulations, is to combine them in the calculation of the collision rates (Spouge 1985; Malyshkin & Goodman 2001; Laurenzi et al. 2002; Laurenzi & Diamond 2003). Since the collision rates of the duplicates are the same, it is efficient to introduce a multiplicity array, g, for all *distinct* particles. This is like saying we have 1 particle of type 1, 5 particles of type 2 ... g_i particles of *species* i. It causes the number of distinct simulation particles ($N_{\rm s}$, or number of species) to become less than the total number of physical particles in the simulation ($N_{\rm p}$) since

$$N_{\rm p} = \sum_{i=1}^{N_{\rm s}} g_i. \tag{5.6}$$

This algorithm is much more efficient, for it is the number of distinct particles (N_s) that matters in the calculation of the collision rates. The collision rate for one collision between species i and j then becomes

$$\lambda_{ij} = g_i g_j C_{ij} \qquad (i \neq j); \qquad \lambda_{ii} = \tfrac{1}{2} g_i (g_i - 1) C_{ii} \qquad (i = j), \tag{5.7}$$

where the C_{ij} are the individual collision rates between two single particles. So the λ_{ij} give the probability that a (single) particle of species i collides with one of species j. After the collision partners are determined, their multiplicity is first decreased ($g_i \rightarrow g_i - 1$, $g_j \rightarrow g_j - 1$). If this means that g_i becomes zero, no particles of type i exist anymore and it is consequently removed ($N_s \rightarrow N_s - 1$). The new particles that result out of the collision are added as a new (and distinct) species ($N_s \rightarrow N_s + 1$). When particles are characterized by only one parameter (mass) it would in this case be more efficient to assess first whether the species is really unique, but in this study we treat a general approach. Duplication causes the occupancy number of the duplicated species k to increase by 1, $g_k \rightarrow g_k + 1$. Laurenzi et al. (2002) describe in-depth how the species formalism can be implemented and quantify its computational efficiency.

We note that this grouping of the collision rates is nothing more than a computational trick, which, within the assumptions of, *e.g.*, the duplication mechanism does not approximate the MC method. Occupation numbers may become very large, however. For example, for monodisperse initial conditions $g_1 = N_p$ initially but g_1 may increase if the constant-N algorithm is enforced and $\mathcal{V}$ grows, as in the case of the sum kernel (Fg. 5.1). In fact, the existence of a large number of identical particles is the basis of the (physical) grouping algorithm.

Limiting N_s.

The accuracy and efficiency of Monte Carlo simulations is then determined by a single parameter, N_s. Ideally, one wants to constrain N_s. In the constant-N_s simulations this means that N_s should fluctuate around a (fixed) target value N_s^*. (There is no need to enforce an exact 1-to-1 correspondence.) Here we list a few mechanisms that can be applied to balance N_s. Operations that increase N_s:

1. Duplication ($g_k \rightarrow g_k + 1$). Although duplication does not directly increase the number of species, the increased multiplicity of a species will decrease the likelihood that it becomes empty of particles ($g_k = 0$) and that it is removed;
2. Coagulation/Fragmentation. Because we generally assume that the collision products are different species, the number of species always increases with coagulation and fragmentation. Especially fragmentation may lead to a proliferation of the number of species.

And operations that decrease the N_s parameter:

1. (Physical) grouping (discussed below). This has the effect that many particles are involved in the collision and therefore increases the likelihood of a disappearing species ($g_i \rightarrow 0$).
2. Coagulation. Requires two particles, with which again a species may disap-

pear.

3. Particle removal. This is the reverse of duplication. If the number of species keeps increasing, we may randomly remove particles to enhance the probability of obtaining $g_i = 0$.
4. Merging. This is the most drastic approach, in which different species are merged together in a single species whose properties reflect the properties of its progenitors. Because of the averaging, this procedure is somewhat against the spirit of the MC methods. It is in fact a smoothing where particles of different properties are averaged, including their structural parameters. However, the mean parameters may still be applicable to describe the present state.

In this work the species-averaging is performed as follows. If a species needs to be merged, we first look for its neighbor species in terms of mass, and then mass average over their (structural) properties. As in this work mass is the only property, it simply means that for species i and j their merged occupation number becomes $g = g_i + g_j$ and the new mass $(g_i m_i + g_j m_j)/(g_i + g_j)$. (If needed, the latter quantity is rounded to integer values). If structural parameters would be present, however, this procedure can be simply extended to any structural property ψ, *i.e.*, $\psi \rightarrow (g_i\psi_i + g_j\psi_j)/(g_i + g_j)$, where ψ may, *e.g.*, represent charges or filling factor.

5.2.2 The grouping algorithm

To simulate a coagulation process by Monte Carlo methods in a way to obtain growth over many orders of magnitude, two criteria have to be met:

I The simulation must involve a large number of physical particles (N_p), such that the population is a proper sample of the continuous distribution. Physically, it means the spatial volume that is sampled will be large enough to account for all various kinds of particles.

II The number of species (N_s) cannot become too large: since there are $\sim N_\mathrm{s}^2$ collision rates to be taken care of, the computational speed will slow down rapidly with increasing N_s.

To meet these conditions—high N_p and low N_s—the occupation numbers g_i must be very large. This can, in principle, be achieved by duplicating particles many times. However, a new problem then arises. Since the total collision rate, C_tot, scales with the total number of physical particles squared, *i.e.*, $C_\mathrm{tot} \sim N_\mathrm{p}^2$, the time step per collision is proportional to N_p^{-2}. The simulations then seem to freeze as the required CPU-time per unit simulation time blows up. In the MC simulation the focus lies on the particles that dominate by number, which may sometimes be irrelevant from a physical point of view. This occurs, for example, with the sum kernel. Here, the most dominant collisional process—a collision between a small particle and a very massive one—is rather meaningless: a single collision neither affects the mass of the massive particle nor the number of small particles. The ubiquity of many of these subleading collisions then overwhelms the more important ones involving more massive particles, a process that together is very CPU intensive. This leads to the conclusion that, given (I) and (II), a third condition must apply:

III A simulation involving a large number of particles (N_p) yet with only 2 physical particles colliding per MC cycle can become very inefficient. Therefore, (small) particles should be grouped together—*i.e.*, considered as a single unit—during the collision.

Because of the duplication mechanism there is a natural way to group particles together. In Eq. (5.7) it was already seen that identical particles can be effectively absorbed in the calculation of the collision rates. We will now take this idea further and write the occupation number g_i of species i as

$$g_i = w_i 2^{z_i}, \tag{5.8}$$

where w_i is the group number and z_i the *zoom number* (an integer equal to zero or larger) of species i. Thus, instead of tracking g_i particles, we now simulate only w_i groups, each containing 2^{z_i} particles. It is then the number of groups (N_g) that determines the collision rate per cycle. Because collisions are now between two groups of particles, involving 2^{z_i} and 2^{z_j} physical particles, coagulation is speeded up significantly. That is,

$$N_\mathrm{g} = \sum_i^{N_\mathrm{s}} w_i; \qquad N_\mathrm{p} = \sum_i^{N_\mathrm{s}} w_i 2^{z_i}, \tag{5.9}$$

and we can, with a limited number of groups (N_g), represent large numbers of physical particles (N_p) by choosing appropriately high zoom factors z_i. This satisfies criteria (I) and (II) and since each collision is now between two groups involving many particles we also avoid the inefficiency described in (III). Note that the base factor of 2 in Eq. (5.8) is arbitrary; however, it must be an integer (g_i is integer) and 2 is probably most convenient. More critical are the choices for the zoom factors, z_i: these must be chosen to reflect the nature of the system that is under consideration (see § 5.2.3).

A group collision is illustrated in Fg. 5.2a. The first group is magnified three times ($z_j = 3$), and the second has $z_i = 1$ ($z_j \geq z_i$ in this and all other examples). The groups thus consist, respectively, of 8 and 2 identical particles. During the collision, assuming sticking, the particles are equally distributed over the groups so that we end up with one group consisting of two identical particles. The mass of the new particle then becomes $m_i + 4m_j$ and the zoom factor $z = z_i = 1$ (the lowest of the two; the grouping may always be adjusted if needed). Note that in Fg. 5.2a only particles of different groups collide: out-of group collisions. However, if their λ_{ii} do not vanish, particles within a group can also collide: in-group collisions. This procedure is illustrated in Fg. 5.2b. The zoom number decreases by one in the final configuration (group collapse).

To generalize, for out-of-group collisions with $z_j \geq z_i$ every i-particle collides with $2^{z_j - z_i}$ j-particles. In total there are 2^{z_j} collisions, whereas for in-group collisions (Fg. 5.2b) there are $2^{z_i}/2$ collisions. Therefore, the collision rates of Eq. (5.7)—the

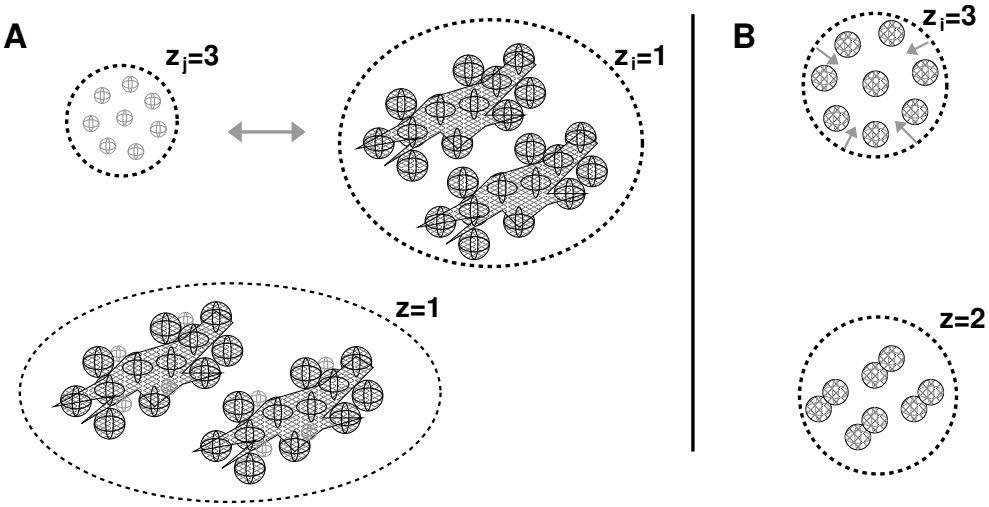

Fig. 5.2: Illustration of collisions in the grouping algorithm. (*a, top*) Two groups with $z_j = 3$ and $z_i = 1$, respectively, collide. The zoom factors (z_i) give the number of particles within the group (2^{z_i}). Less massive particles have higher zoom factors than particles of higher mass. All particles within the group are identical. (*a, bottom*) Assuming sticking, the collision product is obtained by equal distribution of the collision partners. The end-product is a new species consisting of one group where the zoom factor corresponds to the lowest z of the progenitor particles. (*b*) Same as (*a*), but for in-group collisions.

rates corresponding to one collision—are divided by 2^{z_j} and 2^{z_i-1}, respectively, *i.e.*,

$$\lambda_{ij}^{G} = g_i g_j C_{ij}/2^{z_j} = w_i w_j 2^{z_i} C_{ij} \qquad (z_i \le z_j,\ i \ne j); \tag{5.10a}$$

$$\lambda_{ii}^{G} = \tfrac{1}{2} g_i (g_i - 1) C_{ii}/2^{z_i-1} = w_i (w_i 2^{z_i} - 1) C_{ii} \qquad (i = j), \tag{5.10b}$$

give the collision rates between two groups. Thus, although collisions between groups are less likely (the rate is decreased by a factor 2^{z_j}), this is 'compensated' by the 2^{z_j} particle-collisions that occur inside the group.

However, grouping does introduce various sources of systematic errors:

1. the outcome of a collision between two groups is fixed; in reality, a distribution of configurations will be present;
2. it is assumed that the grouped collision rates obey Poisson statistics like the single particle collision rate;
3. the individual collision rates $\{C_{ij}\}$ do not change *during* the group collision process to ensure that Eq. (5.10) is applicable.

A fixed configuration for the outcome of the grouping process is required because it prevents (unwanted) proliferation of the diversity of species, which would increase the N_s parameter and strain CPU requirements. However, the diversity of the simulation is already specified by the N_s parameter and we may simply check how N_s

affects the accuracy of the collisional process. This point is similar to the second concern where all collisions are forced to occur at one point in time. Also, note that we must use the memoryless property of Poisson statistics; otherwise all collision rates must be adjusted at each timestep. However, it can be shown that, provided the collision rates stay constant, the grouped rates in Eq. (5.10) will conserve the mean of the particle distribution if $i \neq j$ (see App. 5.A). The last assumption is the weakest: the individual rates between the particles in principle change after each individual collision as the collision affects the properties of the particles. Therefore, expressions such as $g_i g_j C_{ij}$ should actually be averaged over the number of collisions that make up the group process. This is of course a very tedious procedure with which we would go back to the one-by-one treatment of the particles. Rather, we prefer to introduce a new parameter, f_ϵ, that limits the amount of mass accretion onto a particle during the group collisions, thereby strengthening the approximation that the C_{ij} stay constant during the group collision process.

Choosing the particle labels again such that j has the high zoom factor ($z_j \geq z_i$) the fractional mass accretion on a single i particle is $\Delta m_i/m_i = 2^{z_j - z_i} m_j/m_i$. From the preceding discussion it is this quantity that should be limited from below by a fixed value, f_ϵ. One way to implement this is to reduce the j-particles that take part in the collision. For example, in Fg. 5.2a this could mean that only 2 j-particles are involved, *i.e.*, only a fraction of the particles in a group. Let this fraction be denoted by 2^{-N_ϵ} with $N_\epsilon \geq 0$ an integer. Then, only $2^{z_j - z_i - N_\epsilon}$ j-particles are involved in the collision and the mass of an i particle increases by $2^{z_j - z_i - N_\epsilon} m_j$, *i.e.*,

$$\frac{\Delta m_i}{m_i} = \frac{2^{z_j - z_i - N_\epsilon} m_j}{m_i} \leq f_\epsilon. \tag{5.11}$$

Solving for the group splitting factor, N_ϵ, gives

$$N_\epsilon = \left[-\log_2 (f_\epsilon 2^{z_i} m_i / 2^{z_j} m_j) \right], \tag{5.12}$$

where the square brackets denote truncation to integer numbers ≥ 0. Consequently, the collision rates, instead of Eq. (5.10), now become

$$\lambda_{ij}^G = g_i g_j C_{ij} / 2^{z_j - N_\epsilon} = w_i w_j 2^{z_i + N_\epsilon} C_{ij}; \qquad z_i \leq z_j, \tag{5.13}$$

(the collision rates for in-group collisions do not change since $N_\epsilon = 0$). Another consequence is that the group numbers are real numbers, *i.e.*, since a fraction 2^{-N_ϵ} of the j-group is removed, its group occupation number decreases accordingly, $w_j \rightarrow w_j - 2^{-N_\epsilon}$. The $\{g_i\}$ cannot become fractional, however, since this would physically split a particle. Also, a situation where $0 < w_i < 1$ is not allowed, because $\Delta w = 1$ for the particle of the lowest zoom factor; when it arises we 'demagnify' the group ($z_i \rightarrow z_i - 1$) such that $w_i \geq 1$ (see below, § 5.2.4).

5.2.3 Choosing the zoom factors

We have implemented the grouping method in such a way that the zoom factors, are free parameters, and there is indeed considerable freedom to choose (an algorithm for) the $\{z_i\}$. However, it is also an important choice as it will determine how *efficient* the Monte Carlo simulation becomes. Here, with "efficient" it is meant that the number of species N_s should not (suddenly) increase. A way that observes this constraint fairly well is to divide the mass inside the simulations equally over the groups. In addition, we present a more general method, in which the zoom factors are determined by the particle distribution.

Equal mass approach

In this method, we assume there is a characteristic mass $m^\star$ after which the zoom factors are determined. Particles of mass larger than $m^\star$ are ungrouped ($z = 0$), whereas particles of mass $m < m^\star$ have zoom factors such that the group mass is around $m^\star$, *i.e.*,

$$z_i = \log_2(m^\star / m_i). \tag{5.14}$$

In the case of constant-V simulations and monodisperse initial conditions of unity mass the simulation then starts with $\mathcal{N}/m^\star$ groups, where $\mathcal{N}$ is the initial number of particles. Therefore, $\mathcal{N}/m^\star$ is a measure for the number of species parameter N_s. The target value of N_s, N_s^*, and $\mathcal{N}$ then determine the value of $m^\star$. For the constant-N_s simulations, where the mass in the simulation varies, the mass peak m_p is a natural value for the characteristic mass, $m^\star = m_p$. It forces most of the groups to represent particles around the mass peak, with those of higher mass ungrouped.

Thus, the equal mass approach resolves the mass density of the distribution, instead of the particle density as in conventional MC methods. Once a species becomes insignificant in terms of mass, $m_i 2^{z_i} < m^\star$, occupancy number approaches unity ($w_i = 1$) and the species will be "removed" from the simulation when it collides at the next collision, completely independent of the actual number of particles a group contains.

Distribution approach

A different way to choose the zoom factors is to force the distribution to be resolved over its entire mass range. This can, for example, be done by dividing the distribution into exponentially-spaced mass bins and to choose the zoom factors such that there are a fixed number of groups per bin. Here the bins are exponentially distributed between a lower mass (most often the initial mass, m_0) and the largest mass M_{L1} present in the simulation. For example, let N_k be the total occupancy number of bin k, then the zoom numbers are determined by the requirement that an equal number of groups is present in each bin, *i.e.*, $N_k/2^{z_k}$ is constant for each bin k. There is no constraint on the number of species per bin, but as this quantity is always less than the number of groups it is limited as well. For a smoother progression of zoom factor with mass we allow for a linear interpolation within each bin, such that the zoom factors become a continuous, piecewise, and decreasing function of mass, $z(m)$. Thus,

z is now determined, not by the particle or mass density, but by the sheer occurrence of particles of a certain mass. The bins and zoom factors are dynamically adjusted, as the simulation progresses, and the distribution changes.

The distribution method has the consequence that (high-m) fluctuations are resolved very well, even if they are completely insignificant by number and mass. The zoom factors of these particles are much reduced in comparison with the equal mass method. For example, if the $m_0 = 1$ particles are still at zoom levels of z_0 situations where $2^{z_0} m_0 \gg 2^{z_i} m_i$ are frequently encountered. A collision between a massive and an $m = 1$ group then takes place at a high value of N_e (Eq. (5.12)) and collision rates involving high-m groups increase (Eq. (5.13)). Since each collision creates a new species, the number of species (N_s) also increases rapidly—too rapid, in fact—and we are forced to merge species (§ 5.2.1). Merging of species is therefore a necessary feature of the distribution method.

5.2.4 (De)magnification

In the grouping method the zoom factors of the groups are determined in accordance with one of the two methods above. The zoom factors will therefore change during the simulation. When z_i increases ($z_i \to z_i + 1$) we speak of *magnification*, whereas when z_i decreases the group is *demagnified* ($z_i \to z_i - 1$). This dynamical adjustment of the zoom factors is the main reason why the method is capable of achieving very high dynamic range. Demagnification furthermore occurs when the occupancy number of a group becomes fractional, $0 < w_i < 1$. However, we note again that the actual number of particles of a species, g_i, is always an integer.

There is a small price to pay in terms of overhead for these re-adjustments. Because the $\{z_i\}$ are an argument of the collision rates (Eq. (5.13)) these rates (or, more accurately, the $\{\lambda_i\}$ quantities, as these are the ones that are stored in the computer's memory, $\sim N_s$ in total) have to be adjusted at each (de)magnification event. This may slow down the simulation by a factor of 2. Finally, we note that (de)magnification is, within the context of the grouping algorithm, an exact procedure; collision rates are not approximated and the total mass of the simulation stays conserved.

5.2.5 Grouping Summary

We have outlined an approach for a Monte Carlo coagulation scheme that can involve many particles—allowing the growth to be orders of magnitude—yet avoids the severe computational problems that would naturally arise with a single particle per collision treatment. In App. 5.B we have summarized the main steps of the algorithm in the context of the grouping method. At its core lies the approximation that many identical particles are present, due to monodisperse initial conditions or the duplication mechanism, which can be efficiently grouped together or (in the distribution method) merged. Collisions are now between two groups of, possibly, many particles and this significantly speeds up the computation. While it is clear that such grouping inevitably approximates the collision process, we have advocated a fundamental shift in the implementation of MC methods, *i.e.*, to focus on the particles in a distribution that really matter—*e.g.*, those around $m = m_p$—and we anticipate that the benefits resulting from the new emphasis will more than justify the approxima-

LIST OF SIMULATIONS

Kernel	Figure	Type	Grouping	N_s^* / N_g^*	$\mathcal{N}$	f_ϵ	N_{sim}
(1)	(2)	(3)	(4)	(5)	(6)	(7)	(8)
sum kernel	Fig. 5.3	cnst-N_p	none	10^5	...	10^{-4}	40
sum kernel	Fig. 5.4a	cnst-N_s	equal mass	2×10^4	...	10^{-4}	40
sum kernel	Fig. 5.4b	cnst-$\mathcal{V}$	distribution	10^4	10^{100}	10^{-4}	40
product kernel	Fig. 5.5	cnst-$\mathcal{V}$	equal mass	2×10^4	10^{20}	10^{-4}	40
product kernel	Fig. 5.6	cnst-$\mathcal{V}$	distribution	10^3	10^{20}	10^{-4}	40
runaway kernels	Fig. 5.7	cnst-$\mathcal{V}$	distribution	$\lesssim 10^5$ [a]	10^{160} [a]	10^{-4}	100[a]
sum: fragment.	Fig. 5.8	cnst-N_s	equal mass	2×10^4	...	10^{-3}	1[b]
cnst: fragment.	Fig. 5.9	cnst-N_s	equal mass	10^4	...	10^{-3}	1[b]

Table 5.2: Summary of all simulations. (1) Collision kernel. (2) Figure reference. (3) Simulation type: fixed or adjustable volume. (4) Grouping method: outlines in which way the zoom factors, $\{z_i\}$, are chosen (no grouping, equal mass, or distribution method). (5) Target number of species (equal mass method), or groups (distribution method) in simulation. When multiple values apply the largest is given. (6) Initial number of monomers, or total mass in simulation for constant-$\mathcal{V}$ simulations. (7) Fractional mass accretion. (8) Number of simulations performed. The initial distribution is monodisperse in all simulations with $m_0 = 1$. *Notes.* [a]Upper limit. [b]In fragmentation simulations a steady state is reached in which the distribution is averaged ∼100 times during the same simulation.

tions inherent to the grouping method. In any case, to validate the new method a comparison must be made with the analytic solutions of the classical kernels, after which the algorithm can be applied to more physically interesting kernels.

5.3 Results

In this section the grouping method—both the equal mass approach, as well as the distribution method—is tested in situations that require a high dynamic range. Its performance is then discussed. First, the grouping method is tested against the sum kernel. We show that both the equal-mass and the distribution methods are capable of following the analytic distribution, whereas conventional MC methods (without grouping) will fail. The grouping method is also tested against the product kernel, which is one of a class of kernels that produces runaway-growth behavior. For these kernels it will be shown that that it is important to accurately follow the fluctuations of the mass distribution, which can only be done by the distribution method. More runaway-models are discussed in § 5.3.3. Finally, we also perform simulations including a simplified form of fragmentation, where the particles are catastrophically fragmented at the largest scale m_{frag} to be injected back at the smallest scale m_0 (§ 5.3.4). We test whether the grouping method can also be applied in these cases. An overview of the simulations is given in Table 5.2, including the adopted numerical parameters. These are chosen such that the CPU-time per simulation is typically several hours on a modern desktop machine (1.8 GHz clock speed). Similar CPU-times apply for the choice of the numerical parameters of the simulations including grouping.

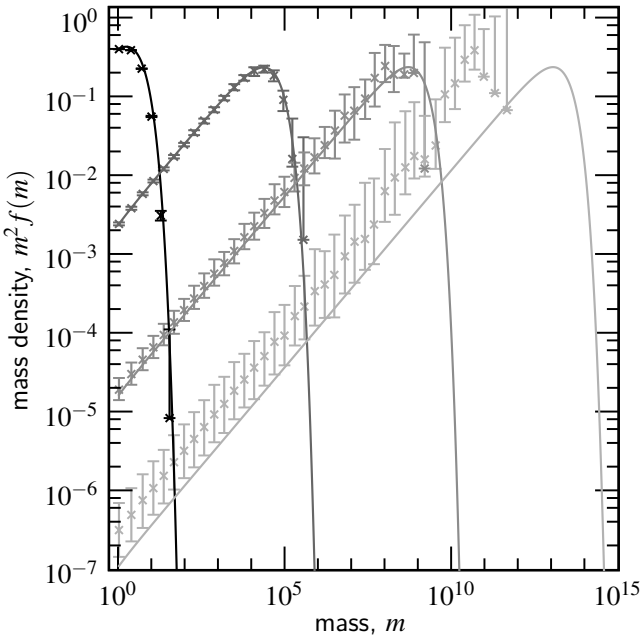

Fg. 5.3: Results for the sum kernel, $K_{ij} = \frac{1}{2}(m_i + m_j)$, *without* grouping for $N_\mathrm{p} = 10^5$. Distributions are plotted at dimensionless times $t = 1, 10, 20$ and 30 and error bars show the spread over 40 simulations. Particles are binned at each factor of two in mass. The correspondence with the analytic results (*solid curves*) deteriorates over time. After $t \simeq 20$ the mass peak is no longer resolved by the simulation.

For the product and other runaway kernels, the system will after a certain time be dominated by a single particle. Hence, no self-similar solutions exist and in order to study the evolution properly, the simulation volume of these systems must be well defined. These simulations are therefore modeled using constant-volume simulations. In most cases the distribution method is used, which also requires a fixed simulation volume. In the other cases, we may assume that a small volume is representative of the parent distributions, which can then be modeled using constant-number simulations. The only exception is Fg. 5.4b, where we have used the distribution method in order to compare it to the results of the equal-mass method simulations of Fg. 5.4a.

5.3.1 Test case I: the sum kernel

Before presenting the results of the grouping mechanism, a case without the grouping method is considered first, illustrating some of the 'deficiencies' mentioned in § 5.1. We do not consider the constant kernel, because in the constant kernel the dynamic range ($m_\mathrm{p}/\langle m \rangle$) stays confined and a grouping method is not required. In Fg. 5.3 the number of simulation particles, N_p, is kept constant at 10^5. The distribution function is plotted at various times during its evolution, $t = 1, 10, 20$ and 30. Times are dimensionless, *i.e.*, in units of $(K_{00} n_0)^{-1}$ where K_{00} and n_0 are the kernel and number density corresponding to the initially monodisperse conditions of particles of mass $m_0 = 1$. In Fg. 5.3, as well as in all other figures that show distributions from the MC simulation, $f(m)$ is determined using exponentially-spaced bins every factor of 2 in mass. Each point shows the average and spread of in total 40 model

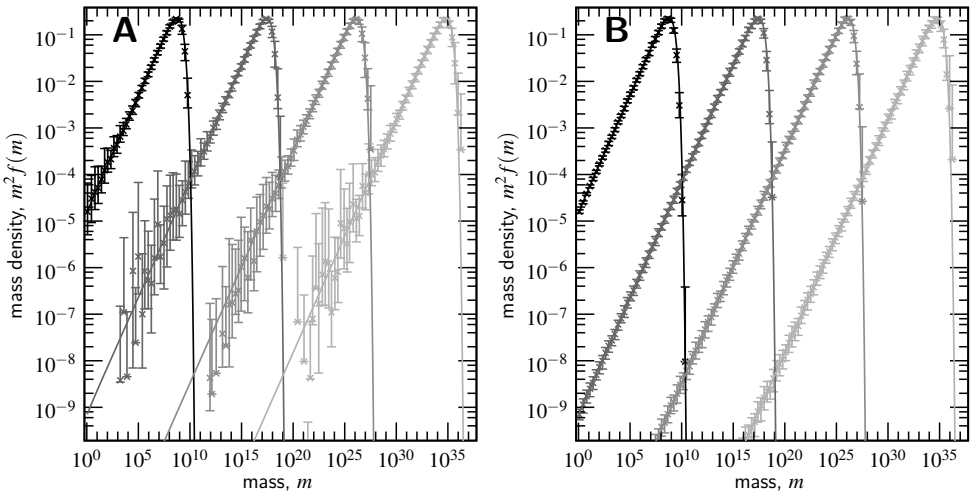

Fig. 5.4: Results for the sum kernel using the grouping algorithm. Particle distributions (*symbols*) are shown at times $t = 20, 40, 60$ and 80. Particles are binned at each factor of two in mass and results from 40 separate simulations are combined. The spread in the simulations is denoted by the error bars. *(a)* Equal mass method, $N_s = 20\,000$. Thanks to the grouping algorithm most of the groups are centered on the mass peak, which favors an accurate computation of the collisional evolution, without introducing systematic errors. *(b)* Distribution method with $N_g^* = 10\,000$, distributed over 20 bins. The zoom factors are adjusted to resolve the distribution over its entire range.

runs in total. The analytic distribution functions at these times are given by the solid curves.

Initially, $t < 10$, the agreement between the MC simulation and the analytic curve is very good. The mass range in the simulation is still rather modest and the 10^5 particles suffice to represent all relevant masses. However, while the peak mass progresses steadily to higher m, the majority of particles stays behind at low masses; that is, although both $\langle m \rangle$ and m_p evolve exponentially with time (Fig. 5.1), $m_p / \langle m \rangle$, which is a measure of the dynamic range, also increases exponentially. Since MC methods sample the number density, increasingly fewer particles become associated with the mass peak, and the simulation loses numerical resolution. The effects of these low-number statistics are a bit alleviated by averaging over many different simulation runs but it is not merely a statistical deterioration; the mass peak dominates the collisional sweep-up of the system and the fluctuations caused by an inaccurate characterization blow up. There is especially a trend to lag the analytic solutions, because, it is impossible to 'recover' from a lagging distribution, because the duplication mechanism does not duplicate the particles that are not present. At $t = 20$ these problems already become apparent when the spread is very high, especially around the mass peak, and there is a slight tendency to lag the analytic curve. At $t = 30$ the effects are disastrous: 10^5 particles are simply too few to sample a large enough volume to represent the large particles.

Because of the duplication mechanism many duplicates are created and N_s slowly decreases. This somewhat speeds up the computation at larger times since collisional rates scale with N_s^2. A more accurate result will be obtained by keeping N_s constant (Ormel et al. 2007). However, now N_p increases and the simulation suffers computational freeze-down as it progresses. Fundamentally, either approach — the constant N_p or constant N_s — is the same since each cycle only treats one collision and each collision is equally important. Clearly, this 'socialist' approach is ineffective as Fg. 5.3 illustrates: the more massive particles deserve more attention than their smaller brethren.

Results with the grouping method applied are shown in Fg. 5.4. In Fg. 5.4a we used the equal mass method for the groups (each group has a mass of $\sim m^\star = m_p$ if $m < m_p$ and particles with $m > m_p$ are not grouped) and chose the zoom factors accordingly (see Eq. (5.14)). The number of species, N_s, is stabilized at a target number of $N_s^* = 2 \times 10^4$ through the duplication mechanism. That is, if N_s due to coagulation falls below N_s^*, duplicates are added to the system until $N_s \geq N_s^*$. The simulation total mass and volume then increase, but their ratio (the mass density) is fixed. As m_p becomes larger during the simulation, zoom factors of particles that do not take part in collisions will increase, according to Eq. (5.14). This 'magnification' causes the occupancy numbers w_i to stay low, despite the ongoing duplication events. When w_i reaches 1, the species will disappear at the next collision, freeing up this slot for more massive particles. The grouping thus forces the particles to act collectively. This procedure prevents the systematic errors (N_p constant, Fg. 5.3) or computational freeze down (constant N_s) of the 'one collision per cycle' approach of the conventional MC methods.

Figure 5.4a shows that the grouping mechanism resolves the mass peak well during its entire simulation. The agreement between the analytic and numerical method remains very good during the entire simulation. Figure 5.4a proves that once the mass peak is resolved, the simulation will accurately compute the collisional evolution, and systematic errors as in Fg. 5.3 are prevented. Thus, the resolution of the mass peak is key. However, at lower mass densities the groups disappear from the simulation as they do not have sufficient mass.

These low-m statistics can be accurately followed when we switch the method for assigning the group's zoom factor $\{z_i\}$ to the distribution method, in which the zoom factors are adjusted such that there are an equal number of groups per exponential mass interval. The zoom number for the low-m particles is then much lower in comparison with the equal mass method. Figure 5.4b shows that the mass density as well as number density are accurately followed over the entire distribution. It can be seen in Fg. 5.4b that the match to the high-m tail slightly deteriorates over time. This is a consequence of the equal spacing in log space of the bins that determine the zoom factors. The high-m tail, which falls off exponentially, becomes associated with only a single bin, and is then less well resolved. A more flexible placement of the bins is expected to give an even better correspondence. Note again that the bins are only needed to determine the zoom factors; there's no actual binning of the particles in the MC simulation.

Although Fg. 5.4b more precisely follows the distribution — *i.e.,* it both follows

the mass density as well as the number density — it requires to *merge* species in order to restrict their numbers (see § 5.2.1). For these test cases, in which only mass is a parameter, Fg. 5.4b shows that this is not problematic. However, when structural parameters are involved, the merging procedure is less obvious; *i.e.*, are species of comparable mass merged or, say, species of comparable porosity? The merging principle is, therefore, somewhat against the spirit of MC simulations, as there is no physical equivalent of 'merging' in nature. Thus, for a MC simulation with many structural parameters, where it is not required to resolve the number density, Fg. 5.4a is probably the preferred method. In the other test cases of this section we therefore first pursue whether these can be modeled by the equal-mass method.

5.3.2 Test case II: the product kernel

The kernel $K_{ij} = m_i m_j$ is the only runaway kernel with an analytic solution. In models that show runaway-behavior a particle will appear that separates from the continuous distribution to consume, in a relatively short time, all the available mass. This separation is an intrinsic feature of the kernel and is not caused by a poor sampling of the distribution. The point at which this separation occurs, t_R, depends on the properties of the kernel and, in some cases, on the initial number of particles ($\mathcal{N}$). In the case of the product kernel it always occurs at $t = 1$, independent of $\mathcal{N}$. The runaway growth properties of other kernels are discussed in § 5.3.3.

In § 5.1 it was noted that the Smoluchowski coagulation equation becomes invalid in the case of the runaway kernel: it keeps assuming that the distribution is continuous and it is therefore ill-suited to describe a discrete system caused by the runaway particle. Wetherill (1990) has adjusted the original (incorrect) solution of Trubnnikov (1971) by inclusion of a term for the runaway body in Eq. (5.1). Although not mathematically rigorous, this approach captures the physics of the runaway: as soon as the (incorrect) numerical solution exhibits a $f(m) \propto m^{-5/2}$ power-law tail, the interaction between the higher mass bins causes the runaway growth. In the Monte Carlo simulations we also expect that the appearance of a power-law tail is a signature that runaway growth is incipient.

In Fg. 5.5 the distributions corresponding to the product kernel with $\mathcal{N} = 10^{20}$ are plotted at dimensionless times $t = 0.4, 0.7, 0.95, 1.0, 1.05, 1.3$ and 2.0, using the equal mass method. Since we start the simulation already with a huge number of particles, large zoom numbers are required. We have fixed the mass peak at $m_\star = \mathcal{N}/10^4$, which causes the particles to be sufficiently magnified, except for the runaway particle. (The 10^4 factor may be thought of as a fudge parameter akin to N_s or N_p in the constant-N simulations.) Theoretical curves correspond to the Trubnnikov (1971) solutions which, as Wetherill (1990) showed, are still valid for the continuous part of the distribution. At $t = 1$, runaway growth is expected and the continuous power-law distribution reaches its furthest extent: the $-5/2$ power-law exponent. After the runaway particle has separated the continuous distribution shrinks, especially in the $-x$ direction since the more massive particles are consumed rapidly by the runaway body, which itself is not shown in Fg. 5.5.

The runaway growth is generally well modeled by the Monte Carlo method. The distribution becomes most sensitive near $t = 1$ where a small change in time means

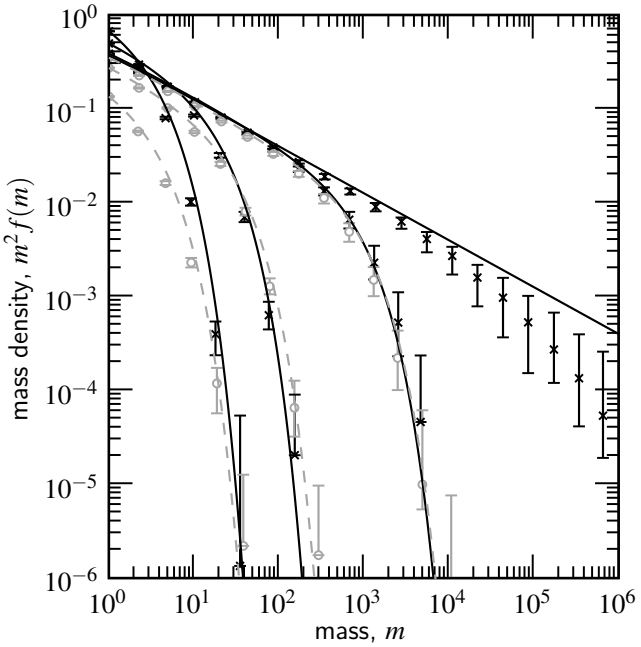

Fig. 5.5: Results for the product kernel, $K_{ij} = m_i m_j$, with $\mathcal{N} = 10^{20}$. The simulated distribution is plotted at times $t = 0.4$, 0.7, 0.95, and 1.0 (from left to right, *crosses*) and $t = 1.05$, 1.3 and 2.0 (from right to left, *circles*). The analytic solution is plotted by solid curves for $t \leq 1$ and by the dashed curves for $t > 1$ (the $t = 0.95$ and $t = 1.05$ curves almost overlap). Error bars denote the spread in the 40 simulations. After $t \approx 1$ a runaway particle of mass $m \sim \mathcal{N}$ appears that consumes most of the mass in the system.

a big change in the high-m distribution function. Because of the stochastic behavior of the Monte Carlo method, the precise timing of the runaway event does not exactly coincide with $t = 1$. Therefore, the $t = 1$ distribution lags the theoretical curve since at $t = 1$ either runaway growth did not yet occur (and the distribution still has to reach the power-law curve) or has already happened (and the distribution is on its way back from the power-law curve). In Fig. 5.6 the relation between the two most massive groups is denoted by the thick solid curve, together with the simulation time t as function of M_{L1}. Figure 5.6 shows that until $t = 1$ there is little difference between the mass of the most massive particle—actually group—M_{L1} and the second-most massive group M_{L2}. However, as runaway is reached at $M_{L1} \sim 10^5$ the masses diverge very quickly.

These results, however, are in disagreement with the theoretical study of Tanaka & Nakazawa (1994). Comparing the solutions to the stochastic and the statistical equation they find that, in the case of the product kernel, the statistical equation (Eq. (5.1)) becomes invalid after $M_{L1} \sim \mathcal{N}^{2/3}$. It is only at this point that M_{L1} and M_{L2} should start to diverge. However, in the equal-mass method (Fg. 5.6, thick solid curve) the divergence happens much earlier: M_{L2} never reaches beyond $10^8 \ll (10^{20})^{2/3}$. This discrepancy can be explained as an artifact of the equal mass method. Because each group is still of considerable mass, $m^\star \sim 10^{16}$, runaway growth is just the collapse of one group by a continuous series of in-group collisions (Fg. 5.2b); that is, until $z_i = 0$, the M_{L1} group does not correspond to a single particle and therefore never really separates. It is thus not a proper modeling of a runaway process. In order to accurately follow the behavior of the particles during runaway growth, the groups should be demagnified much more rapidly than Eq. (5.14) al-

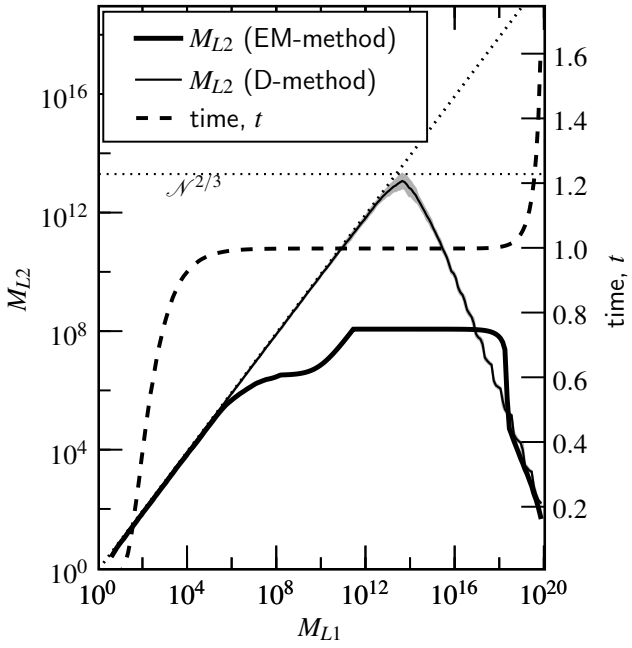

Fg. 5.6: Statistics for the simulations involving the product kernel. As function of the mass of the largest species, M_{L1}, are shown: the mass of the second-largest species, M_{L2}, according to the equal-mass method (*thick solid curve*) and the distribution method (*thin solid curve*); and the time (*dashed curve*). Values are averaged over 40 runs. The auxiliary lines $M_{L2} = M_{L1}$ and $M_{L2} = \mathcal{N}^{2/3}$ are also given (*dotted lines*).

lows. It is perhaps surprising that the equal-mass method still works fine — *i.e.*, its distribution agrees with the analytical case (Fg. 5.5) — despite the fact that it does not resolve the runaway particles. However, in general this is not the case: the fluctuations present at high-m require more resolution than what is attributed to them through the equal representation of mass density (Eq. (5.14)).

In Fg. 5.6 the M_{L1} and M_{L2} statistics of the product kernel are recalculated with the distribution method for the zoom factors (thin solid curve). According to the Tanaka & Nakazawa (1994) prediction M_{L1} and M_{L2} should then separate at $M_{L1} \sim \mathcal{N}^{2/3}$. This is exactly the trend seen in Fg. 5.6. We therefore conclude that the distribution method is the appropriate choice to compute the collisional evolution of runaway kernels.

5.3.3 Strong Runaway kernels

There is an extensive literature on the phenomenon of runaway growth, especially mathematical ($\mathcal{N} \to \infty$), where the phenomenon is termed *gelation*. In general, three growth modes can be considered (see Table 5.3): (i) kernels where runaway growth does not appear, as in the constant or sum kernel; (ii) kernels that exhibit growth after some characteristic time, as in the product kernel; and (iii) kernels in which gelation is *instantaneous*.[2] The occurrence of instantaneous gelation for the class of kernels $K \propto (m_i m_j)^\nu$ with $\nu > 1$ was conjectured by Spouge (1985) on the basis of MC

[2]We note that in a physical situation where runaway growth tends towards instantaneity, causality should not be violated. As we will see, $\mathcal{N}$, even in astrophysical circumstances, does not become so large that the process is instantaneous.

Runaway models		
type	conditions	growth mode
(i)	$\nu \leq 1, \beta \leq 1$	Orderly growth
(ii)	$\nu \leq 1, \beta > 1$	Runaway growth at t_0
(iii)	$\nu > 1$	Instantaneous runaway growth[a]

Table 5.3: Properties of runaway models according to the study of Lee (2000). The exponents ν and μ give the mass dependence of the kernel on a heavy and light particle, respectively, with $\beta = \nu + \mu$ the total mass dependence, $K_i j \propto m_i^\nu m_j^\mu$ ($m_i \gg m_j$). *Notes:* [a]Instantaneous in the limit $\mathcal{N} \to \infty$.

coagulation experiments and was proved by Jeon (1998). Lee (2000) illustrates these distinct modes of solution by a simple coagulation model, in which the distribution is approximated by a characteristic mass m, *e.g.*, the peak mass, and a test particle of mass $M > m$. Particles of mass m dominate the total mass and hence $n(m) \propto m^{-1}$. Furthermore, the coagulation kernel is characterized by two exponents, ν and μ, that give the dependence of $K(m_i, m_j)$ in the case of a heavy (i) and a light particle (j), *i.e.*, $K_{ij} \propto m_i^\nu m_j^\mu$, for $m_i \gg m_j$. The total mass dependence is then given by $\beta = \mu + \nu$. For example, in the case of the product kernel $\nu = \mu = 1$ and $\beta = 2$. Setting the physical density equal to unity, the equations for the simplified merger problem become (Lee 2001)

$$\frac{\mathrm{d}m}{\mathrm{d}t} = \tfrac{1}{2} m^\beta; \tag{5.15a}$$

$$\frac{\mathrm{d}M}{\mathrm{d}t} = m^\mu M^\nu. \tag{5.15b}$$

These can also be combined to obtain

$$\frac{\mathrm{d}M}{\mathrm{d}m} = 2 \left(\frac{M}{m} \right)^\nu. \tag{5.16}$$

Equation (5.15a) can be solved as

$$m = \begin{cases} \left[1 + \tfrac{1}{2}(1-\beta) \right]^{1/(1-\beta)} & \text{for } \beta \neq 1; \\ \exp[\tfrac{1}{2} t] & \text{for } \beta = 1, \end{cases} \tag{5.17}$$

where we have for simplicity taken $m_0 = m(t = 0) = 1$. Equation (5.16) can be solved in terms of m as

$$M(m) = \begin{cases} \left(M_0^{1-\nu} + 2m^{1-\nu} - 2 \right)^{1/(1-\nu)} & \text{for } \nu \neq 1; \\ M_0 m^2 & \text{for } \nu = 1, \end{cases} \tag{5.18}$$

where $M_0 > 1$ is the initial mass of the test particle. Three qualitatively distinct growth modes follow from these equations: (i) if $\nu \leq 1$ and $\beta \leq 1$ both Eq. (5.17) and Eq. (5.18) have finite solutions at all t: orderly growth. (ii) If $\nu \leq 1$ and $\beta > 1$, Eq. (5.17) reaches a singularity at a time $t = t_R = 2/(\beta - 1) > 0$,[3] while Eq. (5.18) does not: both m and M become infinite at the same time t_R that does not depend on M_0. (iii) If $\nu > 1$, Eq. (5.18) reaches infinity for a finite value of m. Furthermore, the gelation time *decreases* with increasing M_0, $t_R \simeq M_0^{1-\nu}/(\nu - 1)$. Then, if the initial mass in the system goes to infinity, a sufficiently strong fluctuation (large M_0) will always be present to satisfy the singularity condition for $M(t)$ even as $t \to 0$; this is the physical reason behind the instantaneous gelation conjecture.

Here, we concentrate on the case $\nu > 1$ and test the instantaneous gelation conjecture for kernels $K = (m_i m_j)^\nu$ with $\nu = 2$ and 3. Malyshkin & Goodman (2001) extend the simplified merger model discussed above to a model with only two kinds of particles — one predator and many preys — and one collisional process (the predator feeds of preys). This is the monotrophic model, *e.g.*, one particle ('mono') that nourishes ('trophein') off the others. Considering this model, Malyshkin & Goodman (2001) compute the probability that the predator occupies any finite mass, which decreases with increasing time. Consequently, the gelation time t_R is computed as

$$t_R \propto (\log \mathcal{N})^{1-\nu}, \tag{5.19}$$

where $\mathcal{N}$ is the initial number of particles present. Thus, the timescale for runaway growth decreases as function of the initial number of particles in the system, but only logarithmically. Equation (5.19) may be anticipated from the discussion above on the simple merger model. Consider a distribution of particle masses $N(m)$ at a fixed time. It is quite likely to expect that the tail of the distribution is exponentially suppressed as in the case with Poisson statistics, *i.e.*, $N(m) \propto \mathcal{N} \exp[-m]$ with $\mathcal{N}$ the total number of particles. Setting $N = 1$ we thus obtain $M_0 \sim n \sim \log \mathcal{N}$. Hence, the logarithmic dependence on the number of particles. Malyshkin & Goodman (2001) tested this model by Monte Carlo simulations and found qualitative agreement: the gelation time decreases as function of $\log \mathcal{N}$, although the power-law exponent is not precisely that of Eq. (5.19): $1 - \nu$. However, the simulations of Malyshkin & Goodman (2001) were limited in their dynamic range; we will extend their study to much larger values of $\mathcal{N}$ to see whether Eq. (5.19) holds over a sizeable range of $\log \mathcal{N}$.

Note that as conjectured above, a good census of the fluctuations is the key to an accurate modeling of the collisional evolution. Therefore, the grouping must then be implemented by the distribution method. There is, however, another catch. At $t = 0$ the number of groups of the monodisperse species is $w_0 \sim N_g^* \ll \mathcal{N}$ and the collision rate for a collision between two monomers according to Eq. (5.10) is $\lambda_{11} \sim \mathcal{N} w_0 C_{11} \sim w_0$. Then, the timescale for collisions involving monomers is $t_{11} = \lambda_{11}^{-1} \sim w_0^{-1}$, which can, however, become comparable to, or larger than, the

[3] Note that this expression disagrees with the product kernel in which $\beta = 2$: the simplified merger model does not give the correct prefactor, see Lee (2001).

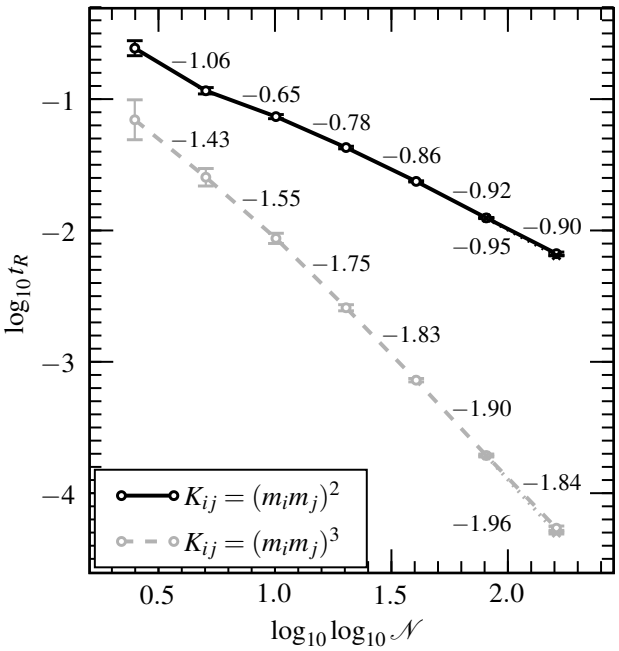

Fig. 5.7: The runaway time t_R as function of the initial number of particles $\mathcal{N}$ for the kernel $K_{ij} = (m_i m_j)^\nu$ with $\nu = 2$ (*solid curve*) and $\nu = 3$ (*dashed curve*). Simulations are run at $\mathcal{N} = 300, 10^5, 10^{10}, 10^{20}, 10^{80}$ and 10^{160}. The power-law index is indicated at every interval of $\log\mathcal{N}$. The agreement with the theoretically expected value for the power-law index, $1-\nu$, becomes better at higher $\mathcal{N}$. At $\mathcal{N} = 10^{160}$ a simulation at a higher numerical resolution gives an even steeper slope (indicated below the line) confirming the converging trend towards, respectively, -1 and -2.

runaway timescale of Eq. (5.19). Therefore, the monodisperse groups have to be demagnified such that $t_{11} \ll t_R$. By forcing the appropriate collision timescale for the monodisperse collisions, the fluctuations are adequately resolved, but it also means that the CPU-time increases, especially at large $\mathcal{N}$. For the $\nu = 2$ simulations we used a number of $N_g^* = 60\,000$, whereas in the $\nu = 3$ simulations we take $N_g^* = 300\,000$. At $\nu = 3$, runaway occurs at a lower value of M_{L1} and we are allowed to start with a higher number of groups. However, the discrepancy between the simulations at different values of $\mathcal{N}$ becomes large in terms of CPU-time: the highest-$\mathcal{N}$ simulations take about half a day to finish.

The results for the kernels $K = (m_i m_j)^2$ and $K = (m_i m_j)^3$ are presented in Fg. 5.7. We extend the model of Malyshkin & Goodman (2001) to an unprecedented 10^{160} particles (about the square of the number of particles in the universe). To speed up the simulations at high $\mathcal{N}$ we have decreased the mass-ratio parameter f_ϵ to 10^{-3} (which we checked to be still sufficiently accurate). The number of simulations varies between $N_{\rm sim} = 100$ at low $\mathcal{N}$ and $N_{\rm sim} = 10$ at $\mathcal{N} = 10^{160}$. We stop the simulations when the ratio between the two largest masses becomes $M_{L1}/M_{L2} \geq 10^4$, which is a measure of t_R. By this time the simulation has either already finished or has reached it asymptotic limit.

According to the analytic prediction (Eq. (5.19), Malyshkin & Goodman 2001) the t_R-$\log\mathcal{N}$ power-law is -1 and -2 for $\nu = 2$ and $\nu = 3$, respectively. In Fg. 5.7 the piecewise exponent is indicated (number above the lines), which shows a declining trend, except for the $\mathcal{N} = 10^{160}$ point. To check convergence, we have additionally performed five simulations at a higher numerical resolution for $\mathcal{N} = 10^{80}$ and 10^{160}

($N_g^* = 2 \times 10^5$ for the $\nu = 2$ simulations and $N_g^* = 2 \times 10^6$ for the $\nu = 3$ simulations). For $\mathcal{N} = 10^{80}$ it was found that the results had converged, but at $\mathcal{N} = 10^{160}$ a reduced t_R compared to the lower resolution simulations was found. This increased the local slope between $\mathcal{N} = 10^{80}$ and 10^{160} (dotted lines, hardly distinguishable from the dashed lines, with the slope indicated below the line). Altogether, Fig. 5.7 suggests that the agreement between the numerical simulation and the monotrophic model becomes better as $\mathcal{N}$ increases, a conjecture already made by Malyshkin & Goodman (2001).

5.3.4 Fragmentation

The grouping method can also be used in steady-state situations where fragmentation balances coagulation. From the simulations in § 5.3.1 we expect that for the distribution method this is not a problem, as it follows both the mass density and the number density. We will therefore concentrate our efforts on the equal-mass method. Fragmentation events in Monte Carlo may seem problematic, because catastrophic destruction can result in the creation of many small particles that consume computational resources. However, due to the grouping method we now have a natural way to deal with fragmentation. In this section we consider a test case of complete destruction—meaning: the breakup of a particle into its smallest constituents (monomers)—that occurs once a mass threshold, $m_{\rm frag}$, is exceeded. We then solve for the emergent, steady-state, mass distribution. Note that due to stochastic fluctuations the number distribution is never really steady-state. We will therefore average over many distributions during the same simulation run to obtain the 'steady-state' mass spectrum.

In Fig. 5.8 the results of the sum kernel, $K_{ij} = m_i + m_j$, are given. In Fig. 5.8a the fragmentation threshold is $m_{\rm frag} = 10^{10}$. The crosses denote the average over $\sim$100 distributions during the simulation after the initial distribution has relaxed to a semi-steady state. The volume of the simulation is stabilized when it incorporates $N_s^* = 10^4$ species at $\mathcal{V} = 2 \times 10^{12} \gg m_{\rm frag}$. Figure 5.8b presents the result for an even larger value of $m_{\rm frag} = 10^{20}$. The same characteristic distribution—resembling a bath tub—is found. These results suggest that, for the sum kernel with catastrophic fragmentation at a cut-off mass, most of the mass density becomes located near the end points. The system may then be approximated by two states at $m = m_0 \sim 1$ and $m = m_{\rm f} \sim m_{\rm frag}$. The mass-loss of the monomer state due to collisions with the high-m state is $m{\rm d}m/{\rm d}t|^- = n_0 n_{\rm f} m_{\rm f}$, and the gain due to fragmentation within the high mass bin becomes $m{\rm d}m/{\rm d}t|^+ = n_{\rm f}^2 m_f^2$. Balancing these we get $n_0 = n_{\rm f} m_{\rm f}$, *i.e.*, equal mass densities for the monomer and high-m state.

However, with other kernels the mass distribution due to fragmentation may also emerge as a power-law. To see this we adopt a simple model (Camacho 2001) in which the mass sweep-up, $\dot{m}$, of a particle of mass m due to particles of lower mass $m' < m$ is assumed to change only the mass in a continuous way. That is,

$$\dot{m} = \int_{m_0}^{m} {\rm d}m' K(m, m') m' f(m'), \tag{5.20}$$

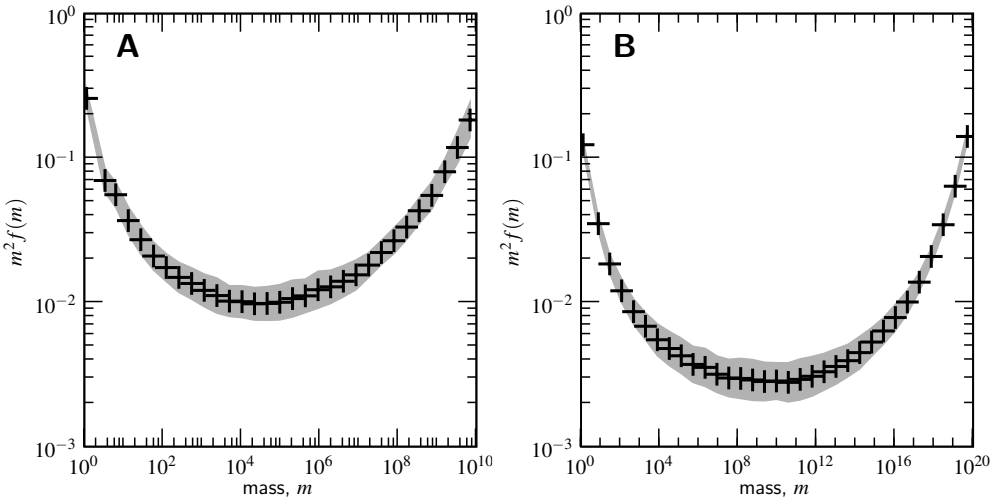

Fig. 5.8: Steady state distributions of the sum kernel. At $m = m_{\rm frag}$ particles are catastrophically disrupted into monomers of mass $m = m_0 = 1$. (*a*) Distribution with $m_{\rm frag} = 10^{10}$ and $N_{\rm s}^* = 10^4$. (*b*) Distribution with $m_{\rm frag} = 10^{20}$ and $N_{\rm s}^* = 2 \times 10^4$. Distributions are averaged over various times during the steady-state process. *Plus signs* denote this average over ∼100 distributions. The spread is indicated by the grey shading.

will shift particles of mass m by an amount $\Delta m = \dot{m}\Delta t$. The total particle change per unit time in the interval $[m, m + \Delta m]$ becomes $-\Delta[\dot{m}f(m)]$ due to gradients in $\dot{m}$ and the distribution function. The other side of the distribution then acts as a sink for the particles of mass m, *i.e.*, $R(m)f(m)\Delta m$ is the number of particles in $[m, m + \Delta m]$ that is 'consumed' by the more massive particles, with

$$R(m) = \int_m^{m_{\rm frag}} {\rm d}m' K(m, m') f(m'), \tag{5.21}$$

as the removal rate. For a steady state we must therefore have

$$\frac{\partial(\dot{m}f(m))}{\partial m} = -f(m)R(m). \tag{5.22}$$

Assuming a power-law for f, $f \propto m^\alpha$, Eq. (5.22) can be solved for α by extending the limits of the integrals in Eq. (5.20) and Eq. (5.21) to 0 and ∞, respectively (Camacho 2001). If $|\beta| < 1$ the integrals converge and the resulting power-law exponent is $\alpha = -(3 + \beta)/2$. The physical reason for the scale-free solution is thus that, contrary to the linear kernel, the behavior of the distribution near the cut-off points is unimportant for the (local) distribution. Other works have confirmed this power-law exponent, (*e.g.*, White 1982; Hayakawa 1987). If $\beta > 1$ the integrals do not converge: *i.e.*, collisions with the boundaries of the distribution dominate and no power-law emerges. However, Klett (1975) has shown that the $\beta = 1$ kernel $K_{ij} = (m_i m_j)^{1/2}$,

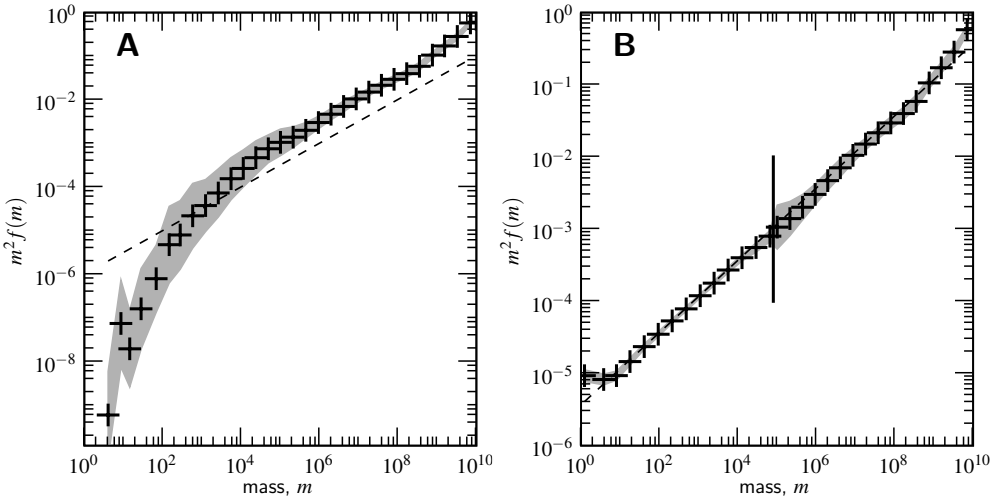

Fig. 5.9: (*a*) Catastrophic fragmentation in the constant kernel, $K = 1$, with $m_{\rm frag} = 10^{10}$. At masses above $m \sim 10^4$ a power-law develops with a slope approximately equal to the predicted slope ($\alpha = -3/2$; *dashed line*). At low-m the simulation lacks resolution and the power-law relation breaks down because of the episodic nature of the monomer injection. (*b*) This discrepancy is solved by performing a follow-up simulation for the low-mass part of the distribution only ($m < m_{\rm cut} = 10^5$) but including a removal rate due to collisions with large masses above $m_{\rm cut}$, $R(m)$, and a monomer injection rate, I, that were obtained in *(a)*. The distribution above $m_{\rm cut}$ is copied from *(a)*.

which therefore somewhat resembles the sum kernel, has an $\alpha = -2$ power-law.

To test whether a power-law emerges, we have performed fragmentation simulations for the constant kernel, $K = 1$, see Fig. 5.9. Thus, as $\beta = 0$ we expect to end up with a slope of $1/2$ for the $m^2 f(m)$ mass distribution. This trend is indeed observed in Fig. 5.9a but only at large masses. The reason why an extension of the power-law to low masses is not seen, is the same as in Fig. 5.4a. Again, due to the equal-mass method, region of low mass density are not represented. In addition, the injection rate at $m = m_0$ is episodic: at one instance many monomers of total mass $\sim m_{\rm frag}$ enter the system, such that the mass density at this particular instance becomes very high (in comparison to the expected power-law distribution) for a very brief period of time. However, as coagulation is a non-linear process, *i.e.*, $dn_0/dt \propto -n_0^2$, these particles coagulate very quickly with each other. In other words, the episodic injection rate has the effect of speeding up the coagulation compared to a smooth rate and, when averaged over time, the true distribution is underestimated at places where the particle density strongly fluctuates with time.

However, this deficiency of the equal-mass method does not affect the results at higher m: here the distribution is well resolved. Additionally, the mean (time-averaged) influx rate of monomers, I, at $m = m_0$ is available, as well as the removal rate of the higher mass particles, $R(m)$. A simple remedy to retrieve the low-m distribution becomes then available. In a separate simulation we have focused only

on the low-m part of the mass spectrum until a cut-off mass $m_{\rm cut}$, and additionally include the fixed rates I and R, which were obtained from the previous simulation. Thus, $R(m)$ is the probability that a particle of mass m collides with *any* particle of the 'frozen' large-m distribution that was previously obtained in Fg. 5.9a. Finally, if particles manage to grow above $m_{\rm cut}$ (*i.e.,* avoid to collide with a high-m particle through R), they are also removed. In this way we effectively re-perform the same fragmentation simulation, but in a reduced simulation volume, where the much smaller inter-collision time-increments Δt are appropriate for the low-m tail. In Fg. 5.9b this procedure is illustrated. Here, we put the cut at $m \approx 10^5$, recalculated the steady-state for small m, and 'glued' it to the high-m distribution of $m > m_{\rm cut}$ from Fg. 5.9a.

5.4 Summary and discussion

5.4.1 Merits of the Method

In the previous section we have applied the grouping method to a variety of situations and found satisfactory behavior, in terms of both accuracy as and required computing power, despite the large dynamic range under consideration. The collisional evolutions of the analytic kernels were tested and agreed with the theoretical distributions. We also confirmed the predictions made for a class of runaway kernels, which required us to model an unprecedented large number of particles. Finally, we applied the grouping method to situations in which fragmentation operates and found excellent agreement with earlier findings (at least for the constant kernel; we are not aware of a prediction for the shape of the distribution function in the sum-fragmentation kernel).

Here we further discuss the (dis)advantages of both the equal mass and distribution methods and compare them with other studies. In short our conclusions are the following: the equal mass method is a true MC method, in the sense that no merging of the species array is required, while the mass density of the distribution is resolved (following a characteristic mass). For non-runaway situations this is therefore the preferred method. Other work along these lines can be found in Shima et al. (2007). These authors implement a superparticle method to model rain drop formation. These super-droplets (like our groups) represent a multiple number of physical particles with the same properties (like mass) and position. However, their collisional setup is different. Where we allow many particles of one group to collide with another, in Shima et al. (2007) there is at most one collision per particle. Also, in the Shima et al. (2007) work the number of superdroplets is conserved and therefore (if we understand their picture correctly) the mean mass of the superdroplets is conserved as well. Thus, they always need a large number of superdroplets in order to resolve the high-m fluctuations (see the discussion on Fig. 2c of Shima et al. 2007). The biggest difference, therefore, is that our method allows a dynamical adjustment of the group sizes. Thus, we think the Shima et al. (2007) work is not capable of achieving the high dynamic range of our grouping method. Still, we do note that their method achieves growth factors of at least 10^6 in mass, and this may be sufficient for application to the atmospheric conditions of rain formation.

With the distribution method we are able to trace well the fluctuations of the mass (or distribution) spectrum, by choosing the zoom factors such that there are a fixed number of groups for all exponentially spaced mass bins. This method is therefore well suited for runaway kernels. However, the consequence is a rapid proliferation of the N_s parameter as many new species (which may be insignificant by, e.g., mass) are created. To limit N_s, these species need to be merged, which somewhat violates the spirit of MC methods as this includes averaging, not only over mass but also over structural parameters. The merging feature renders this method similar to Wetherill's discrete 'batches' technique (Wetherill 1990). However, in our method structural parameters, like porosity and charge, can be included and there is considerable (useful) freedom in how the averaging can be performed. These structural parameters survive, in averaged form, the merging process in our distribution method, and can be fundamental in the process of coagulation. For example, fractal grain structure (porosity) and dust charging can lead to, respectively, strong particle growth and even gelation (Konopka et al. 2005; Ormel et al. 2007).

Both the Wetherill (1990) method and our approach give the correct behavior for the most massive and second most massive particles in the case of the product kernel (see Inaba et al. 1999 for verification). Still, Wetherill's method has to deal with a number of free parameters: the spacing between the discrete batches and a parameter that determines the timestep, which must be fine-tuned. Our MC method, although not free of them either, does have the advantage that the free parameters correspond to physically-identifiable quantities, such as the mass-fraction parameter, f_ϵ. Another key advantage of our code is that the timestep, Δt, follows naturally from the MC code and is not required to be specified a priori. Especially in the super-runaway kernels with $\nu = 2, 3$, growth can be very erratic: during the runaway-process there is a large amount of growth during a small time step. The success of Wetherill's approach lies in 'discretizing' the original (mean-field) Smoluchowski equation in an efficient way. Naturally, in Monte Carlo codes, discreteness is assured.

The existence of two separate methods might appear to be a drawback. That is, runaway kernels (modeled with the distribution method) and information on structural parameters (through the equal mass method) are difficult to treat simultaneously, especially because one does not know a priori if a runaway situation will materialize. However, information about the kernel is 'hard-wired' into the Monte Carlo program and it is therefore clear at which point the situation is susceptible to runaway growth. Then, these particles (the high-m particles) have to be further resolved, and this can be achieved by switching to the distribution method. Thus, we feel that it is possible to model runaway kernels with MC methods, provided one implements a hybrid switch that signals runaway growth through the effective mass scaling exponent that a kernel exhibits during the simulation. For example, consider the cross section of Eq. (5.5). Obviously, the mass scaling of σ, m^ν, becomes stronger than unity ($\nu \approx 4/3$) for sufficiently large masses. It does so in a smooth manner, allowing a hybrid switch to be implemented. That is, as the program signals a large value of ν for a particular kernel, it switches from the equal mass to the distribution method, *i.e.*, assigning lower zoom factors for the high-m particles and, if needed,

merging structural parameters. This kernel adaptation technique is analogous to adaptive mesh refinement (Wise & Abel 2007), where the latter is grid based/spatial and we take a particle/stochastic approach. Both numerical treatments require one to look carefully at the consequences of the switch, i.e., the impact of the merging prescription or the under-resolved part of the grid.

The bottom-line on MC methods thus becomes clear: there is *a priori* no universal way in which the correct, accurate result can be guaranteed. Each situation requires interpretation and, if necessary, (re)adjustment of some aspects related to the grouping method; most notably through the choices for the grouping factors, *i.e.*, the $\{z_i\}$. However, MC methods are flexible enough to do so in physically meaningful way. As such, they are a very powerful tool to describe any dynamical system in which particles interact in a manner that can be statistically represented. In fact, the techniques presented in this work allow one to treat a wide range of, astrophysically relevant, kernels. The nicest feature of MC methods is that besides mass, structural properties of particles, like porosity and charge, can be directly incorporated into the collisional dynamics.

5.4.2 Astrophysical implications

There are several astrophysical situations where a large dynamic range is required and for which our algorithm may be applicable. In protoplanetary disks, one of the key questions is how the tiny (sub)micron-sized grains are transferred to planetesimals (Dominik et al. 2007). Because of the increasing relative velocities with particle growth, it may very well be the case that, while grains grow, the likelihood of fragmentation increases. An additional argument for fragmentation is that collisional growth very efficiently removes the smallest grains, contrary to what observations indicate (Dullemond & Dominik 2005). Recently, Brauer et al. (2008a) has solved the steady-state coagulation-fragmentation equation for the dust distribution. It would be worthwhile to investigate whether these results are also obtained with the grouping method, and how this picture changes by inclusion of structural parameters, *e.g.*, the porosity of aggregates (Ossenkopf 1993; Kempf et al. 1999; Ormel et al. 2007).

If particles reach the planetesimal size ($\sim$1 km) self-gravity may be sufficient to keep the collision products together. Furthermore, gravitational focusing, enhancing the gravitational cross-section, will turn the accretion process into a runaway process ($\nu > 1$). Goldreich et al. (2004b) has outlined under which conditions runaway growth proceeds. Greenberg et al. (1978) followed the collisional evolution (including fragmentation) of a population of initially 10^{12} km-sized planetesimals until sizes of $\sim$500 km were reached (after which particle-in-a-box approximations fail). We again note that a bin-based approach may have difficulty in modeling the runaway stage unless it uses an ad-hoc extension to include the runaway particle explicitly (Wetherill 1990). Bromley & Kenyon (2006) have developed a hybrid code that combines a N-body and statistical approach. However, these models can only treat one variable; with a Monte Carlo approach the internal structure of the particles can be included and a rubble pile structure can be distinguished from a homogeneous one.

In stellar clusters, too, conditions may be feasible for runaway growth. Because of dynamical friction (equipartition) the more massive stars will sink to the center of

the cluster and we may even have $\nu = 2$ (Malyshkin & Goodman 2001; Lee 2000). Moreover, the cluster will eject the smaller members and contract as a whole. These processes lead to *core collapse* in which the inner cut-off for the power law density function, r_0, disappears, $r_0 \to 0$, and the density seemingly becomes singular. This condition is very favorable for a runaway-growth scenario, and may well be the mechanism for the formation of high mass stars, seed black holes or even gamma ray bursts (Portegies Zwart et al. 1999; Freitag et al. 2006; Portegies Zwart & van den Heuvel 2007). Globular clusters are already successfully modeled by MC methods where the structural parameters are now the energy and angular momentum characterizing an orbit on which a particle (group) resides (e.g. Joshi et al. 2000). Here, the grouping mechanism may then be well suited to model systems with a very large number of stars and stellar ejecta. Similarly, the collapse, and possible fragmentation, of an interstellar gas cloud, leading to the formation of a stellar cluster or black hole, could be treated by following many (porous) gas clumps.

Acknowledgment. We appreciate the efforts of Volker Ossenkopf to proof-read the manuscript and the useful suggestions and comments of the two referees, which significantly improved the structure and presentation of this work.

Final note. Recently, the authors became aware of the work of Zsom & Dullemond (2008), in which Monte Carlo methods are also used to solve the collisional growth. Their work has been developed independently of ours. Like in this chapter, the method by Zsom & Dullemond is specialized to achieve high orders of magnitude growth, and their result features some resemblance to our 'equal mass approach.'

5.A Grouped collision rates

We justify the expressions for the grouped collision rates, Eq. (5.10), where the collision rates are divided by the number of collisions during the group collisions. We show that, provided the individual rates C_{ij} do not change as particles accrete, the mean collision rate is independent of the grouping.

Consider a species of N identical particles that react with an individual rate a_0 with an external particle. In the language of the grouping method of § 5.2 the N particles are of species j that, during the group process, react with a particle from species i and $a_0 = C_{ij}$. Let the process be such that the N particles react in groups of N/w, where $1 \leq w \leq N$ is the total number of such events.

Let P_i be the probability that the system is in state i, meaning that the i-th event (out of w) has occurred. At $t = 0$ the system is in the first state, so $P_0(t = 0) = 1$ and $P_i(t = 0) = 0$ for $i \neq 1$. Let the rate at which the system evolves from state i to the

next state $(i+1)$ be given by λ_i, then

$$\frac{dP_0}{dt} = -\lambda_0 P_0; \tag{5.23a}$$

$$\frac{dP_1}{dt} = -\lambda_1 P_1 + \lambda_0 P_0; \tag{5.23b}$$

$$\frac{dP_i}{dt} = -\lambda_i P_i + \lambda_{i-1} P_{i-1}; \qquad (1 < i < w) \tag{5.23c}$$

$$\frac{dP_w}{dt} = +\lambda_{w-1} P_{w-1}. \tag{5.23d}$$

Let $\overline{R(t)}$ be the mean reactivity of the system measuring the mean number of particles that has reacted at time t $(0 \leq R \leq 1)$. Likewise, let $\overline{R^2}$ measure the square number of reactants, *i.e.*,

$$\overline{R^k}(t) = \frac{1}{N^k} \sum_{i=0}^{w} P_i \left(\frac{iN}{w}\right)^k = \sum_{i=0}^{w} P_i \left(\frac{i}{w}\right)^k. \tag{5.24}$$

If we weigh the state-equations (Eq. (5.23)) with i/n and $(i/n)^2$, respectively, and sum over i we obtain:

$$\frac{d\overline{R}}{dt} = \frac{1}{w} \sum_{i=0}^{w} \lambda_i P_i; \tag{5.25a}$$

$$\frac{d\overline{R^2}}{dt} = \frac{1}{w^2} \sum_{i=0}^{w} (2i+1) \lambda_i P_i. \tag{5.25b}$$

Now the λ_i are proportional to the amount of particles left, *i.e.*, $\lambda_i \propto (1 - i/w)N$. In the case of group collisions, furthermore, we have argued that the rates should be divided by the number of reactants, such that the collision rate stays the same. We thus obtain

$$\lambda_i = (w - i) a_0, \tag{5.26}$$

where a_0 is the individual collision rate between two single particles. Equation (5.25) then transform to

$$\frac{d\overline{R}}{dt} = a_0 \left(1 - \overline{R}\right); \tag{5.27a}$$

$$\frac{d\overline{R^2}}{dt} = a_0 \left(-2\overline{R^2} + \frac{2w-1}{w}\overline{R} + \frac{1}{w}\right). \tag{5.27b}$$

This first equation of the first moment (average value) is independent of w. Its solution is of course the well known exponential decay corresponding to Poisson statis-

tics, *i.e.*,

$$\overline{R}(t) = 1 - \exp[-at]. \tag{5.28}$$

Inserting $\overline{R}$ into the equation for the second moment we solve for $\overline{R^2}$ as

$$\overline{R^2}(t) = \left(1 - e^{-at}\right)\left(1 - e^{-at}\left(1 - w^{-1}\right)\right). \tag{5.29}$$

The spread σ in the distribution then becomes

$$\sigma^2(w) = \left(1 - e^{-at}\right)\frac{e^{-at}}{w}. \tag{5.30}$$

That is, for $w \to \infty$, $\sigma \to 0$ and we are certain about the fraction of objects that have collided. For small w, however, there can be a significant spread.

By choosing the collision rates as in Eq. (5.26) — which is simply the rate for a collision with one particle, $a_0(N - iN/w)$, divided by the number of particles in the group (N/w) — we end up with Eq. (5.28) for the mean number of collisions. Since this is independent of w the mean reactivity of the system is also unaffected by the choice of w. For the mean reactivity it does not matter whether $w = N$ (no grouping) or $w = 1$ (all particles in the same group) as long as a_0 stays constant during the group process. However, the spread in $\overline{R}$ does depend on the choice of w, which is quite natural, of course. A similar procedure cannot be performed for the in-group collisions since here Eq. (5.23) involves i^2 terms. The group collision rates for in-group collisions are not exact. However, the rates of Eq. (5.10) are still a good approximation, and will become exact for large w. Besides, in-group collisions are a relatively minor occurrence.

5.B Outline Monte Carlo Program

1. Initialization

The prerequisites to run a MC simulation involving grouping are:

1. Identification of the (independent) particle properties **x**. Here, **x** can represent various particle properties: *e.g.*, mass, porosity, charge, chemical composition, etc. Particles of unique **x** are called species; identical particles are called duplicates and their multiplicity is denoted g_i. An example of a possible state vector is given in Table 5.4.
2. Interaction rate. This outlines the collision kernel K_{ij} between any two particles. The individual collision rate, $C_{ij} = K_{ij}/\mathcal{V}$, gives the probability of collision between particle i and j within the simulation volume $\mathcal{V}$.
3. A grouping mechanism. This determines the "choice" for the zoom-factor $\{z_i\}$ of the species. The group number then follows, $w_i = g_i/2^{z_i}$ $(w_i \geq 1)$. We have outlined two methods to regulate $\{z_i\}$. (i) Equal mass method: z_i is related to the mass peak and requires duplication; (ii) distribution method: z_i is determined by the distribution.

STATE VECTOR EXAMPLE

species	group number	zoom factor	particle properties **x**
1	w_1	z_1	$(m_1,\dots)$
2	w_2	z_2	$(m_2,\dots)$
$\vdots$	$\vdots$	$\vdots$	$\vdots$
N_s	$w_{N\mathrm{s}}$	$z_{N\mathrm{s}}$	$(m_{N\mathrm{s}},\dots)$

Table 5.4: Particles are defined by their mass, m_i, and, possibly, structural parameters. The group number w_i is a real number larger than unity ($w_i \geq 1$); z_i is integer. The number of particles of species i, $g_i = 2^{z_i} w_i$, is also an integer. The total number of species, N_s, fluctuates around a target value N_s^*.

4. A collision module. It gives the outcome of a collisions between particles i and j; *i.e.,* how the particles are modified and whether any new particles are created, in terms of the properties **x**.

2. Calculate group collision rates

The collision rate between a species i containing w_i groups each of 2^{z_i} particles and a species j (w_j, z_j) is given by:

$$\lambda_{ij}^G = \begin{cases} w_i w_j 2^{z_i + N_\epsilon} C_{ij} & \text{if } i \neq j \\ w_i (w_i 2^{z_i} - 1) C_{ii} & \text{if } i = j, \text{in-group collision.} \end{cases} \tag{5.31}$$

The partial rates, $\lambda_i = \sum_{k=i}^{N_\mathrm{s}} \lambda_{ik}^G$ $(i = 1 \dots N_\mathrm{s})$, and total rate, $\lambda_\mathrm{tot} = \sum_i^{N_\mathrm{s}} \lambda_i$, are stored in the memory of the computer program. The group splitting factor, N_ϵ, regulates mass accretion of j-particles on i-particles (here, $z_j \geq z_i$) to avoid excessive instantaneous mass load. It is defined as

$$N_\epsilon = \left[-\log_2 (f_\epsilon 2^{z_i} m_i / 2^{z_j} m_j) \right], \tag{5.32}$$

where f_ϵ is the maximum allowed fractional increase in mass of the larger particle i.

3. Pick collision particles

This follows the "full conditioning" method of Gillespie (1975). The time increment Δt and collision partners i, j are determined successively from the collision rates

$\{\lambda_i^G\}$ and three random deviates $\overline{r}_k$:

$$\text{time increment:} \qquad \Delta t = \lambda_{\text{tot}}^{-1} \ln(1/\overline{r_1}); \tag{5.33a}$$

$$i-\text{particle:} \qquad \sum_{k=1}^{i-1} \lambda_k \leq \overline{r_2}\lambda_{\text{tot}} \leq \sum_{k=1}^{i} \lambda_k; \tag{5.33b}$$

$$j-\text{particle:} \qquad \sum_{k=1}^{j-1} \lambda_{ik}^G \leq \overline{r_3}\lambda_i^G \leq \sum_{k=1}^{j} \lambda_{ik}^G. \tag{5.33c}$$

4. Perform collision

Each i-particle ($z_i \leq z_j$) collides with $N = 2^{z_j - z_i - N_\epsilon}$ j-particles. Perform the group collision: the sequential collision of N j-particles with the i-particle. Determine the new (structural) properties of the particles from the collision module. The multiplicity of the new particles that are created is 2^{z_i}. If $i = j$ (in-group collisions) one group of 2^{z_i} particles "collapses": there is one collision per particle and the multiplicity is $2^{z_i - 1}$.

5. Update collision rates, state vector

1. Reduce the group number of collision species: $w_i \to w_i - 1$, $w_j \to w_j - N_\epsilon$. If w_i or w_j becomes 0, remove this row from the state vector ($N_\text{s} \to N_\text{s} - 1$) and remove the entry from $\{\lambda_k^G\}$. If w_i becomes fractional ($w_i < 1$), demagnify (re-group) this species.
2. Add the new species to the state vector at index $q = N_\text{s} + 1$ ($N_\text{s} \to N_\text{s} + 1$). Determine z_q and $w_q \geq 1$ for the new species q.
3. Update the collision rates $\{\lambda_k\}$. For every $k = 1 \ldots N_\text{s}$ look to see whether the rates λ_{ik}^G and λ_{jk}^G should be subtracted (if $k \leq i$, respectively, $k \leq j$) and add the rate λ_{qk}^G if $k \geq q$ where q denotes the 'new' particle. Recalculate λ_{tot}.

6. Adjust $\{z_i\}$, merge species, choose duplicates

These steps are necessary for a smooth progression of the program to keep N_s and N_g (the total number of groups) around their target values, but do not have to be processed at every cycle. Adjust the collision rates, $\{\lambda_i\}$ accordingly. Zoom factors can be adjusted up or down:

1. Magnification: the zoom factor of the species is increased, $z_i \to z_i + 1$ and $w_i \to w_i/2$.
2. Demagnification: the zoom factor of the species is decreases, $z_i \to z_i - 1$ and $w_i \to 2w_i$.
3. Merging: properties of similar species are averaged to one species. This regulates the number of groups per (logarithmic) mass interval.
4. Duplication (constant-N_s simulations only): pick species-k randomly from the state vector (with weights $\{w_i\}$) and increase it by one ($w_k \to w_k + 1$).

Although (de)magnification and duplication do not directly increase (or decrease) N_s, increasing (decreasing) group numbers make an occurrence of an empty row, caused by disappearance of $w_i = 1$ species, less (more) likely. If particles are duplicated the simulated volume $\mathcal{V}$ also increases. Constant-$\mathcal{V}$ simulations do not use duplication.

End of cycle → return to 3.

6

Dust coagulation and fragmentation in molecular clouds

—C. W. Ormel, D. Paszun, C. Dominik, A. G. G. M. Tielens—

The cores in molecular clouds are the densest and coldest regions of the interstellar medium (ISM). These are the places, therefore, where the ISM-dust grains can coagulate. Here, we study the coagulation and fragmentation process from first principles; through direct quantification of the outcomes of detailed numerical simulations that cover a wide parameter space characterized by four dimensions: energy, porosity, angle of impact, and size ratio. Collisions can result in sticking or fragmentation (shattering, breakage, and erosion) and affect the internal structure of the particles. In combination with a Monte Carlo coagulation code the dust aggregate collision model is applied to a homogeneous and static cloud of temperature 10 K and gas densities that range from $n = 10^3$ cm^{-3} to 10^7 cm^{-3}. The coagulation is followed locally for timescales of $\sim 10^7$ yr. We find that the growth can be divided into two stages: a growth-dominated phase and a fragmentation-dominated phase, in which the evolution evolves towards steady state. In the first stage the mass distribution is relatively narrow, peaking at a particular size that shifts to larger size with time. At some point, however, collision velocities are energetic enough to fragment particles, which decrease the growth rate and start to replenish the particles of lower mass. Eventually, a steady state is reached, where the mass distribution is characterized by a relatively flat $m^2 f(m)$ mass-spectrum (equal amount of mass per logarithmic size bin). The amount of growth depends on

the density of the gas (setting the coagulation timescale) compared to the lifetime of the cloud, as well as on the material properties of the dust grains. Coagulation between silicates are always in the fragmentation regime, whereas ice-coated particles show a large potential for growth due to their better sticking properties. If clouds evolve on free-fall timescales, however, little coagulation is expected to take place in either case. However, if clouds have long-term support mechanism and live in isolation, the impact of coagulation is important, leading to a significant decrease of the opacity if the fragmentation-dominated phase has not yet been reached.

6.1 Introduction

Dust plays a key role in molecular clouds. Extinction of penetrating FUV photons by small dust grains allows molecules to survive. At the same time, gas will accrete on dust grains forming ice mantles consisting of simple molecules (Tielens & Hagen 1982; Hasegawa et al. 1992; Bergin & Langer 1997). Moreover, surface chemistry provides a driving force towards molecular complexity (Charnley et al. 1992; Aikawa et al. 2008). Dust also plays an active role in the star formation process. The smallest grains set the degree of ionization in the cloud, which controls the ambipolar diffusion rate and therefore regulates the magnetic support of prestellar cores (Ciolek & Mouschovias 1994). Radiation pressure on grains limits the mass accretion onto luminous protostars and hence grains may play a role in the upper mass cut off of stellar masses (Kahn 1974; Wolfire & Cassinelli 1987). Furthermore, after entering a protoplanetary disk, interstellar dust grains also provide building blocks from which ever larger bodies such as chondrules, planetesimals and cometesimals can be built. Finally, dust is often used as a proxy for the total gas (H_2) column density, either through near-IR extinction measurements or through sub-millimeter emission studies (Johnstone & Bally 2006; Alves et al. 2007; Jorgensen et al. 2008). Dust is often preferred as a tracer in these types of studies because it is now well established that — except for pure hydrides — all species condense out in the form of ice mantles at the high densities of prestellar cores (Flower et al. 2006; Bergin & Tafalla 2007; Akyilmaz et al. 2007). Thus, it is clear that our assessment of the molecular contents of clouds, as well as the overall state of the star and planet formation process, are tied to the properties of the dust grains — in particular, its size distribution.

The properties of interstellar dust are, however, expected to change during its sojourn in the molecular cloud phase. In particular, dust grains are expected to grow in size and this has profound influence on many of the processes involving dust. Grain sizes will increase due to the growth of ice mantles but this has only a limited effect because the total ice volume will be dominated by the smallest grains — which dominate the total grain surface area — and, if all the condensible gas freezes out, the thickness of the ice mantles is still only 175 Å, independent of core size (Draine 1985). In dense clouds, coagulation is potentially a much more important promoter of dust growth. Observationally, the decreased visual extinction per H-nucleus in the ρ-Oph cloud is evidence for dust growth by coagulation (Jura 1980). Indirect evidence for grain coagulation is also provided by a comparison of visual absorption

studies (*e.g.*, star counts) and sub-millimeter emission studies which imply that the smallest grains have been removed efficiently from the interstellar grain size distribution (Stepnik et al. 2003). On a long time scale ($>10^8$ yr), the interstellar grain size distribution is thought to reflect a balance between coagulation in dense clouds and shattering in interstellar shocks as material constantly cycles between dense and diffuse ISM phases (Jones et al. 1996; O'Donnell & Mathis 1997). Thus, because coagulation controls the total surface area of dust in molecular cloud cores, it in turn affects many of the direct and indirect observational manifestations in these environments.

Because it is the site of planet formation, coagulation studies have largely focused on grain growth in protoplanetary disks (Weidenschilling & Cuzzi 1993). In molecular clouds, dust coagulation has been theoretically modeled by Ossenkopf (1993) and Weidenschilling & Ruzmaikina (1994). In these studies, coagulation is driven by processes that provide grains with a relative motion. For larger grains ($\gtrsim$100 Å) turbulence in particularly is important in providing relative velocities. These motions—and the outcomes of the collisions—are very sensitive to the coupling of the particles to the turbulent eddies, which is determined by the surface area-to-mass ratio of the dust particles. At low velocities, grain collisions will lead to the growth of very open and fluffy structures, while at intermediate velocities compaction of aggregates will occur. At very high velocities, cratering and even catastrophic destruction will provide a powerful counterforce to the coagulation process (Dominik & Tielens 1997; Paszun & Dominik 2008a; Blum & Wurm 2008). It is clear then that understanding grain growth requires us to know the relationships between the macroscopic velocity field of the molecular cloud, the internal structure of aggregates (which follows from its collision history), and the microphysics of dust aggregates collisions. In view of the complexity of the coagulation process and the then existing, limited understanding of the coagulation process itself, previous studies of coagulation in molecular cloud settings have been forced to make a number of simplifying assumptions concerning the characteristics of growing aggregates.

Theoretically, our understanding of the coagulation process has been much helped by the development of the atomic force microscope, which has provided much insight in the binding of individual monomers. This has been translated into simple relationships between velocities and material parameters, which prescribe under which conditions sticking, compaction, and fragmentation occur (Chokshi et al. 1993; Dominik & Tielens 1997). Over the last decade, a number of elegant experimental studies by Blum and coworkers (*e.g.*, Blum & Wurm 2008) have provided direct support for these concepts and in many ways expanded our understanding of the coagulation process. Numerical simulations have translated these concepts into simple recipes, which link the collisional parameters and the aggregate properties to the structures of the evolving aggregates (Paszun & Dominik 2008a). Together with the development of Monte Carlo methods, in which particles are individually followed (Ormel et al. 2007; Zsom & Dullemond 2008), these studies provide a much better framework for modeling the coagulation process than hitherto possible.

In this chapter, we reexamine the coagulation of dust grains in molecular cloud cores in the light of this improved understanding of the basic physics of coagula-

tion with a two-fold goal. First, we will investigate the interrelationship between the detailed prescriptions of the coagulation recipe and the structure, size, and mass of the resulting aggregates. While these collisional recipes are very general, we have elected here to apply them to the relatively simple setting of a molecular cloud core. This will serve as an efficient way to investigate the implication of the detailed collision experiments. In a future study, we may apply these recipes to more convoluted models for the structure of molecular clouds, as well as studying grain growth and planet formation in protoplanetary disks. Second, we will give a simple prescriptions for the temporal evolution of the total grain surface area, thereby capturing its observational characteristics, in terms of the physical conditions in the core. Because the surface area holds the key to many of the physical effects involving grains in dense cores — including opacity and surface chemistry — we expect that a simple, but reliable, description of the coagulation process will be of great benefit to the larger field of molecular cloud physics.

This chapter is organized as follows. In § 6.2 the static cloud model that is adopted for the gas properties is presented and linked to the turbulent velocity structure. Section 4.2.3 describes the results from the collisional experiments, and quantifies their outcome in the collision recipe. A significant effort is invested to make the outcomes of the numerical collision experiments applicable to a size regime much larger than the collision experiments can handle. Also, the outcome is quantified in such a way to treat a Monte Carlo approach, discussed in § 6.4. In § 3.3 the results are presented: we discuss the imprints of the collision recipe on the coagulation and also present a parameter study, varying the cloud gas densities and the dust material properties. The merits of our approach are discussed in § 6.6, together with some caveats. In § 6.7 we review the implications of our result to molecular clouds. Section 2.6 summarizes the main conclusions of this study.

6.2 Density and velocity structure of molecular clouds

The physical structure — the gas density and temperature profiles — of molecular clouds is determined by its support mechanisms. Various support mechanisms can be envisioned: thermal, rotation, magnetic fields, or turbulence. If there is only thermal support to balance the cloud's self-gravity and the temperature is constant, its structure is that of an isothermal sphere where the gas density (ρ_g) falls-off with radius (r) as $\rho \propto r^{-2}$. However, the isothermal sphere is unstable as it heralds the collapse phase (Shu 1977). The cloud will then collapse on a free-fall timescale

$$t_{\rm ff} = \sqrt{\frac{3\pi}{32 G \rho_g}} = 1.1 \times 10^5 \text{ yr} \left(\frac{n}{10^5 \text{ cm}^{-3}} \right)^{-1/2}, \tag{6.1}$$

where G is Newton's gravitational constant, $n = \rho_g / m_H \mu$ the number density of the molecular gas with m_H the hydrogen mass and μ the molecular mass $\mu = 2.34$. Thermally supported cores are only stable if the thermal pressure wins over gravity, a situation described by the Bonnor-Ebert sphere (still assuming a constant temperature), where an external pressure confines the cloud. The critical Bonnor-Ebert mass

is (Ebert 1955; Bonnor 1956)

$$M_{\rm BE} = c_{\rm BE} \frac{c_{\rm g}^4}{P_{\rm out}^{1/2} G^{3/2}}, \tag{6.2}$$

where $c_{\rm g}$ is the isothermal sound speed, $P_{\rm out}$ the external pressure, and $c_{\rm BE} \simeq 1.18$. Inserting $P_{\rm out} = \rho_{\rm g} c_{\rm g}^2$, $c_{\rm g}^2 = kT/\mu$ and $\rho_{\rm g} = n\mu m_{\rm H}$ we obtain

$$M_{\rm BE} = c_{\rm BE} \frac{c_{\rm g}^3}{G^{3/2}\sqrt{n\mu m_{\rm H}}} = 0.31\ M_\odot \left(\frac{T}{10\ {\rm K}}\right)^{3/2} \left(\frac{n}{10^5\ {\rm cm}^{-3}}\right)^{-1/2}, \tag{6.3}$$

where, n is the density at the outer radius of the cloud. Because Bonnor-Ebert spheres have a modest density gradient, the density in the center of the core is a factor of $\sim$10 larger. Thermally-supported subcritical Bonnor-Ebert spheres ($M \lesssim M_{\rm BE}$) are stable and can in principle exist on long timescale — as long as they are not disturbed by dynamical interactions.

Magnetic fields in particular are important to support the cloud against the opposing influence of gravity, because the ions, which are tied to the field, will prevent the cloud from collapsing. Ion-molecule collisions will move the magnetic field out of the cloud, which can be a prolonged process. The ambipolar diffusion timescale can be estimated from the ion-molecular collision rate, $K_{in} \sim 2 \times 10^{-9}$ cm^3 s^{-1}. The force on a neutral particle through momentum transfer due to collisions with ions is $F_{\rm ad} = m_{\rm n} v_{\rm dr} K_{in} n_i$, where $m_{\rm n}$ is the neutral mass, $v_{\rm dr}$ the ion-molecule drift velocity, and n_i the number density in ions. This force balances the gravitational force, from which the drift velocity can be obtained. The ambipolar diffusion timescale, $t_{\rm ad} = r/v_{\rm dr}$, then becomes,

$$t_{\rm ad} = \frac{3K_{in}}{4\pi\mu m_{\rm H} G} \left(\frac{n_i}{n}\right) \simeq 3.7 \times 10^6\ {\rm yr} \left(\frac{n}{10^5\ {\rm cm}^{-3}}\right)^{-1/2}, \tag{6.4}$$

where we have assumed a degree of ionization due to cosmic rays of $n_i/n = 2 \times 10^{-5}/\sqrt{n}$ (Tielens 2005).

Turbulence is another possible support mechanism of molecular cores, but its nature is dynamic — rather than (quasi)static. At large scales it provides global support to molecular clouds, whereas at small scales it locally compresses the gas. If these overdensities exist on timescales of Eq. (6.1), collapse will follow. This is the gravo-turbulent fragmentation picture of turbulence-dominated molecular clouds, where the (supersonic) turbulence is driven at large scales, but also reaches the scales of quiescent ($\sigma_{\rm turb} < c_{\rm g}$) cores (Mac Low & Klessen 2004; Klessen et al. 2005). In this dynamical, turbulent-driven picture both molecular clouds and cores are transient objects.

Thus, cloud cores will dynamically evolve due to either ambipolar diffusion and loss of supporting magnetic fields or due to turbulent dissipation, or simply because the core is only a transient phase in a turbulent velocity field. In this work, for reasons of simplicity, we constrain ourselves to a static cloud model, where turbulence

is unimportant for the support of the core, but we do include (subsonic) turbulence in the formalism for the calculation of relative motions between the dust particles. In the following we present the working model for the structure of the cloud.

6.2.1 Working model

In this exploratory study we will for simplicity adopt an homogeneous core of mass given by the critical Jeans mass. Moreover, we assume the cloud is turbulent, but neglect the effects the turbulence has for the support of the cloud. Thus, our approximation is probably applicable for high density, low mass cores as velocity dispersions increase towards high mass cores (Kawamura et al. 1998). The homogeneous structure causes collision timescales to be the same throughout the cloud, *i.e.,* the coagulation and fragmentation is treated locally and not affected by diffusion. In our calculations, we will study the sensitivity of the coagulation process on the gas density n and compare the calculated coagulation/fragmentation timescales to the other relevant timescales in the problem.

Starting from the isodense sphere, we derive the turbulent velocity structure. First, the cloud outer radius is given by the Jeans length (Binney & Tremaine 1987)

$$L_{\rm J} = \frac{1}{2}\sqrt{\frac{\pi v_{\rm g}^2}{G\rho_{\rm g}}} = 0.033 \text{ pc } \left(\frac{n}{10^5 \text{ cm}^{-3}}\right)^{-1/2} \left(\frac{T}{10 \text{ K}}\right)^{1/2}, \tag{6.5}$$

From which the Jeans mass is obtained as

$$M_{\rm J} = \frac{4\pi}{3}\rho_{\rm g} L_{\rm J}^3 = 0.90 \, M_\odot \left(\frac{n}{10^5 \text{ cm}^{-3}}\right)^{-1/2} \left(\frac{T}{10 \text{ K}}\right)^{3/2}. \tag{6.6}$$

and the sound crossing time of the core is

$$t_{\rm cross} = \frac{L_{\rm J}}{c_{\rm g}} = 1.7 \times 10^5 \text{ yr } \left(\frac{n}{10^5 \text{ cm}^{-3}}\right)^{-1/2}, \tag{6.7}$$

independent of temperature. At the Jeans mass, the crossing time is of course equal to the free-fall time of the cloud.

We now assume (i) that the largest eddies decay on the sound crossing time of Eq. (6.7) (*i.e.,* $t_{\rm L} = t_{\rm cross}$), and (ii) that the fluctuating velocity at the largest scale is given by the sound speed *i.e.,* $v_{\rm L} = c_{\rm g}$. Thus, the turbulent viscosity is $\nu_{\rm t} = L v_{\rm L} = v_{\rm L}^2 t_L = c_{\rm g} L_{\rm J}$ with $L = L_{\rm J}$ the size of the largest eddies. Although our parameterization of the large eddy quantities seems rather ad-hoc, we can build some trust in this relation by considering the energy dissipation rate $v_{\rm L}^3/L$ per unit mass. Balancing the energy dissipation with the heating, requires a heating rate $n\Gamma$ of

$$n\Gamma = \frac{v_L^3}{L}\rho_{\rm g} = 2.5 \times 10^{-23} \text{ erg cm}^{-3} \text{ s}^{-1} \left(\frac{T}{10 \text{ K}}\right) \left(\frac{n}{10^5 \text{ cm}^{-3}}\right)^{3/2}. \tag{6.8}$$

Based upon observational studies of turbulence in cores, Tielens (2005) give a heating

rate of $n\Gamma = 3 \times 10^{-28} n$ erg s^{-1}, with which Equation (6.8) reasonably agrees for the range of densities we will consider. Additionally, the adoption of the crossing time and sound speed for the large eddy properties are natural upper limits. A higher value for the sound speed means that turbulence becomes supersonic, which may be difficult to sustain. A much reduced value, on the other hand, would give an energy dissipation that may be too low. Note again that turbulence does not act as a support mechanism in our working model.

The turbulent properties further follow from the Reynolds number, which is the ratio of the turbulent viscosity ν_t over the molecular viscosity ν_m,

$$Re = \frac{\nu_\mathrm{t}}{\nu_\mathrm{m}} = \frac{v_\mathrm{L} L}{c_\mathrm{g} \ell_\mathrm{mfp}/3} = 6.2 \times 10^7 \left(\frac{n}{10^5 \text{ cm}^{-3}}\right)^{1/2} \left(\frac{T}{10 \text{ K}}\right)^{1/2}, \tag{6.9}$$

where ν_m is the molecular viscosity and ℓ_mfp the mean free path of a gas particle. Assuming a Kolmogorov cascade, the turn-over time and velocity at the inner scale follow from the Reynolds number as,

$$t_\mathrm{s} = Re^{-1/2} t_\mathrm{L} = 2.2 \times 10^2 \text{ yr} \left(\frac{n}{10^5 \text{ cm s}^{-1}}\right)^{-3/4} \left(\frac{T}{10 \text{ K}}\right)^{-1/4} \tag{6.10}$$

$$v_\mathrm{s} = Re^{-1/4} v_\mathrm{L} = 2.1 \times 10^2 \text{ cm s}^{-1} \left(\frac{n}{10^5 \text{ cm s}^{-1}}\right)^{-1/8} \left(\frac{T}{10 \text{ K}}\right)^{3/8}. \tag{6.11}$$

We note that the fluctuating velocity of the smallest eddies is a few m/s.

6.2.2 Relative velocities between dust particles

The quantity that determines the amount of interaction a particle experiences with the gas is the friction time τ_f,

$$\tau_\mathrm{f} = \frac{3}{4\pi c_\mathrm{g} \rho_\mathrm{g}} \frac{m}{A}, \tag{6.12}$$

where m is the mass of the particle and A the average projected surface area. For compact grains of size a_0 and density ρ_0, Eq. (6.12) scales linearly with radius, $\tau_\mathrm{f} = a_0 \rho_0 / c_\mathrm{g} \rho_\mathrm{g}$. However, for porous particles A can have a much steeper dependence on mass (in the case of flat structures, $A \propto m$) and τ_f a much weaker dependence.

Ossenkopf (1993) considers a variety of sources for inducing relative velocities between dust particles in molecular clouds: asymmetric drift velocities, Brownian motion, gravitational settling, and turbulence. Except for combinations of high densities and small particles, turbulence dominates the velocity field between the particles. This becomes clear from considering the friction time of particles of radius a_0

$$\tau_0 = \tau_\mathrm{f}(a_0) = \frac{\rho_0 a_0}{c_\mathrm{g} \rho_\mathrm{g}} = 1.1 \times 10^2 \text{ yr} \left(\frac{n}{10^5 \text{ cm}^{-3}}\right)^{-1} \left(\frac{T}{10 \text{ K}}\right)^{-1/2} \left(\frac{a_0}{0.1 \ \mu\text{m}}\right), \tag{6.13}$$

where we take the bulk density $\rho_0 = 2.65$ g cm^{-3} applicable to silicates. Specifically, the '0' subscript denotes the smallest constituent dust particle (monomer). Because $\tau_0 > t_s$ the particle motion will not align with the eddies of shorter turn-over time. These 'class II' eddies (Völk et al. 1980) are responsible for giving random kicks to the particle motion—an important source for sustaining relative velocities of at least $\Delta v \sim v_s$. These velocities are rather insensitive to density as (i) v_s has a very shallow dependence on n; and (ii) the ratio τ_f/t_s, which we define as the Stokes number $\mathrm{St_s}$[1] is also weakly dependent on density

$$\mathrm{St_s} \equiv \frac{\tau_f}{t_s} = 5.2 \left(\frac{a_0}{0.1\ \mu\mathrm{m}}\right) \left(\frac{n}{10^5\ \mathrm{cm}^{-3}}\right)^{-1/4} \left(\frac{T}{10\ \mathrm{K}}\right)^{-1/4}. \tag{6.14}$$

It is only for densities above $\sim 10^7$ cm^{-3} that 10^{-5} cm size dust grains have $\mathrm{St_s} < 1$. Specifically, for identical particles of $\mathrm{St_s} > 1$, $\Delta v \approx \sqrt{3} v_s \mathrm{St_s}^{1/2}$ (Ormel & Cuzzi 2007). The relative velocity between two dust monomers is then

$$\Delta v_0 \approx \sqrt{3} v_s \mathrm{St_s}^{1/2} = 8.3 \times 10^2\ \mathrm{cm\ s^{-1}} \left(\frac{a_0}{0.1\ \mu\mathrm{m}}\right)^{1/2} \left(\frac{n}{10^5\ \mathrm{cm}^{-3}}\right)^{-1/4} \left(\frac{T}{10\ \mathrm{K}}\right)^{1/4}. \tag{6.15}$$

Thus, velocities between silicate dust particles are $\sim$10 m/s, and decrease only very slowly with density. The same expression holds when the silicates are coated by an ice mantle that is not too thick, as we will assume throughout this chapter (*i.e.*, ρ_0 is then still the silicate bulk density). Dust monomers then collide on a collision timescale of

$$\begin{aligned} t_{\mathrm{coll},0} &= \left(n_d \Delta v_0 4\pi a_0^2\right)^{-1} = \frac{\rho_0 a_0 \mathcal{R}_{gd}}{3\rho_g \Delta v_0} \\ &= 8.5 \times 10^4\ \mathrm{yr} \left(\frac{a_0}{0.1\ \mu\mathrm{m}}\right)^{1/2} \left(\frac{n}{10^5\ \mathrm{cm}^{-3}}\right)^{-3/4} \left(\frac{T}{10\ \mathrm{K}}\right)^{-1/4}, \end{aligned} \tag{6.16}$$

where $\mathcal{R}_{gd} = 100$ is the standard gas-to-dust density ratio by mass. Thus, if dense cores exist on timescales less then Eq. (6.16) coagulation is of little importance. This happens, *e.g.*, when the cores exist on free-fall timescales (Eq. (6.1)) at densities less than $n = 10^4$ cm^{-3}. On the other hand, if the lifetime of molecular clouds is longer than Eq. (6.16) we do expect that coagulation is significant. At very high densities ($n \gg 10^5$ cm^{-3}) $t_{\mathrm{coll},0}$ can become much less than the lifetime of the core — especially if long term support mechanisms are available — and we do therefore expect significant potential for coagulation.

6.2.3 Particle sticking, restructuring and fragmentation

Although a detailed model for the outcome of collisional encounters between dust aggregates will be discussed in § 6.3, it is instructive to present order-of-magnitude

[1] The more usual definition is $\mathrm{St} = \tau_f/t_L$.

COLLISIONAL OUTCOMES

Energy	Outcome of Collision
$E < 5E_{\rm roll}$	Sticking without restructuring
$E \approx 5E_{\rm roll}$	Onset of restructuring local to the impact area
$E \approx N_{\rm c}E_{\rm roll}$	Maximum compression
$E \approx 3N_{\rm c}E_{\rm br}$	Onset of erosion (start to lose monomers)
$E > 10N_{\rm c}E_{\rm br}$	Catastrophic disruption

Table 6.1: Collision outcome predicted by Dominik & Tielens (1997) for 2d aggregates. The breaking energy, $E_{\rm br}$, corresponds to the energy to break a single contact, whereas the rolling energy, $E_{\rm roll}$, corresponds to the energy required for visible restructuring of the contact area through rolling. The number of contacts in an aggregate, denoted by $N_{\rm c}$, is typically similar to the number of monomers the aggregate contains, N.

expressions for the sticking behavior of dust aggregates. This requires us to compare the critical threshold for sticking with the expected relative velocity between two dust particles derived above.

Dominik & Tielens (1997) provide a simple recipe for the outcome of aggregate collisions, see Table 6.1. According to Dominik & Tielens (1997) the outcome of a collision depends on the impact energy,

$$E = \frac{1}{2} m_\mu (\Delta v)^2, \tag{6.17}$$

where m_μ is the reduced mass, relative to two critical energy thresholds: the energy required to break a contact, $E_{\rm br}$, and the energy required to roll a contact, $E_{\rm roll}$. From the Dominik & Tielens (1997) study,

$$E_{\rm br} = A_{\rm br} \frac{\gamma^{5/3} a_\mu^{4/3}}{\mathcal{E}^{\star 2/3}}; \tag{6.18a}$$

$$E_{\rm roll} = 6\pi^2 \xi_{\rm crit} \gamma a_\mu, \tag{6.18b}$$

where $a_\mu = a_1 a_2/(a_1 + a_2)$ is the reduced radius of the aggregates colliding (in our case we shall always consider two equal-size monomers such that $a_\mu = a_0/2$), and γ and $\mathcal{E}^\star$ are, respectively, the surface energy density and the reduced elastic modulus of the material. The model parameters $\xi_{\rm crit}$ and $A_{\rm br}$ result from the Dominik & Tielens (1997) study: $\xi_{\rm crit} = 10^{-8}$ cm and $A_{\rm br} = 43$. The critical energies of Eq. (6.18) were obtained by Dominik & Tielens (1997) from theoretical considerations; however, laboratory experiments performed by Poppe et al. (2000) showed that monomers stick at a much higher velocity than predicted from the derived theoretical limit. Although the nature of this discrepancy remains unclear, the constant $A_{\rm br}$ in Eq. (6.18a) had to be increased by about two orders of magnitude. Moreover, Heim et al. (1999) find that the energy $E_{\rm roll}$ is also an order of magnitude higher than the threshold given by the theory. This indicates that the critical displacement $\xi_{\rm crit}$ must be about 10 times larger than assumed by Dominik & Tielens (1997). Blum & Wurm (2000), however, confirmed the quantitative picture proposed by the theory,

provided that the experimental threshold energies are used ($\xi_{\rm crit} = 2 \times 10^{-7}$ cm and $A_{\rm br} = 2.8 \times 10^3$). In this study we will adopt these experimentally-measured values.

Using the critical energies, we briefly review contact breaking and restructuring. Contact breaking occurs when $E > E_{\rm br}$, where E is the collision energy. The critical velocity is therefore,

$$v_{\rm br} = \sqrt{\frac{2E_{\rm br}}{m_\mu}} = \sqrt{2A_{\rm br}}\frac{\gamma^{5/6}a_\mu^{4/6}}{\mathcal{E}^{\star 1/3}m_\mu^{1/2}} = \sqrt{\frac{6A_{\rm br}}{4\pi}}\rho_0^{-1/2}\gamma^{5/6}a_\mu^{2/3}a_0^{-3/2}\mathcal{E}^{\star -1/3} \tag{6.19}$$

$$= 7.4 \text{ m s}^{-1}\, N_\mu^{-1/2}\left(\frac{a_\mu}{a_0}\right)^{2/3}\left(\frac{a_0}{0.1\ \mu\text{m}}\right)^{-5/6}\left(\frac{\rho_0}{2.65 \text{ g cm}^{-3}}\right)^{-1/2}$$

$$\times \left(\frac{\gamma}{25 \text{ erg cm}^{-2}}\right)^{5/6}\left(\frac{\mathcal{E}^\star}{2.8 \times 10^{11} \text{ dyn cm}^{-2}}\right)^{-1/3}.$$

In this expression we have introduced the reduced number of monomers in the collision, $N_\mu = N_1N_2/(N_1 + N_2) = m_\mu/m_0$ and inserted the material properties measured for small silicate grains. Given the expected velocities in molecular cores we see that breaking of contacts is important for silicate grains of 0.1 μm. However, ice formation on the surface of dust particles will change this picture. Adhesion forces are governed in this case by the material properties of ice, where the surface energy density is $\gamma = 370$ erg cm^{-2} and the reduced elasticity modulus is $\mathcal{E}^\star = 3.7 \times 10^{10}$ dyn cm^{-2}. This results in a higher velocity threshold of $v_{\rm br} = 1.2 \times 10^4$ cm s^{-1} between two monomers. However, in aggregates the collisional energy is distributed over multiple monomers so that a more realistic threshold for shattering is $E \sim N_{\rm c}E_{\rm br}$, even increasing the threshold for fragmentation. Besides, the collisional energy can also be dissipated by restructuring. From these considerations it is clear that for ices (or ice-coated silicates) high velocities, $>10^2$ m s^{-1}, are required to fully fragment aggregates. There are two exceptions, however. In very fluffy fractal aggregates that have an open structure (*e.g.*, string-like), removal of a central contact may result in its breakup. Secondly, if the impact energy is localized in a small region of the aggregate we may expect that collisions of velocity $v \gtrsim v_{\rm br}$ produce some local damage in the form of cratering. This local aspect will feature prominently in the collision recipe of § 6.3.

At collision energies less than the restructuring limit, $E < 5E_{\rm roll}$, aggregates collide without affecting their internal structure. Then, the collision is in the 'hit-and-stick' regime (Blum & Wurm 2000). Translating the collision energy to a velocity thresholds gives

$$v_{\rm hs} = \sqrt{\frac{10E_{\rm roll}}{m_\mu}} = \sqrt{45\pi}\, a_\mu^{1/2}a_0^{-3/2}\rho_0^{-1/2}\xi_{\rm crit}^{1/2}\gamma^{1/2}N_\mu^{-1/2} \tag{6.20}$$

$$= 16.3 \text{ m s}^{-1}\, N_\mu^{-1/2}\left(\frac{a_\mu}{a_0}\right)^{\frac{1}{2}}\left(\frac{a_0}{0.1\ \mu\text{m}}\right)^{-1}\left(\frac{\rho_0}{2.65 \text{ g cm}^{-3}}\right)^{-\frac{1}{2}}\left(\frac{\gamma}{25 \text{ erg g}^{-1}}\right)^{\frac{1}{2}}.$$

It should be noted that Eq. (6.20) is applicable to aggregates, whereas Eq. (6.19) gives

the breaking velocity between two monomers. Because we consider aggregates, we give preference to the $v_{\rm hs}$ threshold (even though it is in the case of silicates higher than $v_{\rm br}$), which has been experimentally verified as the onset for restructuring (Blum & Wurm 2000).

Comparing the critical sticking velocities (Eqs. (6.19), (6.20)) with the velocities in the molecular cloud (Eq. (6.15)), we may expect that collisions between silicate aggregates are prone to fragmenting behavior from the outset, whereas for ices the onset of fragmentation is delayed — if enough time is available — to a stage where particles are much larger, compact, and have much larger relative velocities. Concerning the structure of aggregates, we expect that restructuring will be important from the outset as $\Delta v \gtrsim v_{\rm hs}$, except perhaps at the highest densities. For ices Eq. (6.20) is a factor of 4 higher, but note that the discrepancy between ice and silicates is less for the rolling energy than for the breaking energy (Eq. (6.18)). Finally, if fragmentation is present, a significant injection of porous material can be expected (see below).

These considerations present, however, only a qualitative picture, which neglects important parameters that may be key to the outcome of the collision, *i.e.*, the particle porosity and the impact parameter. It may therefore be dangerous to provide a full collision model from these energy considerations alone. For a quantitative model, therefore, we will use the results of detailed numerical simulations for collisions between two colliding aggregates, which have been recently performed (Paszun & Dominik 2008a). We will review these numerical experiments in the next chapter and provide a collision recipe that quantifies their outcome and can be applied to a Monte Carlo coagulation model.

6.3 Collision model

Collisions between aggregates are modeled using the soft aggregates numerical dynamics (SAND) code (Dominik & Nübold 2002; Paszun & Dominik 2008b). This code treats interactions between individual monomers held together by the surface forces in a contact area (Johnson et al. 1971; Derjaguin et al. 1975). The SAND code calculates the equation of motion for each grain individually and simulates vibration, rolling, twisting and sliding of the monomers that are in contact. These interactions lead to energy dissipation via different channels. When two monomers in contact are pulled away, the connection may break causing loss of the energy. Monomers may also roll or slide over each other, which also involves energy dissipation. These mechanisms are discussed in details by Dominik & Tielens (1995, 1996) and Dominik & Tielens (1997). For further details regarding this model and testing it against laboratory experiments we refer the reader to the paper by Paszun & Dominik (2008b).

6.3.1 Collision setup

To understand mechanisms that determine a collision outcome, we performed a large number of simulations covering a wide parameter space. Although all simulations are described in detail by Paszun & Dominik (2008a) we present here a setup of these numerical experiments and provide a qualitative picture of the mechanisms that influence the outcome of a collision.

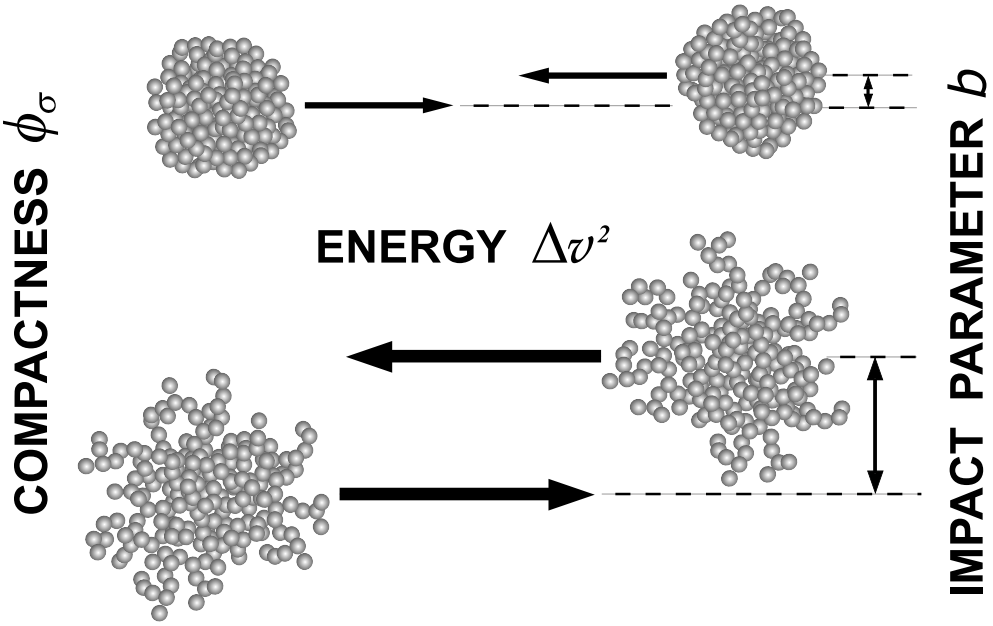

Fg. 6.1: Sketch of the initial setup of our simulations. Different parameters are shown in the plot. We varied collision energy, impact parameter, and compactness.

The outcome of a collision is shaped by five key parameters: (i) the collision energy E, (ii) the impact parameter b, (iii) the initial compactness of aggregates, (iv) the mass ratio N_1/N_2, and (v) the material properties of the monomers. Using an appropriate normalization, we can describe the collisional outcome independently of the latter parameter (the material properties) so that only four parameters are left. The applied scaling is discussed in § 6.3.5. An example of the setup of a simulation is shown in Fg. 6.1. It illustrates three parameters that determine the outcome of a collision: the initial compactness as represented by the *geometrical* filling factor ϕ (see below), the collision energy E, and the impact parameter b.

A collision for each parameter set is repeated 6 times at different orientations. This provides an overview of the possible range of outcomes. However, some orientations do not result in a collision hit. This is caused by the high porosity of aggregates, where a small particle can fly through voids in a larger aggregate without colliding with it, or, more simply, if the path of the protuberances that characterize fractal, fluffy aggregates do not cross. The fraction of these missing collisions depends on two parameters: the structure of the particle characterized by the geometrical filling factor and the impact parameter.

The range of the parameters we use in our study is summarized in Table 6.2. We sample the collisional energy parameter space from the pure hit-and-stick collisions, where particles grow without changing the internal structure of the colliding aggregates, up to catastrophic destruction, where the aggregate is shattered into small

SIMULATION PARAMETERS

v [m/s]	$b/b_{\max}$	mass ratio	ϕ
0.05	0.0	1.0	0.070
0.30	0.25	0.8	0.090
0.50	0.5	0.6	0.122
0.75	0.75	0.4	0.127
1.0	0.875	0.2	0.155
2.0	0.95	0.1	0.161
4.0		0.05	0.189
6.0		0.01	0.251
8.0		0.001	
10.0			

Table 6.2: Parameters used in the numerical simulations. Note that not all combinations are sampled.

fragments. In the intermediate energy regime, we observe restructuring, where the growth process leads also to a change of the internal structure of an aggregate.

The dimensionless impact parameter space is also well sampled. We probe central collision ($b = 0$), where aggregates can be compressed, grazing impacts ($b \sim 1$), where particles can be stretched due to inertia, and several intermediate cases. The impact parameter is taken relative to the outer radius of the particles, $b_{\max} = a_{\text{out},1} + a_{\text{out},2}$. Here the outer radius a_{out} is the radius of the smallest sphere centered at the center-of-mass of the particle that fully encloses it.

The third parameter that determines the collision outcome is the mass ratio. To verify its influence on a collision outcome, we simulate impacts of different mass aggregates onto a target made of 1000 monomers. In this way we explore the mass ratio in the range from 1 to 10^{-3}. Additional experiments are performed at a mass ratio of unity containing aggregates made of 200 monomers each. The two extreme cases (mass ratio of 1 and 10^{-3}) will affect the outcome of the collision in two qualitatively distinct ways. In collisions between equal-size aggregates the properties of the particle change *globally*, whereas if the colliding particles have very different masses the impact of the collision can be described *locally* (except if the collision energy is very high, see below) The intermediate cases may be classified into one of the two categories of collisions (see below).

The last, fourth, parameter is the initial compactness. To express the compactness of an aggregate we use the geometrical filling factor, defined as

$$\phi = N\left(\frac{a_0}{a}\right)^3, \tag{6.21}$$

where $a = \sqrt{A/\pi}$ is the projected surface equivalent radius. The projected surface area, πa^2, is averaged over a large number of different orientations of the particle. The compactness parameter ϕ is the inverse of the enlargement factor ψ adopted as the structural parameter in the study by Ormel et al. (2007). Although the friction time τ_{f} follows easily from the geometrical filling factor, it is not straightforward to

determine the outer radius $a_{\rm out}$ of an aggregate based on this quantity. The outer radius is of importance because it determines the collisional cross section (uncorrected for missing collisions) between the aggregates. Therefore, a relation between the radii ($a_{\rm out}$ and a) has to be provided, see § 6.3.4.relation between the radii.

The parameter space of the filling factor ϕ is chosen such that we sample both very porous, fractal aggregates that grow due to the Brownian motion (Krause & Blum 2004; Paszun & Dominik 2006), through intermediate compactness aggregates that form by particle-cluster aggregation (PCA), up to compact aggregates that may result from collisional compaction events. It is not trivial to assign an upper limit for collisional compaction of an aggregate, as unilateral compression is countered by sideways spreading of monomers. Although the upper limit for collisional compression is that of random packing (66%) here, following Ormel et al. (2008), we use $\phi = 33\%$ for the upper limit of (rolling) compression, which is in turn based on laboratory findings of Blum & Schräpler (2004). The compactness influences the collisional output in a few different ways. These are described in § 6.3.2, where we discuss the prescription for a collision outcome.

6.3.2 Collision recipe: an overview

To provide both a qualitative and a quantitative description of a collision, Paszun & Dominik (2008a) perform a large number of simulations exploring an extensive parameter space. They formulate a simple, quantitative, collision recipe that determines the influence of the kinetic energy, compactness, and mass ratio on the outcome of aggregate-aggregate collisions. The outcomes of a collision are averaged over the impact parameter b. In this case the contribution from off-center impacts is dominant. The fragment size distribution consists in such a case of two main components: large fragments are produced at large impact parameter collisions and small fragments form mostly in central impacts. An offset hit leads to a very limited interaction that may result in an outcome very similar to the initial setup (two large fragments of weakly changed structure). Moreover, collisions at large b have a higher probability to miss than porous aggregates. Central impacts, on the other hand, are less likely to miss and lead to a better distribution of energy in aggregates. Therefore, collisions at energies above the fragmentation threshold produce many small particles.

For an impact energy above the restructuring energy threshold, a different impact parameter results in a different outcome. In head-on impacts monomers are pushed into the center of an aggregate, filling the pores and compressing the aggregate. On the other hand, in offset collisions, the overlap of interacting aggregates is smaller, and the amount of compression is limited. In this case monomers are pushed further from the center of an aggregate and an elongated particle may be produced. Therefore, tensile forces present in off-center impacts lead to stretching, *decompressing* the agglomerates.

In this chapter we reformulate the recipe to probe directly the effect of the impact parameter on the collision evolution of dust aggregates. In this way we explicitly resolve the effects of off-center impacts and compare this to the simplified case of head-on collisions only. Therefore, the recipe becomes four-dimensional and depends on

the impact energy, initial compactness, the impact parameter, as well as mass-ratio. The complete presentation of the redesigned recipe is discussed in § 6.3.3.

Given the level of complexity, it is not feasible to provide simple analytical expressions for the outcome parameters of Table 6.3 as function of the collision parameters ($E, \phi, b, N_1/N_2$). Therefore, like in Paszun & Dominik (2008a), the results are expressed in a tabular form, where each table provides one of the output quantities as a function of a normalized collision energy ε and initial filling factor $\phi^{\rm ini}$. The exception is the fraction of missed collisions, $f_{\rm miss}$, which is given as function of $a_{\rm out}/a$, instead of ϕ. Since the recipe contains a large number of tables we provide them in a digital form only.[2] See App. 6.A for further discussion on the format of the collision recipe.

In this study the reshaped recipe is applied to the Monte Carlo model developed by Ormel et al. (2007). This method resolves individual collisions and includes structural parameters. Therefore, our recipe may be easily implemented to study both coagulation and compression of aggregates. In addition, our recipe broadens the range of models, where it can be applied to. The original formulation by Paszun & Dominik (2008a) was designed for applications to continuous methods. Here, the method is extended to become applicable to the particle-oriented approach of the Monte Carlo (MC) method.

6.3.3 Porting the recipe to a Monte Carlo model

An outcome of a collision consists of two essential parts: the mass distribution and the compactness of aggregates in this mass spectrum. The new implementation of our recipe provides these two elements of a collision product in a different form than the original recipe formulated by Paszun & Dominik (2008a). In this study we use the impact parameter as one of the input quantities. Therefore, as discussed above, collision outcomes are not averaged over impact parameter. Additionally, the nature of the Monte Carlo approach requires us to treat discrete quantities. Two components characterize the mass distribution of a collision experiments: (i) a power-law component that describes the small fragments and, (ii) a large fragment component (one or two fragments). The border line between the two components is at a quarter of the total mass $N_{\rm tot}$. The power-law distribution spans the range from monomer mass up to the $N = 0.25N_{\rm tot}$, while the second component consists of aggregates larger than $0.25N_{\rm tot}$. In this work, the large fragment component is described by different parameters than in Paszun & Dominik (2008a), where a Gaussian distribution was used. In the new recipe we provide a number of large fragments $N_{\rm f}$ with a standard deviation $S_{\rm f}$. The spread in the number of large fragments is found by averaging several simulations performed at different orientations for the same set of parameters.

Table 6.3 presents all quantities describing a collision outcome. The first one is the fraction of missing collisions, $f_{\rm miss}$. This number is a correction factor that needs to be applied when the collision cross-section is determined using the outer radius of an aggregate $a_{\rm out}$. The small fragments are described by two quantities: the exponent of

[2] These tables will be presented as *online material* once this chapter is submitted to the journal. In App. 6.A we provide an example of the structure of these tables.

OUTPUT QUANTITIES

Symbol	Description
f_{miss}	Fraction of collisions that resulted in a miss
N_{f}	Mean number of large fragments
S_{f}	Standard deviation of the N_{f}
f_{pwl}	The fraction of the total mass $(N_1 + N_2)$ in the small fragments component
q	Exponent of the power-law distribution of small fragments
$C_\phi = \phi/\phi^{\mathrm{ini}}$	Relative change of the geometrical filling factor.

Table 6.3: Quantities provided by the Monte Carlo suited recipe.

the power-law distribution q and the normalized mass of this component f_{pwl}. The normalization of this and other quantities are discussed in § 6.3.5.

To fully describe a collision outcome, the recipe also provides the relative change in filling factor, C_ϕ. It describes the compaction or decompaction of aggregates in the large fragment component. Concerning the small fragments that are produced by erosive or fragmenting collisions and constitute the power-law component, a common filling factor can be assigned. The compactness of these particles depends only on mass and is presented in Fg. 6.2, where fragments produced in many simulations are plotted. Almost all particles are located along the power-law with the slope of -0.33. This provides a very easy prescription for the filling factor of small fragments. This dependence indicates a fractal structure (with the fractal dimension of about $D_{\mathrm{f}} \approx 2.0$) of aggregates formed in a fragmentation event, since the non-fractal aggregates have filing factor independent of mass.

As shown by Paszun & Dominik (2008a) after reaching the maximum compaction, further increase of the impact energy causes more restructuring and results in a flattening of the produced aggregate. Therefore, very fluffy particles can be produced in collisions of massive aggregates, where the power-law component extends to larger N. This behavior is also observed in Fg. 6.2, where fluffy, small fragments follow the power-law relation, while some large, still compact particles are above the dashed line.

6.3.4 Relation between a_{out} and a

In this study we distinguish two different radii of an aggregate: the outer radius a_{out} and the projected surface equivalent radius a. The first one is used as a reference of our impact parameter b. The collision offset is limited by the largest impact parameter $b_{\mathrm{max}} = a_{\mathrm{out},1} + a_{\mathrm{out},2}$. The cross-section equivalent radius a defines our structural parameter ϕ (see Eq. (6.21)). We determine the relation between the two radii (a_{out} and a) empirically. Both a_{out} and a are determined for many aggregates of various shape and mass. We sample particles with the fractal dimension in the range of $D_{\mathrm{f}} = 1 \ldots 3$ and masses from several to a few thousands monomer masses. These aggregates were produced using an algorithm developed by Filippov et al. (2000).

Figure 6.3 shows the filling factor determined for different aggregates versus the ratio of the outer radius over the cross-section equivalent radius. The mass dependence, as determined in § 6.3.3, is shown by plotting $\phi\, N^{0.33}$. Interestingly, the data

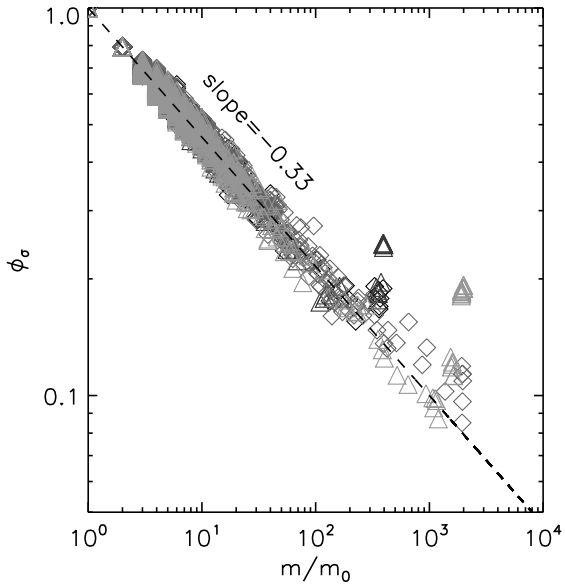

Fg. 6.2: The geometrical filing factor as a function of fragment mass. Many simulations with different sets of parameters are overplotted. The dashed line indicates the least square method fit of the power-law to the small mass fragments.

for all aggregates are very well confined along a single curve. At small ratio of $a_{\rm out}/a$ the curve decreases very steeply with increasing $a_{\rm out}/a$. This corresponds to compact particles for which $a_{\rm out}/a$ does not depend much on filling factor. The line, however, breaks at about $a_{\rm out}/a \approx 1.2$ and turns in to a power-law with a slope of -0.3. This shallow relation represents fluffy aggregates that show a large discrepancy between the projected surface equivalent radius and the outer radius.

In order to provide a simple relation between the two radii, two power-law functions are fitted to the two regimes: compact particles below $a_{\rm out}/a = 1.2$ and fluffy aggregates above that limit. These two functions are given by

$$\phi^{\rm compact} = \left(\frac{a_{\rm out}}{a}\right)^{(0.75-4.21\log N)} \tag{6.22a}$$

$$\phi^{\rm fluffy} = 1.21\left(\frac{a_{\rm out}}{a}\right)^{-0.3} N^{-0.33}. \tag{6.22b}$$

To further verify these relations we use particles produced in several simulations performed by Paszun & Dominik (2008a). These aggregates are indicated in Fg. 6.3 by black squares. They show a very similar relation to the one obtained in Eq. (6.22). Points that are slightly shifted above the fitted lines correspond to aggregates that are partly compressed (they did not reach the maximum compaction). Their compact cores are still surrounded by a fluffy exterior that causes a small increase of the ratio of the outer radius over the projected surface equivalent radius $a_{\rm out}/a$. This behavior, however, occurs at a relatively small value of $a_{\rm out}/a < 2$. At a larger size ratio the filling factor falls back onto the power-law given in Eq. (6.22b).

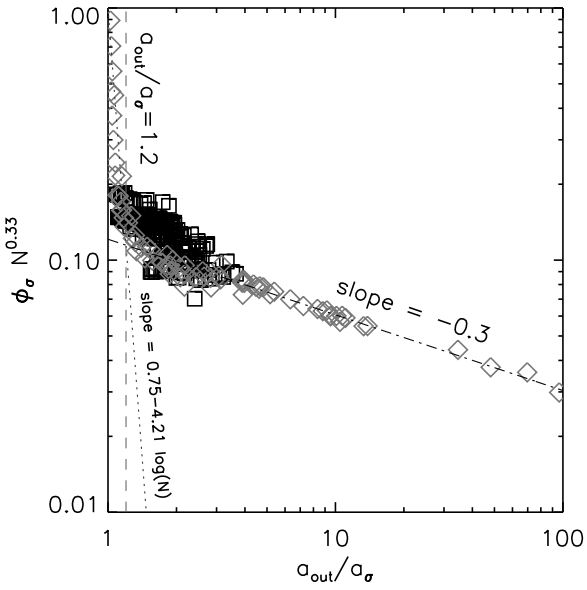

Fg. 6.3: The geometrical filling factor dependence on the ratio of outer to geometrical radii. In this figure we plot $\phi N^{0.33}$ to scale the data for aggregates of different mass.

6.3.5 Parameter space and normalizations

We list the five key parameters that shape the outcome of aggregate collisions:

1. the collision energy, E;
2. the impact parameter, b;
3. the structure of aggregates, ϕ;
4. the mass ratio, N_1/N_2 (local or global influence);
5. monomer properties, $\gamma, \mathcal{E}$.

The influence of the material properties and monomer size can be eliminated by a proper scaling of the energy to the rolling and breaking energies corresponding to the material properties. Thus, we normalize to $E_{\rm roll}$ where it concerns the change in the filling factor, *i.e.*, the C_ϕ parameter reflecting restructuring, and to $E_{\rm br}$ for the other parameters of Table 6.3 that describe the fragmentation behavior.

Another parameter that affects collisions is the mass ratio. This influences mostly the collision outcome in terms of compactness. Impacts of similar size aggregates show compression for small impact parameters ($b \approx 0$) and decompaction for large offsets ($b \sim 1$). On the other hand, impact of a smaller particle onto a larger target results in a similar outcome regardless of the impact parameter. This discrepancy is dealt with by providing two separate sub-recipes: the local and the global recipe. Collisions of similar mass aggregates result in changes throughout both particles. We refer to this behavior as the *global recipe*. When a mass ratio is smaller than 0.1 the changes become more localized. In this case the energy is concentrated in the region local to the impact area, which may, *e.g.*, result in cratering. This confined behavior is

provided in the *local recipe*. The energy in the global recipe is normalized to the total number of monomers, $N_{\rm tot}$, which represents the extended influence of the collision. However, in the local recipe the energy scales by the reduced number of monomers N_μ, which is basically the number of monomers of the smaller collision partner. The dimensionless energy parameter is then defined as

$$\varepsilon = \frac{E}{N_{\rm eff} E_{\rm crit}}, \tag{6.23}$$

where $E_{\rm crit}$ and $N_{\rm eff}$ depend on the context: The energy $E_{\rm crit}$ can be either one of $E_{\rm br}$ or $E_{\rm roll}$, whereas $N_{\rm eff}$ is one of $N_{\rm tot}$ or N_μ. The distinction of the two sub-recipes is presented in § 6.3.9.

The remaining three quantities (the normalized energy ε, the impact parameter b, and the filling factor ϕ) form the 3D space of input parameters of the recipe. Their influence on the collision outcome is described in § 6.3.7 and 6.3.8, where we first discuss quantities defining the result of an impact. However, before we present the effect of different parameters on a collision outcome in both the local and the global recipes, we discuss impacts in the hit-and-stick energy regime.

6.3.6 Hit and stick

At very low energies ($E \leq 5E_{\rm roll}$) two aggregates will stick where they meet, without affecting the internal structure of the particles. This is the 'hit-and-stick' regime in which the collisional growth can often be described by fractal laws. Two important limits are cluster-cluster coagulation (CCA) and particle-cluster coagulation (PCA). In the former, two particles of equal size meet, which often leads to very fluffy structures, whereas PCA describes the process in which the projectile particles are small with respect to the target. The filling factor then saturates to a constant value. For example, in the case of monomers, the filling factor will reach the PCA limit of 15% (Kozasa et al. 1992).

In general particles do not merely collide with either similar-size particles or monomers. Every size-ratio is possible and leads to a different change in filling factor. Ormel et al. (2007) provide an analytical expression, based upon fits to collision experiments of Ossenkopf (1993), that give the increase in void space as function of the geometrical volume of the collision partners. Here, the geometrical volume V is the volume that corresponds to the geometrical radius, a. Although the expressions of Ormel et al. (2007) are easily convertible into filling factor, we have used additional numerical collision experiments to further constrain these analytical fits. These experiments involved several 'PCA-bombardments' (repeated collisions by monomers) of several aggregates. Using these data, the adopted expressions in the 'hit-and-stick' regimes are now, in terms of the geometrical volumes ($V_1 > V_2$) of the particles

$$\frac{V_{\rm void}}{V_0} = \max\left[(V_1+V_2)\left(\left(1+\frac{V_2}{V_1}\right)^{3\delta/2-1}-1\right), \frac{N_2}{0.087\phi_2}\exp\left[-\left(\frac{15V_2}{V_1}\right)^{0.25}\right]\right]. \tag{6.24}$$

The first term converges to CCA in the limit of $V_2 = V_1$, and is the same as in Ormel et al. (2007). Here, δ is an exponent that reflects the fractal growth in this limit, which, following Ossenkopf (1993), we put at $\delta = 0.95$. The second expression converges to PCA in the limit of $V_2 \ll V_1$. The rationale of providing a second expression is that in the case of $V_2 \ll V_1$ (PCA) the first expression goes to zero very quickly (no voids are added), which is clearly inappropriate as PCA must result in a filling factor of 15%. From the results of our new collision experiments we have altered the dependence of the PCA-part on the volume ratio (V_2/V_1) by inclusion of the exponent of 0.25, which, compared to Ormel et al. (2007), smooths out the fall-off with increasing mass ratio.

In fitting the numerical values in the PCA-part we note, however, that not all numerical experiments could be fitted equally well. In fact, we had to compromise: some experiments were better fit by a more 'smoothed' PCA expression, while others were not. It is probable that for a complete description more parameters are required, *e.g.*, the elongation of the aggregates or their fractal dimension. Here, we have adopted approximate fits that follow the qualitative picture in both the CCA ($V_1 = V_2$) and the PCA ($V_2 \ll V_1$) limit. We note, finally, that 'hit-and-stick' collisions are more prevalent in dense environments like protoplanetary disks, rather than in molecular clouds. In our case, therefore, the hit-and-stick regime is only relevant in the initial stages of coagulation at densities of $n \geq 10^5$ cm^{-3}.

6.3.7 Local recipe

In the local recipe the scaling of the energy parameter ε depends on the quantity it is applied to. When it concerns erosion, it scales with N_μ, the reduced number of monomers of the aggregates, which renders the collision outcome insensitive to the size of the larger aggregate. In the case of restructuring, however, the outcome of a collision depends very much on the size of the large particle. The compaction may be local and moderate, but the affected quantity — the filling factor — describes the particle globally. Thus, C_ϕ is normalized to the total number of aggregates, whereas the other quantities that describe the fragmentation process are normalized to N_μ.

In the local recipe the number of large fragments rarely increases above unity (the exception are 'lucky projectiles' that destroy the central contacts of fluffy aggregates, causing the two sides of the aggregate to become disconnected). This deep penetration of a particle may also result in more severe damage. Fragments produced in a cratering event and on their way out of the eroded aggregate may result in secondary impacts causing stronger erosion. This process is the main cause of fragmentation of large targets, since the energy transfer into the target is not efficient and a large fraction of the kinetic energy is carried away by the ejecta.

Figure 6.4a shows how much of the mass is ejected during collisions at different energies. This mass may exceed the mass of the small projectile by even two orders of magnitude. The collision energy is not transported deep into the target but rather used at the surface to break contacts between monomers. Thus, collisions between particles of different mass result in erosion if sufficient energy is available (a few times $N_\mu E_{\rm br}$).

The local recipe describes cratering that does not fully shatter the target. Erosion events generate a similar distribution, where the slope oscillates between $q = -1.3$

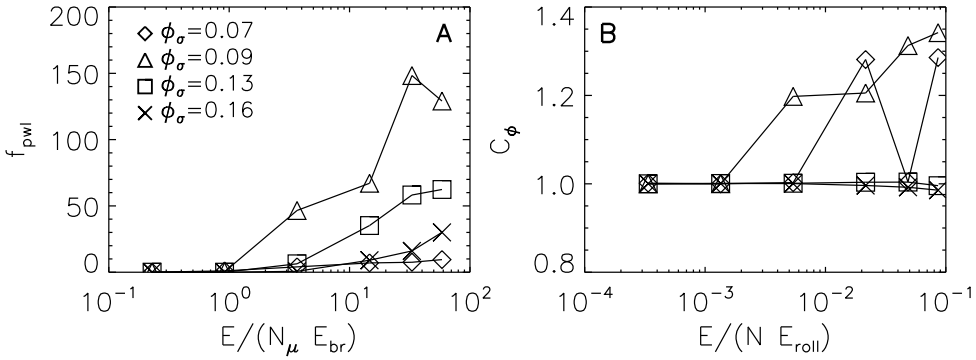

Fg. 6.4: Quantities provided by the local recipe. *(a)* The mass of small fragments, power-law component, normalized to the reduced mass of the colliding aggregates. *(b)* The relative change in the geometrical filling factor C_ϕ.

and $q = -2.0$. This is comparable to the slopes obtained for erosive collisions of equal mass projectiles in the global recipe (see § 6.3.8).

Since the influence of the impact is local, the degree of compression is relatively small. However, increasing collision energy results in an increasing degree of compression. The very fluffy and elongated aggregates may break in half causing an artificial increase of the filling factor. This can be observed in Fg. 6.4b for aggregates with $\phi^{\rm ini} = 0.07$, where the change in filling factor shows a strong variation for energies above $E = 10^{-2}\ N\ E_{\rm roll}$.

6.3.8 Global recipe

The two key quantities that follow from the recipe are the mass distribution (small and large fragment component) and the change in filling factor of the large fragment component. Figures 6.5a and 6.5b show the number of the largest particles that remain after a collision. The left panel (Fg. 6.5a) shows the result for central impacts of particles of different initial filling factor and at different collision energies. The right panel (Fg. 6.5b) shows the result for collisions at an impact parameter of $b = 0.75$.

Central impacts at low energy produce one large fragment. An increase of the impact energy results in erosion, where a few small fragments are removed from the surface. In the limit of very high energies ($E > 5NE_{\rm br}$), the interaction leads to catastrophic disruption. Offset collisions, on the other hand, produce two large fragments at high energy collisions. At large impact parameter aggregates interact with their outer parts. This can lead to the formation of only a few contacts that can be easily broken at high impact energies.

The mass distribution of the collision products depends on both energy and impact parameter. The higher the energy, the smaller the two fragments are. An increase of the impact parameter, however, results in a weaker interaction and an increase of the mass of the fragments. In the limiting case of a grazing collision, two particles are almost unaffected regardless of the impact energy. Collisions between

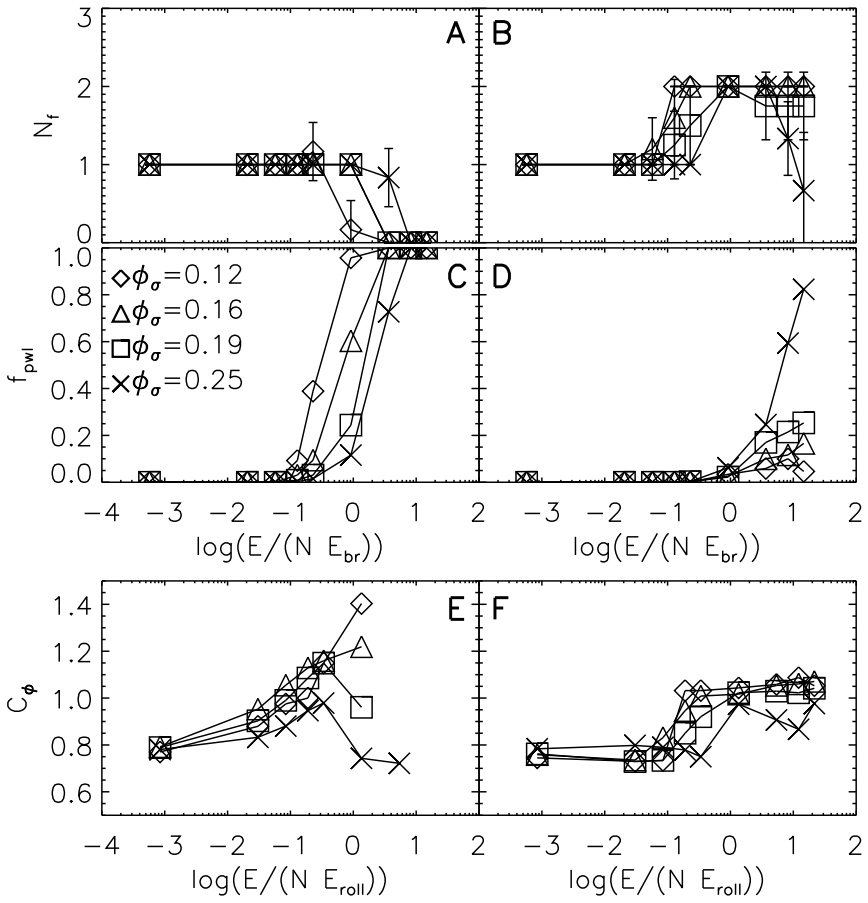

Fig. 6.5: Quantities provided by the global recipe. Left panels correspond to central collisions, while the right panels correspond to off-center collision at impact parameter $b = 0.75$. From top to bottom: Number of large fragments N_f (*A, B*); mass of the small fragments component, M_p, normalized to the total mass of the two aggregates M_{tot} (*C, D*); relative change in the geometrical filling factor $C_\phi = \phi/\phi^{ini}$ *(E, F)*.

compact aggregates colliding at a very high energy and at a very large impact parameter result in two large fragments, containing in total over 80% of the initial mass.

The number of large fragments N_f is very well defined for central and grazing collisions. In the first case one large fragment remains, while in an off-center impact both collision partners survive. Intermediate impact parameters introduce some ambiguity. Some orientations cause sticking, which leads to one large aggregate, and others produce two large particles. This is reflected in the standard deviation S_f. If all orientations lead to the same outcome, the situation is unambiguous and $S_f = 0$. However, when the spread in N_f is larger, it defines the probability of a collision to

produce one or two fragments.

Figures 6.5c,d show the mass of the power-law component (small fragments). Central collisions result in an equal distribution of energy among the monomers. A collision energy of $3NE_{\rm br}$ is sufficient to shatter an aggregate catastrophically. In the case of a fluffy aggregate, the entire particle is destroyed and all fragments belong to the power-law distribution. The most compact aggregate is, however, able to survive these energy inputs. In this case over 70% of the mass is in the power-law component, whereas the rest is in a large fragment. However, the average number of large fragments is below unity and in some cases only the power-law component remains.

An increase of the impact parameter makes the distribution of energy over the aggregate less efficient. This results in a higher threshold for catastrophic destruction: more energy must be provided to completely shatter aggregates. Figure 6.5c,d show that at the energy sufficient to fully shatter compact aggregates at central impact, only 25% of the mass is shattered in an offset collision at impact parameter $b = 0.75$. Fluffy aggregates 'feel' the effect of an increased impact parameter even more, because in this case, the redistribution of the kinetic energy is even weaker. For example, very fluffy aggregates of filling factor $\phi = 0.122$ colliding at an impact parameter of $b = 0.75$ produce small fragments which add up to only about 6% of the total mass. The rest of the mass is locked into 2 large fragments.

The degree of damage can also be assessed through the slope of the power-law distribution of small fragments. The steeper the slope, the stronger the damage. Heavy fragmentation produces many small fragments and results in a steepening of the power-law. Although destruction is very strong in the case of a central impact (the slope reaches values of $q = -3.7$ at energy of $>20NE_{\rm br}$), it weakens considerably for offset collisions ($q > -2.0$).

At low energies, the amount of aggregate restructuring, as quantified in the C_ϕ parameter Fg. 6.5e,f, is independent of impact parameter. This is simply because the collision energy is insufficient to cause visible restructuring. Then, the aggregate volume increases in a hit-and-stick fashion, resulting in a decrease of the filling factor as compared to the initial state of the colliding aggregates.

With increasing collision energy the degree of restructuring is enhanced, and therefore compression occurs. Central impacts strongly affect the filling factor ϕ. Figure 6.5e shows that the compression is maximal at an impact energy of about $E = NE_{\rm roll}$. Those aggregates that are initially compact are difficult to further compress. For static compression, the critical filling factor is $\phi = 0.33$ (Blum et al. 2006; Paszun & Dominik 2008b). Any further restructuring can only move monomers sideways, which causes a decrease of the packing density and flattening. Offset collisions, however, lead to much weaker compression as shown in Fg. 6.5f. In this case the main reason is that forces acting on monomers in the impacting particles are more tensile, contrary to the compressive forces present in the central collisions. Large offset impacts at velocities above the sticking velocity of about 1 m s^{-1} (Poppe et al. 2000) result in two large fragments with the unaffected filling factor ($C_\phi = 1$).

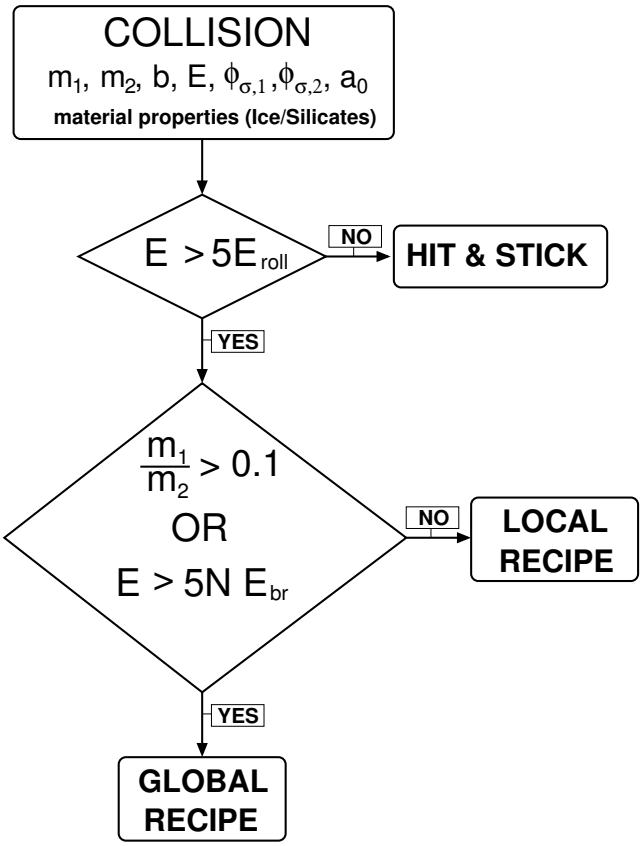

Fg. 6.6: Schematic decision chain of distinction between the hit-and-stick, global, and local recipes.

6.3.9 The recipe's manual

The local and global recipes are generally distinguished by the mass ratio of the colliding aggregates. However, at very high collision energies the results are always well described by the global recipe, even if the mass ratios involved are large. In this case the aggregate is catastrophically disrupted, which, of course, affects the aggregate globally. For example, at a mass ratio of $N_2/N_1 = 0.01$ the velocity required to shatter the target is a 10 times higher than for equal mass aggregates (cf. Eq. (6.19)). At low energies the hit-and-stick recipe will always apply. Figure 6.6 presents the adopted algorithm that provides the distinction between the recipes.

When two aggregates collide at a given impact parameter b and energy E, we first check whether the impact is in the hit-and-stick regime or that energies are above the restructuring limit: $E = 5E_{\rm roll}$. If $E < 5E_{\rm roll}$ no restructuring takes place and the hit-and-stick analytical description discussed above follows. Otherwise, we perform another test. The global influence of the collision occurs if one of two conditions is satisfied:

1. the masses of colliding particles must not differ by more than a factor of 10;
2. the energy must be sufficient to cause global changes to both interacting aggre-

gates.

This latter criterion means that if particles are very different by mass, they will still result in a global change to the properties of the aggregates if the energy is sufficient to break the entire target aggregate. Otherwise, the effect is local and cratering occurs. Equal mass projectiles, however, always affect aggregates globally.

6.4 The Monte Carlo program

In the previous section we have seen that four parameters — the collisional energy E, the filling factor ϕ, the impact parameter b, and the mass ratio in terms of the local and global recipe — determine the outcome of a collision between two aggregates. As the collisional energy depends on mass and the impact parameter is random, we discern two (independent) particle properties: mass and filling factor. From these two quantities all other particle properties are derived. For example, the collisional energy E between two particles depends on the particle masses and the particle's friction times through the relative velocities (see § 6.2), which, in turn, depend on the particle filling factors and masses.

Characterizing particles by only two properties does not fully define their internal structure. For example, we assume that aggregates are spherically symmetric, even though numerical experiments show a distinct elongation (Paszun & Dominik 2006). Still, the collision model contains a significant level of sophistication. The modeling of collisions can be divided in three steps. First, the particle properties (m, ϕ) and the collision properties (Δv) are turned into a collision 'grid point' given by ε, ϕ and b. Then, the outcome of the collision is specified by 6 collision quantities (Table 6.3). Finally, these quantities specify the change to the initial particle properties (m, ϕ) and also describe the properties of the collision fragments.

An important goal of our collision recipe is to make it applicable to a wide range in mass: *e.g.*, it is intended to be applicable to the scales at which the collisional experiments were performed ($\sim 10^3$ monomers) but also to particles of much larger size. This is the rationale behind the scaling of the collision energy to the rolling or the breaking energy, and the distinction between the global and local recipes. We are, therefore, fully equipped to compute the full collisional evolution, even if it takes us well beyond the domain of the numerical experiments, *i.e.*, $N \gg 10^3$. However, we acknowledge that as a consequence of this extrapolation we may not account for physical processes that show up at a different scale; *e.g.*, it may well be the case that particles that have reached a macroscopic proportion will bounce, rather than stick (Langkowski et al. 2008). We will return to these issues in § 6.6.

The formulation of the collision recipe in terms of the 6 output quantities enables a Monte Carlo (MC) oriented approach to the calculation of the collisional evolution. The advantage of a MC approach is that collisions are modeled individually and therefore have a direct correspondence to the collision model. Furthermore, structural parameters (like ϕ) can be easily included and the collisional outcome can be quantified in detail. Indeed, the outcomes of the collision experiments are quantified by (a change in) 6 critical parameters (see previous section), with the MC program merely sampling the appropriate values (or an interpolation between the appropri-

ate values; see below). We emphasize that our MC model does not represent individual aggregates as in Kempf et al. (1999) but that the particle's structure is merely characterized by two values: the mass of the aggregate or the number of grains, N, and the filling factor ϕ.

In setting up the MC model we have followed previous work of Ormel et al. (2007, 2008). Furthermore, we implement the new grouping method outlined by Ormel & Spaans (2008). In this method the 1-1 correspondence between a simulation particle and a physical particle is dropped; instead, the simulated particles are represented by *groups* of identical physical particles. Ormel & Spaans (2008) have shown that the method is very well suited to simulate a large dynamic range, which, in the light of the anticipated fragmentation, is exactly what is required. The group's mass is determined by the peak of the $m^2 f(m)$ mass distribution — denoted $m_{\rm p}$ — and particles of smaller mass 'travel' together in groups of total mass $m_{\rm p}$. Grouping entails that a large particle can collide with many small particles simultaneously — a major but necessary approximation of the collision process. This happens when the mass-ratio is less than 1% ($f_\epsilon = 10^{-2}$).

We now continue with an overview of one cycle in the Monte Carlo program, emphasizing in particular the role of the collision recipe and its implementation within the context of the grouping method. Other details concerning the architecture of the MC setup have been discussed in Ormel & Spaans (2008).

6.4.1 One collision cycle

Collision rates

The cycle starts with the calculation (or update) of the collision rates between the groups of the simulation. The individual collision rate between two particles i and j is $C_{ij} = K_{ij}/\mathcal{V}$ (units: s^{-1}), where $\mathcal{V}$ is the simulation volume and K the collision kernel. For grouped collisions C_{ij} is larger because many particles are involved in the collision. The collision kernel K is defined as $K_{ij} = \sigma_{ij}\Delta v_{ij}$ with $\sigma_{ij} = \pi a_{\rm out}^2$ the collisional cross section (uncorrected for missing collisions) and Δv_{ij} the average root-mean-square relative velocity. Thus, to calculate the collision rates we need the relative velocities and the relation between the geometrical and the outer radius (Fg. 6.3).

Determination of collision partners

Random numbers determine which two groups collide and the number of particles that are involved from the i and j groups, η_i and η_j. Then, each i-particle collides with η_j/η_i j-particles. The grouping method implicitly assumes that collision rates do not change significantly during the collision process. For erosion or sticking the procedure is appropriate as we only apply grouping when the mass ratio between the i (the large particles) and the j particles (the smaller projectiles) is large. However, in collisions that result in breakage the grouping assumption is potentially problematic, since the particle properties — and hence the collision rates — then clearly change *during* the collisions. Fortunately, breakage is not a frequent occurrence as grouped collisions are only applicable in the local recipe due to the large mass-ratio's. Catastrophic disruptions (shattering) is problematic for the same reasons, because when

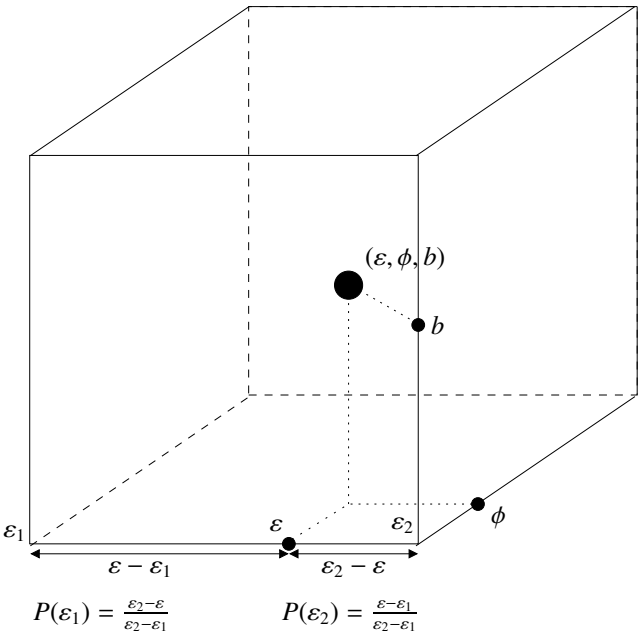

Fg. 6.7: Illustration of the picking of the grid points. The collision takes place at (ε, ϕ, b): a point that is generally surrounded by eight grid points (here corresponding to the nodes of the cube). Each node is then assigned a probability inversely proportional to the distance to the grid point. Thus, the probability that the energy parameter $\varepsilon = \varepsilon_1$ is picked (corresponding to four of the eight grid nodes) is $P_1 = (\varepsilon - \varepsilon_1)/(\varepsilon_2 - \varepsilon_1)$. The procedure is identical for the other parameter grid points.

it occurs, there is no 'large' aggregate left. However, for energetic reasons we expect that shattering occurs mainly when two equal-size particles are involved, for which the global recipe would apply (and no grouping). In the following we continue with a collision of $\eta_t = \eta_j/\eta_i$ j-particles colliding with a single i-particle.

Interpolation of data cubes

When the collision is in the 'hit-and-stick' regime the properties of the new particles are easily found by adding the masses of the j-particles to the i-particle and calculating their filling factor using Eq. (6.24). In the following we will outline only the changes in either the local or global recipe. The collision is then characterized by three parameters: normalized collision energy ε, filling factor ϕ and impact parameters b. The energy parameter ε is different for the local and the global recipe and is normalized with respect to the breaking energy except in the case of the C_ϕ quantities where it is normalized to the rolling energy (§ 6.3.5). These three parameters constitute an arbitrary point in the 3D (ε, ϕ, b)-space, and will in general be 'surrounded' by 8 grid points (k) which correspond to the parameters at which results from the collision experiments are available. We next distribute the η_t collisions over the grid point in which the weight of a grid point is inversely proportional to the 'distance' to (ε, ϕ, b) as explained in Fg. 6.7. Taking account of the collisions that result in a miss, we have

$$\eta_t = \eta_{\text{miss}} + \sum_k \eta_{k\cdot}, \qquad \eta_{\text{miss}} = \sum_k \eta_{\text{miss},k}, \tag{6.25}$$

where $\eta_{\mathrm{miss},k} = [\eta_t P_k f_{\mathrm{miss},k}]$ denotes the number of collisions at the grid point resulting in a miss. Here, P_k denotes the weight of the grid point, f_{miss} the fraction of missed collisions at the grid point and the brackets indicates this number is rounded to integer values. Similarly, the number of 'hits' at a grid point is given by $\eta_k \simeq \eta_t P_k (1 - f_{\mathrm{miss},k})$. Not all of these grid points have to be occupied (*i.e.*, η_k can be zero). In the special case without grouping $\eta_t = 1$ and only one grid point at most is occupied.

We continue here to outline the general case of multiple occupied grid points. First, we consider the mass that is eroded, given by the $f_{\mathrm{pwl},k}$ quantities. The mass eroded at one grid point per collision is given by $M_{\mathrm{pwl},k} = f_{\mathrm{pwl},k}(m_i + m_j)$. Then, the total mass eroded by the group collision is

$$M_{\mathrm{pwl}} = \sum_k M_{\mathrm{pwl},k} \eta_k. \tag{6.26}$$

If this is more than m_i, then clearly there is no large fragment component.[3] Otherwise, the mass of the large fragment component is $M_{\mathrm{large}} = m_i + (\eta_t - \eta_{\mathrm{miss}}) m_j - M_{\mathrm{pwl}}$. Each $M_{\mathrm{pwl},k}$ quantity is distributed as a power-law with the exponent provided by the slope q_k of the grid point (see below). Concerning the large-fragment component, there is a probability that it will break, given by the $N_{\mathrm{f},k}$ and $S_{\mathrm{f},k}$ quantities. As argued before, breakage within the context of the grouping algorithm cannot be consistently modeled. Notwithstanding these concerns, we choose to implement it in the grouping method. Because its probability is small, we assume it happens at most only once during the group collision. The probability that it occurs is then

$$P_2 = 1 - \prod_k (1 - P_{2,k})^{\eta_k}, \tag{6.27}$$

where $P_{2,k}$ is the probability that breakage occurs at a grid point and follows from the S_{f} and N_{f} quantities. If breakage occurs, the masses M_{pwl} are removed first and we divide the remaining mass M_{large} in two.

The last quantity to determine is the change in the filling factor of the large aggregate, denoted previously by the C_ϕ parameter. Like Eq. (6.27) we multiply the changes in C_ϕ at the individual grid nodes,

$$C_\phi = \prod_k C_{\phi,k}^{\eta_k}, \tag{6.28}$$

and $\phi_{\mathrm{large}} = C_\phi \langle \phi \rangle_m$. This completes the implementation of the collisional outcome within the framework of the grouping mechanism. That is, we have the masses and the new ϕ-values of the large fragment component(s), and have computed the distribution of the power-law component in terms of mass. Note again that all these results are *per i*-particle, and that the multiplicity of the results is η_i.

[3] Recall that in grouped collisions ($\eta_{\mathrm{t}} > 1$) this implies that the grouping method is not fully accurate as the change in mass is of the order of the mass itself; but the procedure is always fine if $\eta_{\mathrm{t}} = 1$.

Picking of the power-law component masses

The final part of the MC cycle is to pick particles according to the power-law distribution, under the constraints of a total mass $M_{\rm pow}$ and slope q. (If $M_{\rm pow} = 0$ there is of course no mass to distribute.) This must be done at each gridpoint k, because the slope q_k in general is different at each grid point. The mass $M_{\rm pow}$ is the mass that goes into fragmentation at the grid point k, $M_{{\rm pwl},k}$, multiplied by η_k and η_i (the collision multiplicity). The general formula for picking the mass of the fragments is

$$m_i = \left[1 + \bar{r}(m_{\rm rem}^{1+q} - 1)\right]^{\frac{1}{1+q}} , \tag{6.29}$$

where $m_{\rm rem}$ is the maximum mass of the distribution (this decreases at every step and should from the definitions above be no more than 25% of the total mass) and $\bar{r}$ a random number between 0 and 1. Equation (6.29) is obtained from

$$\bar{r} = \int_1^m x^q {\rm d}x \Big/ \int_1^{m_{\rm rem}} x^q {\rm d}x \; . \tag{6.30}$$

In the MC program the number of *distinct* fragments that can be produced is limited to a few per grid point. This is to prevent an influx of a very large number of species (non-identical particles; in this case, particles of different mass), which would lead to severe computational problems, filling-up the statevector array (see below). Therefore, if the same mass m_i is picked again it is considered to be the same species, and the multiplicity of this species is increased by one. After we have obtained a maximum of $\eta_{\rm dis}$ *distinct* species, we redistribute the mass $M_{\rm pow}$ over the species. In this way the fragment distribution is only sampled at a few discrete points.

Merging/Duplication

The final part of the MC program consist of an inventory, and possible adjustment, of the amount of groups and species ($N_{\rm s}$) present in the program. To combine a sufficiently high resolution with an efficient computation in terms of speed is one of the virtues of the grouping method. One key parameter, determining the resolution of the simulation, is the $N_{\rm s}^*$ parameter (the target number of species in a simulation). In order to obtain a sufficient resolution we require that a total mass of $\sim m_{\rm p} N_{\rm s}^*$ is present in the simulation. Particles are *duplicated* to fulfill this criterion, adding mass to the system. To prevent a pileup of species we have adopted the 'equal mass method' as described in Ormel & Spaans (2008). However, we found that due to the fragmentation many species were created at any rate—too many, in fact ($N_{\rm s} > N_{\rm s}^*$) which would severely affect the efficiency of the program. Therefore, if $N_{\rm s} = 2N_{\rm s}^*$ we used the 'merging algorithm,' in which neighboring species are combined into one species, averaging over their (structural) parameters. This significantly improved the efficiency (*i.e.*, speed) of the simulation, although the many fragments created by the collisions (all contributing to a higher $N_{\rm s}$) can be regarded as a redundancy, because it requires a lot of subsequent regrouping. The alternative would be to produce only 1 new species per collision event (Zsom & Dullemond 2008); here, we prefer to stick with a more detailed representation of each collision

MODEL RUNS

id	Density n [cm^{-3}]	Type	Grain size a_0 [μm]	Figure reference
(1)	(2)	(3)	(4)	(5)
1	10^3	ice	0.1	
2	10^4	silicates	0.1	Fg. 6.13
3	10^4	ice	0.1	Fg. 6.13
4	10^5	silicates	0.1	Fg. 6.13
5	10^5	silicates	1	
6[a]	10^5	ice	0.1	Figs. 6.8, 6.10, 6.9
7	10^5	ice	1	Fg. 6.14
8	10^5	ice	0.03	Fg. 6.14
9	10^5	ice, compact[b]	0.1	Fg. 6.11
10	10^5	ice, head-on[c]	0.1	Figs. 6.10, 6.11
11	10^6	silicates	0.1	Fg. 6.13
12	10^6	ice	0.1	Fg. 6.13
13	10^7	ice	0.1	

Table 6.4: Overview of the model runs. (1) Model number. (2) Number density of the gas. (3) Collision type, describing material parameters and collision setup. Here 'ice' refers to ice-coated silicates of bulk density that is the same to that of silicates, $\rho_0 = 2.65$ g cm^{-3}, and material parameters $\gamma = 370$ erg cm^{-2} and $\mathcal{E}^\star = 3.7 \times 10^{10}$ dyn cm^{-2}. For bare silicates, $\gamma = 25$ erg cm^{-2} and $\mathcal{E}^\star = 2.8 \times 10^{11}$. (4) Monomer radius. (5) Figure reference. *Notes:* [a]the standard model; [b]filling factor of particles restricted to a minimum of 33%; [c]central impact collisions only ($b = 0$).

event by creating many particles, but we acknowledge that this amount of detail is to some extent lost by the subsequent *merging*.

6.5 Results

All requirements to calculate the collisional evolution of dust grains are now in place. In § 6.4 we have discussed how the collision model of § 6.3 is treated in the context of a MC model. We have calculated a large set of models varying the relevant parameters: the density, grain size and material properties. We investigated grains consisting of silicates, and silicates with ice mantles. These properties of the simulation runs are summarized in Table 6.4. Only static models are considered, characterized by a constant density. To obtain a measure of the influence of the density on the coagulation process — timescales and amount of growth — a large range in density is considered. The coagulation is followed for 10^7 yr in most of the models, unless a steady state has clearly appeared before this time. Other parameters that affect the coagulation process but which are fixed here *i.e.*, $T = 10$ K, $\mu = 2.34$, *etc.* are discussed in § 6.2.

We continue in § 6.5.1 with the analysis of the standard model ($n = 10^5$ cm^{-3}, $a_0 = 0.1$ μm, ice-coated silicates). In § 6.5.2, the results of our parameter study are presented.

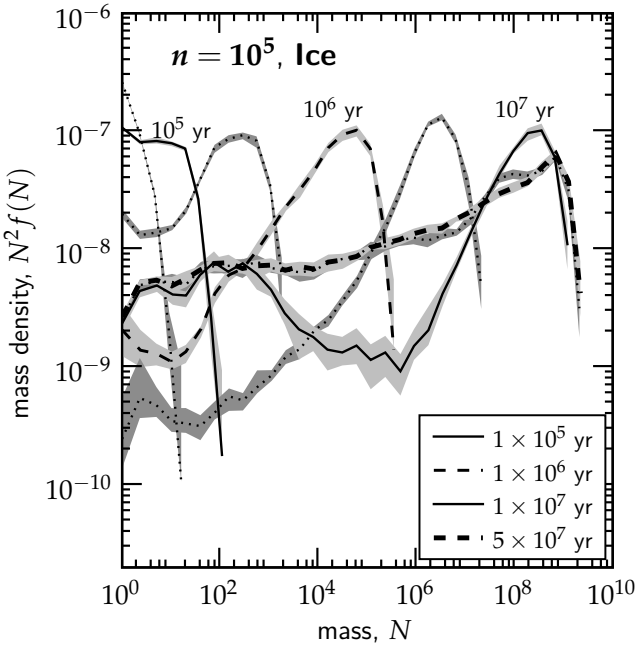

Fig. 6.8: Mass distribution of the standard model ($n = 10^5$ cm^{-3}, $a_0 = 10^{-5}$ cm, ice-coated silicates) at several times during its collisional evolution, until $t = 5 \times 10^7$ yr. The distribution is plotted at times of 10^i yr (*solid curves*, except for the 10^6 yr curve, which is plotted with a *dashed curve*) and 3×10^i yr (all *dotted curves*), starting at $t = 3 \times 10^4$ yr. The grey shading denotes the spread in 10 runs. Mass is given in units of monomers. The final curve (*thick dashed curve*) corresponds to 5×10^7 yr and overlaps the 3×10^7 yr curve almost everywhere, indicating that steady-state has been reached.

6.5.1 The standard model

Figure 6.8 shows the progression of the collisional evolution of ice-coated silicates at a density of $n = 10^5$ cm^{-3} (the standard model). Each curve shows the average of 10 simulations, where the grey shading denotes the 1 σ spread in the simulations. At $t = 0$ the distribution starts out monodisperse at size $N = 1$. Here, N denotes the number of monomers in an aggregate and is a dimensionless measure of the mass. The distribution function $f(N)$ gives the number of aggregates per unit volume such that $f(N)\mathrm{d}N$ is the number density of particles in a mass interval $[N, N + \mathrm{d}N]$. Thus, at $t = 0$ the initial distribution has a number density of $f(0, t = 0) = n\mu m_\mathrm{H}/\mathcal{R}_\mathrm{gd} m_0 = 3.5 \times 10^{-7}$ cm^{-3} in the case of $n = 10^5$ cm^{-3} and $a_0 = 0.1$ μm. On the y-axis $N^2 f(N)$ is plotted at several distinct times during the collisional evolution, which shows the mass of the distribution in a logarithmic interval. The mass where $N^2 f(N)$ peaks in Fg. 6.8 is denoted the mass peak: it corresponds to the particles in which most of the mass is contained. The peak of the distribution curves stays on roughly the same level during its evolution, reflecting conservation of mass density.

After $t = 10^5$ yr (first solid line) a second mass peak has appeared at $N = 10$ that separates itself from the initial distribution. The peak at $N = 1$ is a remnant of the compact ($\phi = 1$) size and smaller collisional cross-section of monomers compared with dimers, trimers, *etc.*—not by fragmentation. Furthermore, the high collisional cross section of, *e.g.*, dimers is somewhat overestimated, being the consequence of the adopted power-law fit between the geometrical and collisional cross section (Fg. 6.3). These effects are modest and do not affect the result of the simu-

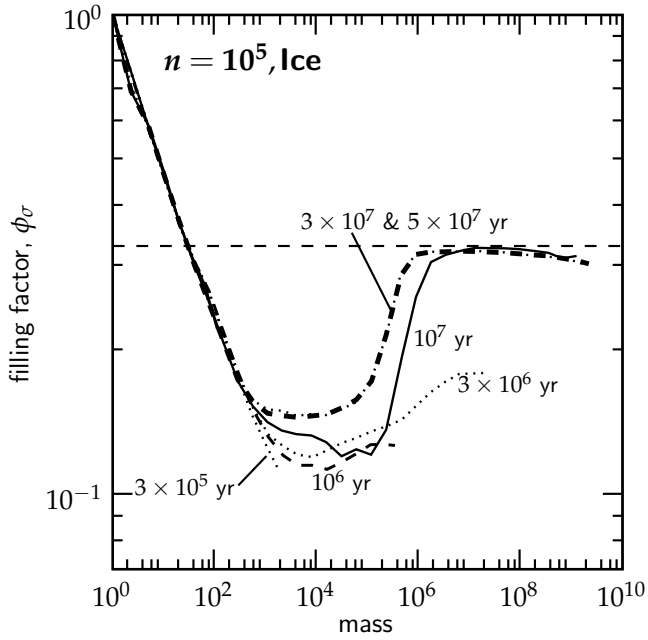

Fig. 6.9: The distribution of the filling factor, ϕ, in the standard model, plotted at various times. In the fractal regime, the porosity decreases as a power-law, $\phi \simeq N^{-0.3}$. Compaction is most severe for the more massive particles, where the filling factor reaches the maximum of 33%. Only mean quantities are shown, not the spread in ϕ.

lation. Meanwhile, the porosity of the aggregates steadily increases, initially by hit-and-stick collisions but after $\sim 10^5$ yr mostly through low-energy collisions between equal-size particles (global recipe) that do not visible compress the aggregate. In Fg. 6.9 the porosity distribution is shown at several times during the collisional evolution. Initially, due to low-energy collisions the filling factor decreases as a power-law with exponent $\simeq 0.3$, $\phi \simeq N^{-0.3}$. This trend ends after $N \sim 10^4$, at which collisions have become sufficiently energetic for compaction to halt the fractal growth. The filling factor then flattens out and increases only slowly. At $t = 3 \times 10^6$ yr the $N \sim 10^7$ particles are still quite porous.

After $t = 3 \times 10^6$ yr collisions have become sufficiently energetic for particles to start fragmenting, significantly changing the appearance of the distribution. Slowly, particles at low mass are replenished and growth decelerates. When inquiring the statistics underlying the fragmenting collisions, we find that collisions that result in fragmentation are mostly of a (very) modest erosive nature, in which only a few percent of the mass of the large aggregate is removed. Therefore, when erosion first appears, growth is not immediately halted, but it is effective in replenishing the particles at low-N. With time, however, the stationary point is unquestionably reached as collisions will eventually enter a regime in which there is no net growth. The collisional evolution does never proceed to a stage in which shattering collisions dominate the fragmentation.

The collision experiment is continued beyond 10^7 yr, until the point where a steady-state has been reached. At 10^7 yr the largest particles have reached the upper limit of 33% for the filling factor. The compaction increases the collision velocities between the particles and therefore enhances the fragmentation. At 3×10^7 yr the

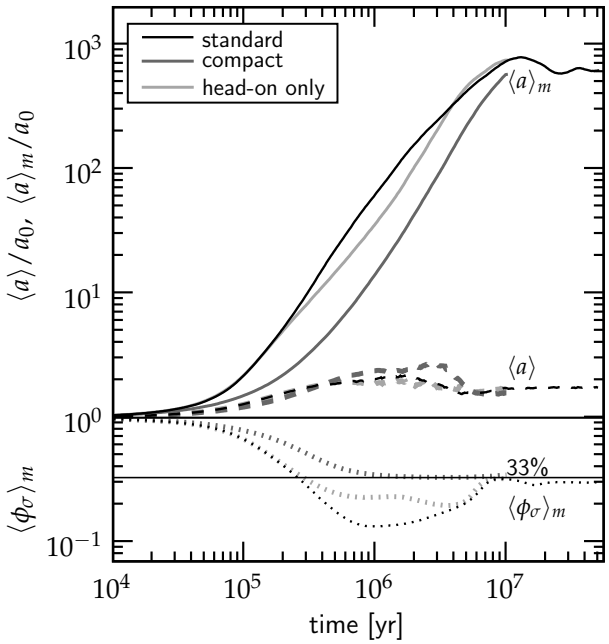

Fig. 6.10: (*black curves*) The temporal evolution of the mean size $\langle a \rangle$ (*dashed curve*), the mass-weighted size $\langle a \rangle_m$ (*dotted curve*) and the mass-weighted filling factor, $\langle \phi \rangle_m$ (*solid curve*) of the distribution for the standard model. (*dark grey curves*) Compact model, in which the filling factor stays above 33%. (*light grey curves*) The standard model restricted to head-on collisions only.

distribution curve has flattened-out significantly. The final curve ($t = 5 \times 10^7$ yr) mostly overlaps the 3×10^7 curve (both in Fgs. 6.8 and 6.9) and therefore indicates that steady-state has been reached. At this stage most of the mass resides in $\sim$100 μm grains. However, small particles, due to the fragmentation, are again dominant by number.

The transition towards a flat mass spectrum is consistent with a scenario in which mass is injected at $N = 1$, and then 'flows' to large-N at which it is fragmented, or, in this case, eroded. Indeed, the erosive nature of fragmenting collisions produces mostly low-N particles. The change in the shape of the mass function with time also provides a clue why the curves in Fg. 6.9 do not overlap in the intermediate-N region. At times before 10^7 yr, the point where the curves terminate correspond to the most massive particles in the distribution. These are quite rare and therefore preferentially collide with particles of lower mass, which suppresses the collisional energies due to the mass-ratios. When the distribution has flattened out, however, equal-mass collisions are more important and the higher energies involved cause compaction to occur at lower N.

Compact and head-on coagulation

To further understand the influence of the porosity on the collisional evolution we plot in Fg. 6.10 the progression of a few key quantities as function of time: the mean size $\langle a \rangle$, the mass-average size $\langle a \rangle_m$, and the mass-average filling factor $\langle \phi \rangle_m$ of the distribution. Here, mass-average quantities are obtained by weighing the particles

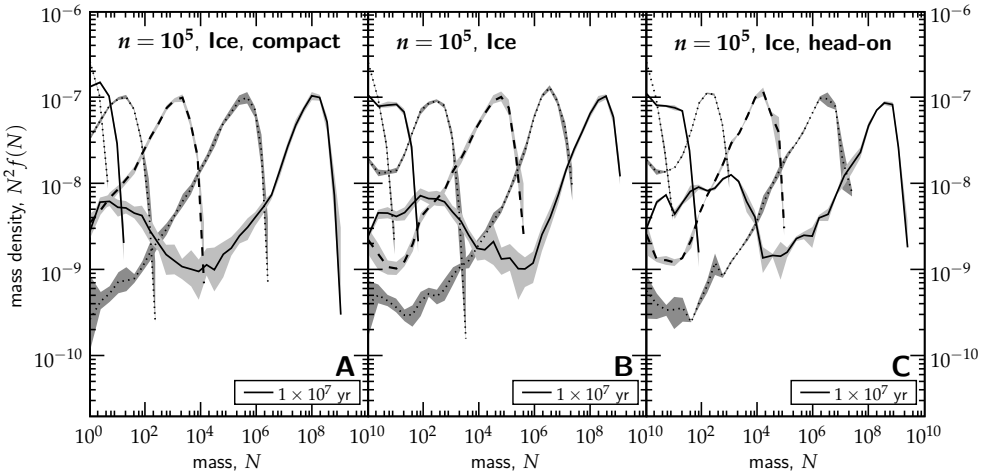

Fig. 6.11: Plots that test the influence of the collision recipe on the evolution of the size distribution for the standard model where ice-coated silicates are treated. *(a)* Compact coagulation, in which the filling factor is restricted to a lower limit of 33%. *(b)* The standard model, shown for comparison. *(c)* Head-on collisions only, where the impact parameter is fixed at $b = 0$ for every collision. The evolution extends until $t = 10^7$ yr.

of the MC program by mass; *e.g.*, the mass-weighted size is defined as

$$\langle a \rangle_m = \frac{\sum_i m_i a_i}{\sum_i m_i}. \tag{6.31}$$

The weighing by mass has the effect that only the massive particles contribute — provided these particles dominate the mass peak, which is mostly the case when the distribution is evolved. On the other hand, in a regular average all particles contribute equally, meaning that this quantity is particularly affected by the particles that dominate the number distribution. Thus, as particles start out monodisperse, $\langle a \rangle_m = \langle a \rangle$. However, over time $\langle a \rangle_m$ starts to move away from the mean size of the distribution, meaning that most of the mass becomes locked up in large particles but that the small particles still dominate the number distribution. This picture is consistent with the distribution plots in Fg. 6.8.

How important is the adopted collision recipe in shaping the distribution? To assess this question we additionally ran simulations in which the collision recipe is varied with respect to the standard model. The distribution functions of these runs are presented in Fg. 6.11, whereas Fg. 6.10 also shows the computed statistical quantities (until $t = 10^7$ yr). In the case of compact coagulation the filling factor of the particles was restricted to a minimum of 33% (small particles like monomers can still have higher filling factors). Clearly, the results show that the initial stages of the growth is much faster for porous aggregates (cf. Fg. 6.11a and Fg. 6.11b). This can be understood by considering the dependence on filling factor of the friction time and

the cross-section

$$\tau_{\rm f} \propto N^{1/3}\phi^{2/3}; \tag{6.32a}$$

$$A \propto N^{2/3}\phi^{-2/3}, \tag{6.32b}$$

where we substituted for simplicity the geometrical cross section A for the collisional cross-section σ_{ij}. Because velocities depend on the square-root of the friction time, the collision rate, $K = \sigma_{ij}\Delta v$, has a $-1/3$ dependence on filling factor, $K \propto N^{5/6}\phi^{-1/3}$. Therefore, the collision rate is increased if filling factors decrease. Porous aggregation, then, shortens the growth timescale.

Figure 6.11c presents the results of the standard model in which collisions are restricted to take place head-on, an assumption that is frequently employed in collision studies. That is, except for the missing collision probability ($f_{\rm miss}$), the collision parameters are obtained exclusively from the $b = 0$ entry. In this way we can assess the importance of offset collisions. The temporal evolution of the head-on only model is also given in Fg. 6.10 by the light-grey curves. It can be seen that the particles are generally less porous than in the standard model. This follows also from the recipe, see Fg. 6.5: at intermediate energies ($E/N_{\rm tot}E_{\rm roll} \sim 1$) central collisions are much more effective in compacting than offset collisions. For these reasons, also, growth in the standard model is somewhat faster during the early stages. However, at later times the differences between Fg. 6.11b and Fg. 6.11c become relatively minor, indicating that head-on or offset collisions do not result in a very different fragmentation behavior.

A simple analytical model

Despite the complexity of the recipe, it is instructive to approximate the initial collisional evolution with a simple analytical model. From the preceding discussion it is clear that the evolution of the filling factor drives the growth, as this quantity implicitly determines the velocity structure and the collision timescales. Continuing from Eq. (6.32) we can write

$$\Delta v \propto \tau_{\rm f}^{1/2} \propto N^{1/6}\phi^{1/3}; \tag{6.33a}$$

$$t_{\rm coll} = \left(n_{\rm d}\Delta v\sigma_{ij}\right)^{-1} \propto N^{1/6}\phi^{1/3}, \tag{6.33b}$$

where the monodisperse assumption $n_{\rm d} \propto N^{-1}$ has been applied. As explained in § 6.2.2 the expression $\Delta v \propto \tau_{\rm f}^{1/2}$ holds only for the square-root part of the turbulence, but this is fully appropriate for the molecular cloud environment. Then, relative velocities and collision timescales have the same dependence on N and ϕ. Concerning ϕ Fg. 6.9 suggest that the initial evolution of ϕ can be divided in two regimes, where the transition point occurs at a mass N_1. Initially ($N < N_1$), the filling factor is in the fractal regime, which can be well approximated by a power-law, $\phi \simeq N^{-3/10}$. We refer to this regime as the fractal regime, because it includes hit-and-stick collisions (no restructuring) as well as collisions for which $E > 5E_{\rm roll}$ but which do not lead to *visible* restructuring, *i.e.*, only a small fraction of the grains take part in the restruc-

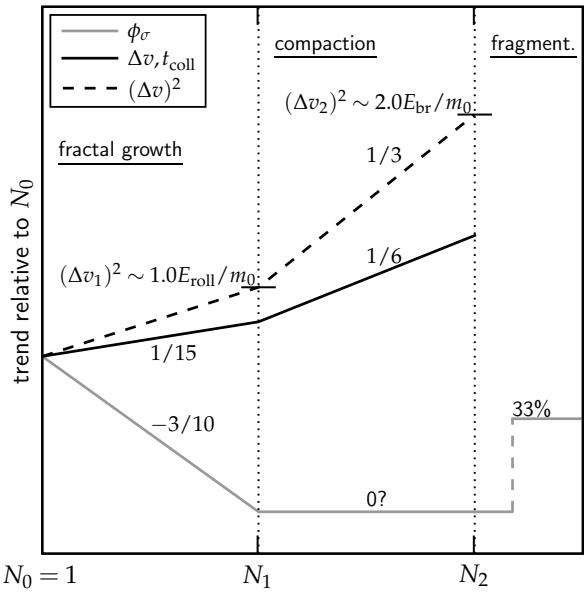

Fig. 6.12: (*grey line*) A simplified model for the behavior of the filling factor with growth. Initially, if Δv_0 is sufficiently low, the porosity decreases (fractal growth regime). This phase is followed by a "status quo" phase where filling factors will be approximately constant. The first compaction event is reached when velocities reach Δv_1 and fragmentation sets in when relative velocities exceeds Δv_2. (*solid line*) Trend of the collision velocity and collision timescale. (*dashed line*) Trend of $(\Delta v)^2$. The numbers denote the power-law exponents.

turing. For $N > N_1$ the filling factor starts to flatten-out. It is difficult to assign a trend for ϕ in the subsequent evolution. Following Fig. 6.9 we may assume that initially ϕ stays approximately constant for several orders of magnitude in N, but at some point it will quickly assume its compact value of 33%. Here, we assume that the collapse of the porous structure takes place *after* the point where the first erosive collisions occurs, at $N = N_2$. A sketch of the adopted porosity structure and the resulting scaling of velocities and timescales is presented in Fig. 6.12.

From the collision recipe (§ 6.3.2) we can identify the critical energies where visible compaction and fragmentation occur. In the first case, the global recipe applies and Fig. 6.5 shows that the transition to compaction ($C_\phi > 1$) corresponds to a normalized energy of $\varepsilon_{\rm roll} = E/NE_{\rm roll} \simeq 0.2$. On the other hand the simulations clearly show that small particles are replenished by fragmentation in the form of erosive collisions. From Fig. 6.4 we can assign an energy threshold of $\varepsilon_{\rm br} = E/N_\mu E_{\rm br} \simeq 1.0$. Working out these expressions and using a typical mass ratio of 3 for the global recipe ($N_\mu = N/6$), we find that these energy criteria corresponds to relative velocities of $(\Delta v_1)^2 \simeq 1.0 E_{\rm roll}/m_0$ and $(\Delta v_2)^2 \simeq 2.0 E_{\rm br}/m_0$, respectively. These energy thresholds are also indicated in Fig. 6.12.

From these expressions and the initial expressions for the relative velocity and the collision timescale (Eqs. (6.15) and (6.16)), the turn-over points N_1 and N_2 can be calculated. We assume that $\Delta v_0 < \Delta v_1$ such that a fractal growth regime exist. Then,

the first transition point is reached at a mass

$$N_1 \sim \left(\frac{\Delta v_1}{\Delta v_0}\right)^{15} = \left(\frac{1.0 E_{\rm roll}}{m_0 (\Delta v_0)^2}\right)^{7.5} \tag{6.34}$$
$$= 2 \times 10^3 \left(\frac{n}{10^5 \text{ cm}^{-3}}\right)^{3.75} \left(\frac{\gamma}{370 \text{ erg cm}^{-2}}\right)^{7.5} \left(\frac{a_0}{0.1\ \mu\text{m}}\right)^{-22.5}.$$

Unfortunately, the high powers make the numeric evaluation rather unstable. In our simulations we find that $N_1 \sim 10^4$. Subsequently, we can write for the second transition point, the onset of fragmentation, N_2,

$$\frac{N_2}{N_1} \sim \left(\frac{\Delta v_2}{\Delta v_1}\right)^6 = \left(2.0 \frac{E_{\rm br}}{E_{\rm roll}}\right)^3 \tag{6.35}$$
$$= 5 \times 10^4 \left(\frac{\gamma}{370 \text{ erg cm}^{-2}}\right) \left(\frac{a_0}{0.1\ \mu\text{m}}\right) \left(\frac{\mathcal{E}^\star}{3.7 \times 10^{10} \text{ dyn cm}^{-2}}\right)^{-2},$$

which corresponds also well to the results from the simulation for which $N_2 \sim 10^8$. In our simulations the *first* fragmentation involves particles that are still relatively porous, such that the assumption in Fig. 6.12 about the porosity of the N_2-particles is justified. However, once steady-state has been reached, particles of $N_2 \sim 10^8$ will have a 33% filling factor (see Fg. 6.9).

Equations (6.34) and (6.35) also provide a clue how the collisional evolution will behave under different conditions. First, Eq. (6.35) shows that the ratio N_2/N_1 depends on the critical energies only, and therefore that this ratio should stay the same for the same material properties. The $n^{3.75}$ dependence on gas density in Equation (6.34) indicates that the transition points shift $\simeq$1 magnitude in size when the gas density increases by a factor of 10. Even more critical is the dependence on grain size, a_0. This follows directly from the requirement that for visible restructuring *all* grains have to participate. A smaller grain size makes this requirement harder to obtain. Together with the lower initial velocity (lower Δv_0) and the extremely shallow way relative velocities evolve in the fractal regime, aggregates are expected to become very large when $a_0 < 0.1\ \mu$m.

Using a monodisperse model we can also obtain the timescales t_1, t_2 at which these transition points are reached. Starting from the expression

$$\frac{\mathrm{d}N}{\mathrm{d}t} = \frac{N}{t_{\rm coll}}, \tag{6.36}$$

the collision time $t_{\rm coll}$ is approximated by a power-law assumption, $t_{\rm coll} = t_{{\rm coll},i}(N/N_i)^\lambda$. Here, $t_{{\rm coll},i}$ is the collision timescale at the point N_i. Specifically, $t_{{\rm coll},0}$ is the initial collision timescale (Eq. (6.16)). Straightforward integration then leads to

$$\frac{t - t_i}{t_{{\rm coll},i}} = \frac{1}{\lambda}\left[\left(\frac{N}{N_i}\right)^\lambda - 1\right]; \qquad (N > N_i). \tag{6.37}$$

For $i = 0$, $\lambda = 1/15$ and $N_1/N_0 \sim 10^4$ it results that the fractal growth stages takes $\sim$12 initial collision timescales, or $\sim 10^6$ yr (*cf.* $\sim 6 \times 10^5$ yr in the simulation). In the second regime $\lambda = 1/6$, $t_{\rm coll,1} \simeq 2t_{\rm coll,0}$ and taking $N_2/N_1 = 10^4$ it follows that $t_2 - t_1 \sim 40 t_{\rm coll,0}$. Altogether, we may expect that the first fragmentation event takes place after $\sim$50 collision timescales. The simulation shows that in the standard model $\sim$65 initial collision times are required. Because the collision timescale only slowly changes, we may expect the calculated timescales present a general picture, *i.e.*, both compaction and fragmentation take place in a $\sim 10 - 100 t_{\rm coll,0}$ interval.

6.5.2 Parameter study

In Fg. 6.13 the collisional evolution of silicates and ice-coated particles are contrasted at densities of $n = 10^4, 10^5$ and 10^6 cm^{-3}. Simulations run until a time of 10^7 yr, except for Fg. 6.13c where steady state has been reached before. The reason to stop the calculation, then, is that in steady-state the average inter-collision timesteps will be constant, whereas in the preceding 'pure-growth' scenario, the inter-collision time increases. The linear behavior makes it computationally intensive to further evolve the distribution for similar timescales. Again, distributions are plotted at fixed logarithmic timesteps between $t = 3 \times 10^4$ yr and $t = 10^7$ yr, where the curves correspond to the same times as in Fg. 6.8.

Figure 6.13a-c show the collisional evolution of silicates at various densities. In most of the models fragmentation is important from the earliest timescales on. This is of course a consequence of the much lower breaking energy $E_{\rm br}$ that silicate monomers have compared with ice-coated silicates. As a result, in terms of size the growth is very modest: only a factor of 10 in the $n = 10^6$ cm^{-3} model, whereas at even lower densities most of the mass stays in monomers. For the same reason, silicates reach steady state much quicker than ice-coated particles, on a timescale of 10^6 yr.

This situation becomes very different, however, if the silicates are coated with ice (Fg. 6.13d-f). Much more energetic collisions are then required to break aggregates and aggregates grow large indeed. In all cases the qualitative picture reflects that of our standard model, discussed in § 6.5.1: porous growth in the initial stages, followed by compaction and fragmentation in the form of erosion. The evolution towards steady-state is a rather prolonged process, and is only complete within $t = 10^7$ yr in Fg. 6.13f. Again, steady state is characterized by a rather flat mass spectrum. In the low density model of Fg. 6.13d fragmentation does not occur within 10^7 yr.

In Fg. 6.14 the collisional evolution is contrasted at three different values for the monomer size: $a_0 = 300$ Å (Fg. 6.14a), 0.1 μm (the standard model, Fg. 6.14b), and $a_0 = 1$ μm (Fg. 6.14c). To obtain a good comparison, Fg. 6.14 uses physical units (grams) for the mass of the aggregates, rather than the dimensionless number of monomers, N. The effects of varying a_0 are twofold. First, as we have seen above, the length of the fractal growth phase (no compaction or fragmentation) is very sensitive to a_0. Second, the monomer size a_0 directly reflects the amount of energy dissipation of the material. In the literature this is often characterized by an impact strength Q, which is the ratio of the excavated mass over the collision energy. Changing the monomer size will affect the strength of the monomers, because it determines

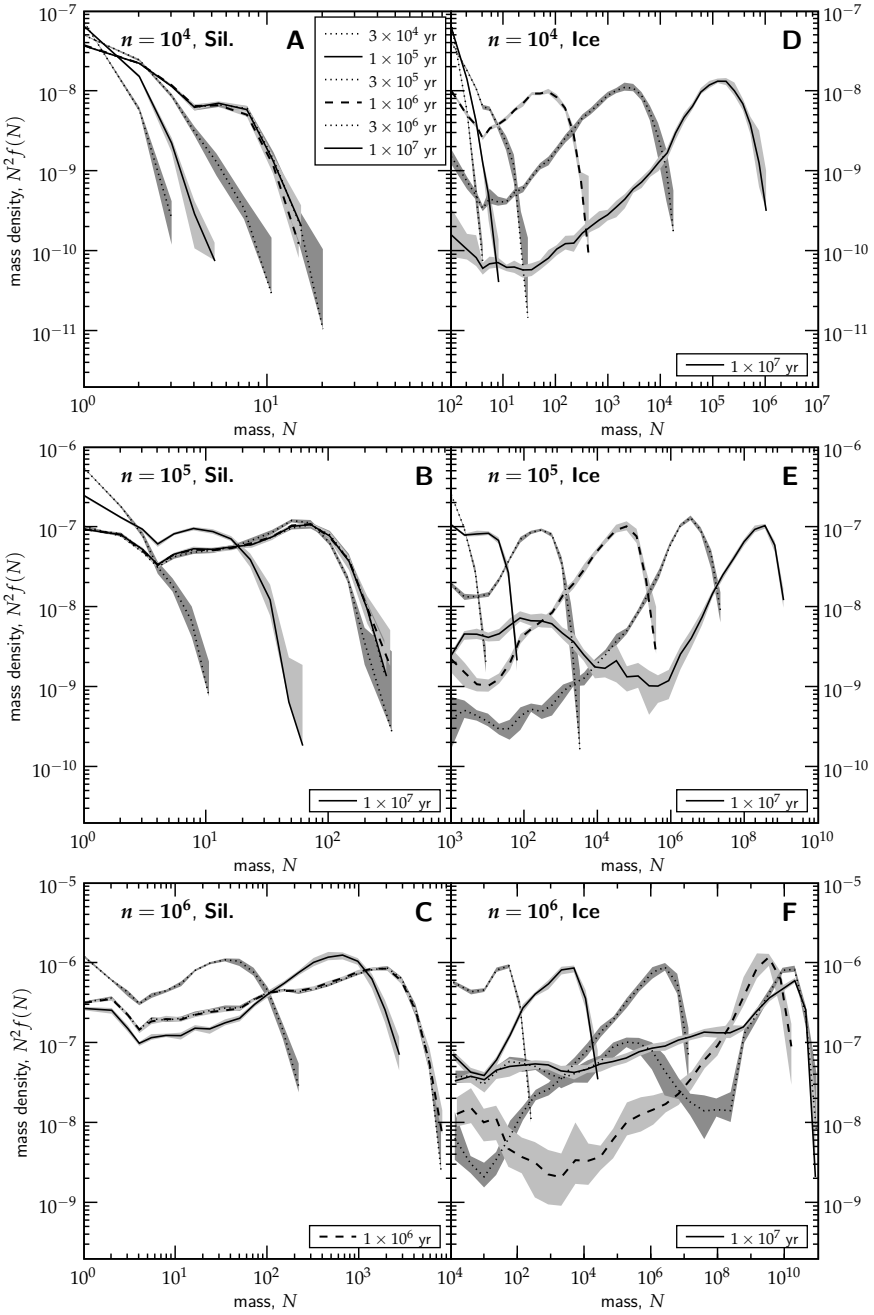

Fig. 6.13: Distribution plots corresponding to the collisional evolution of silicates (*left* panels) and ice-coated silicates (*right* panels) at densities of $n = 10^4, 10^5$ and 10^6 cm^{-3} until $t = 10^7$ yr. For the silicates a steady-state between coagulation and fragmentation is quickly established on timescales of $\sim 10^6$ yr, whereas ice-coated silicates grow much larger before fragmentation kicks in. The initial distribution is monodisperse at $a_0 = 10^{-5}$ cm. Note the different x-scaling.

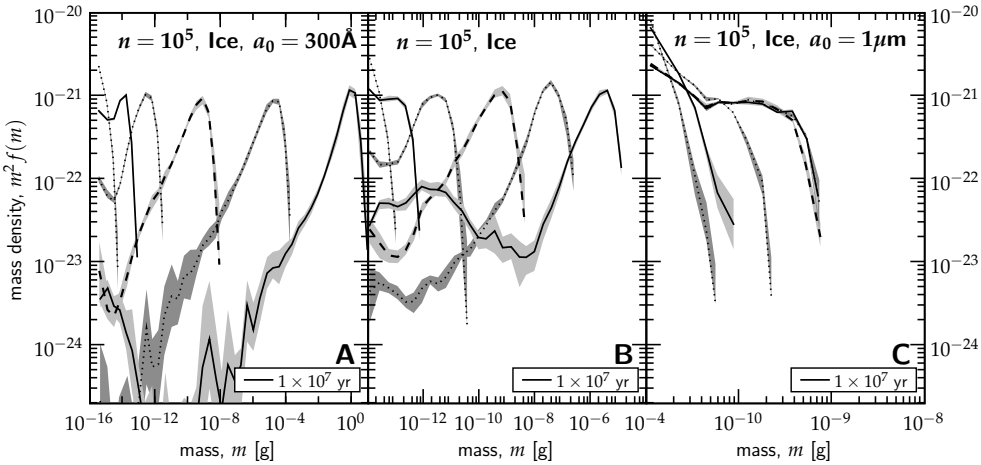

Fig. 6.14: Effects of a varying monomer size a_0 on the evolution of the size distribution for the ice-coated silicates of the standard model: (*a*) $a_0 = 300$ μm, (*b*) $a_0 = 0.1$ μm (the default, shown for reasons of comparison), and (*c*) $a_0 = 1$ μm. To facilitate the comparison, physical units are used (grams) for the mass of aggregates, rather than the dimensionless number of monomers (N).

the amount of surface area that must be broken. Taking the breaking energy as a typical threshold for fragmentation, we obtain $Q \sim E_{\rm br}/m_0 \sim 10^7$ erg g^{-1} for $a_0 = 0.1$ μm size aggregates and a scaling with size of $Q \propto a_0^{-5/3}$. Therefore, aggregates that consist of smaller grains are much more resistant against energetic collisions than aggregates consisting of larger monomers. Likewise, silicate grains due to their much lower γ have a correspondingly lower strength. We do point out that in reality Q must be determined by experiment; however, our definition ($Q \sim E_{\rm br}/m_0$) serves explanatory purposes.

These effects are best seen in Fg. 6.14c where a tenfold increase in monomer size compared to the standard model (Fg. 6.14b) results in completely different distribution curves. Due to the much reduced strength of the aggregates, fragmenting collisions occur already from the outset. The curves, therefore, resemble the silicate models of Fg. 6.13b, which are also dominated by fragmentation. Figure 6.14a, on the other hand, shows the effects of reducing the size of the monomers by about a factor three ($a_0 = 0.03$ μm). Despite starting out at a lower mass, the 300 Å model quickly catches up with the standard model and overtakes it at $t \sim 10^6$ yr. This results because significant compaction fails to occur, in line with the results of the simple analytic model of § 6.5.1; until 4×10^6 yr no significant compaction takes place, and aggregates become really porous indeed ($\phi \simeq 4 \times 10^{-4}$). The consequence is that fragmentation is also delayed, and has only tentatively started at the close of the simulations.

Tables 6.5 and 6.6 present the results of the coagulation/fragmentation process in tabular format. In Table 6.5 the mass-weighted size of the distribution (reflecting

MASS-WEIGHTED SIZE

	$\langle a \rangle_m$ [cm]					
model	10^4 yr	10^5 yr	10^6 yr	10^7 yr	$t_{\rm ff}(n)$	$t_{\rm ad}(n)$
(1)	(2)	(3)	(4)	(5)	(6)	(7)
$n = 10^3$, ice	1.0(−5)	1.0(−5)	1.2(−5)	8.3(−5)	1.2(−5)	8.3(−5)
$n = 10^4$, silicates	1.0(−5)	1.1(−5)	1.4(−5)	1.4(−5)	1.2(−5)	1.4(−5)
$n = 10^4$, ice	1.0(−5)	1.1(−5)	4.6(−5)	8.5(−4)	1.5(−5)	8.5(−4)
$n = 10^5$, silicates	1.0(−5)	1.9(−5)	4.0(−5)	4.0(−5)	2.0(−5)	4.0(−5)
$n = 10^5$, silicates, $a_0 = 10^{-4}$	1.0(−4)	1.0(−4)	1.0(−4)	1.0(−4)	1.0(−4)	1.0(−4)
$n = 10^5$, ice	1.0(−5)	2.2(−5)	6.4(−4)	7.4(−3)	2.3(−5)	3.2(−3)
$n = 10^5$, ice, $a_0 = 10^{-4}$	1.0(−4)	1.1(−4)	2.2(−4)	2.3(−4)	1.1(−4)	2.3(−4)
$n = 10^5$, ice, $a_0 = 3 \times 10^{-6}$	3.2(−6)	1.1(−5)	1.3(−3)	4.3	1.2(−5)	2.4(−1)
$n = 10^5$, ice, compact	1.0(−5)	1.5(−5)	1.4(−4)	5.8(−3)	1.6(−5)	1.3(−3)
$n = 10^5$, ice, head-on	1.0(−5)	2.2(−5)	3.6(−4)	7.5(−3)	2.4(−5)	3.1(−3)
$n = 10^6$, silicates	1.4(−5)	1.2(−4)	1.3(−4)	1.3(−4)	4.4(−5)	1.3(−4)
$n = 10^6$, ice	1.4(−5)	2.7(−4)	3.7(−2)	2.0(−2)	4.6(−5)	2.9(−2)
$n = 10^7$, ice	7.9(−5)	3.7(−2)	5.2(−2)	6.1(−2)	8.6(−5)	7.8(−1)

Table 6.5: The mass-weighted size of the distribution, $\langle a \rangle_m$, at several distinct events during the simulation run. Col. (1) list the models in terms of the density (n) and material properties. The monomer size (a_0) is 0.1 μm, unless otherwise indicated. Cols. (2)–(5) give the mass-weighted size of the distribution at fixed coagulation times. Likewise, cols. (6)–(7) give value of $\langle a \rangle_m$ at the free-fall and the ambipolar diffusion timescale of the cloud that corresponds to the gas density n. These are a function of density and are given in Eq. (6.1) and Eq. (6.4), respectively. Values $a \times 10^b$ are denoted $a(b)$.

GEOMETRICAL OPACITY

	$\langle \kappa \rangle$ [cm^2 g^{-1}]					
model	10^4 yr	10^5 yr	10^6 yr	10^7 yr	$t_{\rm ff}(n)$	$t_{\rm ad}(n)$
(1)	(2)	(3)	(4)	(5)	(6)	(7)
$n = 10^3$, ice	2.8(4)	2.8(4)	2.7(4)	1.5(4)	2.7(4)	1.5(4)
$n = 10^4$, silicates	2.8(4)	2.8(4)	2.7(4)	2.6(4)	2.7(4)	2.6(4)
$n = 10^4$, ice	2.8(4)	2.8(4)	2.0(4)	2.5(3)	2.6(4)	2.5(3)
$n = 10^5$, silicates	2.8(4)	2.5(4)	2.0(4)	2.0(4)	2.5(4)	2.0(4)
$n = 10^5$, silicates, $a_0 = 10^{-4}$	2.8(3)	2.8(3)	2.8(3)	2.8(3)	2.8(3)	2.8(3)
$n = 10^5$, ice	2.8(4)	2.4(4)	5.1(3)	2.3(3)	2.4(4)	8.4(2)
$n = 10^5$, ice, $a_0 = 10^{-4}$	2.8(3)	2.8(3)	2.4(3)	2.4(3)	2.8(3)	2.4(3)
$n = 10^5$, ice, $a_0 = 3 \times 10^{-6}$	9.3(4)	7.1(4)	1.4(4)	4.4(2)	6.9(4)	1.7(3)
$n = 10^5$, ice, compact	2.8(4)	2.6(4)	8.0(3)	1.9(3)	2.6(4)	1.0(3)
$n = 10^5$, ice, head-on	2.8(4)	2.4(4)	4.9(3)	3.1(3)	2.4(4)	9.3(2)
$n = 10^6$, silicates	2.7(4)	1.4(4)	1.4(4)	1.4(4)	2.0(4)	1.4(4)
$n = 10^6$, ice	2.7(4)	1.2(4)	6.7(2)	2.2(3)	2.0(4)	1.5(3)
$n = 10^7$, ice	1.7(4)	1.8(3)	1.4(3)	1.7(3)	1.6(4)	6.4(2)

Table 6.6: Like Table 6.5 but for the geometrical opacity of the particles. The opacity κ gives the total surface area per unit (dust) mass.

the largest particles) are given, and in Table 6.6 the opacity of the distribution is provided, which reflects the behavior of the small particles. Here, opacity means geometrical opacity — the amount of surface area per unit mass — which would be applicable for visible or UV radiation, not to the IR. Its definition is, accordingly,

$$\langle \kappa \rangle = \frac{\sum \pi a_i^2}{\sum m_i}, \tag{6.38}$$

where the summation is over all particles in the simulation. These tables show, for example, that in order to grow chondrule-size particles ($\sim 10^{-3}$ g), dust grains need to be ice-coated and, except for the $n = 10^6$ cm^{-3} model, coagulation times of $\sim 10^7$ yr are required. Furthermore, concerning the observational properties, Table 6.6 shows that a decrease of the opacity by a factor of 10 at most can be expected, for ice models at long timescales.

6.6 Assessment of the collision recipe

Our study of coagulation in Molecular Clouds is the first study that applies the results of detailed numerical simulations — simulations, that have previously succeeded in explaining laboratory experiments (Paszun & Dominik 2008b) — to the global evolution of molecular clouds. This includes modeling the impact parameter and porosity of aggregates as independent variables. Much effort has been invested in the collision model. Fragmentation, especially, is modeled in detail, being characterized by three parameters and distinguished through the local and global recipe. In summary, we have presented the first model that couples the collisional growth of aggregates to the evolution of their internal structure while simultaneously accounting for the diverse collision outcomes that follow from the changing velocities between the particles as they grow. The collision model, certainly, is state-of-the-art.

The drawback of relying on a sophisticated numerical model is, however, that their results are in the strictest sense only applicable to the same size regime, *i.e.*, for $N \lesssim 10^3$ particles. For silicates, this limited dynamic range of the numerical models is appropriate, because coagulation does not proceed beyond $N \sim 10^3 - 10^4$ (Fg. 6.13). Ice grains, on the other hand, are capable to grow to much larger sizes. For the recipe to become applicable for these large aggregates *extrapolation* of the results of the collision experiments is required. This is a critical point of the recipe in which we have invested considerable effort. The outcome was that we divided collisions in two groups — local and global — scaled their results to the critical energies involved ($E_{\rm br}$ and $E_{\rm roll}$), and the number of particles (either the total number, $N_{\rm tot}$, or the reduced number, N_μ). The idea behind these normalizations is to make the collision recipe scale-independent: applicable to the low-N regime as well as the large-N regime.

Extrapolating the collision recipe is nonetheless risky. Because of the large dynamic range involved and the embedding of the results in a MC approach, collisions of many small particles with a large particle are considered simultaneously through the grouping method. Tiny deviations of the recipe then have the potential to blow up. Furthermore, the extrapolation assumes that the collision physics at large scale

is the same to the size of the collision experiments. This, too, is a crucial assumption in which collisional outcomes like *bouncing* are *a priori* not possible because these do not take place at the low-N part of the simulations.

Below, we present some of the limitations of the collision recipe, and offer suggestions for future improvement. These points concern the physics represented in the collision recipe (bouncing, irregular grains, and a size distribution of grains) or its implementation into the coagulation model. Although we acknowledge that by including a more sophisticated treatment, it is probable that the quantitative outcome of the collision experiments will change to some extent, we do not expect that the main results of our model — the initial coagulation phase, followed by the transition to a flat steady-state distribution — and their dependence on gas density and material properties will be much affected.

6.6.1 Bouncing

Bouncing of aggregates is observed in laboratory experiments (Blum & Münch 1993; Blum 2006), whereas it does not occur in our simulations. For silicates, the bouncing phenomenon occurs at sizes above approximately 100 μm (*i.e.*, $N > 10^9$ particles) and is not fully understood. It is a challenge to investigate in the laboratory the microphysics of these large particles.

In the case of ice-coated silicate grains, which provide stronger adhesion forces, our simulations show that growth proceeds to $\sim$100 μm sizes where bouncing becomes potentially important. In this case, therefore, the growth might slow down earlier than observed in our experiments, especially when the internal structure has already re-adjusted to a compact state, where energy dissipation is no longer available. It is presently unclear how these laboratory experiments apply to ice aggregates and hence whether and to what extent the Monte Carlo results would be affected by bouncing. We recognize that this may, potentially, present a limitation to growth of aggregates in molecular clouds, but also emphasize it will not affect the main conclusions from this study as in only few models aggregates grow to sizes $\gg$100 μm.

6.6.2 Size distribution of grains

Our recipe is based on simulations of aggregates that are built of monomers of a single size. Therefore, we treat a monodisperse distribution. However, ISM-dust typically consist of a size distributions of small grains and larger grains. The most frequently used size distribution is the MRN-distribution where the grain distribution scales as a $-7/2$ power-law of size, between a lower (a_i) and an upper (a_f size) (Mathis et al. 1977). Thus, in the MRN-distribution the smallest grains are dominant by number, whereas the larger grains dominate the mass. For an MRN distribution we take, $a_\mathrm{i} = 50$ Å and $a_\mathrm{f} = 0.25$ μm. Therefore, the collision outcome may differ when the colliding particles are made of grains of several sizes.

To illustrate this point, we quantitatively compare the aggregates' strength for a monodisperse and an MRN size distribution using the Q prescription. As described in § 6.5.2 the strength of aggregates is determined by the breaking energy, which scales proportional to the contact radius as $E_\mathrm{br} \propto a_\mu^{4/3}$. We will assume that in the MRN distribution a typical contact area always involves a small grain, so that we

can substitute $a_\mu = a_i$ in the $E_{\rm br}$ expression. Next, we assume that the number of contacts is of the order of the number of grains. Then, in order to determine their strength, we calculate the number of grains per unit of mass,

$$\frac{N}{m} \propto \frac{\int_{a_i}^{a_f} n(a)\mathrm{d}a}{\int_{a_i}^{a_f} n(a)a^3\mathrm{d}a} \simeq a_{\rm f}^{-1/2} a_{\rm i}^{-5/2}/5, \tag{6.39}$$

where we have used that $a_{\rm f} \gg a_{\rm i}$. In the monodisperse case, the equivalent quantity is $(N/m)_0 \propto a_0^{-3}$.

The strength of the MRN-grains can then be estimated by considering the energy dissipation per unit of mass. Thus, we multiply their typical breaking energy, which from the reasons given above is determined by the smallest grains a_i, by N/m. Comparing this to the monodisperse case we obtain

$$\frac{Q_{\rm MRN}}{Q_0} = \frac{a_i^{4/3}(N/m)_{\rm MRN}}{(a_0/2)^{4/3}(N/m)_0} = \frac{\frac{1}{5}a_{\rm f}^{-1/2}a_{\rm i}^{-7/6}}{(\frac{1}{2})^{4/3}a_0^{-5/3}} \simeq 0.5\left(\frac{a_f}{a_0}\right)^{-1/2}\left(\frac{a_0}{a_i}\right)^{7/6}. \tag{6.40}$$

(Note again that this calculation assumes that $a_{\rm f} \gg a_{\rm i}$; otherwise the numerical prefactor would be different.) In our study, where the monomer size was mostly fixed at $a_0 = 0.1$ μm, this ratio is about 10. Equation (6.40) therefore shows that the size distribution can increase the strength of an aggregate. In this picture, small grains act as the 'glue' that holds the bigger grains together and efficiently absorbs the incoming energy, because there is more contact surface. This occurs only if small monomers dominate by number. Otherwise, the mass dominated by big grains is held by much weaker contacts provided by small grains.

The results above show that in our standard case of $a_0 = 0.1$ μm the strength of aggregates is underestimated by a factor of $\sim$10, compared to the MRN-distribution. In the case of $a_0 = 0.03$ μm, the aggregate strength would be approximately the same as an MRN-distribution of grains. Remark, finally, that the above analysis only concerns the intrinsic strength of aggregates, not the relative velocities. These are determined by the friction times of the particles and the question therefore is how a distribution of grains affect the filling factor of aggregates, or, rather, the mass-to-surface area of aggregates. These will be active areas of future research.

6.6.3 Irregular particles

In this study we approximate grains with spheres, because irregular monomers are virtually impossible to simulate. Numerical modeling of these randomly shaped particles is very difficult and computationally expensive. Here, we try to assess the effect of irregular grains on the strength of aggregates and on the collision outcome.

The strength of an aggregate can be defined as the amount of the contact area per mass that is held by these inter-grain connections. The contact size in the case of irregular monomers depends on the radius of curvature local to the place where the grains touch each other. Therefore, highly irregular grains are held by contacts of much smaller size, because they are connected by surface asperities. This must result

in a much weaker strength of aggregates. On the other hand, irregular monomers may form more than one contact with each other. This results in a higher restructuring threshold, as the energy required to initiate rolling is comparable to the energy needed to break a contact.

Poppe et al. (2000) determined the critical sticking velocity for monomers of different size, shape, and material properties. They showed that irregular enstatite grains can stick at much higher velocities than silica spheres, $5 - 25$ m s^{-1} for enstatite and $1.5 - 2.3$ m s^{-1} for silica. This discrepancy suggests that additional energy dissipation may occur during a collision. The mechanism that allow sticking at this high velocity remains unknown.

Since the physical processes that determine the behavior of irregular monomers are not fully understood, we leave this issue to further study. We remark, however, that the geometry of the grains does not pose a bottleneck to the validity of the collision model; instead the consequences of irregular monomers will merely be reflected in a different energy scaling.

6.6.4 Structure of particles

In the recipe the internal structure of particles is described by only one parameter: the geometrical filling factor, ϕ. Thus, in our model the full structure of an aggregate follows from ϕ. Therefore, the collision model always assumes a spherically symmetric structure, despite the fact that elongation appears in the output results of the numerical model, especially in grazing collisions. Moreover, the filling factor is an averaged quantity and does not determine whether the aggregate structure is homogeneous or fractal; *e.g.*, the structure of a PCA particle is very different from a $D_\mathrm{f} = 2$ fractal but they can have the same filling factor if N is small. However, these are mostly second order effects and to use more variables that describe the internal structure requires a significant increase in the load of the recipe model.

6.6.5 The tabular format

In App. 6.A the tabular format of the recipe is discussed at length. The tabular format was first presented in the Paszun & Dominik (2008a) study, but here additional tables were required in order for the recipe to become applicable to the MC program. The alternative would have been to provide analytic fits that would depend on three parameters (energy, impact parameter, and porosity). Fits have the advantage that the behavior of the low and high energy regimes are immediately evident; indeed, it would become easier to include boundary constraints from an analytical prescription. However, providing 3D-analytical fits turned out to be impractical, particularly because phenomena as restructuring are somewhat erratic in nature. On the other hand, the advantage of the tabular format is that the results are implemented in the recipe in a straightforward and unbiased way.

6.7 Discussion

As can be seen from Tables 6.5 and 6.6 coagulation of bare silicates only marginally affects the collisional evolution. Therefore, we do not expect that coagulation of bare

silicates in molecular cloud cores will leave significant imprints on either the large particles or the observational diagnostics. At $T \sim 10$ K we do consider ice-coating of grains the more relevant scenario, however. Freeze-out of H_2O-ice on grains proceeds at thermal motions and is therefore faster than coagulation, provided the dust particles are well-shielded from UV-photons (Bergin et al. 1995). Then, our results suggest that grains have the potential to grow significantly, if densities are high and long coagulation timescales are available ($\gtrsim 10^6$ yr). But do these conditions materialize in molecular clouds? We will address these questions and compare our results to previous studies on dust coagulation in molecular clouds.

Ossenkopf (1993) and Weidenschilling & Ruzmaikina (1994) have pioneered studies of dust coagulation in molecular clouds. As is the case with this study, these models contain significant detail. Ossenkopf (1993) includes a structural parameter (essentially the geometrical filling factor, ϕ), an MRN size distribution for the initial distribution of dust particles (covering the range of $50 - 2500$ Å), and presents a model for the change in collisional properties upon collisions for the hit-and-stick regime. The model of Ossenkopf (1993), however, does not include aggregate restructuring and fragmentation and is therefore only applicable to the first stages of coagulation. Ossenkopf (1993) evolves his models for $\sim 10^5$ yr, usually at rather high densities ($n \gtrsim 10^6$ cm^{-3}) for which fragmenting collisions between ice(-coated) particles are indeed of no concern. The coagulation then proceeds to produce particles of compact size, ~ 0.5 μm. It can be seen from Table 6.5 that the growth in the corresponding model of our study (ice, $n = 10^6$) is higher: 1.9 μm. This may be caused by the somewhat lower turbulent velocities Ossenkopf (1993) adopts and, the fewer big ~ 0.1 μm grains the MRN distribution contains compared to our monodisperse models. At any rate, the study of Ossenkopf (1993) is mainly focused on understanding the IR dust-opacities during this relatively short timescale (Ossenkopf & Henning 1994).

On the other hand, Weidenschilling & Ruzmaikina (1994) evolve their models for much longer timescales, until $t = 10^7$ yr. Like our study, Weidenschilling & Ruzmaikina (1994) include fragmentation in the form of erosion and, at high energies, shattering. Their particles are characterized by a strength of $Q \sim 10^6$ erg g^{-1}, which are, therefore, somewhat weaker than the particles of our standard model. Although their work lacks a dynamic model for the porosity evolution, it is assumed that the initial growth follows a fractal law until 30 μm. At these sizes the filling factor then becomes less than 1%, lower than in our models.

Weidenschilling & Ruzmaikina (1994) model a Bonnor-Ebert sphere where the density at the inner region is ten times higher than at the surface. They find that the coagulation proceeds initially faster at the lower density outer regions than inside the cloud. This is caused by the assumption that the turbulent pressure stays the same throughout the cloud, providing higher turbulent motions in the outer regions. Still, coagulation is significant. Particles grow to $\gtrsim 100$ μm in their nominal model at timescales of $\sim 10^6$ yr, which is comparable to our standard model. More striking is that the nature of the growth is different: while in our model the mass-peak always occurs at the high-mass end of the spectrum, in the Weidenschilling & Ruzmaikina (1994) calculations most of the mass stays in the smallest particles. In this respect,

our findings qualitatively agree with the coagulation-fragmentation model of Brauer et al. (2008a) for protoplanetary disks. In contrast, the lack of massive particles in the Weidenschilling & Ruzmaikina (1994) models may be a result of the diffusion processes Weidenschilling & Ruzmaikina (1994) include; massive particles produced at high n mix with less massive particles from the outer regions. Thus, although the models agree on the amount of growth that is obtained, there is some difference in detail, which result from the different collisional behavior of aggregates as well as the adopted cloud model.

In our models we observe that the shape of the initially monodisperse dust size distribution evolves rapidly, first to a Gaussian-like distribution and eventually to a flat steady-state distribution. For timescales longer than the coagulation timescale (Eq. (6.16)) we can expect that this result is independent of the initial conditions, even if the coagulation starts from a power-law distribution. Essentially, these distributions are a direct result of the physics of the coagulation: the Gaussian-like distribution reflects the hit-and-stick nature of the agglomeration process at low velocities while the flat $f(N)N^2$ distribution at later times results from a balance between fragmentation — erosion but not catastrophic destruction — and growth. In contrast, in interstellar shocks grains acquire much larger relative velocities and grain-grain collisions will then quickly shatter aggregates into their constituent monomers (Jones et al. 1996) . Hence, the interstellar grain size distribution will be very different in the dense phases of the interstellar medium than in the diffuse ISM and studies of the effects of grains on the opacity, ionization state and chemical inventory of molecular clouds will have to take this into account.

To further assess the impact of grain coagulation we must compare the coagulation timescales with the lifetimes of molecular clouds. In a study of molecular clouds in the solar neighborhood Hartmann et al. (2001) hint the lifetime of molecular cloud is short, because of two key observations: (i) most cores do contain young stars, rather than being starless; and (ii) the age of the young stars that are still embedded in a cloud is $1-2$ Myr at most. From these two arguments it follows that the duration of the preceding starless phase is also $1-2$ Myr. Therefore, the grain population will not leave significant imprints on either (i) the large particles produced, or (ii) the removal of small particles, if core lifetimes are limited to the free fall time (Eq. (6.1)). This can be seen from Tables 6.5 and 6.6 where the growth in terms of the mass-weighted size ($\langle a \rangle_m$, Table 6.5) and the reduction of the geometrical surface (κ, Table 6.6) is given at the free-fall time of the simulation (col. 6). From Table 6.5 it is seen that the sizes of the largest particles all stay below 1 μm, except for the models that started off at monomer sizes of $a_0 = 1$ μm. Similarly, Table 6.6 shows that the opacities from the $t_{\rm ff}$ entry (col. 6) are similar to those of the 10^4 yr column.

This information is also displayed in Fg. 6.15. In Fg. 6.15a the decrease of the opacity with respect to the initial opacity is, κ/κ_0, is plotted against time, normalized by the initial coagulation timescale, for all $a_0 = 10^{-5}$ cm ice-coated silicate models. The similarity of the curves for the first $\sim$10 $t_{\rm coll,0}$ is in good agreement with the simple analytic model presented in § 6.5.1. In the models where small particles are replenished by fragmentation, κ first obtains a minimum and later levels-off at $\kappa/\kappa_0 \sim 0.05$. In Fg. 6.15b the coagulation timescale is plotted as function of gas

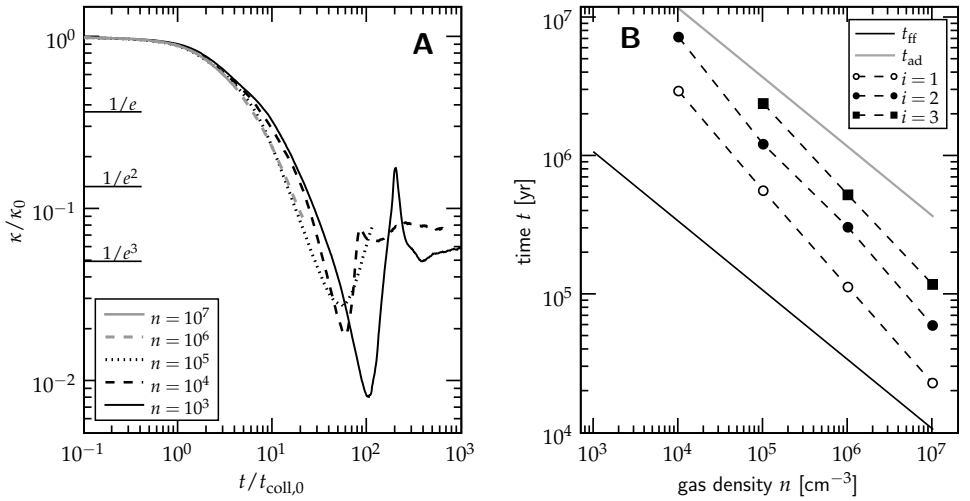

Fig. 6.15: Coagulation timescales of the $a_0 = 0.1$ μm ice-coated silicates models at five different gas densities. (*a, curves*) The opacity κ normalized to its initial value *vs.* time in units of the initial collision time $t_{\rm coll,0}$. The decrease in opacity occurs on timescales of $\sim$10 $t_{\rm coll,0}$. In the simulations that last long enough, however, κ starts to increase again, reflecting the re-emergence of small grains due to fragmentation. (*b, dashed curves*) Coagulation timescales in units of years as function of density. The timescales correspond to the point where the geometrical opacity, κ, has been reduced by a factor of $\exp[i]$ with $i = 1$ (open circles), $i = 2$ (*filled circles*) and $i = 3$ (*squares*), respectively. The free-fall timescale (Eq. (6.1)) and ambipolar diffusion timescale (Eq. (6.4)) are plotted for comparison by *solid lines*. If no symbol is plotted, the corresponding $i^{\rm th}$ e-folding reduction timescale has not been reached.

density (dashed lines), where the solid black line shows the free-fall time (Eq. (6.1)). Open circles denote the time required to reduce the opacity by a factor e; filled circles by a factor $e^2 \sim 7$, and black cubes refer to a third e-fold reduction ($\sim$20). At $n = 10^3$ cm^{-3} the opacity is not reduced by even a single e-folding factor within 10^7 yr, and no symbols are shown at this density. At the free-fall timescale, no significant reduction occurs and the dust coagulation will not affect the chemistry in the dense core.

However, there is still lively debate whether the fast SF picture — or, rather, a fast timescale for molecular clouds — is generally attainable, as cores may have additional support mechanisms. If clouds are magnetically supported, the fast collapse phase is retarded by ambipolar diffusion. Then, star formation takes place on a much longer timescale, perhaps 10^7 yr (see Eq. (6.4)), much longer than the free-fall timescale. Thus, if ions couple to the magnetic field and retard the collapse, growth can be significant. Table 6.5 shows grains are then able to reached chondrule size proportions, $\sim$100 μm, in the densest models. Also, the observational appearance of such a core will change significantly, as is clear from Fg. 6.15. If clouds exist on AD-timescales, Table 6.6 and Fg. 6.15 suggest the UV-opacity, which is directly proportional to κ, will be reduced by a factor of $\sim$10. In this case, studies that relate the

A_V extinction measurements to column densities through the standard dust-to-gas ratio possibly underestimate the amount of gas that is actually present.

6.8 Conclusions and outlook

We have studied the collisional aggregation of dust in the environments of the molecular cloud (cores). In this study we have particularly focused on the collision model and the analysis of the collisional growth stages. Much effort was invested to apply the outcomes of the detailed numerical experiments to a collisional evolution model. We have treated a general approach, and outcomes of future experiments — either numerical or laboratory — can be easily included. One important feature of the collision model is its scaling to the relevant masses and critical energies, which allows the coagulation model to proceed to much larger sizes than covered by the original collision experiment. Our method is therefore also applicable to the dust coagulation and fragmentation stages in protoplanetary disks.

In this study we discussed the observational implications of our model in a very coarse way, by considering the total amount of geometrical surface, captured in the κ parameter. We find that its behavior can be largely expressed as function of the initial collision timescale, $t_{\rm coll,0}$. It would be worthwhile to further investigate the extinction properties of the cloud as function of wavelength, and to quantify the importance of porous grains in it. Recently, Min et al. (2008) have presented a method to calculate the optical properties of porous aggregates, in which the filling factor is a key ingredient. In a follow-up study we will use this method in order to *e.g.*, study the consequences of this study to the 10 μm silicate absorption feature.

We list below the key results that can be concluded from this study:

1. Coagulation can be roughly divided into two phases: a growth stage, where the $N^2 f(N)$ mass spectrum peaks at a well-defined size, and a fragmentation stage, where the $N^2 f(N)$ mass spectrum is relatively flat due to the replenishment of small particles by fragmentation. Fragmentation is primarily caused by erosive collisions.
2. A large porosity speeds up the coagulation of aggregates in the early phases. This effect is self-enhancing, because very porous particles couple very well to the gas, preventing energetic collisions capable of compaction. Grazing collisions are largely responsible for obtaining fluffy aggregates.
3. Silicates dust grains (without ice-coating) are always in the fragmentation regime. This is caused by their relatively low breaking energy.
4. The enhanced sticking capabilities of ices are conducive for growth. Likewise, a smaller grain size (or a distribution of grain sizes where small grains dominate the surface contacts) also enhance the growth phase.
5. If cloud lifetimes are restricted to free-fall times, little coagulation can be expected. However, if additional support mechanism are present and freeze-out of ice has commenced, dust aggregates of $\sim$100 μm are produced, also significantly changing the UV-opacity of the cloud.

SMALL FRAGMENT MASS FRACTION

ε	$\phi^{\rm ini}$			
	0.121938	0.155263	0.189273	0.250536
0.000572118	0.00000	0.00000	0.00000	0.00000
0.0205945	0.00000	0.002500	0.00000	0.00000
0.0572069	0.000833	0.00000	0.00000	0.00000
0.128715	0.092500	0.030417	0.008750	0.0029167
0.228827	0.388750	0.094167	0.030417	0.01500
0.915310	0.957500	0.603333	0.243750	0.115833
3.66124	1.00000	1.00000	1.00000	0.727083
8.23779	1.00000	1.00000	1.00000	1.00000
14.6450	1.00000	1.00000	1.00000	1.00000

Table 6.7: Fraction of mass in the power-law component $f_{\rm pwl}$ at $b = 0$ in the global recipe.

6.A The collision recipe format

Our collision recipe is provided as a set of 72 tables. They describe six output quantities (see Table 6.3) for six impact parameters b and for both the local and the global recipes. Since listing all these tables here is impractical, we will provide them in the digital form as *online material* once this chapter is submitted to the journal. In this appendix we present two examples to illustrate the format.

Each table lists one quantity as function of the dimensionless energy parameter ε and the initial filling factor of aggregates ϕ. The only exception concerns the fraction of missed collisions, $f_{\rm miss}$. This quantity provides a correction to the collision cross-section of particles, in our case calculated from the outer radius of an aggregate $a_{\rm out}$ (*cf.* § 6.4.1). The filling factor ϕ is not an appropriate quantity to use here, because it is ambiguous where it concerns the structure of particles. For example, low ϕ could mean either a very fractal structure (and correspondingly high number of missing collisions) or a porous but homogeneous structure (and low number of missing collisions). Therefore, it is more appropriate to relate the probability of a collision miss directly to the radii with which the particle is characterized. Thus, $f_{\rm miss}$ is provided as a function of the ratio of the outer radius over the projected surface equivalent radius, $a_{\rm out}/a$.

Each table is preceded by a header that specifies: the corresponding recipe (keyword: `GLOBAL` or `LOCAL`), the corresponding impact parameter b, and the quantity listed in the table (keywords are: `fmiss`, `Nf`, `Sf`, `fpwl`, `q`, `Csig`). In the case of Table 6.7 the header is

```
# GLOBAL, b=0.0, Q=fpwl
```

Therefore, Table 6.7 presents the fraction of mass in the power-law component, $f_{\rm pwl}$, for the global recipe and for head-on collision.

In each table the first column and the first row specify the normalized energy parameter ε and the initial filling factor $\phi^{\rm ini}$ (or the ratio of the outer over the geometrical radii $a_{\rm out}/a$ in the case of $f_{\rm miss}$), respectively. In this case ε is scaled by the total number of monomers (the global recipe scaling) and by the breaking energy

NORMALIZATION FACTORS

quantity	Local	Global
$f_{\rm miss}$	$N_\mu\, E_{\rm br}$	$N_{\rm tot}\, E_{\rm br}$
$N_{\rm f}$		
$S_{\rm f}$		
$f_{\rm pwl}$	⋮	⋮
q		
C_ϕ	$N_{\rm tot}\, E_{\rm roll}$	$N_{\rm tot}\, E_{\rm roll}$

Table 6.8: Normalization factor of the dimensionless energy parameter ε for all output quantities in both local and global recipes.

$E_{\rm br}$ (erosion/fragmentation scaling). The normalizations for all quantities are listed in Table 6.8 to avoid any confusion with other tables. The intersection of a row corresponding to ε with a column corresponding to ϕ provides the output quantity for this set of parameters $(\varepsilon_i, \phi_i, b)$.

Table 6.9 is the second example. It is taken from the local recipe and it presents the $f_{\rm pwl}$ quantity for the head-on collision. The dimensionless energy parameter ε has fewer entries in the local recipe than in the global recipe. It is also normalized to different quantities. In Table 6.9 the energy is scaled by reduced number of monomers N_μ (local recipe scaling) and by the breaking energy $E_{\rm br}$ (erosion scaling) as indicated in Table 6.8. The header in this case is

```
# LOCAL, b=0.0, Q=fpwl
```

Note that in the local recipe the filling factors are lower. In this case larger aggregates are used to model collisions of large mass ratio. The fractal structure of these aggregates result in lower filing factor. Also, the size of these aggregates causes strong variation of the filling factor. Small difference in arrangement of monomers may change the filling factor by several percent when a few more monomers are exposed.

ERODED MASS FROM THE POWER-LAW COMPONENT

ε	$\phi^{\rm ini}$			
	0.0700907	0.0904748	0.126801	0.160992
0.228847	0.00000	0.00000	0.00000	0.00000
0.915388	1.00100	0.333667	0.00000	0.00000
3.66124	4.00400	46.5465	6.33967	0.667333
14.6450	7.00700	67.0670	35.2018	9.00900
32.9511	7.50750	148.315	58.2248	16.0160
58.5798	9.50950	129.129	62.3957	30.0300

Table 6.9: Normalized mass in the power-law component $f_{\rm pwl}$ at $b = 0$ in the local recipe.

7

Conclusions and outlook

The goal of this thesis has been to obtain a better understanding on the way dust coagulates during the first stages of planet formation. This requires to calculate the collisional evolution of the dust as a function of time. It is therefore natural to focus on the dust component, and treat the influence of the gas, *i.e.,* the gas-dust coupling, using analytical expressions. In this thesis the development of a detailed collision model is emphasized in particular, in which the collisional outcome depends on the properties of the colliding dust particles. The Monte Carlo method was instrumental in achieving this goal.

Because this thesis touches many diverse topics, I briefly emphasize a few of them individually and identify prospects for further work.

7.1 The Monte Carlo model

In chapter 2 we have introduced the Monte Carlo method and applied it to the upper layers of the protoplanetary disk. This approach was also used in chapter 4 for the evolution of chondrules in a dusty environment and in chapter 6 for the collisional evolution of dust in molecular clouds.

In all these cases the MC method merely reflects the particle-oriented approach, in which the state of the particle is characterized by a few parameters, *e.g.,* the porosity and mass in chapter 2 and chapter 6, and the mass fractions of the chondrule, compact dust, and porous dust components in chapter 4. This approach is therefore a middle course between the formalism followed by Kempf et al. (1999), where the position of each grain *within* an aggregate is stored, and the usual binning-methods. It is this compromise that makes our method so easily applicable, and allows us to connect to the finding of numerical or laboratory collision experiments; that is, the

output of these experiments can be converted to (a change in) particle properties as was seen, *e.g.*, in chapter 6.

The bottleneck of MC-methods are the $\sim N^2$ collision rates that must be continuously tracked during the evolution of the system. The consequence is that traditional MC-methods have difficulty to model broad distributions, where many simulation particles are required to follow both the low-mass particles (often dominating the numbers) and the large-mass particles (dominating the mass). Indeed, in chapters 2 and 3 the size distribution remained relatively narrow. However, fragmentation of dust will change this picture: a large dynamic range is then required. Therefore, in chapter 5 we have introduced a new method for MC-coagulation, the *grouping* method. In the grouping method, the numerous similar particles are considered collectively, like in the binning method. The key difference is that in MC the particles retain their individual behavior.

The grouping method described in chapter 5 is applicable to systems that experience runaway growth. An obvious application to extend this work is to apply the method to the planetesimal accretion stage of planet formation. Because of their gravitational focusing, planetesimals (km-size bodies and larger) have a collisional cross-section that scales with the $4/3$ power of mass. Thus, this phase is characterized by runaway growth, which cannot be modeled accurately by the usual binning approach (Wetherill 1990). Modeling this phase by a MC-method with its advantages in terms of the additional structural parameters may shed a new light on this key accumulation phase.

Perhaps the main drawback the MC-approach currently has, is that it is strictly 0-dimensional. The requirement, therefore, is that particles are distributed evenly throughout the volume, *i.e.*, there cannot be differentiation in position. For example, in chapter 4 we checked *a posteriori* whether the local assumption remained justified. However, there is no fundamental reason against including spatial information to the MC-particles — as long as their rate of interaction can be expressed in terms of probabilities. Another, more straightforward, approach is to 'cut' the system in several zones and calculate the collisional evolution separately in each of them. These are interesting avenues for further study.

7.2 The internal structure of particles

In this thesis MC-models are used as a tool to follow the internal structure of the particles. The most important structural parameter is probably the parameter that determines the porosity of particles, referred to as *enlargement* parameter in chapter 2 and *geometrical filling factor* in chapter 6. Thus, using this structural parameter the surface area-to-mass ratio is no longer confined to the $-1/3$ exponent as in the case of compact particles, which results in a very different velocity structure.

However, the most important property of the internal structure is that it affects the outcome of collisions. In this thesis we have related all collisional outcomes — sticking, bouncing, or fragmentation — to the internal structure of particles. Collisions are the key physical process that drive growth, and an understanding of planet formation is impossible without understanding individual collisions. Even in the

models in which the dust layer becomes gravitationally unstable at some point, it is still important to assess how collisions would affect the starting conditions (can particles grow to this size?) or the subsequent collapse phase. The theme of this work has been to connect the (microphysical) properties of dust particles to the outcome of collisions. In Chapters 2, 4, and 6 we have included results of numerical and laboratory findings. To connect the output of these experiments to the collisional evolution of physical systems will undoubtedly be the topic of many further studies.

7.3 Turbulence

Turbulence is arguably the most important mechanism to drive relative velocities between particles. Although the high gas densities in protoplanetary disk ensure a strong coupling ('strong' in astrophysical standards), which somewhat suppresses these velocities (and makes Brownian motion important for very small particles), as growth continues turbulence takes over. Furthermore, it mixes particles efficiently, both in the vertical as well as in the radial direction.

In chapter 3 relative velocities between particles in a turbulent velocity field were derived. It is a result that follows a long history. The framework of this approach—*i.e.,* the division of turbulent eddies into distinct classes—was already introduced by Völk et al. (1980), and improved by subsequent works (*e.g.,* Markiewicz et al. 1991; Cuzzi & Hogan 2003). By extending some of the simplifying assumptions in Cuzzi & Hogan (2003) the results of the Völk et al. (1980) study could now be put in closed form, at the level of $\sim$10% in accuracy.

In future research this work may be expanded to treat an even more general approach, *e.g.,* by changing the spectrum of the turbulence other than Kolmogorov. Moreover, it is worthwhile to compare directly the results of this analytic work with hydrodynamical simulations of, *e.g.,* Carballido et al. (2008), who find a good correspondence. On the other hand, Johansen et al. (2007) find that velocities between particles at close distance are suppressed compared to the analytical expressions. Identifying the sources of this discrepancy and understanding the particle-gas interactions is important, in particular for models in which the dust component becomes gravitationally unstable.

7.4 The meter size barrier

Even were turbulence is unimportant, high particle velocities would still be present because of the intrinsically distinct nature of gas and dust (*e.g.,* Weidenschilling 1977a). This meter-size barrier — or, rather, the $\mathrm{St} = 1$ barrier — is characterized by high, ~ 10 m s^{-1}, relative velocities between dust particles. These relative velocities seem to be too high for particles to avoid fragmentation, and many works have subsequently focused on circumventing this barrier, either by producing local pressure gradients in the gas disk (Kretke & Lin 2007; Brauer et al. 2008b) or by studying the amount of particle concentration before they reach the $\mathrm{St} = 1$ regime (Cuzzi et al. 2008). However, this thesis may offer some clues to 'revive' the idea to cross the $\mathrm{St} = 1$ barrier by incremental growth. First, the impact of high velocities could

be remedied by mechanisms that dissipate the collision energy, *e.g.*, the particle's porosity. Second, if particles are fluffy, a sudden compaction (and corresponding increase in Stokes number) could help to cross this barrier. In chapter 4 some models came close to cross the $\mathrm{St} = 1$ barrier, although the chondrule component did not contribute to the sticking capability and we did not include the collective effects that could have somewhat reduced particle velocities.

This idea is not new, of course. Cuzzi et al. (1993) have shown that if growth in the midplane regions is rapid, radial drift is not important. In the models of Weidenschilling (1997) growth also proceeded past the *m*-size barrier, despite the erosive processes that were included. However, Brauer et al. (2008a) using a "hard" fragmentation threshold of 10 m s^{-1} did not observe growth past $\mathrm{St} = 1$. On the other hand, taking account of the internal structure, an array of new possibilities in terms of the collisional outcome becomes available (and the outcome is much harder to predict *a priori*). Therefore, it would be worthwhile to *simultaneously* model the internal structure, the location in the disk, and the growth of the particles and assess whether energy dissipation process can help to overcome the *m*-size barrier.

References

Aikawa, Y., Wakelam, V., Garrod, R. T., & Herbst, E. 2008, The Astrophysical Journal, 674, 984

Akyilmaz, M., Flower, D. R., Hily-Blant, P., Pineau Des Forêts, G., & Walmsley, C. M. 2007, Astronomy and Astrophysics, 462, 221

Alexander, R. D., Clarke, C. J., & Pringle, J. E. 2006, Monthly notices of the Royal Astronomical Society, 369, 229

Alibert, Y., Mordasini, C., Benz, W., & Winisdoerffer, C. 2005, Astronomy and Astrophysics, 434, 343

Alves, J., Lombardi, M., & Lada, C. J. 2007, Astronomy and Astrophysics, 462, L17

Ashworth, J. R. 1977, Earth and Planetary Science Letters, 35, 25

Balbus, S. A. & Hawley, J. F. 1991, The Astrophysical Journal, 376, 214

Beckwith, S. V. W., Henning, T., & Nakagawa, Y. 2000, Protostars and Planets IV, 533

Beckwith, S. V. W. & Sargent, A. I. 1991, The Astrophysical Journal, 381, 250

Benz, W. 2000, Space Science Reviews, 92, 279

Bergin, E. A. & Langer, W. D. 1997, The Astrophysical Journal, 486, 316

Bergin, E. A., Langer, W. D., & Goldsmith, P. F. 1995, The Astrophysical Journal, 441, 222

Bergin, E. A. & Tafalla, M. 2007, Annual Rev. Astron. and Astroph, 45, 339

Binney, J. & Tremaine, S. 1987, Galactic dynamics (Princeton, NJ, Princeton University Press, 1987, 747 p.)

Blum, J. 2000, Space Science Reviews, 92, 265

Blum, J. 2004, in ASP Conf. Ser. 309: Astrophysics of Dust, ed. A. N. Witt, G. C. Clayton, & B. T. Draine, 369

Blum, J. 2006, Advances in Physics, 55, 881

Blum, J. & Münch, M. 1993, Icarus, 106, 151

Blum, J. & Schräpler, R. 2004, Physical Review Letters, 93, 115503

Blum, J., Schräpler, R., Davidsson, B. J. R., & Trigo-Rodríguez, J. M. 2006, The Astrophysical Journal, 652, 1768

Blum, J. & Wurm, G. 2000, Icarus, 143, 138

Blum, J. & Wurm, G. 2008, Annual Rev. Astron. and Astroph, 46, in press.

Blum, J., Wurm, G., Poppe, T., Kempf, S., & Kozasa, T. 2002, Advances in Space Research, 29, 497

Blum, J. et al. 2000, Physical Review Letters, 85, 2426

Bockelée-Morvan, D., Gautier, D., Hersant, F., Huré, J.-M., & Robert, F. 2002, Astronomy and Astrophysics, 384, 1107

Bonabeau, E., Dagorn, L., & Freon, P. 1999, Proceedings of the National Academy of Science, 96, 4472

Bonnor, W. B. 1956, Monthly notices of the Royal Astronomical Society, 116, 351

Boogert, A. C. A., Pontoppidan, K. M., Lahuis, F., et al. 2004, The Astrophysical Journal Supplements, 154, 359

Boss, A. P. 2000, The Astrophysical Journal, 536, L101

Bouwman, J., de Koter, A., van den Ancker, M. E., & Waters, L. B. F. M. 2000, Astronomy and Astrophysics, 360, 213

Bouwman, J., Henning, T., Hillenbrand, L. A., et al. 2008, The Astrophysical Journal, in press, ArXiv e-prints 0802.3033
Brauer, F., Dullemond, C. P., & Henning, T. 2008a, Astronomy and Astrophysics, 480, 859
Brauer, F., Dullemond, C. P., Johansen, A., et al. 2007, Astronomy and Astrophysics, 469, 1169
Brauer, F., Henning, T., & Dullemond, C. P. 2008b, Astronomy and Astrophysics, 487, L1
Brearley, A. J. 1993, Geochimica et Cosmochimica Acta, 57, 1521
Brearley, A. J. 1996, in Cambridge: Cambridge Univ. Press, Vol. 35, Chondrules and the Protoplanetary Disk, ed. R. H. Hewins, R. H. Jones, & E. R. D. Scott, 137–151
Brearley, A. J. & Jones, R. H. 1998, in Reviews in Mineralogy, Vol. 36, Planetary Materials, ed. J. J. Papike (Washington: Mineral. Soc. America), chap. 3
Bridges, F. G., Supulver, K. D., Lin, D. N. C., Knight, R., & Zafra, M. 1996, Icarus, 123, 422
Bromley, B. C. & Kenyon, S. J. 2006, The Astronomical Journal, 131, 2737
Brownlee, D. et al. 2006, Science, 314, 1711
Brownlee, D. E. 1979, Meteoritics, 14, 358
Calvet, N., Muzerolle, J., Briceño, C., et al. 2004, The Astronomical Journal, 128, 1294
Camacho, J. 2001, Physical Review E, 63, 046112
Camacho, J. & Solé, R. V. 2001, Europhysics Letters, 55, 774
Carballido, A., Stone, J. M., & Turner, N. J. 2008, Monthly notices of the Royal Astronomical Society, 386, 145
Carpenter, J. M., Wolf, S., Schreyer, K., Launhardt, R., & Henning, T. 2005, The Astronomical Journal, 129, 1049
Chambers, J. E. 2001, Icarus, 152, 205
Charnley, S. B., Tielens, A. G. G. M., & Millar, T. J. 1992, The Astrophysical Journal, 399, L71
Chiang, E. I. 2004, in Astronomical Society of the Pacific Conference Series, Vol. 309, Astrophysics of Dust, ed. A. N. Witt, G. C. Clayton, & B. T. Draine, 213
Chiang, E. I. & Goldreich, P. 1997, The Astrophysical Journal, 490, 368
Chokshi, A., Tielens, A. G. G. M., & Hollenbach, D. 1993, The Astrophysical Journal, 407, 806
Ciesla, F. J. 2006, Meteoritics and Planetary Science, 41, 1347
Ciesla, F. J. 2007, The Astrophysical Journal, 654, L159
Ciesla, F. J. & Cuzzi, J. N. 2007, in Lunar and Planetary Institute Conference Abstracts, Vol. 38, Lunar and Planetary Institute Conference Abstracts, 1386
Ciolek, G. E. & Mouschovias, T. C. 1994, The Astrophysical Journal, 425, 142
Cuzzi, J. N. 2004, Icarus, 168, 484
Cuzzi, J. N. & Alexander, C. M. O. 2006, Nature, 441, 483
Cuzzi, J. N., Ciesla, F. J., Petaev, M. I., et al. 2005, in ASP Conf. Ser. 341: Chondrites and the Protoplanetary Disk, ed. A. N. Krot, E. R. D. Scott, & B. Reipurth, 732
Cuzzi, J. N., Dobrovolskis, A. R., & Champney, J. M. 1993, Icarus, 106, 102
Cuzzi, J. N. & Hogan, R. C. 2003, Icarus, 164, 127
Cuzzi, J. N., Hogan, R. C., Paque, J. M., & Dobrovolskis, A. R. 2001, The Astrophysical Journal, 546, 496
Cuzzi, J. N., Hogan, R. C., & Shariff, K. 2007, in Lunar and Planetary Institute Conference Abstracts, Vol. 38, Lunar and Planetary Institute Conference Abstracts, 1439
Cuzzi, J. N., Hogan, R. C., & Shariff, K. 2008, The Astrophysical Journal, in press, ArXiv e-prints 0804.3526
Cuzzi, J. N. & Weidenschilling, S. J. 2006, Particle-Gas Dynamics and Primary Accretion (Meteorites and the Early Solar System II), 353–381
D'Alessio, P., Canto, J., Calvet, N., & Lizano, S. 1998, The Astrophysical Journal, 500, 411
Derjaguin, B. V., Muller, V. M., & Toporov, Y. P. 1975, Journal of Colloid and Interface Science, 53, 314
Desch, S. J. 2007, The Astrophysical Journal, 671, 878
Desch, S. J. & Connolly, Jr., H. C. 2002, Meteoritics and Planetary Science, 37, 183
Dobrovolskis, A. R., Dacles-Mariani, J. S., & Cuzzi, J. N. 1999, Journal of Geophysical Research, 104, 30805
Dominik, C., Blum, J., Cuzzi, J. N., & Wurm, G. 2007, Protostars and Planets V, 783
Dominik, C. & Nübold, H. 2002, Icarus, 157, 173
Dominik, C. & Tielens, A. G. G. M. 1995, Philosophical Magazine A, 72, 783
Dominik, C. & Tielens, A. G. G. M. 1996, Philosophical Magazine A, 73, 1279
Dominik, C. & Tielens, A. G. G. M. 1997, The Astrophysical Journal, 480, 647
Draine, B. T. 1985, in Protostars and Planets II, ed. D. C. Black & M. S. Matthews, 621–640
Dubrulle, B., Morfill, G., & Sterzik, M. 1995, Icarus, 114, 237
Dubrulle, B. & Valdettaro, L. 1992, Astronomy and Astrophysics, 263, 387

Duchêne, G. 2008, New Astronomy Review, 52, 117
Dullemond, C. P. & Dominik, C. 2005, The Astrophysical Journal, 434, 971
Durisen, R. H., Boss, A. P., Mayer, L., et al. 2007, in Protostars and Planets V, ed. B. Reipurth, D. Jewitt, & K. Keil, 607–622
Ebert, R. 1955, Zeitschrift für Astrophysik, 37, 217
Einstein, A. 1905, Annalen der Physik, 322, 549
Eisenhour, D. D. 1996, Meteoritics and Planetary Science, 31, 243
Estrada, P. R. & Cuzzi, J. N. 2008, The Astrophysical Journal, 682, 515
Filippov, A., Zurita, M., & Rosner, D. 2000, Journal of Colloid and Interface Science, 229, 261
Fleming, T. & Stone, J. M. 2003, The Astrophysical Journal, 585, 908
Flower, D. R., Pineau Des Forêts, G., & Walmsley, C. M. 2006, Astronomy and Astrophysics, 456, 215
Freitag, M., Rasio, F. A., & Baumgardt, H. 2006, Monthly notices of the Royal Astronomical Society, 368, 121
Gail, H.-P. 2004, Astronomy and Astrophysics, 413, 571
Gammie, C. F. 1996, The Astrophysical Journal, 457, 355
Gammie, C. F. & Johnson, B. M. 2005, in Astronomical Society of the Pacific Conference Series, Vol. 341, Chondrites and the Protoplanetary Disk, ed. A. N. Krot, E. R. D. Scott, & B. Reipurth, 145
Gibb, E. L., Whittet, D. C. B., Boogert, A. C. A., & Tielens, A. G. G. M. 2004, The Astrophysical Journal Supplements, 151, 35
Gillespie, D. T. 1975, Journal of Atmospheric Sciences, 32, 1977
Glaschke, P. 2006, PhD thesis, PhD Thesis, Combined Faculties for the Natural Sciences and for Mathematics of the University of Heidelberg, Germany. XIV+134 pp. (2006)
Goldreich, P., Lithwick, Y., & Sari, R. 2004a, The Astrophysical Journal, 614, 497
Goldreich, P., Lithwick, Y., & Sari, R. 2004b, Annual Rev. Astron. and Astroph, 42, 549
Goldreich, P. & Ward, W. R. 1973, The Astrophysical Journal, 183, 1051
Greenberg, R., Hartmann, W. K., Chapman, C. R., & Wacker, J. F. 1978, Icarus, 35, 1
Hartmann, L. 2005, in Astronomical Society of the Pacific Conference Series, Vol. 341, Chondrites and the Protoplanetary Disk, ed. A. N. Krot, E. R. D. Scott, & B. Reipurth, 1003
Hartmann, L., Ballesteros-Paredes, J., & Bergin, E. A. 2001, The Astrophysical Journal, 562, 852
Hasegawa, T. I., Herbst, E., & Leung, C. M. 1992, The Astrophysical Journal Supplements, 82, 167
Hatzes, A. P., Bridges, F., Lin, D. N. C., & Sachtjen, S. 1991, Icarus, 89, 113
Hawley, J. F. & Balbus, S. A. 1991, The Astrophysical Journal, 376, 223
Hayakawa, H. 1987, Journal of Physics A Mathematical General, 20, L801
Hayashi, C. 1981, Progress of Theoretical Physics Supplement, 70, 35
Heim, L.-O., Blum, J., Preuss, M., & Butt, H.-J. 1999, Physical Review Letters, 83, 3328
Hillenbrand, L. A. 2005, ArXiv Astrophysics e-prints astro-ph/0511083
Hollenbach, D. J., Yorke, H. W., & Johnstone, D. 2000, Protostars and Planets IV, 401
Hood, L. L., Ciesla, F. J., & Weidenschilling, S. J. 2005, in Astronomical Society of the Pacific Conference Series, Vol. 341, Chondrites and the Protoplanetary Disk, ed. A. N. Krot, E. R. D. Scott, & B. Reipurth, 873
Housen, K. R. & Holsapple, K. A. 1990, Icarus, 84, 226
Hua, X., Wang, J., & Buseck, P. R. 2002, Meteoritics and Planetary Science, 37, 229
Hubbard, A. & Blackman, E. G. 2006, New Astronomy, 12, 246
Hubickyj, O., Bodenheimer, P., & Lissauer, J. J. 2005, Icarus, 179, 415
Hueso, R. & Guillot, T. 2005, Astronomy and Astrophysics, 442, 703
Huss, G. R., Alexander, C. M. O., Palme, H., Bland, P. A., & Wasson, J. T. 2005, in Astronomical Society of the Pacific Conference Series, Vol. 341, Chondrites and the Protoplanetary Disk, ed. A. N. Krot, E. R. D. Scott, & B. Reipurth, 701
Huss, G. R., Keil, K., & Taylor, G. J. 1981, Geochimica et Cosmochimica Acta, 45, 33
Inaba, S., Tanaka, H., Nakazawa, K., Wetherill, G. W., & Kokubo, E. 2001, Icarus, 149, 235
Inaba, S., Tanaka, H., Ohtsuki, K., & Nakazawa, K. 1999, Earth, Planets, and Space, 51, 205
Jeon, I. 1998, Communications in Mathematical Physics, 194, 541
Johansen, A., Oishi, J. S., Low, M.-M. M., et al. 2007, Nature, 448, 1022
Johnson, K. L. 1987, Contact Mechanics (Contact Mechanics, by K. L. Johnson, pp. 464. ISBN 0521347963. Cambridge, UK: Cambridge University Press, August 1987.)
Johnson, K. L., Kendall, K., & Roberts, A. D. 1971, Proceeding of the Royal Society A, 324, 301
Johnstone, D. & Bally, J. 2006, The Astrophysical Journal, 653, 383

Jones, A. P., Tielens, A. G. G. M., & Hollenbach, D. J. 1996, The Astrophysical Journal, 469, 740
Jones, R. H., Grossman, J. N., & Rubin, A. E. 2005, in Astronomical Society of the Pacific Conference Series, Vol. 341, Chondrites and the Protoplanetary Disk, ed. A. N. Krot, E. R. D. Scott, & B. Reipurth, 251
Jones, R. H., Lee, T., Connolly, Jr., H. C., Love, S. G., & Shang, H. 2000, Protostars and Planets IV, 927
Jorgensen, J., Johnstone, D., Kirk, H., et al. 2008, The Astrophysical Journal, in press, ArXiv e-prints 0805.0599
Joshi, K. J., Rasio, F. A., & Portegies Zwart, S. 2000, The Astrophysical Journal, 540, 969
Jura, M. 1980, The Astrophysical Journal, 235, 63
Juric, M. & Tremaine, S. 2007, ArXiv Astrophysics e-prints astro-ph/0703160
Kahn, F. D. 1974, Astronomy and Astrophysics, 37, 149
Kawamura, A., Onishi, T., Yonekura, Y., et al. 1998, The Astrophysical Journal Supplements, 117, 387
Kempf, S., Pfalzner, S., & Henning, T. K. 1999, Icarus, 141, 388
Kessler-Silacci, J., Augereau, J.-C., Dullemond, C. P., et al. 2006, The Astrophysical Journal, 639, 275
Kita, N. T., Huss, G. R., Tachibana, S., et al. 2005, in Astronomical Society of the Pacific Conference Series, Vol. 341, Chondrites and the Protoplanetary Disk, ed. A. N. Krot, E. R. D. Scott, & B. Reipurth, 558
Kleine, T., Halliday, A. N., Palme, H., Mezger, K., & Markowski, A. 2006, in Lunar and Planetary Institute Conference Abstracts, Vol. 37, 37th Annual Lunar and Planetary Science Conference, ed. S. Mackwell & E. Stansbery, 1884
Klessen, R. S., Ballesteros-Paredes, J., Vázquez-Semadeni, E., & Durán-Rojas, C. 2005, The Astrophysical Journal, 620, 786
Klett, J. D. 1975, Journal of Atmospheric Sciences, 32, 380
Kokubo, E. & Ida, S. 1996, Icarus, 123, 180
Kokubo, E. & Ida, S. 1998, Icarus, 131, 171
Kokubo, E. & Ida, S. 2000, Icarus, 143, 15
Kokubo, E. & Ida, S. 2002, The Astrophysical Journal, 581, 666
Konopka, U., Mokler, F., Ivlev, A. V., et al. 2005, New Journal of Physics, 7, 227
Kostoglou, M. & Konstandopoulos, A. G. 2001, J. Aerosol Sci, 32, 1399
Kovetz, A. & Olund, B. 1969, Journal of Atmospheric Sciences, 26, 1060
Kozasa, T., Blum, J., & Mukai, T. 1992, Astronomy and Astrophysics, 263, 423
Krause, M. & Blum, J. 2004, Physical Review Letters, 93, 021103
Kress, M. E. & Tielens, A. G. G. M. 2001, Meteoritics and Planetary Science, 36, 75
Kretke, K. A. & Lin, D. N. C. 2007, The Astrophysical Journal, 664, L55
Langkowski, D., Teiser, J., & Blum, J. 2008, The Astrophysical Journal, 675, 764
Laurenzi, I. J., Bartels, J. D., & Diamond, S. L. 2002, Journal of Computational Physics, 177, 418
Laurenzi, I. J. & Diamond, S. L. 2003, Physical Review E, 67, 051103
Lauretta, D. S. & McSween, Jr., H. Y. 2006, Meteorites and the Early Solar System II (Meteorites and the Early Solar System II)
Lee, M. H. 2000, Icarus, 143, 74
Lee, M. H. 2001, Journal of Physics A Mathematical General, 34, 10219
Leyvraz, F. 2003, Physics Reports, 383, 95
Liffman, K. 1991, J. Comput. Phys., 100, 116
Lissauer, J. J. 1993, Annual Rev. Astron. and Astroph, 31, 129
Lissauer, J. J. & Stevenson, D. J. 2007, in Protostars and Planets V, ed. B. Reipurth, D. Jewitt, & K. Keil, 591–606
Lommen, D., Wright, C. M., Maddison, S. T., et al. 2007, Astronomy and Astrophysics, 462, 211
Mac Low, M.-M. & Klessen, R. S. 2004, Reviews of Modern Physics, 76, 125
Malyshkin, L. & Goodman, J. 2001, Icarus, 150, 314
Markiewicz, W. J., Mizuno, H., & Völk, H. J. 1991, Astronomy and Astrophysics, 242, 286
Marshall, J. & Cuzzi, J. 2001, in Lunar and Planetary Inst. Technical Report, Vol. 32, Lunar and Planetary Institute Conference Abstracts, 1262
Marshall, J. R., Sauke, T. B., & Cuzzi, J. N. 2005, Geoph. Res. Lett., 32, 11202
Martin, C. L., Bouvard, D., & Shima, S. 2003, J. Mech. Phys. Solids, 51, 667
Mathis, J. S., Rumpl, W., & Nordsieck, K. H. 1977, The Astrophysical Journal, 217, 425
Meakin, P. 1988, Ann. Rev. Phys. Chem., 39, 237
Meakin, P. & Donn, B. 1988, The Astrophysical Journal, 329, L39
Meeus, G., Sterzik, M., Bouwman, J., & Natta, A. 2003, Astronomy and Astrophysics, 409, L25
Metzler, K., Bischoff, A., & Stoeffler, D. 1992, Geochimica et Cosmochimica Acta, 56, 2873

Meyer, M. R., Backman, D. E., Weinberger, A. J., & Wyatt, M. C. 2007, in Protostars and Planets V, ed. B. Reipurth, D. Jewitt, & K. Keil, 573–588
Min, M., Hovenier, J. W., Waters, L. B. F. M., & de Koter, A. 2008, Astronomy and Astrophysics, in press, ArXiv e-prints 0806.4038
Mizuno, H., Markiewicz, W. J., & Voelk, H. J. 1988, Astronomy and Astrophysics, 195, 183
Morfill, G. E., Durisen, R. H., & Turner, G. W. 1998, Icarus, 134, 180
Mukhopadhyay, B. 2006, The Astrophysical Journal, 653, 503
Nagahara, H. 1984, Geochimica et Cosmochimica Acta, 48, 2581
Nakagawa, Y., Sekiya, M., & Hayashi, C. 1986, Icarus, 67, 375
Natta, A. & Testi, L. 2004, in Astronomical Society of the Pacific Conference Series, Vol. 323, Star Formation in the Interstellar Medium: In Honor of David Hollenbach, ed. D. Johnstone, F. C. Adams, D. N. C. Lin, D. A. Neufeeld, & E. C. Ostriker, 279
Natta, A., Testi, L., Calvet, N., et al. 2007, in Protostars and Planets V, ed. B. Reipurth, D. Jewitt, & K. Keil, 767–781
Nelson, V. E. & Rubin, A. E. 2002, Meteoritics and Planetary Science, 37, 1361
Nomura, H. & Nakagawa, Y. 2006, The Astrophysical Journal, 640, 1099
O'Donnell, J. E. & Mathis, J. S. 1997, The Astrophysical Journal, 479, 806
Ormel, C. W. & Cuzzi, J. N. 2007, Astronomy and Astrophysics, 466, 413
Ormel, C. W., Cuzzi, J. N., & Tielens, A. G. G. M. 2008, The Astrophysical Journal, 679, 1588
Ormel, C. W. & Spaans, M. 2008, The Astrophysical Journal, 684, 1291
Ormel, C. W., Spaans, M., & Tielens, A. G. G. M. 2007, Astronomy and Astrophysics, 461, 215
Ossenkopf, V. 1993, Astronomy and Astrophysics, 280, 617
Ossenkopf, V. & Henning, T. 1994, Astronomy and Astrophysics, 291, 943
Palla, F. & Stahler, S. W. 1999, The Astrophysical Journal, 525, 772
Paque, J. M. & Cuzzi, J. N. 1997, in Lunar and Planetary Institute Conference Abstracts, Vol. 28, Lunar and Planetary Institute Conference Abstracts, 1071
Paraskov, G. B., Wurm, G., & Krauss, O. 2007, Icarus, 191, 779
Pascucci, I., Gorti, U., Hollenbach, D., et al. 2006, The Astrophysical Journal, 651, 1177
Paszun, D. & Dominik, C. 2006, Icarus, 182, 274
Paszun, D. & Dominik, C. 2008a, in prep.
Paszun, D. & Dominik, C. 2008b, Astronomy and Astrophysics, 484, 859
Pollack, J. B., Hubickyj, O., Bodenheimer, P., et al. 1996, Icarus, 124, 62
Poppe, T., Blum, J., & Henning, T. 1999, Advances in Space Research, 23, 1197
Poppe, T., Blum, J., & Henning, T. 2000, The Astrophysical Journal, 533, 454
Portegies Zwart, S. F., Makino, J., McMillan, S. L. W., & Hut, P. 1999, Astronomy and Astrophysics, 348, 117
Portegies Zwart, S. F. & van den Heuvel, E. P. J. 2007, Nature, 450, 388
Pringle, J. E. 1981, Annual Rev. Astron. and Astroph, 19, 137
Przygodda, F., van Boekel, R., Àbrahàm, P., et al. 2003, Astronomy and Astrophysics, 412, L43
Rafikov, R. R. 2003, The Astronomical Journal, 126, 2529
Rice, W. K. M., Lodato, G., Pringle, J. E., Armitage, P. J., & Bonnell, I. A. 2006, Monthly notices of the Royal Astronomical Society, 372, L9
Ridgway, K. & Tarbuck, K. 1967, J. Br. Chem. Eng., 12, 384
Rubin, A. E. & Keil, K. 1984, Meteoritics, 19, 135
Russell, S. S., Hartmann, L., Cuzzi, J., et al. 2006, Timescales of the Solar Protoplanetary Disk (Meteorites and the Early Solar System II), 233–251
Safronov, V. S. 1969, Evolution of the protoplanetary cloud and the formation of the Earth and planets; NASA TTF-667
Sano, T., Miyama, S. M., Umebayashi, T., & Nakano, T. 2000, The Astrophysical Journal, 543, 486
Sano, T. & Stone, J. M. 2002, The Astrophysical Journal, 577, 534
Schräpler, R. & Henning, T. 2004, The Astrophysical Journal, 614, 960
Scott, E. R. D., Barber, D. J., Alexander, C. M., Hutchinson, R., & Peck, J. A. 1988, Primitive material surviving in chondrites—Matrix (Meteorites and the Early Solar System), 718–745
Scott, E. R. D. & Krot, A. N. 2005a, in Astronomical Society of the Pacific Conference Series, Vol. 341, Chondrites and the Protoplanetary Disk, ed. A. N. Krot, E. R. D. Scott, & B. Reipurth, 15
Scott, E. R. D. & Krot, A. N. 2005b, The Astrophysical Journal, 623, 571
Scott, E. R. D., Rubin, A. E., Taylor, G. J., & Keil, K. 1984, Geochimica et Cosmochimica Acta, 48, 1741

Sears, D. W. G., Benoit, P. H., & Jie, L. 1993, Meteoritics, 28, 669
Sekiya, M. 1998, Icarus, 133, 298
Shakura, N. I. & Sunyaev, R. A. 1973, Astronomy and Astrophysics, 24, 337
Shima, S.-i., Kusano, K., Kawano, A., Sugiyama, T., & Kawahara, S. 2007, ArXiv Physics e-prints
Shu, F., Najita, J., Ostriker, E., et al. 1994, The Astrophysical Journal, 429, 781
Shu, F. H. 1977, The Astrophysical Journal, 214, 488
Shu, F. H., Adams, F. C., & Lizano, S. 1987, Annual Rev. Astron. and Astroph, 25, 23
Silk, J. & Takahashi, T. 1979, The Astrophysical Journal, 229, 242
Sirono, S.-I. 2004, Icarus, 167, 431
Smith, M. & Matsoukas, T. 1998, Chem. Eng. Sci., 53, 1777
Smoluchowski, M. V. 1916, Zeitschrift für Physik, 17, 557
Spaute, D., Weidenschilling, S. J., Davis, D. R., & Marzari, F. 1991, Icarus, 92, 147
Spouge, J. L. 1985, Journal of Colloid and Interface Science, 107, 38
Stepnik, B., Abergel, A., Bernard, J.-P., et al. 2003, Astronomy and Astrophysics, 398, 551
Stone, J. M., Gammie, C. F., Balbus, S. A., & Hawley, J. F. 2000, Protostars and Planets IV, 589
Suttner, G. & Yorke, H. W. 2001, The Astrophysical Journal, 551, 461
Takeuchi, T. & Lin, D. N. C. 2002, The Astrophysical Journal, 581, 1344
Tanaka, H., Himeno, Y., & Ida, S. 2005, The Astrophysical Journal, 625, 414
Tanaka, H. & Nakazawa, K. 1994, Icarus, 107, 404
Tanaka, H., Takeuchi, T., & Ward, W. R. 2002, The Astrophysical Journal, 565, 1257
Tanwongwan, W., Manonukul, A., & Carmai, J. 2005, JSME Int J., Ser. A, 48, 376
Taylor, G. J., Scott, E. R. D., & Keil, K. 1983, in Chondrules and their Origins, ed. E. A. King, 262–278
Throop, H. B. & Bally, J. 2005, The Astrophysical Journal, 623, L149
Tielens, A. G. G. M. 2005, The Physics and Chemistry of the Interstellar Medium (The Physics and Chemistry of the Interstellar Medium, by A. G. G. M. Tielens, pp. . ISBN 0521826349. Cambridge, UK: Cambridge University Press, 2005.)
Tielens, A. G. G. M. & Hagen, W. 1982, Astronomy and Astrophysics, 114, 245
Trigo-Rodriguez, J. M., Rubin, A. E., & Wasson, J. T. 2006, Geochimica et Cosmochimica Acta, 70, 1271
Trubnnikov, B. A. 1971, Doklady Akad. Nauk USSR, 196, 1316
Tsiganis, K., Gomes, R., Morbidelli, A., & Levison, H. F. 2005, Nature, 435, 459
van Boekel, R., Min, M., Leinert, C., et al. 2004, Nat., 432, 479
van Boekel, R., Min, M., Waters, L. B. F. M., et al. 2005, Astronomy and Astrophysics, 437, 189
van Boekel, R., Waters, L. B. F. M., Dominik, C., et al. 2003, Astronomy and Astrophysics, 400, L21
Völk, H. J., Morfill, G. E., Roeser, S., & Jones, F. C. 1980, Astronomy and Astrophysics, 85, 316
Wada, K., Tanaka, H., Suyama, T., Kimura, H., & Yamamoto, T. 2007, The Astrophysical Journal, 661, 320
Wasson, J. T. & Trigo-Rodriguez, J. M. 2004, in Lunar and Planetary Institute Conference Abstracts, Vol. 35, Lunar and Planetary Institute Conference Abstracts, ed. S. Mackwell & E. Stansbery, 2140
Watson, A. M., Stapelfeldt, K. R., Wood, K., & Ménard, F. 2007, Protostars and Planets V, 523
Watson, P. K., Mizes, H., Casterlanos, A., & Pérez, A. T. 1997, in Powders & Grains 97, ed. R. Behringer & J. T. Jenkins (Balkema, Rotterdam, 1997), 109–112
Weidenschilling, S. J. 1977a, Monthly notices of the Royal Astronomical Society, 180, 57
Weidenschilling, S. J. 1977b, Astrophysics and Space Science, 51, 153
Weidenschilling, S. J. 1980, Icarus, 44, 172
Weidenschilling, S. J. 1984a, Icarus, 60, 553
Weidenschilling, S. J. 1984b, in Lunar and Planetary Institute Conference Abstracts, 900–901
Weidenschilling, S. J. 1988, Formation processes and time scales for meteorite parent bodies (Meteorites and the Early Solar System), 348–371
Weidenschilling, S. J. 1997, Icarus, 127, 290
Weidenschilling, S. J. 2000, Space Science Reviews, 92, 295
Weidenschilling, S. J. 2004, Comets II, 97
Weidenschilling, S. J. 2006, Icarus, 181, 572
Weidenschilling, S. J. & Cuzzi, J. N. 1993, in Protostars and Planets III, ed. E. H. Levy & J. I. Lunine, 1031–1060
Weidenschilling, S. J. & Ruzmaikina, T. V. 1994, The Astrophysical Journal, 430, 713
Weisberg, M. K., McCoy, T. J., & Krot, A. N. 2006, Systematics and Evaluation of Meteorite Classification (Meteorites and the Early Solar System II), 19–52
Wetherill, G. W. 1990, Icarus, 88, 336

Whipple, F. L. 1972, in From Plasma to Planet, ed. A. Elvius, 211
White, W. H. 1982, Journal of Colloid and Interface Science, 87, 204
Wise, J. H. & Abel, T. 2007, The Astrophysical Journal, 665, 899
Wolfire, M. G. & Cassinelli, J. P. 1987, The Astrophysical Journal, 319, 850
Wood, J. A. 2005, in ASP Conf. Ser. 341: Chondrites and the Protoplanetary Disk, ed. A. N. Krot, E. R. D. Scott, & B. Reipurth, 953
Wurm, G., Paraskov, G., & Krauss, O. 2005, Icarus, 178, 253
Youdin, A. N. 2005, ArXiv Astrophysics e-prints astro-ph/0508659
Youdin, A. N. & Chiang, E. I. 2004, The Astrophysical Journal, 601, 1109
Youdin, A. N. & Goodman, J. 2005, The Astrophysical Journal, 620, 459
Youdin, A. N. & Lithwick, Y. 2007, Icarus, 192, 588
Youdin, A. N. & Shu, F. H. 2002, The Astrophysical Journal, 580, 494
Zega, T. J. & Buseck, P. R. 2003, Geochimica et Cosmochimica Acta, 67, 1711
Zolensky, M., Barrett, R., & Browning, L. 1993, Geochimica et Cosmochimica Acta, 57, 3123
Zolensky, M. E. et al. 2006, Science, 314, 1735
Zsom, A. & Dullemond, C. P. 2008, Astronomy and Astrophysics, in press, ArXiv e-prints 0807.5052

Glossary

Term	Description
AD	Ambipolar diffusion
AU	Astronomical Unit. The distance from the Earth to the Sun, 1.5×10^8 km.
Accretion (I)	The conversion of primordial material, *i.e.,* interstellar dust, to macroscopic objects: pebbles, rocks, planetesimals, and eventually planets.
Accretion (II)	The gravitational attraction of matter (mostly gas) onto a central, *e.g.,* stellar, object. A consequence of processes through which angular momentum is lost.
CAI	Ca-Al-rich inclusion. A relatively large particle ($\sim$mm-cm) found in chondrites that is enriched in the refractory elements of Ca and Al.
CCA	Cluster-cluster aggregation
Chondrite	An old meteorite consisting of material (mostly chondrules) that dates back from the birth of the solar system.
Chondrule	Solid particles composed mostly of olivine and pyroxene typically $\sim$300 μm in size. Chondrules often are the dominant constituent of chondrites.
Compound	The name given in chapter 4 for the objects that are obtained from the aggregation process which involves chondrules and (porous) dust.
DSMC	Direct simulation Monte Carlo
Debris disk	Gas-free or gas-poor disk, in which 'second-generation' dust is produced from a collisional cascade.

Continued on next page

—continued

Term	Description
Eddy	Part of a turbulent flow characterized by the same velocity structure. Phenomenologically, turbulence is the superposition of eddies of different scales.
IDP	Interplanetary dust particle
IR	Infra-red
ISM	Interstellar medium
Incremental accretion	The steady accumulation of small dust particles to form larger bodies.
MC	Monte Carlo
MMSN	Minimum Mass Solar Nebula
MRI	Magneto-Rotational Instability
Matrix	Predominantly silicate material that fills the spaces between chondrules in chondrites. The grain sizes of the matrix material are typically $\sim$1 μm but large variations exist.
Monodisperse	A distribution (of, *e.g.*, dust particles) that is composed of a single size.
Monomer	Smallest constituent particle (dust grain)
PCA	Particle cluster aggregation
Parent body	The body in which the meteorites were contained before its disintegration.
Planetesimal	A body large enough for its self-gravity to become important to capture or hold together smaller bodies. Typically $\gtrsim$km in size.
Protoplanetary disk	A flattened, gas-rich disk around a young star in which the planet formation process takes place.
RCP	Random Close Packing (filling factor $\approx$ 65%)
SED	Spectral energy distribution
Solar nebula	A synonym for protoplanetary disk, used mostly in relation to the young solar system.
T-Tauri star	A pre main-sequence star that obtains its energy mostly from gravitational contraction.
UV	Ultra-violet

List of Symbols

Symbol	Description
$\mathcal{E}^*$	reduced modulus of elasticity
Δv or Δv_{12}	relative velocity
Σ	surface density
Ω	angular (Keplerian) rotation frequency
Φ	gravitational potential
A	geometrical cross-section (1 particle)
C_ϕ	change in geometrical filling factor, $C_\phi = \phi/\phi^{\mathrm{ini}}$
C_{ij}	collision rate between particles i, j
D_f	fractal dimension
E	collision energy
E_restr, $E_\mathrm{max\text{-}c}$, E_frag	energy limits for particle restructuring/ maximum-compression/ fragmentation (§ 2.2.3)
$E_\mathrm{roll}, E_\mathrm{br}$	monomer rolling/breakup energy (§ 1.2.2)
G	Newton's gravitational constant
H_g	scale height of gas disk (Eq. (1.15)
K_{ij}	coagulation kernel or rate coefficient [$\mathrm{cm}^3\ \mathrm{s}^{-1}$] (velocity $\times$ collisional cross-section)
M_k	k-th moment of mass distribution
M_{L1}, M_{L2}	first, second most massive particle
$\mathcal{N}$	initial number of particles, $N_p(0)$ (chapter 5)
N	(mostly) total number of monomers within aggregate
N_ϵ	group splitting factor (Eq. (5.12))
N_μ	reduced number of monomers in collision $N_\mu = N_1 N_2/(N_1 + N_2)$
N_c	total number of contacts
N_f	number of big fragments
N_g	number of groups, $\sum_{i=1}^{N_s} w_i$

Continued on next page

—continued

Symbol	Description
N_p	number of total particles in simulations
N_s	number of species (distinct particles)
N_{tot}	total number of monomers in aggregates
M_{pwl}	mass in power-law component
R	heliocentric radius
$\mathcal{R}_{\text{gd}}$	spatial gas-dust ratio by mass
$\mathcal{R}_{\text{gc}}$	spatial gas-chondrule ratio by mass
$\mathcal{R}_{\text{cd}}$	spatial chondrule-dust ratio by mass
$\mathcal{V}$	simulation volume
Re	Reynolds number
S_{f}	spread in number of fragments of big component
St	particle Stokes number
P	pressure
T	temperature
V	geometrical volume (§ 2.2.2)
α	turbulent strength parameter (§ 1.2.1)
β	mass dependence of kernels as in $K \propto m^{\beta}$
γ	specific surface adhesion energy (surface energy density)
δ	exponent in surface area-mass ($A \sim m^{\delta}$) in fractal regime
ϵ	size ratio ($\epsilon \leq 1$)
η	nebula pressure parameter, number of particles or groups (§ 6.4.1)
$\phi, \phi_{\text{PCA}}, \phi_{\text{pd}}$	filling-factor (PCA/porous dust)
κ	number of coagulations
ℓ_{mfp}	mean free path of gas molecules
λ_{ij}	collision rate [s^{-1}] between species i and j (including duplicates)
ν_1/ν_2	Poisson ratios
$\nu_{\text{m}}/\nu_{\text{T}}$	molecular/turbulent viscosity
μ	molecular mass in units of unified atomic mass ($\mu \approx 2.34$)
ψ	enlargement parameter
ρ_{X}	gas density over MSN
$\rho_{\text{d}}, \rho_{\text{g}}$	spatial dust/gas density
$\rho_{\text{c}}^{(\text{s})}, \rho_{\text{d}}^{(\text{s})}$	specific material chondrule/dust density (bulk densities)
ρ_1, ρ_2	internal particle density
σ_{ij}	collision cross-section
τ_{f}	friction time
τ_{rain}	friction time at which particles are removed from simulation due to rain-out (chapter 2)
ξ_{crit}	critical displacement to initiate rolling of a contact area
a	geometrical radius (surface area equivalent radius)
a_σ	aggregate geometrical radius (projected surface equivalent radius)
a_μ	reduced radius
a_0	monomer radius
a_{c}	chondrule radius
a_{e}	equilibrium contact radius

Continued on next page

—continued

Symbol	Description
$a_{\rm dust}$	dust aggregate radius
$a_{\rm out}$	aggregate outer radius
b	impact parameter
$c_{\rm g}$	thermal sound speed
f_ϵ	maximum allowed fractional mass change of a particle during group collisions (chapter 5)
$f(m)$	particle distribution function (number density spectrum)
$f_{\rm comp}$	required dust fraction at collision for sticking (Eq. (4.16))
$f_{\rm d}$	compound dust fraction by mass (Table 4.2)
$f_{\rm geo}$	geometry factor (§ 4.2.3)
$f_{\rm miss}$	fraction of collision misses
$f_{\rm pwl}$	fraction of mass in power-law component
$f_{\rm p}$	compound porous dust fraction with respect to total dust mass (Table 4.2)
g_i	occupancy number of species i; number of duplicates
$h_{\rm p}$	particle (or dust) scale height
$k_{\rm B}$	Boltzmann constant
ℓ	eddy length scale
m	mass
m_μ	reduced mass
$m_\star$	characteristic mass of distribution determining the $\{z_i\}$ (§ 5.2.3)
$\langle m \rangle$	mean mass of the distribution M_1/M_0
$m_{\rm H}$	hydrogen mass
$m, m_{\rm d}, m_{\rm ch}$	(dust/chondrule) mass
m_p	peak mass of the distribution M_2/M_1
mw-.. or $\langle .. \rangle_m$	mass-weighted averages (see Eq. (2.26))
n	particle density (gas)
$\bar{r}$	random deviate
q	power-law exponent (size distribution)
t	time
$t_{\rm dd}, t_{\rm dc}, t_{\rm cc}$	dust-dust/dust-chondrule and chondrule-chondrule collision times (§ 4.2.4)
$t_{\rm L}/t_{\rm s}$	large/small eddy turn-over time (§ 1.2.1)
$v_{\rm K}$	orbital (Kepler) velocity
$v_{\rm rd}$	particle radial drift velocity (Eq. (1.25))
$v_{\rm K}$	orbital (Kepler) velocity
$v_{\rm s}/v_{\rm L}$	velocity smallest/largest eddies
w_i	group number; number of groups for species i
z_i	zoom number of species i

Color figures

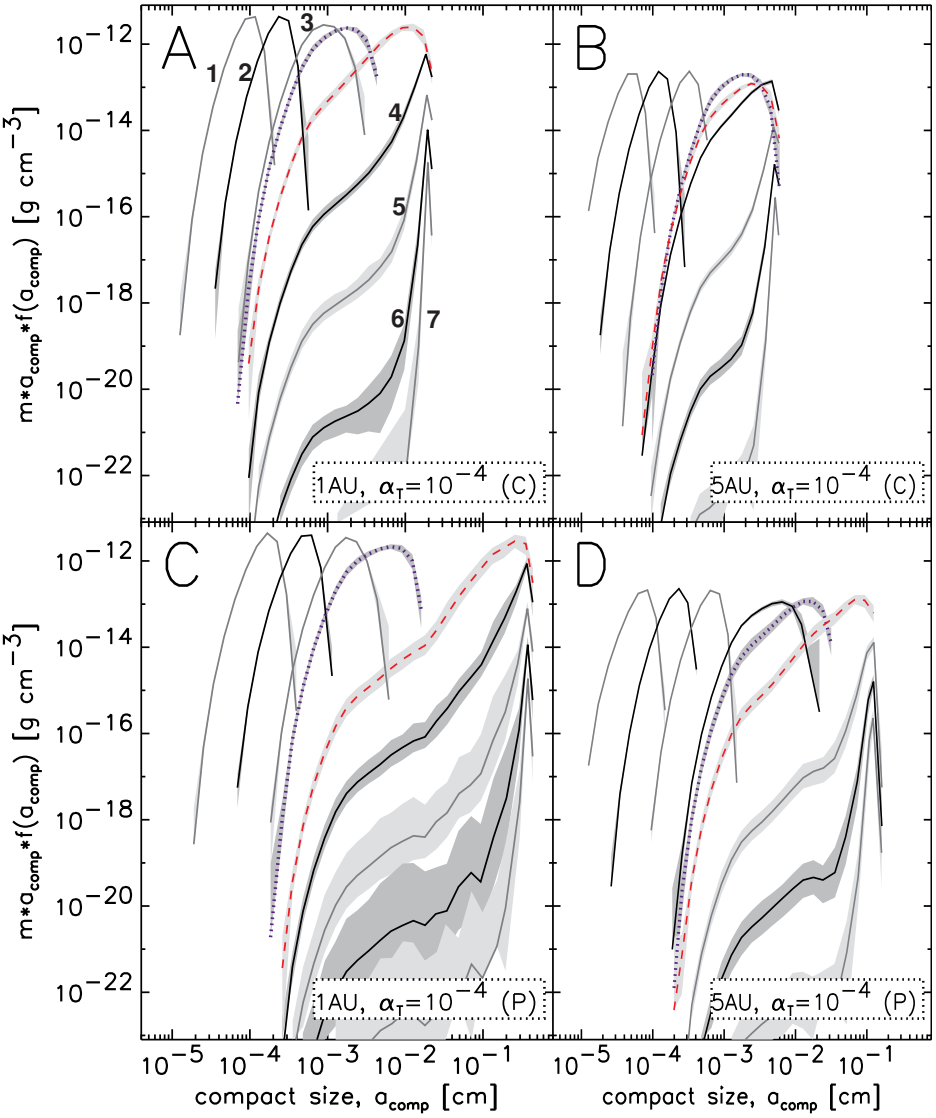

Fig. 2.10: The mass function plotted at various times for the $\alpha = 10^{-4}$ models. The panels compare the coagulation of the compact models ($\psi = 1$, *top* panels) with those where porosity effects are included (*bottom* panels). *Left* (right) panels show the coagulation of quartz (ice) particles at 1 AU (5 AU). Each plot shows the mass function at every logarithmic interval in time from $t = 10$ yr until $t = 10^7$ yr. In the first $\sim 10^2$ yr Brownian motion dominates the coagulation. Subsequent evolution is driven by turbulence-induced velocity differences and includes the moment of first compaction (*blue, dotted curve*) and first rain-out (*red, dashed curve*). After rain-out ($t \gtrsim 10^4$ yr), the mass density in the gaseous nebula decreases and the mass function collapses. In the compact models the blue, dotted curve also corresponds to the first time that $E > E_{\rm roll}$. Greyscales indicate the spread in the 50 realizations of the simulation.

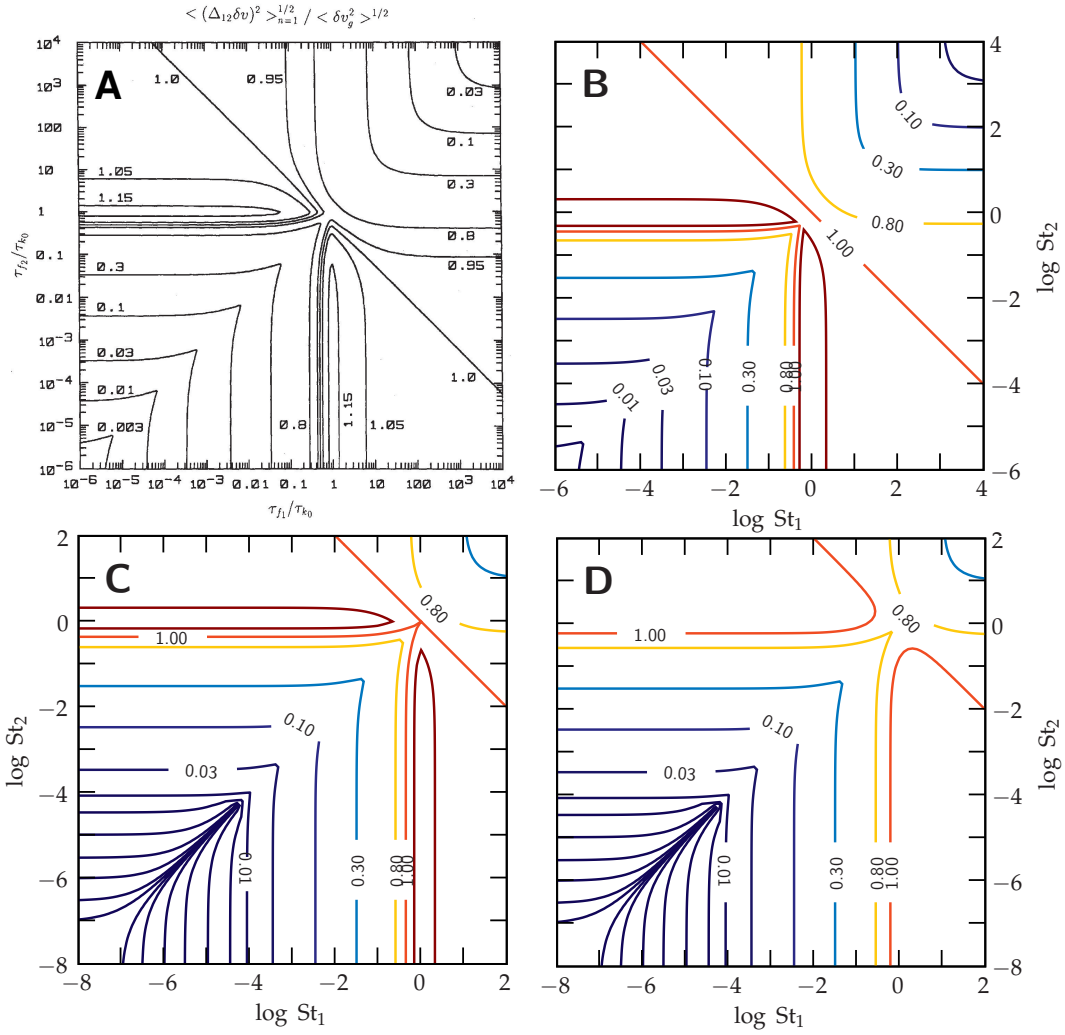

Fig. 3.4: (Chapter 2) Contour plots of particle-particle, turbulence induced, relative velocities Δv_{12} normalized to v_g. *(a)* Numerical results of Markiewicz et al. (1991), without inner scale (Re $\to \infty$). *(b)* Analogous result from our closed-form expressions with the fixed $y^* \approx y_a^* = 1.6$ approximation (§ 3.3.2). *(c)* Like *(b)*, but with an exact solution for y^* and with Re $= 10^8$. *(d)* Using the CH03 formula for k^*, $k^*/k_L = 0.5\mathrm{St}^* + 1$, and also with Re $= 10^8$. Contours are drawn twice per logarithmic decade (at $\Delta v_{12}/v_g = 3 \times 10^i$ and at 10^i) with an additional contour at 0.8 and 1.15.

Nederlandse Samenvatting

Gebaseerd op '*Werelden in Wording*'
Zenit, mei 2008

Sinds de jaren negentig worden met de regelmaat van de klok planeten buiten ons zonnestelsel gevonden. Deze zogeheten exoplaneten zijn vaak erg zwaar en staan in veel gevallen dicht bij de moederster. In bijna alle gevallen worden de exoplaneten overstraald en dat maakt het vinden van deze objecten erg lastig. Door de ontwikkeling van nieuwe, gevoelige instrumenten worden steeds meer exoplaneten ontdekt: in januari van dit jaar stond de teller op 271 planeten. In dit artikel bekijken we de vorming van planeten.

De eerste exoplaneet werd in 1995 ontdekt door de Zwitserse astronoom Michel Mayor. Hij vond een planetaire begeleider bij de ster 51 Pegasi in het sterrenbeeld Pegasus. Deze exoplaneet wordt sindsdien 51 Pegasi B genoemd. Zoals gezegd in de inleiding is het vinden van exoplaneten lastig en ontdekkingen zijn altijd indirect. Het bestaan van de planeet (of planeten) kan namelijk afgeleid worden uit de beweging van de moederster. Dit principe is een direct gevolg van de derde wet van Newton: als een voorwerp A een gegeven kracht op een voorwerp B uitoefent, dan gaat deze kracht gepaard met een even grote, maar tegengestelde kracht van B op A. De zon (A) trekt aan de aarde (B), wat resulteert in een beweging van de aarde om de zon met een snelheid van 30 km/s. Het omgekeerde geldt ook: de zon ondervindt een tegengestelde, maar even grote kracht. Oftewel: actie = reactie. De zon is echter veel zwaarder en is daarom de beweging een stuk kleiner. De mate van bewegen is omgekeerd evenredig aan de massa: aangezien de zon ongeveer 300 000 maal zwaarder is dan de aarde, is de snelheid van de zon als gevolg van onze planeet ongeveer tien cm/s. De beweging van de moederster is groter naarmate de planeten grotere massa's hebben en voor planeten die dichter bij de ster staan. De beweging van de

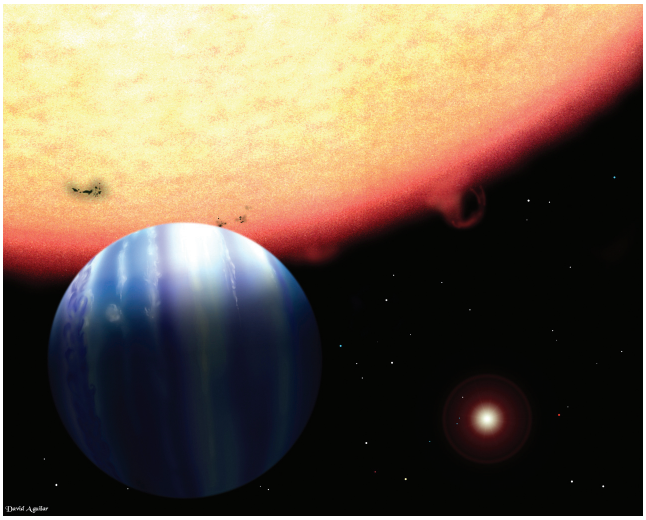

Figuur 3.1: Een impressie van een gasplaneet dicht bij de ster. Dit soort planeten wordt ook wel aangeduid als hete Jupiterachtigen. Artist impression: (David A. Aguilar, Harvard-Smithsonian CfA)

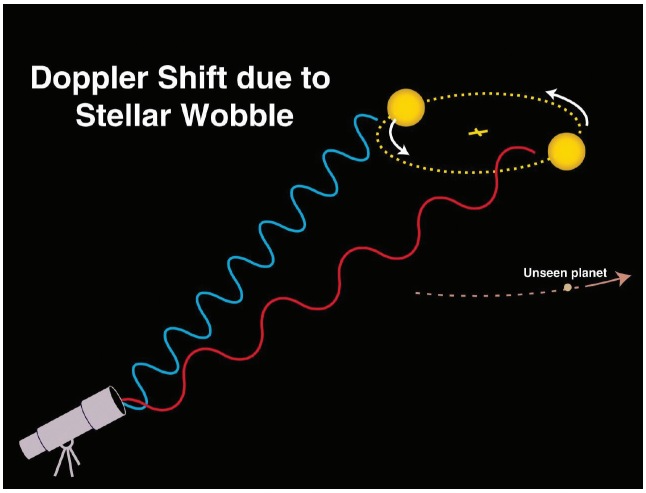

Figuur 3.2: Een schematische weergave van het Dopplereffect. De beweging van de ster ten opzichte van de waarnemer veroorzaakt een blauwverschuiving als de ster naar ons toe beweegt en een roodverschuiving als de ster van ons af beweegt. Deze verschuiving kan gemeten worden in het spectrum van de ster en zodoende kan de massa van de planeet bepaald worden. (Illustratie: obswww.unige.ch)

zon die door Jupiter wordt veroorzaakt is zo'n tien m/s en zou dertig m/s bedragen wanneer de reuzenplaneet op de plek van de aarde zou staan.

Deze beweging vinden we terug in het spectrum van de ster. Wanneer de ster naar ons toe beweegt, schuift het spectrum naar een kortere golflengte (het blauw) en wanneer de ster van ons af beweegt, gebeurt het omgekeerde (een verschuiving naar het rood). Dit verschijnsel staat bekend als het Dopplereffect. We kennen dit effect allemaal: wanneer een ambulance met loeiende sirene naar ons toe rijdt is de toon hoog en wanneer de ambulance passeert neemt de toonhoogte af.

In het geval van de ster is de verschuiving in golflengte heel klein, maar ze is toch te zien in het spectrum en vooral als het gaat om een zware planeet die dicht bij de ster staat. De indirecte methode van zoeken is succesvol, want momenteel zijn er 271

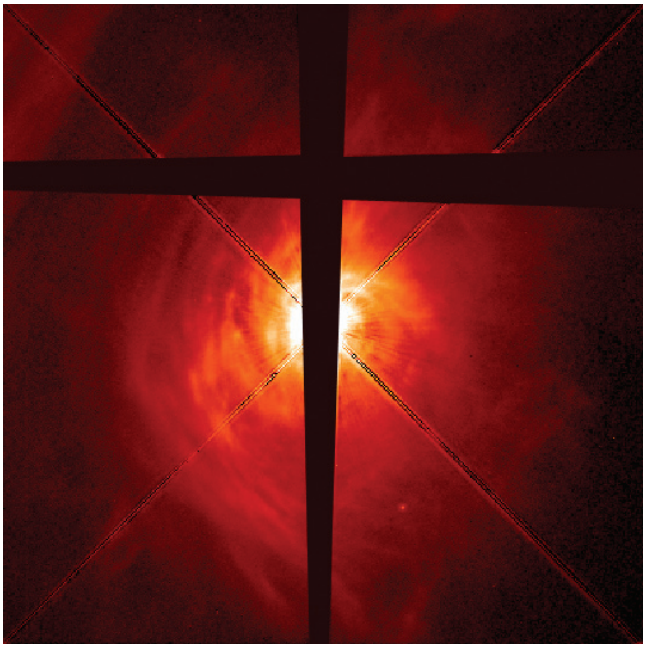

Figuur 3.3: Een opname van de protoplanetaire schijf rond de ster AB Aurigae. De ster bevindt zich op 469 lichtjaren van de aarde in het sterrenbeeld Voerman. Het licht van de ster is ten dele geblokkeerd om overbelichting te voorkomen. De schijf is erg uitgestrekt en meet ongeveer 1300 AE in diameter. Worden hier planeten gevormd? (Illustratie: Hubble Heritage Team/NASA)

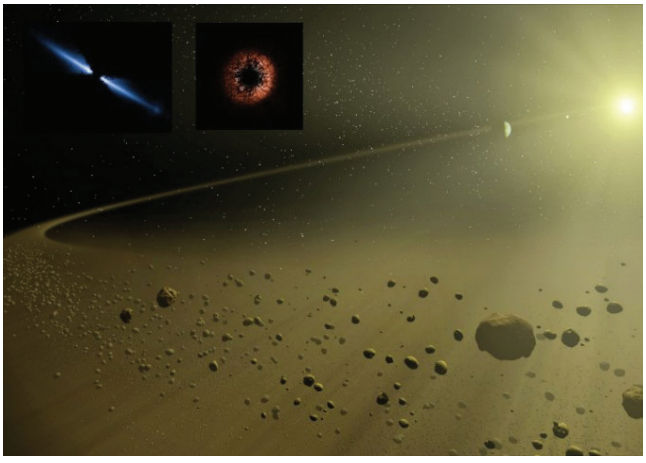

Figuur 3.4: Puinschijven zijn oude schijven waarvan het gas al verwijderd is. Alleen de brokstukken van botsingen tussen grotere objecten zijn overgebleven. Dit puin wordt door de stralingsdruk van de ster langzaam uit het planetenstelsel verwijderd. (Artist impression: Hubble Heritage Team/NASA)

exoplaneten bekend. Het is dan ook duidelijk dat planeetvorming een verschijnsel is dat vaker optreedt. Ons zonnestelsel is waarschijnlijk niet zo uniek als eens werd aangenomen.

Protoplanetaire schijf

Hoe ontstaan planeten? Deze vraag is niet eenvoudig te beantwoorden, want niemand heeft ooit een planeet zien ontstaan. Bovendien vindt de vorming van planeten dicht bij de ster plaats en ook nog eens in een schijf van kleine stofdeeltjes

(vergelijkbaar met roet). De stofdeeltjes vormen een gordijn waarachter het planeetvormingsproces zich afspeelt. Planeten ontstaan dus uit een schijf van gas (voornamelijk waterstof en helium) en stof. De roet- of stofdeeltjes zijn in feite diverse zware elementen die gecondenseerd zijn uit het gas.

De schijf is 'slechts een bijproduct van de ineenstorting: planeten ontstaan doordat de gaswolk ineenkrimpt. De gaswolk heeft een kleine rotatiesnelheid, maar door de ineenkrimping neemt de snelheid toe. Door de toenemende rotatiesnelheid valt niet alle materie op de protoplaneet, maar vormt ze een schijf: de zogeheten protoplanetaire schijf. Moderne bureaustoelen zijn ideaal om deze natuurwet in beeld te brengen: neem plaats en draai rond, met armen en benen gespreid. Trek na een aantal rondjes armen en benen in: de rotatiesnelheid zal dan toenemen. Het bestaan van protoplanetaire schijven werd in 1983 bevestigd door waarnemingen met de Infra-Rood Astronomische Satelliet (IRAS).

Vormingsproces

Hoe worden planeten nu precies gevormd? Het is bekend dat het gas in de schijf door allerlei processen langzaam verwijderd wordt. Dit gebeurt bijvoorbeeld doordat het op de ster valt, maar ook door foto evaporatie. In dat laatste geval wordt een waterstof (H_2) molecuul uit de schijf vernietigd door botsing met een UV-foton (lichtdeeltje). Hierbij komt zoveel energie vrij dat het gasdeeltje uit de schijf kan ontsnappen. Men schat dat deze processen een protoplanetaire nevel binnen enkele miljoenen jaren kunnen schoonvegen.

Planeten zoals Jupiter moeten dus binnen enkele miljoenen jaren zijn ontstaan, want anders had Jupiter nooit een gasmantel kunnen krijgen. Hoe moeten we ons dit voorstellen? Volgens een van de theorieën is de gasschijf zeer zwaar en ontstaan planeten op dezelfde wijze als de zon: de zwaartekracht veroorzaakt instabiliteit die leidt tot de vorming van een gebonden object. Volgens dit model worden planeten zoals Jupiter dus in een keer gevormd.

De andere aanname is iets minder ambitieus en gaat er vanuit dat planeetvorming een geleidelijk proces is van stofdeeltjes die aan elkaar plakken. Dit begint bij stofdeeltjes ter grootte van een micron, zoals die overal in het Melkwegstelsel voorkomen (een micron is 1/1000 van een millimeter). Deze deeltjes plakken aan elkaar en vormen stofdeeltjes van een millimeter. Deze groeien tot metersgrote stofballen en naarmate dit proces vordert ontstaan objecten met een doorsnede van een kilometer; dit worden planetesimalen genoemd (voorlopers van planeten). De planetesimalen groeien sneller, want de zwaartekracht bespoedigt het samenklonteren.

De rol van het stof

Dat stof een belangrijke rol speelt in het planeetvormingsproces is iets wat buiten kijf staat. De aarde bijvoorbeeld bestaat (met uitzondering van een zeer dunne dampkring) alleen uit zware elementen zoals ijzer en silicium. De voor het leven zo belangrijke koolstof is in mindere mate vertegenwoordigd. Er zijn aanwijzingen dat ook de gasplaneten Jupiter en Saturnus een rotsachtige kern hebben die groter is dan op grond van de samenstelling verwacht mag worden.

Het beste bewijs komt misschien wel van de exoplaneten. Uit de waarnemingen

is gebleken dat bij sterren met een relatief grote hoeveelheid zware elementen de kans op een exoplaneet groter is. Het lijkt er dus op dat er zware elementen nodig zijn om een planetenstelsel zoals het onze te kunnen vormen; de zon is wat dit betreft inderdaad meer dan gemiddeld bedeeld in het aandeel zware elementen. Dit betekent niet dat de theorie van het geleidelijke proces geen obstakels kent.

Belemmeringen

Er zijn genoeg belemmeringen te bedenken: een van de belangrijkste is dat het plakken van deeltjes niet zo eenvoudig is als het klinkt. Hoe goed iets plakt, hangt af van het materiaal (ijsdeeltjes plakken beter dan zanddeeltjes), de grootte en snelheid van de botsende deeltjes. Voor stofdeeltjes kleiner dan een millimeter is het geen probleem: het kleine spul plakt gewoon goed en de snelheden waarmee ze botsen zijn laag.

Voor macroscopische objecten–in de orde van een centimeter en groter–ligt dit anders. Door hun grootte plakken ze moeilijker aan elkaar. Dit komt doordat de plakkracht in relatie staat tot het oppervlak, terwijl de hoeveelheid materiaal die aan elkaar geplakt een directe relatie heeft met het volume (of de massa). De effectiviteit van het plakken neemt af voor grotere deeltjes. Bovendien zorgt de interactie met het gas ervoor dat juist deze objecten grote onderlinge snelheidsverschillen zullen hebben. Het is heel moeilijk om onder deze omstandigheden het plakken te bewerkstelligen; je zou eerder verwachten dat deze deeltjes uit elkaar spatten. Relatieve snelheden mogen daarom niet te hoog zijn.

Botsingen

Objecten groter dan ruwweg 100 meter worden qua botsingsgedrag beïnvloed door de zwaartekracht. Dit heeft twee gevolgen voor het samenklonteringsproces: de kans op een botsing wordt vergroot, omdat objecten elkaar aantrekken, en de aantrekkingskracht zorgt voor een natuurlijk plakmechanisme. Het samenklonteringsproces verloopt in dit stadium dan ook vrij snel. Grotere deeltjes zullen sneller groeien dan kleinere. In vaktermen wordt dit 'runaway growth' genoemd: de grote jongens eten alles op. Echter, de groei van een planeet is beperkt door de hoeveelheid materiaal die hij kan oprapen. Een aantal grote lichamen consumeert al het kleine materiaal, maar houdt een onderlinge afstand omdat ze zich in verschillende banen bevinden.

Een rotsachtige planeet zoals de aarde is ontstaan nadat een groot aantal objecten ter grootte van de maan op elkaar botsten. Tijdens deze megabotsingen (krachtiger dan de explosie van 100 miljard x miljard ton TNT) is de aarde in haar geheel gesmolten en gevormd, wat heeft bijgedragen aan haar differentiatie: de zwaarste elementen (ijzer) kwamen in de kern en de lichtere (zoals koolstof) vinden we in de buitenste lagen.

De grote planeten in het buitenste deel van het zonnestelsel ontstonden door gas te ontrekken aan de protoplanetaire nevel. Dit gebeurde al bij een tiende van de aardmassa, maar kwam bij ongeveer tien aardmassa's pas echt op gang. In het vroege zonnestelsel waren botsingen meer regel dan uitzondering: de vele kraters op de maan zijn hier een bewijs van. Veel van deze botsingen veroorzaakten een

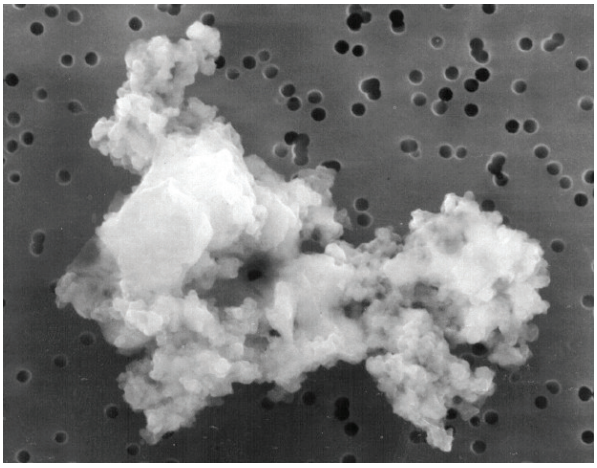

Figuur 3.5: Dit stofdeeltje met een diameter van ongeveer tien micrometer (1/100 millimeter) is letterlijk uit de bovenste lagen van de aardse atmosfeer geplukt. De samenstelling van dit soort stofdeeltjes verschaft veel informatie over de processen die in het jonge zonnestelsel van belang waren. (Bron: NASA)

Figuur 3.6: Volgens een van de theorieën is de maan ontstaan door een botsing in het vroege zonnestelsel. De maan stond vroeger veel dichter bij de aarde en bijvoorbeeld zonsverduisteringen kwamen veel vaker voor. De jonge aarde was het slachtoffer van veel meteorietinslagen, waarvan de grotere catastrofale gevolgen hadden. (Artist impression: David A. Aguilar, Harvard-Smithsonian CfA)

complete vernietiging van het materiaal. Het stof uit de tweede generatie wordt ook wel puin genoemd en de schijf wordt in zon geval een debris disk (puinschijf) genoemd.

Uiteindelijk nam het aantal planeten en planetesimalen af en werden de botsingen minder talrijk. Het zonnestelsel belandde hierdoor in een stabiele fase. Het proces, waarbij puin langzaam werd vermalen tot gruis, is nog steeds gaande. Op een heldere nacht kunnen we de sterk uitgedunde stofschijf zien in de vorm van het zodiakaal licht. Uiteindelijk zal het gruis door de stralingsdruk van de zon uit het zonnestelsel worden verwijderd.

Bijproducten

De voorgaande alinea's beschrijven voornamelijk de situatie van ons zonnestelsel. De planetenstelsels die zijn waargenomen bij andere sterren (met Jupiter-achtige planeten dicht bij de moederster) steken echter heel anders in elkaar. Dit is ten dele te

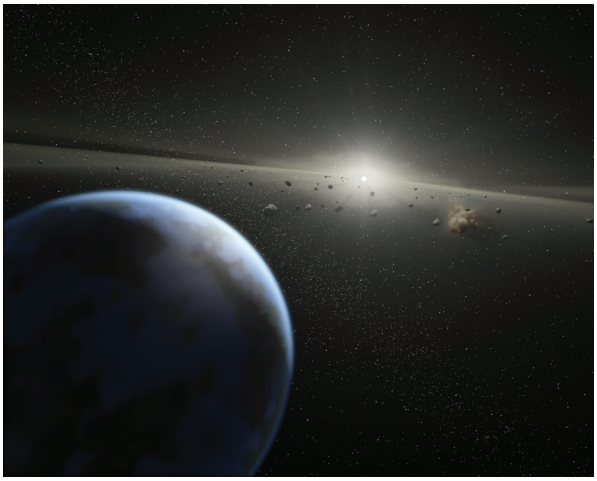

Figuur 3.7: Een asteroïdengordel rond de oranje dwergster HD 69830 in Puppis. De gordel werd ontdekt door NASA's Spitzer Space Telescope, die warm stof ontdekte in de nabijheid van de ster. Waarschijnlijk is dit warme stof ontstaan door de botsing van twee asteroïden. Op de voorgrond zien we een van de drie exoplaneten die om de dwergster draaien. (NASA/ JPL-Caltech/T. Pyle (SSC).

verklaren doordat deze planeten veel gemakkelijker met de Dopplertechniek worden opgemerkt dan wanneer ze zich op een afstand van vijf Astronomische Eenheden (AE) of verder zouden bevinden. Het kan zijn dat deze gasachtige planeten wel ontstaan zijn in de buitenste delen van het stelsel, maar in een latere periode naar binnen zijn geëmigreerd. Het zal nog een wel een tijd duren voordat het hele planeetvormingsproces volledig duidelijk is, maar het staat vast dat planeten minder exotisch zijn dan aanvankelijk gedacht werd. In feite zijn het de bijproducten van sterren.

Acknowledgments

After an effort of four years—a period occasionally troubled by frustration but quite enjoyable for most of the time—this work has (momentarily) come to a close. It was, altogether, a good time. Perhaps one of the more attractive features of an academic profession is that there is considerable freedom in making choices, and that the future is therefore unknown. This work, then, can to some extent be regarded as the product of opportunism—its existence being unimaginable four years ago.

I owe a lot of this opportunistic element to my promotor, Xander Tielens. His tentacles stretched across 5 000 miles. When I thought that our understanding on issues had finally settled, I often thought wrong: this scientific maverick could always find another twist or suggest an extension to an already voluminous work. I sometimes felt this thesis would cross the 1 000 mark had I followed all of Xander's suggestions. Understandably, it sometimes led to rather fierce debates. But in the process they also significantly improved the quality of this thesis.

One of the more defining moments, of course, was Xander's decision to move to a sunnier place on this planet. It was here, at NASA-Ames, that I came into contact with Jeff Cuzzi and, in a broader context, the great world of the meteoriticists. I really enjoyed the visits to the bear state, which also turned out to be very productive.

This thesis also owes a lot to my second promotor, Marco Spaans. Marco's ability to very quickly understand my often ill-ordered thoughts always gave a satisfactory turn to our frequent meetings. It really was as if we were tuned to the same frequency when discussing science problems. Over the years our relationship strengthened, resulting in a series of enjoyable dinners—a tradition that I hope is set to continue.

I also enjoyed the many visits to our sister institute, the Anton Pannekoek, in Amsterdam. After a journey of $\sim$3 hours by public transport I was always welcomed by a fresh cup of coffee and the familiar faces of Carsten Dominik and my comrade-in-arms, Dominik Paszun. It was really from the Dominiks that I learned the intimate details of the fabulous world of dusty aggregates.

Life as an astronomer is unthinkable without experiencing a different atmosphere from time-to-time. Indeed, I visited many places and the people I encountered always greeted me with the greatest hospitality. As an example, I recall the visits to NASA Ames (Andy, Joe, Josh, Lou, Els & Jan, and the 'South Bay Belgians') and to the planetary science group of Jürgen Blum at the TU-Braunschweig.

Back in Groningen (which literally and figuratively 'tops' the Netherlands) I always appreciated the cosmopolitan environment of the Kapteyn Institute. Indeed, I sometimes wonder what makes this place in 'old Europe' so attractive to all these foreigners. I would like to thank everybody who contributed to this thesis for their support. These include: the secretaries for helping me with the university bureaucracy; the computer-group for their patience with my 'CPU-experiments;' the ISM-group for its casual meeting format; the University of Groningen, NWO, and LKBF for their financial support; Niels Bos for the thesis cover; and many fellow PhD-students for their advice, corrections to my writing skills, and the necessary relaxation. Last, but not least, I must pay tribute to the 'hard core' (whose definition I leave intentionally vague) with whom I shared many enjoyable evenings.

Ultimately, I must attribute this thesis to my immediate family. I want to thank my father for his continuous support to pursue an academic career, my mother for always offering a welcome break to the sometimes hectic city life, and the rest of my family for their encouragement and curiosity.

Christiaan Wessel Ormel
Groningen, August 2008